Investigation on Coupling Phenomena between Morphological Variations and Mass Transfer Rate on Lithium Metal Negative Electrode for Rechargeable Batteries with High Performance and Safety

Tetsuo Nishida

Contents

3. Galvanostatic Li Electrodeposition in LiTFSI-PC Electrolyte: Part II. Coupling Phenomena in Growth Process   50

4. Galvanostatic Li Electrodeposition in LiTFSI-PC Electrolyte: Part III. Nucleation Behavior   79

5. Potentiostatic Li Electrodeposition in LiTFSI-PC Electrolyte

8. Improvement of Non-flammable Phosphoric Ester Electrolyte for Lithium Metal Batteries by Mixed Salts of LiPF$_6$, LiPO$_2$F$_2$ and LiNO$_3$

Chapter 1

General Introduction

1.1 Old but new Li metal negative electrode in battery progress

Human beings are facing the challenge of realizing a sustainable society as we are witnessing abnormal weather conditions caused by the rapid progression of global warming, and are being forced to search for alternative energy sources to depleting fossil fuels due to resource issues surrounding securing the world's ever-increasing energy consumption. Higher-performance energy storage devices are increasingly required. Although lithium-ion batteries have established a prominent position due to their excellent properties, further performance improvements are eagerly awaited. Achieving both increasing energy density, i.e., how much electricity can be stored in a limited space, and ensuring safety are key issues to be addressed at present.

Since Lewis [1] demonstrated the redox potential of lithium (~3.04 V vs SHE), which also possesses the lightest weight (0.534 g cm^{-3}), it has been long considered as a promising negative electrode material. In 1958, Harris reported [2] that lithium metal is stable in nonaqueous solvents despite its high reactivity. It was noted that the passive film formed on the surface of lithium inhibited its continuous reaction with organic solvents. From the 1960s to the 1970s, primary lithium batteries were successively commercialized [3-6].

The development of lithium metal rechargeable batteries began earlier than lithium ion batteries. This is because the commercialization of primary lithium batteries strengthened the need for rechargeable secondary batteries. In 1976, Exxon's Whittingham first proposed and developed a lithium metal rechargeable battery with a TiS_2 positive electrode and Li metal negative electrode [7]. In the 1980s, Moli Energy commercialized a Li metal rechargeable battery [8] that combined a MoS_2 positive electrode with a Li metal negative electrode (MOLICELL TM), and millions of cylindrical cells came on the market. However, as we have experienced in the electrodeposition of

various metals in aqueous solution, metal electrodeposition is accompanied by the formation of so-called dendrites. Li was not an exception. In 1989, Li metal batteries used in cellular phones frequently caught fire, presumably due to short circuits, eventually resulting in a recall [9-10]. Although NEC and Mitsui, the investors, conducted a thorough investigation and identified dendrite formation as the cause, they were unable to overcome the safety issue. This event marked a turning point in the disappearance of lithium metal rechargeable batteries. The path of lithium metal as negative electrode was closed. Thereafter, intercalation-type lithium-ion batteries using graphite were first commercialized by Sony in 1991. It has gained market support due to its superior safety compared to lithium metal batteries. As a result, research and development of Li metal negative electrodes has virtually stopped, and the focus and trend of R&D has shifted to Li-ion batteries. The performance of Li-ion batteries has been developing progressively, and the capacity of 18650-type Li-ion batteries has been dramatically improved, as shown in Figure 1-1[11]. However, lithium ion batteries are currently beginning to show limitations in energy density. There is a common view that an extension of the evolution will not provide the solutions necessary for the sustainable society. The development of next-generation batteries that will play a role of post-Li ion battery is gaining momentum. These next-generation battery have the potential to double the cell energy of conventional lithium-ion batteries. Li metal negative electrodes are essential in Li-S (sulfur) batteries and Li-air batteries, which are being actively studied as next-generation storage batteries [12-14]. State-of-the-art lithium-ion batteries have an energy density of 300 Wh kg^{-1}, but an energy density of 500 Wh kg^{-1} or higher is considered to be necessary to achieve a cruising range equivalent to a gasoline car. If Li-S and Li-air systems are realized having energy densities of about 600 Wh kg^{-1} and 1000 Wh kg^{-1}, respectively, they will be comparable to gasoline cars.

Humanity may have faced the need for a Li metal negative electrode even without experiencing the past difficulties of Li metal batteries. However, as we look back, the technology was not yet mature at that time. It is precisely because of these failures that the high-performance Li ion battery was born and has supported the development of today's society. It is now time to

attempt to revive the Li metal negative electrode, and understanding the mysterious dendrites and their suppression is a new field of research. Fundamental understanding of Li deposition and dissolution reactions during charging and discharging is proceeding along with the progress of evaluation technology. A revolution is underway toward the realization of Li metal negative electrodes.
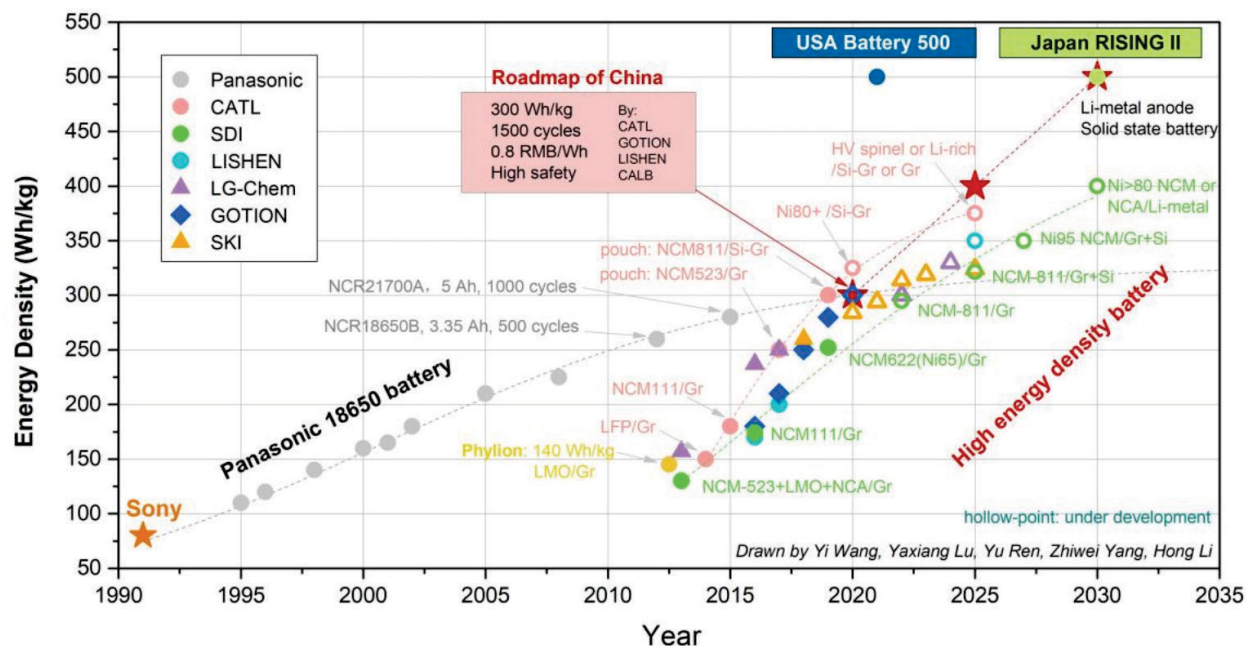
Figure 1-1. The roadmap stated in the EU's Battery 2030+ [11].

1.2 Dendrite formation during metal electrodeposition in aqueous solution

Electrodeposition of metals in aqueous solution has been extensively studied over the years in the fields of such as electrorefining, metal plating and lead batteries with respect to the effect of electrodeposition conditions on the deposited morphology [15]. The relationship between dendrite growth and concentration boundary layer thickness and electrode surface roughness in metal electrodeposition in aqueous solution has been reported [16]. Fukunaka et al [17-18] made

measurements of the concentration distribution around dendrites of Ag electrodeposited in 3M AgNO$_3$ solution with holographic interferometry. Ag$^+$ is reduced on the substrate surface, Ag atoms form clusters, surface diffusion agglomeration occurs, dendrite precursors surpass the surface roughness of the substrate, and dendrites begin to grow. In other words, (1) a steep concentration gradient is formed at the tip of the dendrite that preferentially grows from the precursor, and a specific dendrite tip preferentially grows as if it breaks through the concentration distribution curve of Ag$^+$ ions formed to surround the tip, and (2) the other parts are left at the electrode surface or at the root of the preferentially growing dendrite, as if they are electrically shielded by the concentration distribution curve around the preferentially growing dendrite tip, or the root of the preferentially growing dendrite is slightly dissolved. The Ag$^+$ ion concentration at the substrate surface calculated from the number of deviations of the interference fringes clearly reaches a depletion state, which reveals the formation of a steep concentration gradient at the dendrite tip. It was also suggested that Ag dendrite growth was progressing at the dendrite tip where the local current density was 30 times higher than the apparent average current density. Furthermore, (3) confocal laser microscopic observation of the preferentially growing Ag dendrite surface revealed that screw transitions with huge steps as thick as 1 μm grow on the terrace surface, which is considered to be a low-index Ag single-crystal plane of several tens of μm in size as if like a debris flow, fill the terrace, spring out from the screw transition source and renew low-index plane one after another [19].

Once dendrite precursor begins to form, dendrite growth is accelerated by the concentration of electric force line and steep concentration gradients at the tip. For controlling the morphology of electrodeposited Li, it is very important to deepen our understanding of the relationship between dendrite formation and a series of coupled phenomena of mass transfer and nucleation & growth in the electrolyte and SEI (Solid Electrolyte Interphase). Based on these previous studies for the coupled phenomena between the morphological variation and ionic mass transfer rate associated with metal electrodeposition reactions in aqueous solution, the dendrite growth phenomenon

associated with lithium electrodeposition should be also examined from the viewpoint of similarities and differences from the materials science point of view.

1.3 Li dendrite growth on electrolyte/electrode interface

Since lithium metal is thermodynamically unstable in organic electrolyte solvents, SEI is formed by decomposition of the electrolyte before Li deposition. SEI formed on the electrode surface is generally considered to have a significant impact on the cycle performance of lithium metal batteries. SEI formation and growth consume lithium metal and electrolyte and cause capacity loss, but they are also responsible for passivation of the lithium metal surface and suppression of side reactions. Dendrites grow on the negative electrode during charging and are electrically isolated from the substrate during discharging because the dissolution rate of Li is non-uniform depending on the dendrite site [20-21]. This "dead lithium" is electrochemically inert, but chemically highly reactive due to its large surface area. SEI layer is not usually robust enough to allow lithium morphological variations and destroyed by Li dendrites growth [22]. Since the SEI growth and dendrite formation are closely related, the characteristics and uniformity of the SEI may significantly affect the morphology of the lithium metal negative electrode.

Li deposition at the electrode/electrolyte interface should be divided into three stages. One is the nucleation and growth process immediately after the start of electrolysis. It differs from the nucleation and growth process of electrodeposition in aqueous solution by the presence of SEI. The second is the process in which the generated nuclei grow in the SEI and protrusion from the SEI layer into the electrolyte. The third process is the development of Li precipitates that protrude from SEI into the electrolyte and grow into dendrites. Solvated Li$^+$ diffuses from the bulk electrolyte to the vicinity of the electric double layer near the electrode and then desolvates. Li cations diffuse through the SEI and are reduced to Li atoms (adatom) at the electrode surface. Li atoms are either involved in nucleation through cluster formation by surface diffusion or agglomeration, or incorporated into an already deposited Li metal lattice. Li nucleation & growth

and Li$^+$ mass transfer in SEI have not been fully discussed in Li dendrite formation, but may influence the subsequent deposit morphology. The growth of Li deposits protruding from the SEI occurs competitively with the SEI formation reaction. As it has been debated whether the Li growth point is tip or root [23-27], the Li growth point is considered to be affected by SEI properties, electrodeposition conditions and mass transfer characteristics. During the development of dendrites into the electrolyte, Li$^+$ transport is affected by diffusion and convection. The concentration gradient becomes steeper near the dendrite tip, and then dendrite growth is accelerated by the concentration of electric force lines. Each deposition process is considered to be closely related to each other. It is necessary to trace back how the deposition conditions affected on each process and how the deposition morphology changed in order to clarify the factors responsible for the dendrite formation.

In recent years, through cutting-edge analytical techniques such as low-temperature transmission electron microscopy (cryo-TEM)[28,29] to analyze the Li/SEI interface, synchrotron radiation tomography for analysis of emerging Li microstructure and in-situ nuclear magnetic resonance (NMR)[30] , the mysterious phenomena is gradually being unveiled. They are shedding light on the phenomena occurring at the Li metal negative electrode.

1.4 Non-flammability electrolyte

The higher the energy density of batteries, the greater the damage in the event of an incident is expected to be, so ensuring safety is also a major issue. When a short circuit occurs in a lithium-ion battery, an extremely large current passes through the shorted area and generates heat. Exothermic reactions such as the reaction between the negative electrode and the electrolyte, the decomposition of the electrolyte, the reaction between the positive electrode and the electrolyte, and the oxygen combustion reaction due to the release of oxygen from the positive electrode occur continuously, resulting in eventual thermal runaway and ignition [31-32]. In particular, conventional electrolytes have a low flash point and boiling point, which can cause fires and

explosions [33]. Many techniques have been reported to improve the safety of rechargeable batteries such as surface modification of separators and negative electrodes [34-36]. However, a charged battery remains a dangerous state since energy is so to speak packed together with a flammable and combustible organic electrolyte. The fundamental solution is to make the electrolyte non-flammable [37-39].

The approach of converting a liquid electrolyte to a solid electrolyte comes to mind at once to prevent the electrolyte from burning. Solid electrolyte will eliminate the risk of liquid leakage. Solid electrolytes can be divided into inorganic solid electrolytes and polymer solid electrolytes [40-41]. Inorganic solid electrolytes have the problem of high interface resistance, and sulfide-based solid electrolytes may cause the generation of hydrogen sulfide. Solid polymer electrolytes are flexible and lightweight, but they are inherently flammable materials, albeit non-volatile. There is a risk of ignition or smoking in the event of a short circuit. For automotive batteries, energy density is important from the standpoint of cruising range, and at the same time, power and regenerating characteristics are also important. Obviously, the Li ion transfer at the active material interface must be smooth. In this respect, it is presumed that the liquid electrolyte still maintains its advantage.

One means of making electrolytes nonflammable is to use ionic liquids as electrolyte solvents. Various ionic liquids have been synthesized and reported because of their low flammability, non-volatility, thermal stability, ionic conductivity and electrochemical stability. As shown in Figure 1-2, a conventional Li ion battery electrolyte will burn immediately if an ignition source is introduced, whereas an ionic liquid will not burn. It is an attractive material as an electrolyte for Li ion or Li metal batteries, which require strict safety requirements. However, the viscosity is considerably higher than that of common organic electrolytes, which inevitably leads to poor rate characteristics. Although there is potential for applications where heat resistance is important and rate characteristics are not strictly required, improving rate characteristics is an issue [42-43].

Another approach to making electrolytes nonflammable is the use of nonflammable solvents or their application as additives. Phosphorus flame retardants have a long history as additives for

resins, such as phosphoric esters/phosphonic acid, phosphorous acid, phosphazene, and other phosphorus compounds. The radical scavenging mechanism of phosphorus provides effective flame retardancy [44]. Among them, phosphoric esters such as trimethyl phosphate (TMP) and triethyl phosphate (TEP) have been studied for application to both Li-ion and Li metal batteries due to their high dielectric constant, favorable viscosity and liquid temperature range [45]. Electrochemical stability and the resulting SEI properties are critical to battery properties. TMP and TEP were not compatible with graphite or Li metal negative electrodes [46-47]. To solve these problems, some attempts have been made to suppress the decomposition of phosphoric ester by increasing salt concentration [48-49] or locally increasing the salt concentration by diluting with an inert solvent [50]. Further improvements are needed for the realization of flame retardants that can provide SEIs enabling high coulomb efficiencies and suppressing dendrite growth for lithium metal negative electrodes.

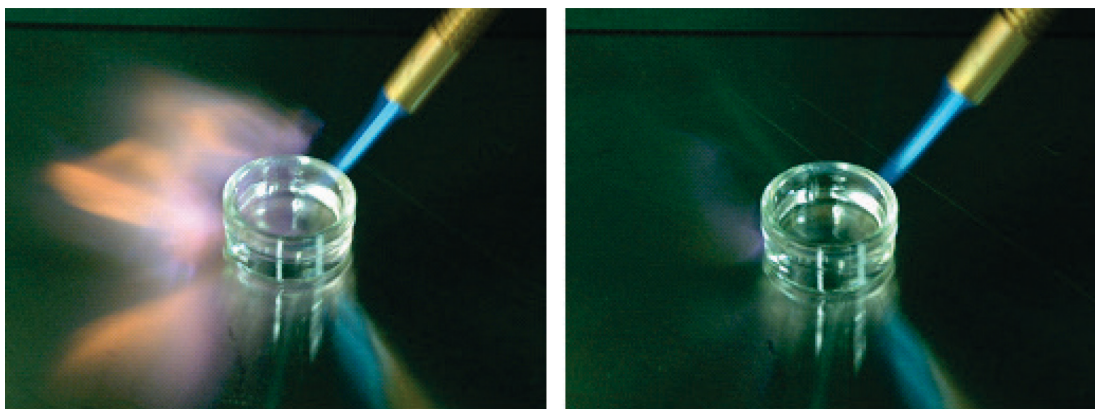Figure 1-2.　Flammability of organic electrolytes (left) and ionic liquid (right).

1.5　Goals and outline of this research

Based on the background mentioned above, purpose of this study is to provide fundamental results for physical modeling of the Li nucleation and growth process at the electrolyte/electrode interface in organic electrolyte and ionic liquid for Li metal batteries mainly from the

phenomenological viewpoint. The author will attempt to reveal the relationship between the morphological change and mass transfer phenomena from the Li nucleation and growth in SEI to the growth in the electrolyte during the very early stage of Li deposition and dendrite development, which will be useful for the material design of safe and efficient Li metal batteries. An outline of this thesis is presented below.

In Chapter 2, galvanostatic electrodeposition up to 100 mC cm^{-2} will be performed in 1M LiTFSI/PC (lithium bis(trifluoromethanesulfonyl)imide/propylene carbonate) electrolyte varying current densities. The purpose of this chapter is to investigate the effect of current density on the deposit morphology by comparing SEM images and potential change behavior during the initial stage of electrodeposition.

In Chapter 3, the objective is to investigate how the deposit morphology identified in the initial process presented in Chapter 2 changes thereafter depending on the current density. Deposition behavior and dendrite generation depending on current density are observed by optical microscopy and compared with the potential change. The author will also attempt to derive the limiting current density of Li deposition on a vertical cylindrical Ni electrode and compare the results with those obtained by LSV (linear sweep voltammetry) measurements.

In Chapter 4, the author will focus on the electrodeposition behavior from the start of electrolysis up to 10 mC cm^{-2}, which is further back than the initial process in Chapter 2, in order to investigate the nucleation and growth process of Li. Image processing is performed on SEM images up to 100,000 times magnification to analyze the number and size of deposits. These results along with the potential changes are discussed with reference to the classical nucleation and growth theory of metal electrodeposition in aqueous solution.

While Chapters 2 to 4 dealt with Li electrodeposition under galvanostatic conditions, Chapter 5 will discuss electrodeposition under potentiostatic conditions. In galvanostatic electrolysis, SEI is formed before Li deposition, but Li deposition and SEI formation are expected to occur simultaneously in potentiostatic electrolysis. The objective of this chapter is to attempt to separate the nucleation process from the growth process by a double-pulse potential method and to

investigate the effects of applied potential on the deposit morphology.

In Chapter 6, Li electrodeposition is performed under galvanostatic conditions using an ionic liquid electrolyte instead of the LiTFSI/PC electrolyte used in Chapters 2 through 5. *N*-methoxymethyl-*N*-methylpyrrolidinium bis (trifluoromethanesulfonyl) imide is used as the ionic liquid from the viewpoint of electrochemical stability and viscosity, and lithium bis(trifluoromethanesulfonyl)imide is dissolved as a lithium salt. As in Chapter 2, the author will observe the deposition behavior by optical microscopy and discuss the effect of current density on the deposition morphology, dendrite generation and growth behavior and corresponding potential changes.

Chapter 7 aims to develop flame-retardant electrolytes using phosphate ester solvents from a more practical viewpoint. The author will investigate Li deposition behavior in a nonflammable electrolyte composed of TEP and lithium difluorophosphate, and evaluate coin-cell characteristics using the electrolyte.

Chapter 8 aims to improve the properties of the nonflammable electrolyte obtained in Chapter 7. The author will use lithium nitrate and lithium difluorophosphate mixed with lithium hexafluorophosphate as the salts and attempt to optimize the composition to maximize the cell performance. The resulting electrolyte is also evaluated for flame retardance by an easy ignition test.

References

[1] G. N. Lewis and F. G. Keyes, The potential of the lithium electrode, J. Am. Chem. Soc., 35, 340–344 (1913).

[2] W. S. Harris, Ph.D. Thesis. Univ. California; Berkeley, CA, USA, Electrochemical Studies in Cyclic Esters, 1958.

[3] W. F. Meyers and J. W. Simmons, U.S. Patent 3,423,242, Electric Current-Producing Cell with Anhydrous Organic Liquid Electrolyte, 1969

[4] A. V. Fraioly, W. A. Barber and A. M. Feldman, U.S. Patent 3,551,205, 1970.

[5] A. A. Schneider and J. Moser, U.S. Patent 3,674,562, 1972.

[6] M. Fukuda and T. Ijima, In Power Sources; Collins, D. H., Ed; Academic Press: London, Vol. 5, p 713, 1975.

[7] M. S. Whittingham, Electrical energy storage and intercalation chemistry, Science, 192, 112 (1976).

[8] M. A. Py and R. R. Haering, Structural destabilization induced by lithium intercalation in MoS_2 and related compounds, Can. J. Phys., 61, 76–84 (1983).

[9] K. Brandt, Historical development of secondary lithium batteries, Solid State Ionics, 69, 173–183 (1994).

[10] M. S. Whittingham, Lithium batteries and cathode materials, Chem. Rev., 104, 4271–4302 (2004).

[11]https://battery2030.eu/wp-content/uploads/2022/07/BATTERY-2030-Roadmap_Revision_FINAL.pdf

[12] W. Xu, J. Wang, F. Ding, X. Chen, E. Nasybulin, Y. Zhang and J. G. Zhang, Lithium metal anodes for rechargeable batteries, Energy Environ. Sci., 7, 513 (2014).

[13] Y. Sun, N. Liu and Y. Cui, Promises and challenges of nanomaterials for lithium-based rechargeable batteries, Nat. Energy, 1, 16071 (2016).

[14] J. Qian, B. D. Adams, J. Zheng, W. Xu, W. A. Henderson, J. Wang, M. E. Bowden, S. Xu, J. Hu, and J. G. Zhang, Anode-Free Rechargeable Lithium Metal Batteries, Adv. Funct. Mater., 26, 7094 (2016).

[15] J. L. Barton and J. M. Bockris, The electrolytic growth of dendrites from ionic, Proceedings of the royal society A, 268, 1335 (1962).

[16] A. R. Despic, K. I. Popov, Modern Aspects of Electrochemistry 7, p 119.

[17] Y. Fukunaka, T. Yamamoto and Y. Kondo, Ionic mass transfer associated with electrocrystallization of silver, Electrochim. Acta, 34 (10), 1393-1400 (1989).

[18] Y. Fukunaka, T. Yamamoto and Y. Kondo, Electrodeposition of silver under direct and pulsed current, J. Electrochem. Soc., 136(11), 3278 & 3630 (1989).

[19] T. Wakatsuki, T. Homma and Y. Fukunaka, 64th ISE Meeting, Lausanne (2014); Coupling Phenomena between Micromorphological Evolution and Ionic Mass Transfer Rate during Ag Electrodeposition in $AgNO_3$ Aqueous Solution

[20] C. Fang, J. Li, M. Zhang, Y. Zhang, F. Yang, J. Z. Lee, M.-H. Lee, J. Alvarado, M. A. Schroeder, Y. Yang, B. Lu, N. Williams, M. Ceja, L. Yang, M. Cai, J. Gu, K. Xu, X. Wang and Y. S. Meng, Quantifying inactive lithium in lithium metal batteries, Nature, 572, 511–515 (2019).

[21] S. Xu, K.-H. Chen, N. P. Dasgupta, J. B. Siegel and A. G. Stefanopoulou, Evolution of Dead Lithium Growth in Lithium Metal Batteries: Experimentally Validated Model of the Apparent Capacity Loss, J. Electrochem. Soc., 166, A3456 (2019).

[22] J.-F. Dingab, R. Xu, C. Yan, B.-Q. Li, H. Yuan, J.-Q. Huang, A review on the failure and regulation of solid electrolyte interphase in lithium batteries, J. Energy Chem., 59, 306-319 (2021).

[23] M. Arakawa, S.-I. Tobishima, Y. Nemoto, M. Ichimura, and J. Yamaki, Lithium electrode cycleability and morphology dependence on current density, J. Power Sources, 43, 27–35 (1993).

[24] O. Crowther and A.C. West, Effect of electrolyte composition on lithium dendrite growth, J. Electrochem. Soc., 155, A806–A811 (2008).

[25] D.R. Ely and R.E. García, Heterogeneous nucleation and growth of lithium electrodeposits on negative electrodes, J. Electrochem. Soc., 160, A662–A668 (2013).

[26] A. Kushima, K.P. So, C. Su, P. Bai, N. Kuriyama, T. Maebashi, Y. Fujiwara, M.Z. Bazant and J. Li, Liquid cell transmission electron microscopy observation of lithium metal growth and dissolution: root growth, dead lithium and lithium flotsams, Nano Energy, 32, 271–279 (2017).

[27] P. Bai, J. Li, F.R. Brushett and M.Z. Bazant, Transition of lithium growth mechanisms in liquid electrolytes, Energy Environ. Sci., 9, 3221–3229 (2016).

[28] Y. Li, Y. Li, A. Pei, K. Yan, Y. Sun, C.-L. Wu, L.-M. Joubert, R. Chin, A. L. Koh, Y. Yu, J. Perrino, B. Butz, S. Chu and Y. Cui, Atomic structure of sensitive battery materials and interfaces revealed by cryo-electron microscopy, Science, 358, 506 (2017).

[29] M. J. Zachman, Z. Tu, C. Snehashis, L. A. Archer and L. F. Kourkoutis, Cryo-STEM mapping of solid–liquid interfaces and dendrites in lithium-metal batteries, Nature 560, 345 (2018).

[30] V. Küpers, M. Kolek, P. Bieker, M. Winter and G. Brunklaus, In situ 7Li-NMR analysis of lithium metal surface deposits with varying electrolyte compositions and concentrations, Phys. Chem. Chem. Phys., 21, 26084-26094 (2019).

[31] A. Hammami, N. Raymond, M. Armand, Runaway risk of forming toxic compounds, Nature, 424, 635–636 (2003).

[32] X. Feng, M. Ouyang, X. Liu, L. Lu, Y. Xia and X. He, Thermal runaway mechanism of lithium ion battery for electric vehicles: A review, Energy Storage Mater, 10, 246–267 (2018).

[33] P. Balakrishnan, R. Ramesh and T.P. Kumar, Safety mechanisms in lithium-ion batteries, J. Power Sources, 155, 401–414 (2006).

[34] S. Deng, B. Xiao, B. Wang, X. Li, K. Kaliyappan, Y. Zhao, A. Lushington, R. Li, T.-K. Sham and H. Wang, New insight into atomic-scale engineering of electrode surface for long-life and safe high voltage Lithium ion cathodes, Nano Energy, 38,19–27 (2017).

[35] K. Liu, W. Liu, Y. Qiu, B. Kong, Y. Sun, Z. Chen, D. Zhuo, D. Lin and Y. Cui, Electrospun core-shell microfiber separator with thermal-triggered flame retardant properties for lithium-ion batteries, Sci. Adv., 3, e1601978 (2017).

[36] K. Liao, S. Wu, X. Mu, Q. Lu, M. Han, P. He, Z. Shao and H. Zhou, Developing a "Water-Defendable" and "Dendrite-Free" lithium-metal anode using a simple and promising $GeCl_4$ pretreatment method, Adv. Mater., 30, 1705711 (2018).

[37] W. Chen, T. Lei, C. Wu, M. Deng, C. Gong, K. Hu, Y. Ma, L. Dai, W. Lv, and W. He, Designing safe electrolyte systems for a high-stability lithium-sulfur battery, Adv. Energy Mater., 8, 1702348 (2018).

[38] N. Chawla, N. Bharti and S. Singh, Recent advances in non-flammable electrolytes for safer lithium-ion batteries, Batteries, 5, 19 (2019).

[39] Q. Wang, L. Jiang, Y. Yu and J. Sun, Progress of enhancing the safety of lithium ion battery from the electrolyte aspect, Nano Energy, 55, 93–114 (2019).

[40] J. Wan, J. Xie, X. Kong, Z. Liu, K. Liu, F. Shi, A. Pei, H. Chen, W. Chen and J. Chen, Ultrathin, flexible, solid polymer composite electrolyte enabled with aligned nanoporous host for lithium batteries, Nat. Nanotechnology, 14, 705–711 (2019).

[41] Y. Shen, Y. Zhang, S. Han, J. Wang, Z. Peng and L. Chen, Unlocking the energy capabilities of lithium metal electrode with solid-state electrolytes, Joule, 2, 1674–1689 (2018).

[42] D.R. MacFarlane, N. Tachikawa, M. Forsyth, J.M. Pringle, P.C. Howlett, G.D. Elliott, J.H. Davis, M. Watanabe, P. Simon and C.A. Angell, Energy applications of ionic liquids, Energy Environ. Sci., 7, 232–250 (2014).

[43] X. Lin, R. Kavian, Y. Lu, Q. Hu, Y. Shao-Horn and M.W. Grinstaff, Thermally responsive, nonflammable phosphonium ionic liquid electrolytes for lithium metal batteries: operating at 100 degrees celsius, Chem. Sci., 6, 6601–6606 (2015).

[44] T. Tsujikawa, K. Yabuta, T. Matsushita, T. Matsushima, K. Hayashi and M. Arakawa, Characteristics of lithium-ion battery with non-flammable electrolyte, J. Power Sources, 189, 429–434 (2009).

[45] X. Wang, E. Yasukawa and S. Kasuya, Nonflammable trimethyl phosphate solvent containing electrolytes for lithium-ion batteries: I. Fundamental properties, J. Electrochem. Soc. 148, A1058–A1065 (2001).

[46] S. Zhang, M.S. Ding, K. Xu, J. Allen and T.R. Jow, Understanding solid electrolyte interface film formation on graphite electrodes, Electrochem. Solid State Lett., 4, A206–A208 (2001).

[47] S. Zhang, K. Xu, T. Jow, EIS study on the formation of solid electrolyte interface in Li-ion battery, Electrochim. Acta, 51, 1636–1640 (2006).

[48] J. Wang, Y. Yamada, K. Sodeyama, E. Watanabe, K. Takada, Y. Tateyama and A. Yamada, Fire-extinguishing organic electrolytes for safe batteries, Nat. Energy, 3, 22−29 (2018).

[49] Z. Zeng, V. Murugesan, K. S. Han, X. Jiang, Y. Cao, L. Xiao, X. Ai, H. Yang, J-G. Zhang, M. L. Sushko and J. Liu, Non-flammable electrolytes with high salt-to-solvent ratios for Li-ion and Li-metal batteries, Nat. Energy, 3, 674−681 (2018).

[50] L. Yu, S. Chen, H. Lee, L. Zhang, M. H. Engelhard, Q. Li, S. Jiao, J. Liu, W. Xu and J-G. Zhang, A Localized High-Concentration Electrolyte with Optimized Solvents and Lithium Difluoro(oxalate)-borate Additive for Stable Lithium Metal Batteries, ACS Energy Lett., 3, 2059−2067 (2018).

Chapter 2

Galvanostatic Li Electrodeposition in LiTFSI-PC Electrolyte: Part I. Effects of Current Density in Initial Stage

2.1 Introduction

Lithium has a small electrochemical equivalent of 6.9 g per Faraday and the lowest standard electrode potential of -3.045 V among metals. These properties may suggest the advanced battery with lithium metal negative electrode, which demonstrates the characteristics of lightweight and a high operating voltage as an ultimate design of energy storage devices for transportation fields. However, lithium metal negative electrodes frequently face to dendrite formation phenomena during charging/discharging operations. It has hindered the practical application of rechargeable batteries due to safety issues arising from short circuits as well as degradation problems in reversibility and durability associated with dead lithium. The key to their practical use as negative electrodes for secondary batteries is the controllability of lithium metal dendrite formation [1].

The electrodeposition of Li in organic electrolytes involves inherently the formation of the solid electrolyte interphase (SEI) unlike the electrodeposition of metals in an aqueous solution. The complexity of the SEI structure makes it more challenging to interpret Li electrodeposition reaction and dendrite growth. Two major models were proposed for the structure of SEI. Peled et al. [2] proposed that SEI has a two-layer structure with a dense inorganic layer near the electrode (inner layer) and a porous organic layer near the electrolyte (outer layer). They proposed a mosaic model in which the inner layer is composed of multiple inorganic materials through which only lithium ions can move and solvated lithium ions and solvent molecules can only penetrate the outer

16

layer. Aurbach et al. [3] subsequently proposed a multilayer model consisting of inorganic and organic layers. Recently, the structure of SEI was successfully characterized at the atomic scale by cryo-electron microscopy analysis by Cui and co-workers [4-5], which greatly advanced the understanding of SEI. They found that the SEI microstructure changes depending on the electrolyte composition and discussed its influence on Li precipitation and dissolution behaviors. Thus, the research from the chemical and structural aspects of SEI is certainly important. The research is still underway for investigating where Li ions receive electrons to produce Li atoms or where the Li atoms diffuse and nucleation occurs underneath or in the above-mentioned heterogeneous-structured SEI layer [6]. It is expected that further discoveries on the SEI structure and Li electrodeposition reaction through the SEI will continue to be made in the future.

On the other hand, a fundamental understanding of the coupling phenomenon between the morphological change of the electrode and ionic mass transfer rate during electrode reactions is also of great significance for the viewpoints of maintaining the reversibility of advanced energy storage devices with Li metal negative electrode and developing prediction methods for their lifetimes. To gain a better understanding of dendrite formation behavior, it is essential to investigate two perspectives. The first is the nucleation and growth behavior of Li in SEI, i.e., the formation behavior of dendrite precursors, and the second is morphological changes of the precursors into dendrites, i.e., the dendrite growth behavior.

As for research on dendrite formation behavior, for example, Mönig et al. [7] reported the observed results of growing Li bush galvanostatically electrodeposited on a copper foil at a low current density of 10 μA cm^{-2}. According to their study, the growth occurred both at the tip and the base of the Li filament in the bush. Bazant et al. [8] reported three growth modes for Li deposition on Li in organic electrolytes depending on current density. The first is the tip growth above limiting current density (Sand capacity) based on the Sand equation due to instability caused by Li ion depletion. The second is the root growth below the threshold value (6mA cm^{-2}) due to internal stress accumulation and release associated with Li precipitation under stable SEI. The third is the surface growth between the threshold value and the limiting current density which

17

develops into a mossy-like shape through isotropic surface growth in regions scarcely covered by SEI due to the Li precipitation. These reports mainly address Li deposition behavior during dendrite development.

The author also observed dendrite growth behavior in organic electrolytes and ionic liquids. A two-step diffusion process was suggested based on the good linearity between dendrites' arm length and the square root of duration time measurements [9-11]. Moreover, our interferometric measurement of the Li^+ concentration distribution near the electrode surface accompanying Li electrodeposition demonstrated an interesting phenomenon: the so-called "incubation period" (roughly 10 mC cm^{-2}) has been noticed during which the interference fringes do not change immediately after the start of electrolysis [12]. The period has been considered to originate from the formation of SEI due to the decomposition of solvents and impurities such as water in the electrolyte. Thus, the transition up to about 100 mC cm^{-2} before the entire appearance of dendrites seems to be very important for the subsequent Li deposition behavior. Furthermore, the author empirically recognizes from our previous Li deposition experiments that the potential change exhibits complex behavior in the initial stage of galvanostatic Li electrodeposition depending on the current density, but there has been no detailed investigation of the relationship between such potential behaviors and morphological variations of electrodeposited Li as far as the author knows. It is indispensable to further investigate where the differences in morphological variations and growth modes are originated back to the initial stage of electrodeposition. The purpose of this study is to focus on the nucleation and growth process of Li deposition on Ni substrate under galvanostatic conditions and to deepen our understanding of the very early stage of Li deposition (below 100 mC cm^{-2}), which may be a growth period of dendrite precursor. Galvanostatic Li deposition is performed at different current densities whose morphological variations are ex-situ observed in detail using an electron microscope. In parallel with the present research, the author is investigating flame-retardant electrolytes that can be applied to batteries consisting of lithium metal negative electrode - ternary oxide positive electrodes. Since a carbonate-based electrolyte is

used as a part of that flame-retardant electrolyte, LiTFSI/PC was chosen as the electrolyte for this research.

2.2 Experimental

The electrolyte is composed of lithium bis(trifluoromethane sulfonyl)imide (LiTFSI) and propylene carbonate (PC). LiTFSI was supplied from Stellachemifa Corporation as a test sample and dried for 24 h at 150 ℃ under a stream of nitrogen gas before use. A nonaqueous solvent of PC purchased from Kishida Chemical Co., Ltd. was used as received. The water content of the electrolyte was confirmed to be less than 20 ppm by Karl-Fisher titration (AQ-7, Hiranuma Sangyo Co., Ltd.).

Cyclic voltammetry (CV) and linear sweep voltammetry (LSV) were performed with a typical three-electrode cell in an argon glove box (dew point < -90 ℃). The working electrode was a 5 mm square Ni sheet with 80 μm thickness (Nilaco Corp.). The Ni sheets were cleaned according to the following procedure before use. First, they were degreased by ultrasonic cleaning in isopropyl alcohol (IPA) for 10 minutes. After sonication in ultrapure water for 10 minutes, they were immersed in a 10%-HCl solution for 10 minutes. Then, ultrasonic cleaning in ultrapure water was engaged for 10 minutes. After being rinsed with IPA, they were vacuum-dried at 100 °C for 8 h. The chamber of the vacuum dryer was replaced with nitrogen gas before heating and cooled to room temperature when taken out. The counter electrode and the reference electrode were made of Li foil with 200 μm thickness (Honjo Metal Co., Ltd.). Glass container used for the cyclic voltammetry cell was wholly installed into an aluminum block combined with a Peltier temperature control unit to keep the temperature at 25 °C. The measurements of CV and LSV were carried out using PGSTAT302N (AUTO LAB).

Chronopotentiometry was also performed with the electrolytic cell illustrated in Fig. 2-1. The working electrode (W.E.) of Ni wire 500 μm in diameter (Nilaco Corp.) was used. The author selected Ni wire in this study because it was used in our previous study on Li deposition behavior

in ionic liquid [10]. The pretreatment of the electrode was performed similarly to a method for Ni sheets. The upper part of Ni wire was coated by a fluorinated ethylene propylene (FEP) tube as a sleeve and the lower part end of Ni wire was capped by the FEP tube of which one side was heat-sealed. The position of the sleeve was adjusted so that the contact part of the nickel wire with the electrolyte becomes 10 mm. The exposed geometric surface area of the Ni wire was 0.157 cm^2, which was used for the calculation of current density. A lithium foil was used as a counter electrode (C.E.) and a reference electrode (R.E.). The electrolytic cell was mounted in the temperature-controlled aluminum block. Chronopotentiometry measurement was performed using a HZ7000 (Hokuto Denko).

The working electrode was rinsed in dimethyl carbonate after electrochemical measurements and dried in a vacuum for 10 h. Then, the substrate was supplied to X-ray photoelectron spectroscopy (XPS) and ultraviolet photoelectron spectroscopy (UPS) analysis (VersaProbe III; ULVAC PHI, Inc.) and scanning electron microscopy (SEM) (JSM-7800F; JEOL) observation of deposits. The prepared electrode sample for analysis or observation was stored in a sealed transfer vessel in the glove box after electrochemical treatment, then transferred to the XPS or SEM chamber without exposure to air.

2.3   Results and Discussion

2.3.1   SEI formation preceding Li deposition

The CV (scan rate: 1 mV s^{-1}) of Li precipitation and dissolution on a Ni foil electrode (0.5 mm × 0.5 mm × 0.1 mm) in 1 M LiTFSI/PC is shown in Fig. 2-2(a).   From the inset enlarged near 0 V, a rapid change in current is observed from around -25 mV after passing through 0 V. This point can be regarded as the potential at which Li deposition begins. Fig. 2-2(b) shows the results of LSV when the end potential was varied from open circuit voltage (OCV) to 2 V, 1 V, 0 V and Li deposition potential, respectively. As the potential sweeps, the reductive current appears around 2.3 V and then reaches its peaks around 1.3 V, 0.8 V, 0.5 V and 0.2 V before Li deposition.

The results of XPS and UPS analysis of the electrode surface are shown in Fig. 2-2(c). Nickel oxides and hydroxides are present on the surface in OCV. From Ni2p, Ni is detected with decreasing intensity as the potential sweep up to 1 V but is no longer detectable below 0 V. The changes in Li1s, C1s, O1s and F1s suggest the formation of LiF along with a slight decrease in nickel oxides and hydroxides during sweeps down to 2 V. At 1 V, the formation of LiF and carbonate becomes more pronounced, and Li_2O becomes slightly visible. The formation of Li_2O is clearly visible on reaching 0 V. Referring to previous reports, the estimated reactions to which each LSV peak is attributed are presented in the Appendix.

The work function is obtained from the UPS measurement. Each of the values is approximately 5.3 eV for Blank, 2 V and 1 V, all of which are close to the work functions of Ni (5.35 eV for <111>). The work function increases rapidly when the potential is swept below 0 V. The electrode surface has some conductivity in the process of sweeping from OCV to 1 V, but it becomes less conductive during sweeping from 1 V to 0 V. Combined with the XPS results, this suggests the existence of an inorganic inner layer and organic outer layer, as has been proposed previously by Aurbach et al. [3].

2.3.2 Chronopotentiometry

Li deposition was performed under galvanostatic conditions from 0.04 to 60 mA cm^{-2} on Ni wire in 1M LiTFSI/PC. Fig. 2-3(a) shows the potential variation curves immediately after the start of electrolysis for coulomb quantities from 0 to 10 mC cm^{-2}. At any current density, the potential reaches a minimum after a coulomb quantity of a few mC cm^{-2} passes. The potential change before reaching such a minimum is not linear but several inclination points can be seen. Since every behavior depends on current density, *dV/dQ* curves up to 10 mC cm^{-2} are shown in Fig. 2-4 for comparison. The arrow indicates the point at which 0V is passed.

Every *dV/dQ* curve shows a steep negative peak immediately after the start of electrolysis over 0.4 mC cm^{-2}. It follows by several weak peaks depending on current density, and then rises

sharply at the point marked with a symbol of filled circle (●) in Fig. 2-4. Each peak seems to be related to the reactions seen in Appendix. It is thought that SEI film composed of LiF or Li_2CO_3 is formed after the start of electrolysis followed by the decomposition reaction of PC and the reduction of Li^+. The growth rate of the SEI decreases with the growth of SEI film due to the lowering of electron transfer and mass transport of organic molecules in the SEI film. From the point where dV/dQ begins to increase rapidly, i.e., the turning point marked by the symbol of filled circle (●), it is considered that the reduction of Li^+ begins to dominate over the preceding competitive reaction between SEI formation and Li deposition. Table 2-1 summarizes the coulomb quantity at the point when 0 V passes (Q_0; arrow in Fig. 2-4), at the point when dV/dQ rises sharply (Q_L; ● mark in Fig. 2-4) and the point of $dV/dQ = 0$ (the potential reach minimum) (Q_m). Q_L and Q_m are larger at lower current densities and (Q_L-Q_0) become larger at higher current density.

It can be deduced from Fig. 2-3(a) that the average rate of potential change before starting Li deposition is about 9 mV s^{-1} at 0.04 mA cm^{-2}, while it is 22500 mV s^{-1} at 60 mA cm^{-2}. The time required from the start of electrolysis to Li deposition differs by a factor of 3500. At higher current densities, the electrode reaction is presumably rushing into the Li deposition reaction region since the slower reaction rate cannot follow. It is expected that there will be differences in the SEI structure, defects, etc. between lower current densities at which multiple reactions occur sequentially and higher current densities at which several reactions cannot follow. Li deposition is expected to occur underneath the SEI with fewer defects at lower current densities than at higher current densities. As Qi et al. reported that the ionic conductivity of SEI depends on the grain size of LiF and Li_2CO_3 nanocrystals [13], characteristics of SEI may change depending on the size of the microcrystals constituting the SEI. The author believes that microcrystals with smaller grain size and larger number density are generated at higher current density because microcrystals are formed in a shorter time, while microcrystals with larger grain size and smaller number density are formed at lower current density because microcrystals are formed in a longer time.

As shown in Fig. 2-3(b) the potential reaches a minimum by 10 mC cm^{-2} and then increases monotonically from 0.04 to 2 mA cm^{-2}, while the potential reaches the second or third minimum

at 4 to 60 mA cm^{-2}. Depending on the current density, the behavior of potential change is characterized by whether it then increases monotonically after reaching the minimum or not. The current density of 4 mA cm^{-2} appears to be the transition boundary judging from Figs. 2-3 & 2-4.

2.3.3   SEM observation

Fig. 2-5 shows SEM images of the electrode surface at (a) 10 mC cm^{-2} and (b) 100 mC cm^{-2} during galvanostatic electrolysis under 0.2, 2, 8, 20 and 50 mA cm^{-2}. A significantly different appearance is noticed between at the lower and at the higher current density. At 10 mC cm^{-2} (Fig. 2-5(a)), a numerous number of initial nanoscale deposits with a size of several tens of nm are formed on the electrode surface at every current density. As the current density increases, the size of precipitates appears to moderately decrease, and their number tends to increase slightly. In the case of 0.2 and 2 mA cm^{-2}, nano-sized morphology apparently characterized as whisker-like precipitate can be already recognized.

Fig. 2-5(b) at 100 mC cm^{-2} illustrates that nanoscale deposits are growing into submicron size. Under 0.2 mA cm^{-2}, there is a mixture of whisker-like or rod-like deposits a few μm in length and granular deposits 300 - 400 nm in size. Whisker-like deposits appear to be shorter in length and more numerous under 2 mA cm^{-2} than the case of 0.2 mA cm^{-2}. Granular deposits are also visible behind the whisker-like deposits similar to SEM taken under 0.2 mA cm^{-2}. On the other hand, only rod-like deposits are found under 8 mA cm^{-2}. At 20 and 50 mA cm^{-2}, the rod length becomes even shorter and more uniform than 8 mA cm^{-2}. At 50 mA cm^{-2}, neighboring submicron deposits are observed to be in contact with each other and change to agglomerated morphology.

Nishikawa et al. [14] observed Li electrodeposition behavior on ultra-micro Cu electrodes. Electrolysis at 2 mA cm^{-2} up to 900 s in 1M LiTFSI/ethylene carbonate+diethyl carbonate (1:1) showed sparse and rather dendritic morphology. It is expected that even higher current densities will result in the development of more dense precipitation morphology similar to those observed in this study at higher current density in Fig. 2-5(b).

Next, the potential change is compared with the deposits' morphological variations. Fig. 2-6 and Fig. 2-7 show the results of SEM observations of the electrode surface at several points up to 100 mC cm^{-2} during electrolysis at 0.2 and 20 mA cm^{-2} respectively as well as the transition of the electrode potential.

As shown in Fig. 2-6, under 0.2 mA cm^{-2}, the potential reaches -39 mV (point A) at 5 mC cm^{-2}. From an equilibrium point of view, it is presumed that Li$^+$ is reduced to Li atoms on the substrate, but anything that looks like a deposit cannot be recognized on the electrode surface within the resolution of the SEM image. The potential then reaches -100 mV (point B) at 6 mC cm^{-2}. The electrode potential has not yet reached the minimum at this point, and the Li$^+$ reduction reaction should be in progress and nanoscale precipitates with a size of several tens of nm are found on the electrode surface. In the very initial process where the electrode potential changes from -39 mV to -100 mV as the coulomb quantity increases from 5 mC cm^{-2} to 6 mC cm^{-2}, it is reasonable to assume the formation of Li atom clusters through the active surface diffusion process on the Ni substrate in contact with the SEI layer, followed by the appearance of growing nano-scale precipitates on the SEI surface. Beyond 6 mC cm^{-2}, the potential reaches a minimum value of about -120 mV and slowly increases along with the increase in coulomb quantity.

At 10 mC cm^{-2} (C point, -29 mV), it is deduced that whisker-like deposits are beginning to be formed discretely nearby where there are expected to be more defect structures in the SEI layer. The formation of discrete whisker-like precipitates is also clearly observed in the images of Fig. 2-5(a), 0.2 mA cm^{-2}. At 15 mC cm^{-2} (D point, -20 mV), their appearance becomes more distinct and grows longer than 1 μm. In addition to the whisker-like deposits, island-shaped deposits appear. As the coulomb quantity increases from 50 mC cm^{-2} (E point, -13 mV) to 100 mC cm^{-2} (F point, -11 mV), the length of the whisker-like deposit increases to 2 - 3 μm and the island-like deposits gradually develop into distinct granular form. Since the originally formed nanoscale precipitates remain behind these growing deposits without much change in appearance, whisker-like and granular deposits are the growth form of nuclei that have survived the growth competition.

On the other hand, under 20 mA cm^{-2}, the potential reaches the minimum value of -375 mV immediately after the start of electrolysis and a rapid reduction reaction of Li$^+$ proceeds (Fig. 2-7). Then, the potential increases and reaches the maximum around -350 mV. This process is considered to correspond to the surface diffusion of Li atoms on the Ni substrate to develop the coagulation-growth process of Li clusters. Thereafter, the potential begins to decrease by the effect of the mass transport of Li ions in the SEI. Numerous nanometer-sized precipitates are almost uniformly formed on the substrate at 10 mC cm^{-2} (G point -380 mV). The appearance of uniform nanometer-size precipitates can be also confirmed in the images of Fig. 2-5(a), 20 mA cm^{-2}. Such a uniform-sized morphology is contrastively compared to discrete growth at a lower current density. Li deposition at higher current density exhibits extremely high overpotential, which may overcome the effect of SEI defect density differences and result in relatively uniform precipitates' growth. Closer observation reveals that some of the nanoscale precipitates have a microscopic bud-like morphology. Around 15 - 20 mC cm^{-2}, the potential again reaches a minimum and then gradually increases.

At 20 mC cm^{-2} (H point -390 mV), there are numerous micro bud-like morphologies. The potential variation to G and H is thought to reflect the transition process of Li cluster aggregates growing and breaking through the SEI layer to the emergence of rod-like morphology. During the period from G to H, the decrease in potential turns into an increase. The overpotential increases probably due to diffusion resistance during the growth process of the Li cluster in the SEI. However, once the growing Li clusters are projected out of the SEI into the electrolyte, the new electrolyte is immediately supplied to the tip of the growth interface, which is thought to be the reason why the overpotential decreases again.

In the stage from H to I (-370 mV), it can be seen that the size of the projecting parts is expanding. At the point H where Li deposits protrude into the electrolyte from the SEI layer, a competitive reaction between Li deposition reaction and the formation reaction of new SEI based on the microstructure of the original SEI layer is presumably taking place, resulting in the growth to the form of I. Some deposits (exemplified in I by yellow arrows) are a little taller than their

25

surroundings and rod-shaped precipitates appear to be formed. The rod-like deposits seem to have nearly the same diameter (seen in J, -360 mV). The transition from I to J can be interpreted as showing the growth process of nano-sized rod-like deposits accompanied by growing from their root.

2.3.4 *Li deposition under lower current density (0.2 – 2 mA cm^{-2})*

At lower current density, the potential increases monotonically after reaching the minimum as described in Fig. 2-8(a). As described in the section of *SEM observation*, it is assumed that a rather sound SEI film with fewer defects is formed at a lower current density. When Li nanoscale deposits grow to induce stochastically nanoscale cracks due to micromechanical friction and penetrate through the SEI film, they come into contact with the organic electrolyte (defined as "sprouting"). During the transition process from the initiation of Li deposition to sprouting, a negligibly small concentration overpotential of less than a few mV may be induced as Li$^+$ concentration at the interface between deposited Li and the SEI. Consequently, at lower current density, the electrode potential increases to a positive direction due to the effect of increased electrode area accompanying Li deposition unlike the complex potential variation that reflects the effect of concentration overpotential under the mass transport limitation at higher current density described later.

It is deduced that sprouting may provide an important event for subsequent growth modes. After sprouting, two possible growth points are expected for Li deposition. One is the thrusting-out point from the SEI into the electrolyte and another may be a kind of root-growth origin inside the SEI as described below. That is, the former means that the Li reduction reaction (Li$^+$(in PC) + e$^-$ = Li) occurs at the tip protruding from the SEI into PC, and the latter means the interface between the SEI and the Li deposits growing in the SEI before penetrating from the SEI where the reduction reaction (Li$^+$(in SEI) + e$^-$ = Li) occurs. In the solid or mechanistically sound part of SEI film, Li deposition is assumed to occur preferentially at the extruded edges from the SEI rather

than at the root in the SEI. The Li deposition at a lower current density can be considered to proceed simultaneously with whisker-like growth followed by granular growth in a manner that reflects the effect of SEI inhomogeneity.

Root growth mode was reported by Crowther et al. [15] and later investigated in detail by Mönig [7] and Bazant et al. [8]. In the present study, whisker-like growth due to root growth is observed over a wider range of current densities up to 100 mC cm^{-2}. Unlike the latter research group's results, such a growth mode is not unique for lower current density conditions. Furthermore, at lower current density, not only whisker-like deposits due to root growth but also granular precipitates were observed. The granular morphology seems to be consistent with the surface growth mode that appears at a current density between 6 mA cm^{-2} and the limiting current density described by them. As far as our speculation is concerned, the SEI began to form immediately after the Li metal substrate was brought into contact with the electrolyte in their experiments. When Li electrodeposition is performed under the pre-existence of stable SEI, whisker-like growth is expected only at lower current densities. In such a case, Li$^+$ is presumed to be depleted quickly around the growing interface in the SEI at a relatively lower current density and mossy lithium growth based on surface growth rather than root growth is expected.

2.3.5 *Li deposition under higher current density (4 - 60 mA cm^{-2})*

Under higher current density, the potential change demonstrates complex behavior as shown in Fig. 2-8(b). The period during which the potential is higher than Li$^+$/Li ranges from 0.93 to 0.033 s and the coulomb quantity consumed for SEI formation is about 3.7 to 2 mC cm^{-2}. The overpotential approaches almost constant after 4 mC cm^{-2}. Fig. 2-3(a) illustrates -140 to -870 mV at 10 mC cm^{-2} depending on the current density. Most of the applied electricity is consumed by Li deposition. Therefore, the nucleation behavior associated with Li deposition surely starts gradually deviating from its dependence on the surface defect chemistry of SEI on the Ni substrate to the mass transfer-controlling mode. Such a coupling phenomenon in the growth scenario is also

suggested by our preserving observations on Li dendrite growth under an optical microscope [9-11].

As imagined from the competitive rates between SEI formation and Li deposition, the reduced Li atom clusters under high overpotential tend to introduce SEI film with high defect density. SEM images show that a large number of Li atom clusters grow with the progress of electrolysis so that highly defective SEI film structures may provide template arrays in a sense. Then, growing deposit-tips thrust into the electrolyte almost simultaneously through the SEI film with high defect density.

In a non-dilute electrolyte with higher conductivity, the applied electricity is distributed almost uniformly over the envelop-surface composed of numerous precipitate tips before sprouting. As easily imagined, such a tip should be immediately covered with rather higher conductive new SEI simultaneously with sprouting because a portion of the current density assigned to the envelope surface should be directly distributed to the tips. After sprouting, root growth and surface growth at the tip proceed concurrently to form the precursor of rod-like precipitates. As the precursor forms the rod-shaped morphology, Li^+ ion concentration becomes depleted in the SEI as well as in organic electrolytes among the rod-like deposits. The lateral surfaces of rod-like deposits might be covered with sound SEI film generated under an electrically shielding condition. Such a shielding characteristic accompanying dendritic growth was interferometrically observed in Ag electrodeposition [16]. Generally, in an early stage of the electrodeposition where mass transfer resistance is negligible, the nucleation rate has an exponential characteristic with the overpotential [17]. Consequently, probably the number density of rods with uniform arm length increases and the length is shortened with increasing current density as shown in Fig. 2-5(b).

As illustrated in Fig. 2-3(b) & 2-8(b), sprouting phenomena may be defined with the appearance of the second minimum possibly due to the overpotential caused by mass transport of Li^+ in the SEI under higher current density. Then, the electrode potential gradually decreases due to the concentration overpotential generated in the SEI and in the Li rod array with the growth of rod-like morphology. Thereafter, the electrode potential again reaches a minimum between 1000

and 1500 mC cm^{-2} under the mass transfer controlling situation including organic electrolytes as demonstrated in Fig. 2-3(b).

As pointed out in our previous report [18-19], the density difference caused by the concentration difference at the electrolyte-deposits' interface and the displacement of the electrolyte according to deposits' growth is induced along with the progress of the electrodeposition. Such a kind of electrolyte convection may contribute to the potential change described above. In other words, it is believed that when these deposits grow in the electrolyte under higher current density, the Li$^+$ transfer rate in the electrolyte as well as in the SEI layer with an extremely large number of defects govern the growth rate of the deposits and significantly influences the coupling morphology of the Li deposits.

2.3.6 Mass transport in SEI

Based on the above discussion, the morphological variation of electrodeposited Li evolves through the nucleation and growth process, which is greatly affected by the defect density distribution within the SEI film and its mass transport properties. A quite simplified one-dimensional diffusion model is proposed as schematically shown in Fig. 2-9 to estimate the Li$^+$ concentration and Li$^+$ transport properties at the interface between deposited Li metal/SEI and between SEI/organic electrolyte under galvanostatic current densities of 4 mA cm^{-2} or higher.

The diffusion rate of Li$^+$ in the organic electrolyte is considerably faster than that in SEI. The non-steady diffusion field of Li$^+$ is treated in organic electrolyte and a quasi-steady diffusion field is assumed within the SEI film with constant thickness δ and with boundary conditions of Li$^+$ concentration at the deposited Li surfaces and at the SEI/PC electrolyte interface, i.e., $C_{EL}(0, t)$ and $C_{SEI}(-\delta, t)$ respectively. Both diffusion fields are coupled by $C_{EL}(0, t)$ over a certain computation period in this model.

$$\frac{\partial C_{EL}}{\partial t} = D_{EL} \frac{\partial^2 C_{EL}}{\partial x^2} \ (0 \ll x) \tag{2-1}$$

$$J_1 = J_2 = \frac{i}{F} = D_{SEI}\frac{\partial C_{SEI}}{\partial x} = D_{EL}\frac{\partial C_{EL}}{\partial x} \qquad (2\text{-}2)$$

$$C_{SEI}(0,t) = C_{EL}(0,t), \ C_{SEI}(x,0) = C_{EL}(x,0) = C_0, C_{EL}(\infty,t) = C_0 \qquad (2\text{-}3)$$

where D_{EL} and D_{SEI} are the diffusion coefficients of Li$^+$ in the electrolyte and in the SEI, respectively; J_1 and J_2 are the mass flux of Li$^+$ at the deposited Li metal/SEI interface and SEI/PC electrolyte interface, respectively; F is Faraday constant; i is current density; C_0 is the bulk concentration of the organic electrolyte.

$C_{SEI}(0,t)$ and $C_{EL}(0,t)$ are calculated with reported value D_{EL} and constant δ by assigning D_{SEI} value in order to adjust the observed sprouting phenomena. Mathematical equations may be simplified as follows, with t^* as the Li$^+$ transference number in the organic electrolyte:

$$C_{EL}(0,t) = C_0 - \frac{2i(1-t^*)}{F\sqrt{\pi D_{EL}}}\sqrt{t} \qquad (2\text{-}4)$$

$$\frac{i}{F} = D_{SEI}\frac{C_{EL}(0,t)-C_{SEI}(-\delta,t)}{\delta} \qquad (2\text{-}5)$$

$$C_{SEI}(-\delta,t) = \left\{C_0 - \frac{2i(1-t^*)}{F\sqrt{\pi D_{EL}}}\sqrt{t}\right\} - \frac{i\delta}{FD_{SEI}} \qquad (2\text{-}6)$$

The concentration overpotential η generated by a decrease in $C_{SEI}(-\delta,t)$ is written by

$$\eta = -\frac{RT}{F}\ln\frac{C_{SEI}}{C_0} \qquad (2\text{-}7)$$

From (2-6), (2-7)

$$D_{SEI} = \frac{i\delta}{F}\left\{C_0 - \frac{2i(1-t^*)}{F\sqrt{\pi D_{EL}}}\sqrt{t} - C_0 exp\left(-\frac{F}{RT}\eta\right)\right\}^{-1} \tag{2-8}$$

Also, the time t_c when Li^+ concentration on Ni substrate becomes depleted in observed sprouting phenomena, that is, $C(-\delta, t) = 0$, is obtained as follows

$$\sqrt{t_c} = \frac{F\sqrt{\pi D_{EL}}}{2i(1-t^*)}\left(C_0 - \frac{i\delta}{FD_{SEI}}\right) \tag{2-9}$$

In Fig. 2-8(b), one assumes that ΔV is induced by the concentration overpotential η generated between the inside of the SEI and the electrolyte. Table 2-2 shows the ΔV and Δt measured from Fig. 2-3(b) for the current density of 8 to 60 mA cm^{-2} where ΔV clearly appears. Here, the starting point of Li deposition was defined as the time of Q_L in Table 2-1 and the thickness of SEI was assumed to be $\delta = 30$ nm measured by ellipsometer [20] and cryo-transmission electron microscopy [21] in previous reports.

The diffusion phenomenon of Li^+ in SEI has been studied extensively using computational methods [22-23]. The diffusion coefficients previously reported vary considerably from 10^{-12} to 10^{-7}. The above-adjusted diffusivity D_{SEI}, as shown in Table 2-2, is found reasonably within these reported values. The time t_c was also evaluated from D_{SEI} and equation [9]. The relationship between t_c and current density is shown as a solid line in Fig. 2-10(a). The time t_c is illustrated as a dashed line when D_{SEI} is assumed to be from 10^{-10} to 10^{-7} (cm^2 s^{-1}) which is independent of the current density. In addition, Fig. 2-10(b) shows the calculated results of $C_{SEI}(-\delta, t)$ and $C_{EL}(0, t)$ up to 100 mC cm^{-2} based on D_{SEI} in Table 2-2, and the evolution of the concentration overpotential in that interval.

In the case of SEI formation with small D_{SEI} or with partially small D_{SEI} due to SEI heterogeneous characteristics reflecting defects density distribution, Li^+ is expected to be depleted immediately in the SEI and root growth is unlikely to occur. Surface growth is expected to advance

after sprouting in these cases. In the case of SEI formation with a relatively large D_{SEI}, root growth is expected to proceed until a certain time. At higher current density, Li ion concentration at the Ni/SEI interface drops more rapidly than at the SEI/electrolyte interface soon after electrolysis begins. Once Li$^+$ begins to be depleted in the SEI and even in the electrolyte, a transition mode on coupling phenomena is expected in the growth process due to an increase in concentration overpotential.

2.4 Conclusions

The effect of current density on the morphological variation during the initial stage (up to 100 mC cm^{-2}) of galvanostatic Li deposition on Ni wire was investigated at current densities ranging from 0.04 to 60 mA cm^{-2} in 1M LiTFSI/PC. The simultaneous growth of whisker-like and granular deposits was identified at lower current densities, while the development of uniform mesoscopic-sized Li rods was observed at higher current densities. A transition of morphological variations was observed at current densities around 4 mA cm^{-2}. The formation behavior of SEI, which occurs prior to the Li deposition reaction, also differed between higher and lower current densities. Due to the effect of current density on the SEI formation process, robust but non-uniform SEI with discrete defects was considered to be formed at lower current densities, while a rather defective SEI at higher current densities.

The event of sprouting, in which Li precipitates nucleated and grown underneath the SEI are extruded from the SEI into the organic electrolyte, was characterized as a change point that may have a significant influence on the subsequent growth mode. After sprouting, two cases were envisioned: one is the case in which Li deposits continue to grow through the SEI and develop into whisker-like morphology as if the pierced SEI layers were a template, and the other is the case in which Li deposits no longer grow through the SEI layers but in the electrolyte due to factors such as Li$^+$ depletion in the SEI or the inferior Li$^+$ transport properties of the SEI. The diffusion coefficient of Li$^+$ in the SEI galvanostatically formed on Ni substrate was estimated to be in the

order of 10^{-9} cm^2 s^{-1} by analyzing the behavior of potential change in the early stage of the electrolysis. It should be considered that the morphological changes during galvanostatic electrodeposition have already started through the nucleation and growth process in the SEI probably with different defect densities. A more detailed study on the coupling phenomena between mass transfer rate of Li$^+$ and morphological variation is needed to control the dendrite formation in the future.

References

[1] H.Zhang, G. G. Eshetu, X. Judez, C. Li, L. M. Rodriguez-Martínez and M. Armand, Angew. Chem. Int. Ed., 57, 15002-15027 (2018).

[2] E. Peled, The electrochemical behavior of alkali and alkaline earth metals in nonaqueous battery systems-the solid electrolyte interphase model, J. Electrochem. Soc., 126, 2047–2051 (1979).

[3] D. Aurbach, B. Markovsky, M. D. Levi, E. Levi, A. Schechter, M. Moshkovich and Y. Cohen, New insights into the interactions between electrode materials and electrolyte solutions for advanced nonaqueous batteries, J. Power Sources, 81, 95–111 (1999).

[4] Y. Li, Y. Li, A. Pei, K. Yan, Y. Sun, C-L. Wu, L-M Joubert, R. Chin, A. L. Koh, Y. Yu, J. Perrino, B. Butz, S. Chu and Y. Cui, Atomic structure of sensitive battery materials and interfaces revealed by cryo-electron microscopy, Science, 358, 506–510 (2017).

[5] Y. Li, W. Huang, Y. Li, A. Pei, D. T. Boyle and Y. Cui, Correlating Structure and Function of Battery Interphases at Atomic Resolution Using Cryoelectron Microscopy, Joule, 2, 2167–2177 (2018).

[6] A. Ramasubramanian, V. Yurkiv, T. Foroozan, M. Ragone, R. Shahbazian-Yassar and F. Mashayek, Stability of Solid-Electrolyte Interphase on the Lithium Metal Surface in Lithium Metal Batteries, ACS Appl. Energy Mater., 3, 10560−10567 (2020).

[7] J. Steiger, D. Kramer and R. Mönig, Microscopic observations of the formation, growth and shrinkage of lithium moss during electrodeposition and dissolution, Electrochim. Acta 136, 529–536 (2014).

[8] P. Bai, J. Guo, M. Wang, A. Kushima, L. Su, J. Li, F. R. Brushett and M. Z. Bazant, Interactions between Lithium Growths and Nanoporous Ceramic Separators, Joule, 2, 2434–2449 (2018).

[9] K. Nishikawa, T. Mori, T. Nishida, Y. Fukunaka and M. Rosso, Li dendrite growth and Li$^+$ ionic mass transfer phenomenon, J. Electroanal. Chem., 661, 84–89 (2011).

[10] T. Nishida, K. Nishikawa, M. Rosso and Y. Fukunaka, Optical observation of Li dendrite growth in ionic liquid, Electrochim. Acta, 100, 333– 341 (2013).

[11] T. Nishida, Y. Fukunaka, T. Homma and T. Nohira, J. Electrochem. Soc., Galvanostatic Li electrodeposition in LiTFSI-PC Electrolyte: Part II. Coupling Phenomena in Growth Process, 169, 090529 (2022).

[12] K. Nishikawa, Y. Fukunaka, T. Sakka Y. H. Ogata and J. R. Selman, Measurement of Concentration Profiles during Electrodeposition of Li Metal from LiPF6-PC Electrolyte Solution, J. Electrochem. Soc., 154 (10), A943 (2007).

[13] J. Pan, Q. Zhang, Xi. Xiao, Y. T. Cheng and Y. Qi, ACS Appl. Mater. Interfaces, Design of Nanostructured Heterogeneous Solid Ionic Coatings through a Multiscale Defect Model, 8, 5687−5693 (2016).

[14] K. Nishikawa, K. Shinoda and K. Kanamura, J. Phys. Chem. C, 3D Structural Transition of the Electrodeposited and Electrochemically Dissolved Li Metal onto an Ultramicroelectrode, 124, 22019−22024 (2020).

[15] O. Crowther and A. C. West, Effect of Electrolyte Composition on Lithium Dendrite Growth, J. Electrochem. Soc., 155(11), A806-A811 (2008).

[16] Y. Fukunaka, T. Yamamoto and Y. Kondo, Ionic Mass Transfer Associated with Electrocrystalization of Silver, Electrochim. Acta, 34(10), 1393-1400 (1989).

[17] M. Morisue, Y. Fukunaka, E. Kusaka, R. Ishii and K. Kuribayashi, Effect of Gravitational Strength on Nucleation Phenomena of Electrodeposited Copper onto a TiN substrate, J. Electroanal. Chem., 559, 155-163 (2003).

[18] M. Ota, S. Izuo, K. Nishikawa, Y. Fukunaka, E. Kusaka, R. Ishii and J.R Selman, Measurement of concentration boundary layer thickness development during lithium electrodeposition onto a lithium metal cathode in propylene carbonate, J. Electroanal. Chem., 559, 175-183 (2003).

[19] K. Nishikawa, M. Ota, S. Izuo, Y. Fukunaka, E. Kusaka, R. Ishii and J. R. Selman, Transient natural convection induced by electrodeposition of Li^+ ions onto a lithium metal vertical cathode in propylene carbonate, J. Solid State Electrochem., 8, 174–181 (2004).

[20] E. J. Dufek, Evaluation of the SEI Using a Multilayer Spectroscopic Ellipsometry Model, ECS Electrochemistry Letters, 3, A108-A111 (2014).

[21] Y. Xu, H. Wu, H. Jia, M. H. Engelhard, J. G. Zhang, W. Xu and C. Wang, Sweeping potential regulated structural and chemical evolution of solid-electrolyte interphase on Cu and Li as revealed by cryo-TEM, Nano Energy, 76, 105040 (2020).

[22] S. Shi, P. Lu, Z. Liu, Y. Qi, L. G. Hector, H. Li and S. J. Harris, Direct calculation of Li-ion transport in the solid electrolyte interphase, J. Am. Chem. Soc., 134, 15476–15487 (2012).

[23] L. Benitez and J. M. Seminario, Ion Diffusivity through the Solid Electrolyte Interphase in Lithium-Ion Batteries, J. Electrochem. Soc., 164 (11), E3159-E3170 (2017).

[24] T. Sawyer, G. Chiericato, C.T. Angells, E.J. Nanni and T. Tsuchiya, Effects of media and Electrode Materials on the Electrochemical Reduction of Dioxygen, Anal. Chem., 54(11) 1720-1724 (1982).

[25] T. A. Lorenzola, B.A. Lopes and M.C. Giordano, Molecular-oxygen electroreduction at Pt and Au Electrodes in Acetonitrile Solutions, J. Electrochem. Soc., 130(6), 1359-1365 (1983).

[26] Q. Qian, Y. Yang and H. Shao, Solid electrolyte interphase formation by propylene carbonate reduction for lithium anode, Phys. Chem. Chem. Phys., 19, 28772 (2017).

[27] S. A. Campbell, C. Bowes and R. S. McMillan, The electrochemical behaviour of tetrahydrofuran and propylene carbonate without added electrolyte, J. Electroanal. Chem., 284(1), 195-204 (1990).

[28] M. Metzger, B. Strehle, S. Solchenbach and H. A. Gasteiger, Hydrolysis of Ethylene Carbonate with Water and Hydroxide under Battery Operating Conditions, J. Electrochem. Soc., 163(7) A1219-A1225 (2016).

[29] A. M. Haregewoin, E. G. Leggesse, J. C. Jiang, F. M. Wang, B. J. Hwang and S. D. Lina, A combined experimental and theoretical study of surface film formation: Effect of oxygen on the reduction mechanism of propylene carbonate, J. Power Sources, 244, 318-327 (2013).

[30] M. Keppeler and M. Srinivasan, Interfacial Phenomena/Capacities Beyond Conversion Reaction Occurring in Nano-sized Transition-Metal-Oxide-Based Negative Electrodes in Lithium-Ion Batteries: A Review, ChemElectroChem, 4, 2727–2754 (2017).

[31] P. Zou, S. W. Chiang, J. Li, Y. Wang, X. Wang, D. Wu, A. Nairan, F. Kang and C. Yang, Ni@Li$_2$O co-axial nanowire based reticular anode: Tuning electric field distribution for homogeneous lithium deposition, Energy Storage Materials, 18, 155–164 (2019).

Table 2-1. Coulomb quantity of Q_0, Q_L, Q_m and Q_L-Q_0 on the dV/dQ curve for each current density

i	Q_0	Q_L	Q_m	Q_L-Q_0
mA cm^{-2}		mC cm^{-2}		
0.04	7.77	8.19	8.30	0.42
0.2	6.12	6.46	6.55	0.34
1	4.28	4.61	4.66	0.33
2	3.93	4.27	4.32	0.34
4	3.70	4.09	4.14	0.39
8	3.52	4.07	4.12	0.55
20	3.08	3.80	4.01	0.72
40	2.39	3.52	3.83	1.13
50	2.04	3.50	3.79	1.46
60	1.95	3.46	3.99	1.51

Table 2-2. ΔV and Δt read from Figure 2-3(b), and the estimated diffusivity of Li$^+$ in the SEI for each current density.

i	ΔV	Δt	D_{SEI}
mA cm^{-2}	V	s	cm^2 s^{-1}
8	0.012	1.08	0.7×10^{-9}
20	0.055	0.55	0.8×10^{-9}
40	0.130	0.25	1.4×10^{-9}
50	0.148	0.20	1.7×10^{-9}
60	0.200	0.18	2.1×10^{-9}
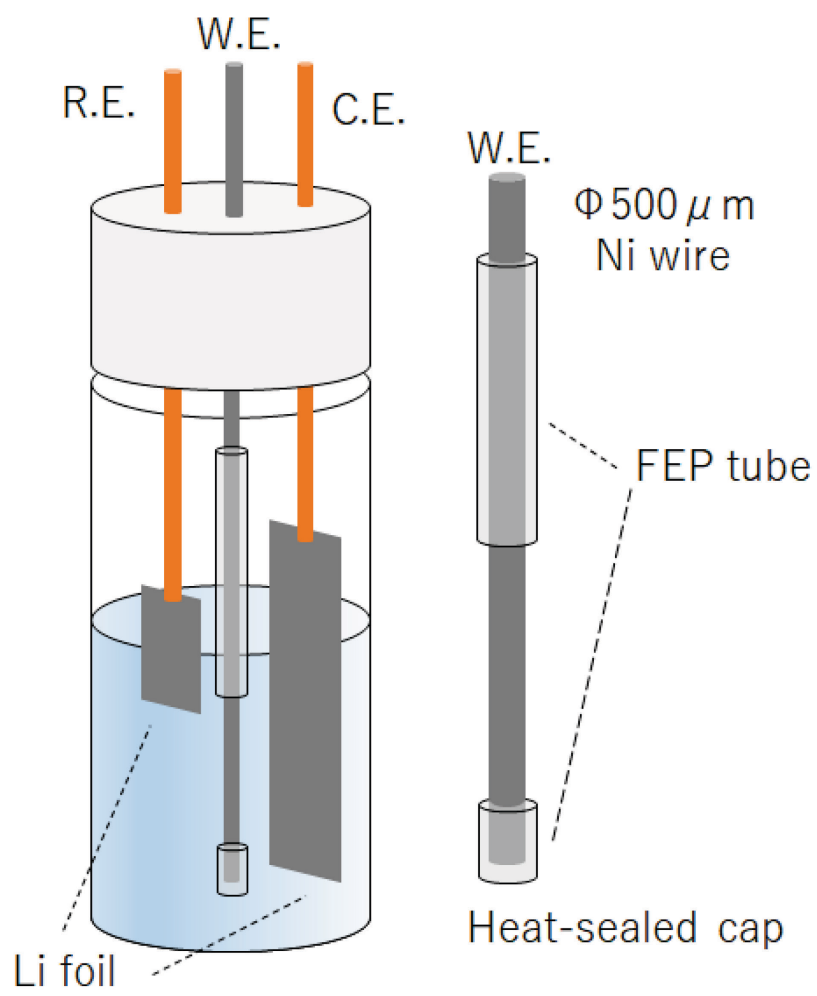
Figure 2-1. Schematic diagram of electrolytic cell for chronopotentiometry.
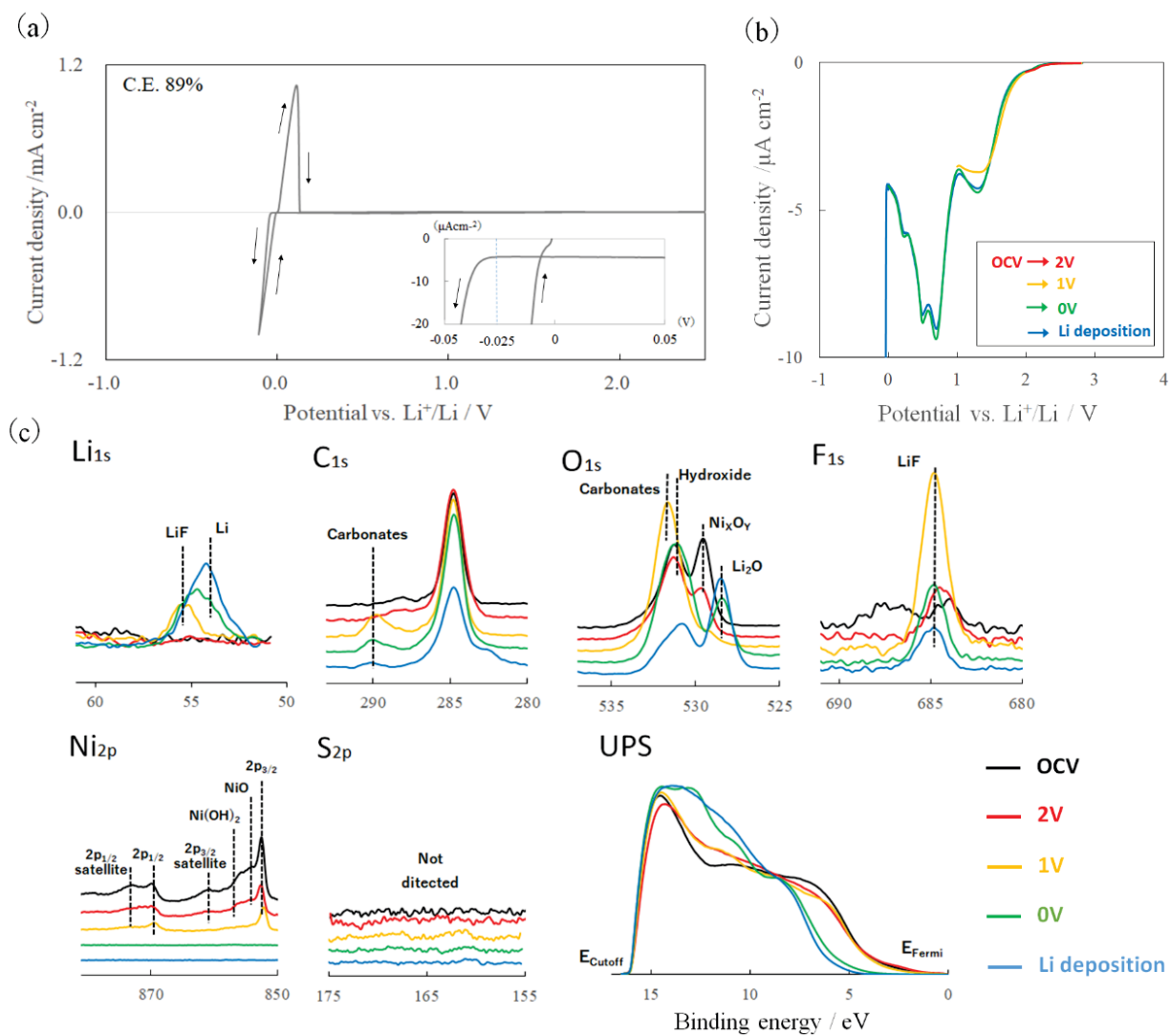
Figure 2-2. (a) Cyclic voltammogram of Li electrodeposition in 1M LiTFSI/PC on Ni electrode. (W.E.: 5 mm × 5 mm × 0.5 mm Ni sheet, C.E. and R.E.: Li foil. Scan rate: 1 mV s^{-1}.) The inset shows enlarged potential and current density around 0 V. (b) Linear sweep voltammograms when the potential is swept from OCV to 2, 1, 0 V and Li deposited potential in 1M LiTFSI/PC (W.E.: 5 mm × 5 mm × 0.1 mm Ni sheet, C.E. and R.E.: Li foil. Scan rate: 1 mV s^{-1}). (c) Corresponding XPS and UPS spectra of the electrode surface after each LSV scan.
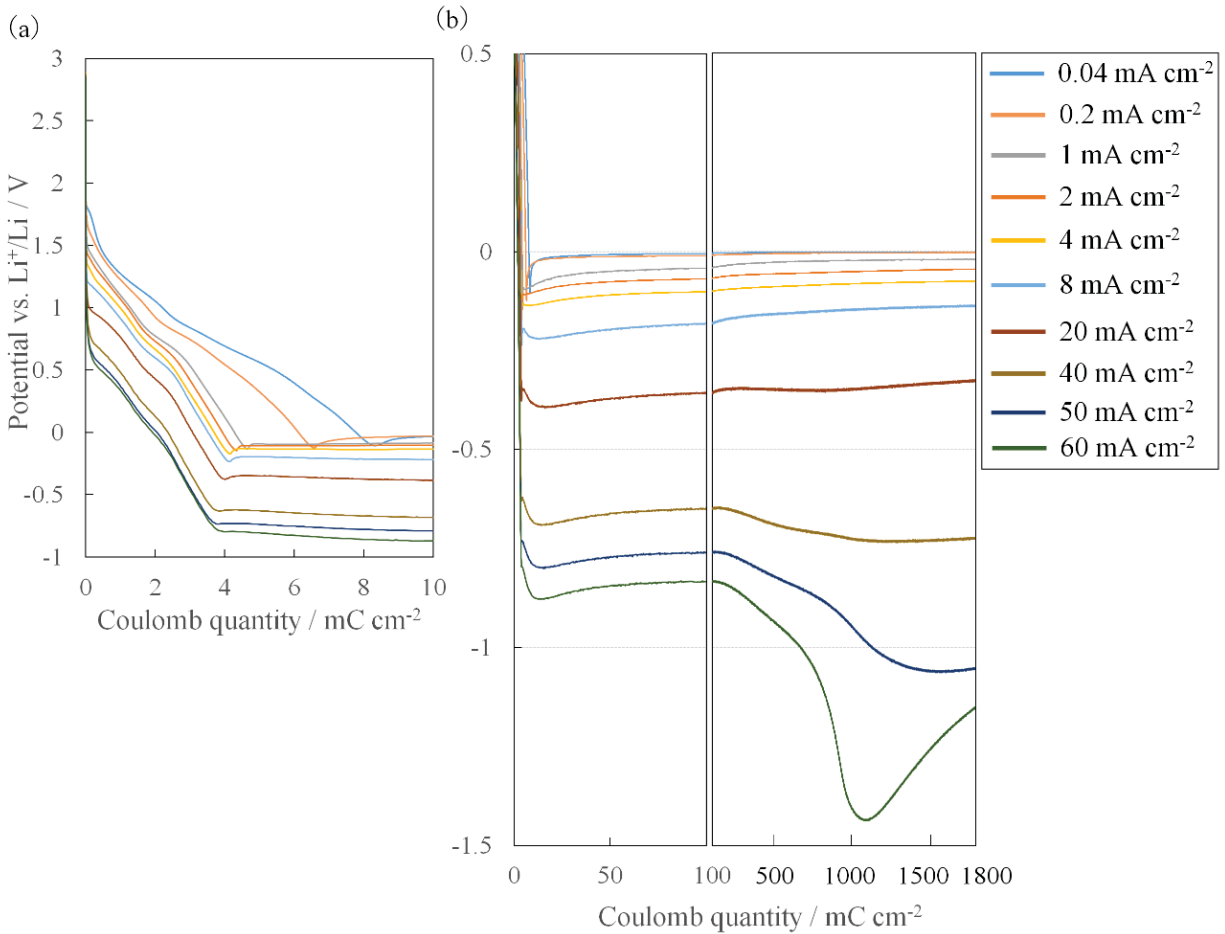
Figure 2-3. Chronopotentiograms after the starts of electrolysis at the current density ranges from 0.04 mA cm^{-2} to 60 mA cm^{-2} for the coulomb quantity of (a) 0 - 10 mC cm^{-2} and (b) 0 - 1800 mC cm^{-2} in 1M LiTFSI/PC at 25℃. Figure (b) shows two figures with each scale of 0-100 mC cm^{-2} and 100-1800 mC cm^{-2} in parallel; the scale of 0-100 mC cm^{-2} is enlarged compared to that of 100-1800 mC cm^{-2}.
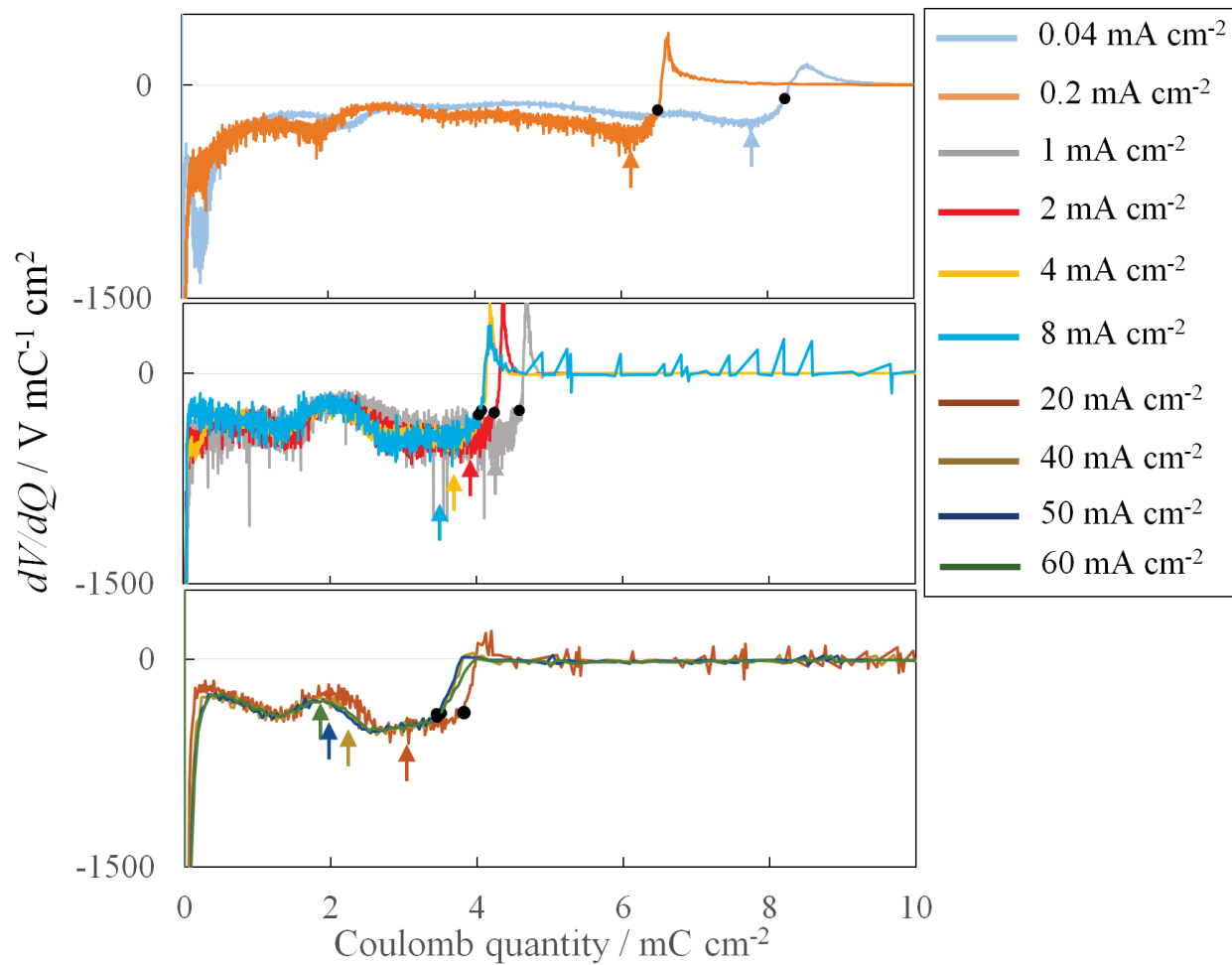
Figure 2-4. *dV/dQ* curves for the potential change of galvanostatic Li electrodeposition from the start of electrolysis to 10 mC cm^{-2} in Figure 2-3(a). The arrow corresponds to the coulomb quantity when the potential passes through 0 V and the filled circle (●) indicates the point at which *dV/dQ* begins to rise rapidly.

(a) 10 mC cm^{-2}

    0.2 mA cm^{-2} 2 mA cm^{-2} 8 mA cm^{-2} 20 mA cm^{-2} 50 mA cm^{-2}

(b) 100 mC cm^{-2}

    0.2 mA cm^{-2} 2 mA cm^{-2} 8 mA cm^{-2} 20 mA cm^{-2} 50 mA cm^{-2}
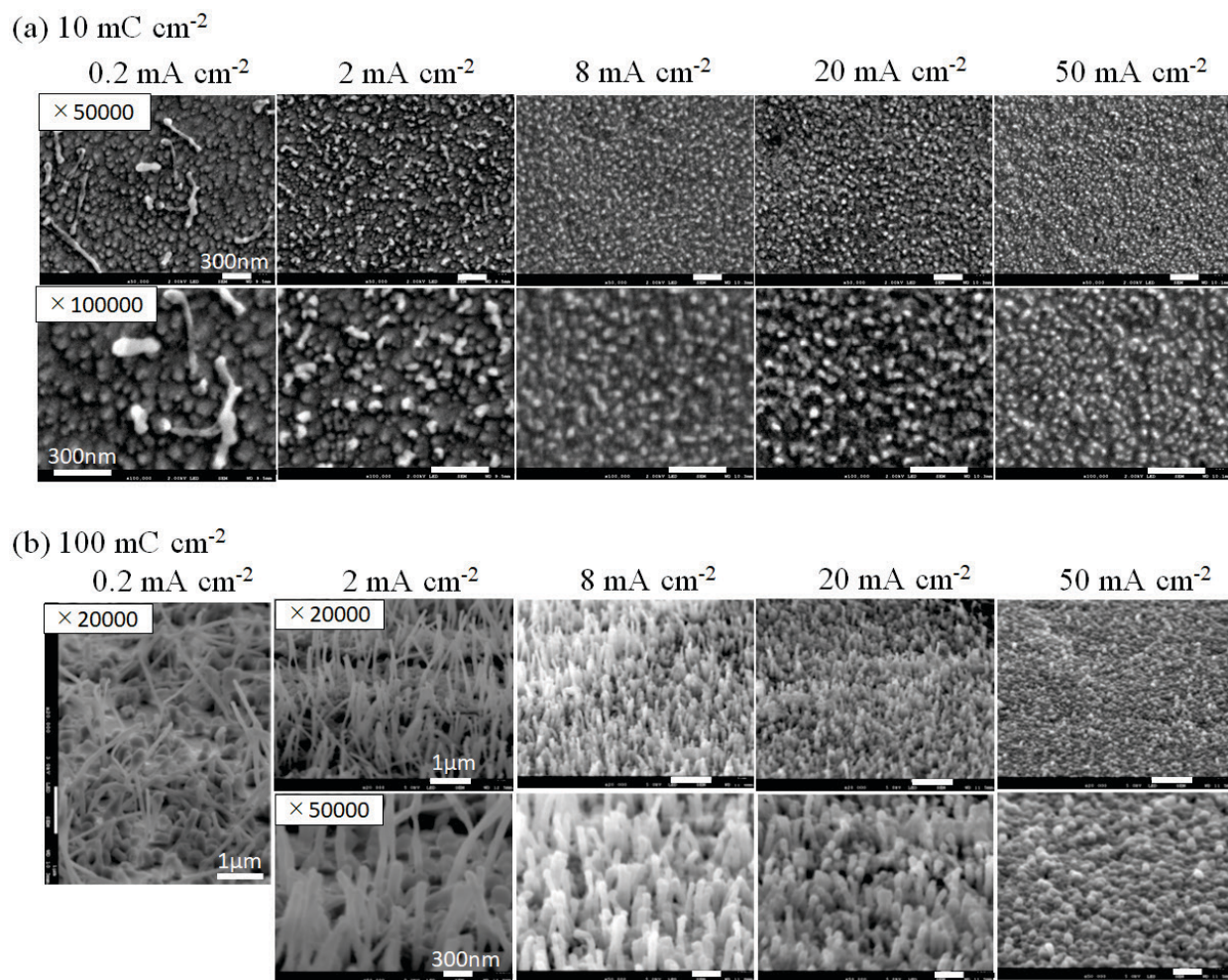
Figure 2-5. SEM images of the electrode surface after electrolysis at the current densities of 0.2, 2, 8, 20 and 50 mA cm^{-2}. Coulomb quantity passed during deposition: (a) 10 mC cm^{-2} and (b) 100 mC cm^{-2}.

43
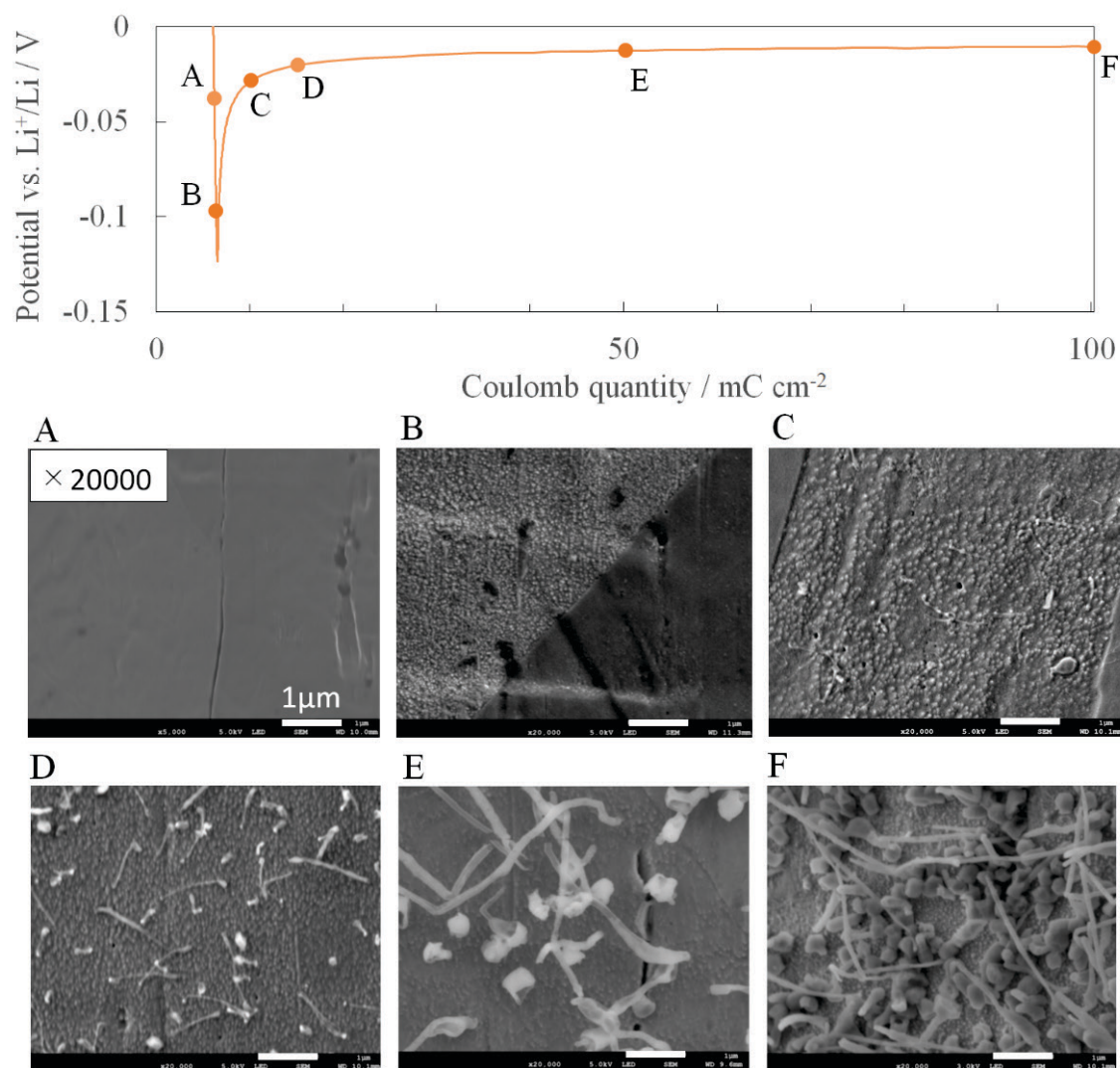
Figure 2-6. Time variation of the potential and top-view SEM images of the electrode surface during galvanostatic Li electrodeposition at 0.2 mA cm^{-2} up to 100 mC cm^{-2} in 1 M LiTFSI/PC. Each SEM image corresponds to coulomb quantities of (A) 5, (B) 6, (C) 10, (D) 15, (E) 50 and (F) 100 mC cm^{-2} on the chronopotentiogram.
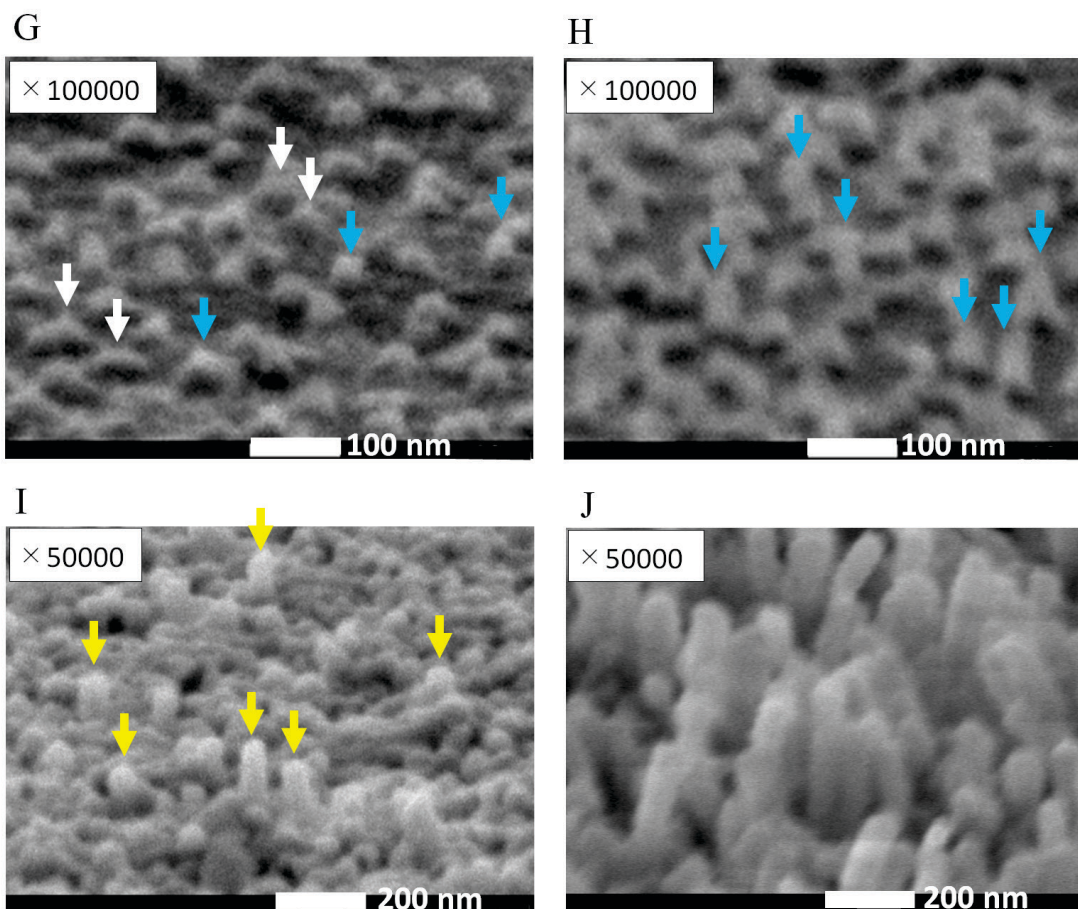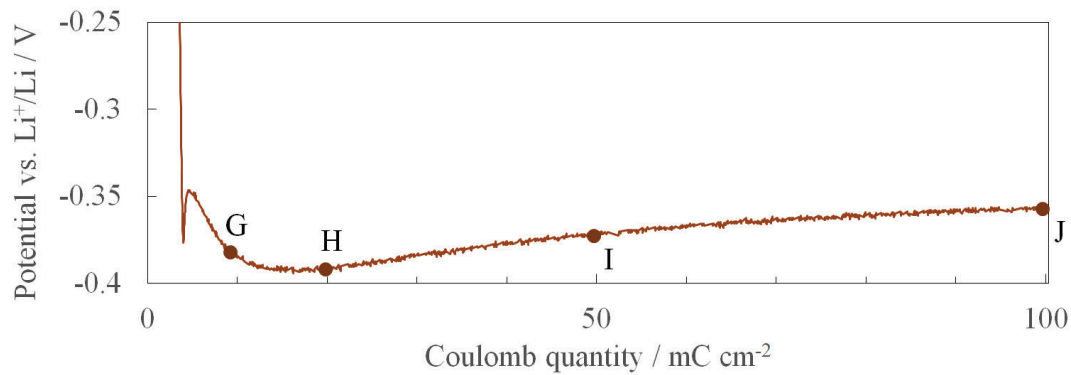
Figure 2-7. Time variation of the potential and tilted-view SEM images of electrode surface during galvanostatic Li electrodeposition at 20 mA cm^{-2} up to 100 mC cm^{-2} in 1 M LiTFSI/PC. Each SEM image corresponds to coulomb quantities of (G) 10, (H) 20, (I) 50 and (J) 100 mC cm^{-2} on the chronopotentiogram. White arrows in image G indicate the swelling of nanoscale precipitates. Blue arrows in images G and H indicate the bud-like morphology. Yellow arrows in image I indicate the beginning of rod-shaped deposits.
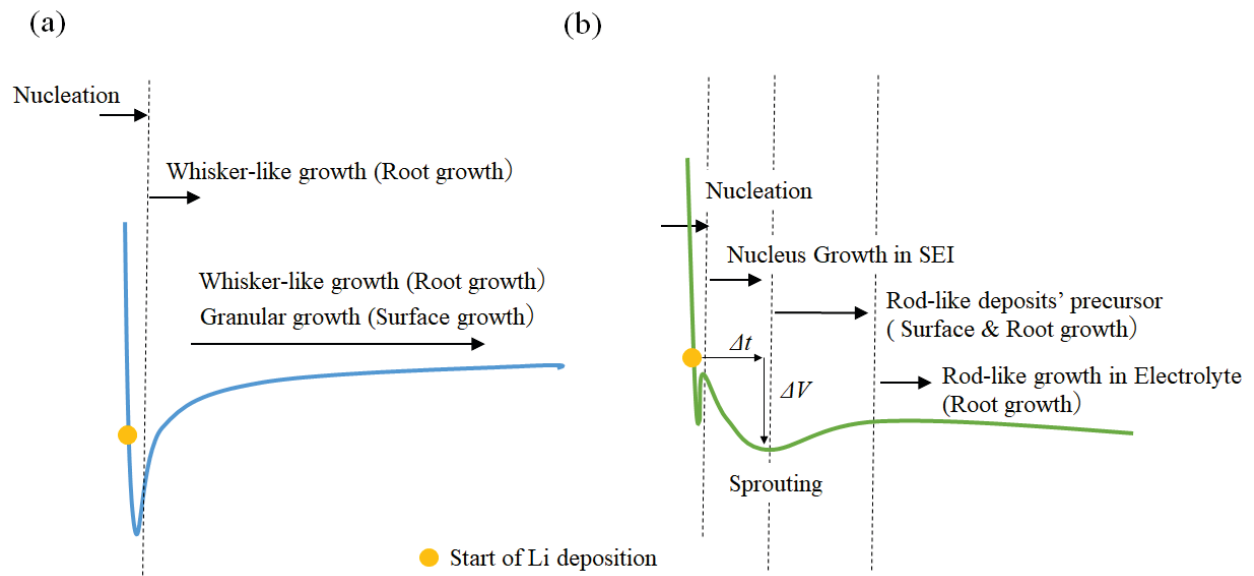
Figure 2-8. Typical potential profiles at (a) lower or (b) higher current density and assumed events at each stage.
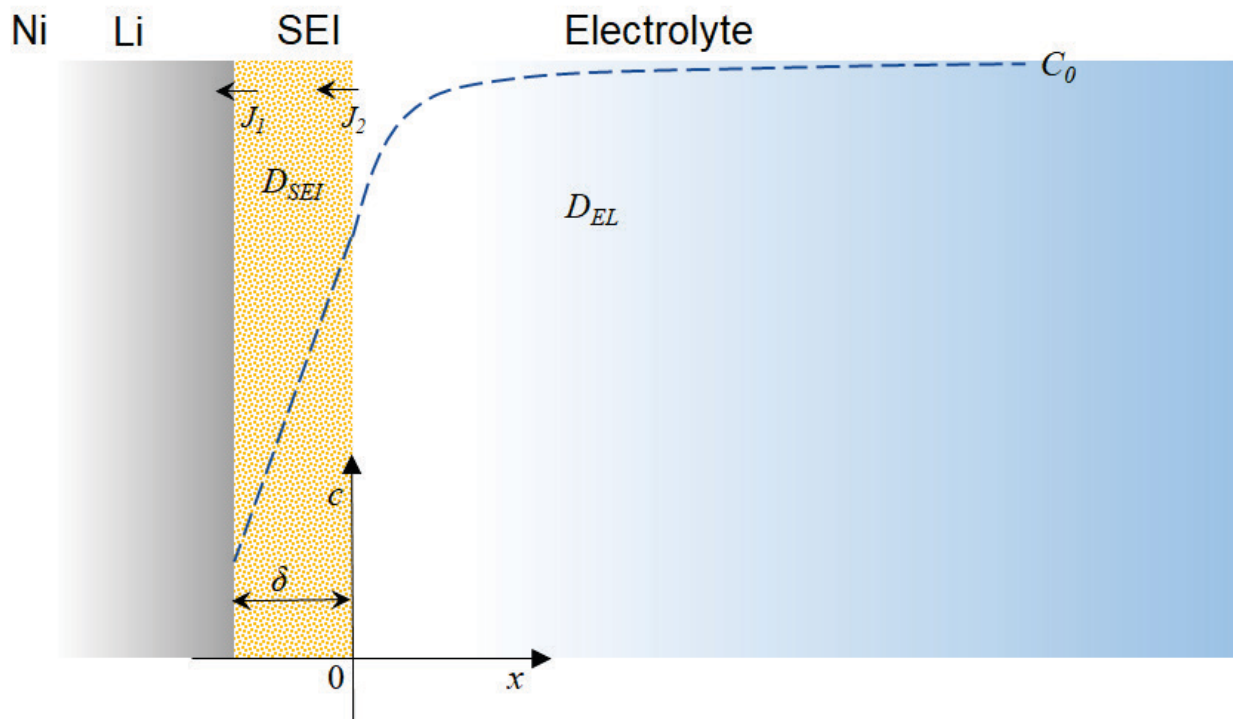
Figure 2-9. Schematic diagram of Li$^+$ concentration distribution at Li metal/SEI interface and SEI/organic electrolyte interface.

(a)

(b)
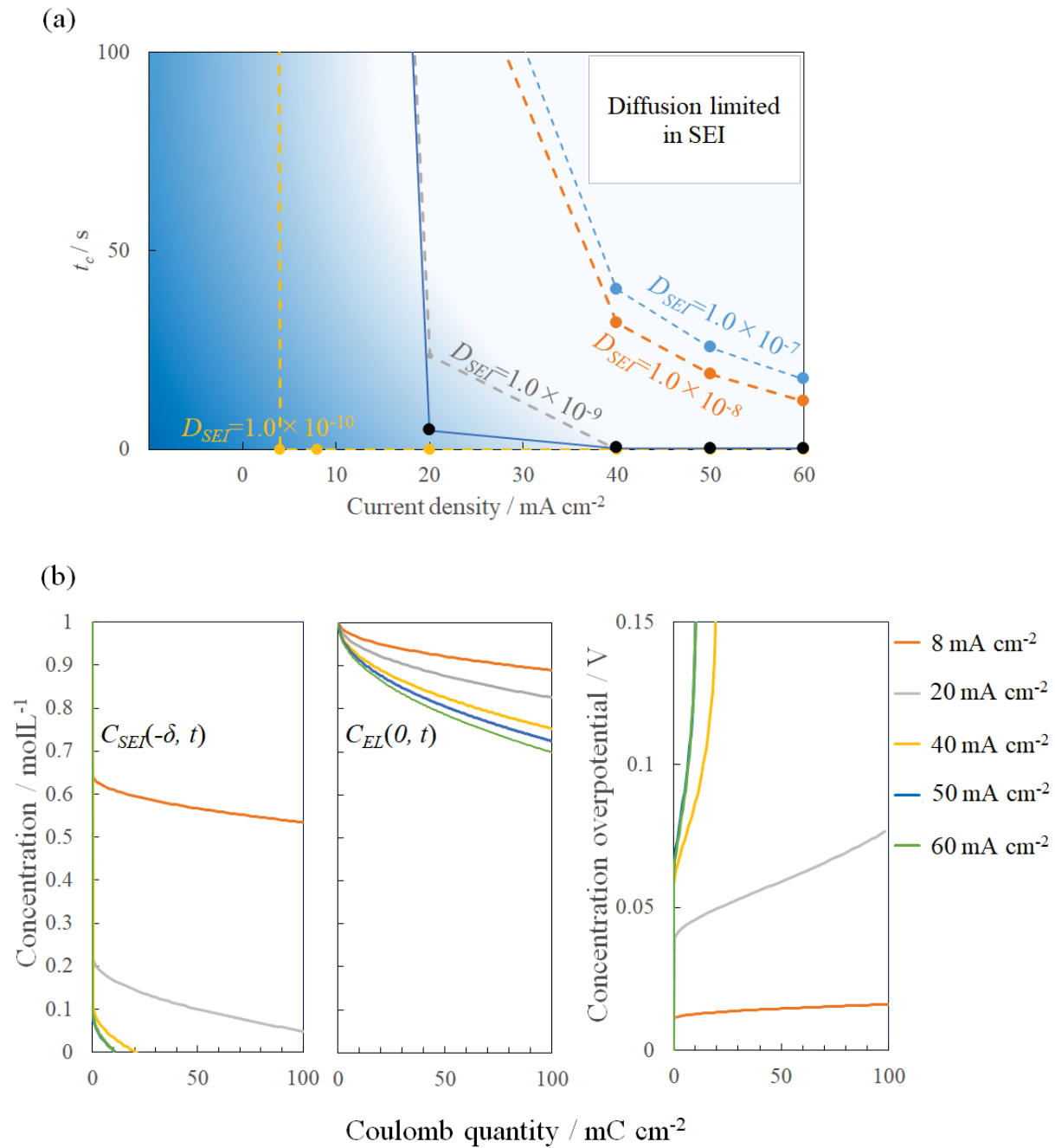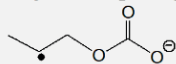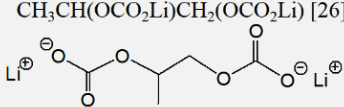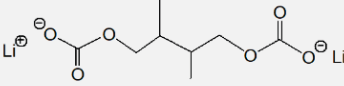
Figure 2-10. (a) Relationships between t_c and current density for each diffusion coefficient of Li$^+$ in the SEI. (b) Time variations of $C_{SEI}(-\delta, t)$ and $C_{EL}(0, t)$ as well as the concentration overpotential calculated at higher current density.

Appendix

Table 2-A. The estimated reactions to which each LSV peak before Li deposition is attributed based on previous reports.

E vs Li$^+$/Li / V	Estimated reaction	Products	Ref.
OCV - 2	Reduction of dissolved oxygen $O_2 + e^- \rightarrow O_2^-$ (H_2O non-contained) $O_2 + H_2O + 2e^- \rightarrow HO_2^- + OH^-$ (under trace H_2O) O_2^- or OH^- Nucleophilic attack to TFSI$^-$	LiF	[24-25]
2 - 1.5	Reduction of water $2H_2O + 2e^- + 2Li^+ \rightarrow H_2 + 2LiOH$ Hydrolysis of PC by OH^-	LiF Li_2CO_3	[26-28]
1.5 - 0.5	Reduction of PC	Alkyl(ene) carbonate Li_2CO_3	$CH_3C^\bullet HCH_2OCO_2^-$ [26] $CH_3CH(OCO_2Li)CH_2(OCO_2Li)$ [26] $(ROCO_2Li)_2, Li_2CO_3$ [29]
0.5 - 0.2	Reduction of NiO $NiO + 2Li^+ + 2e^- \rightarrow Ni + Li_2O$	Li_2O	[30-31]

Chapter 3

Galvanostatic Li Electrodeposition in LiTFSI-PC Electrolyte: Part II. Coupling Phenomena in Growth Process

3.1 Introduction

EV innovation is underway worldwide toward the realization of a society with zero CO_2 emissions, which is the goal of the United Nations SDGs. The development of high-performance energy storage devices is extremely important for achieving this goal [1]. The energy density of Li-ion batteries has tripled over the past two decades as in the case of cylindrical 18650 cells for example. The capacity has almost reached its limit in the current battery configuration. To further increase the energy density, it is indispensable to replace the active material. The key technology might be the controllability of dendrite formation on Li metal negative electrode [2-4].

Let us consider a battery composed of ternary oxide positive electrode active material and Li metal negative electrode. Setting a positive electrode active material capacity of 180 - 190 mAh g^{-1} and a cell capacity of 3.1 Ah for a 18650 cell with an appropriate current collector and active material thickness, it is necessary to deposit approximately 2.22 mAh cm^{-2} of Li metal during a charging operation. In such an urgent case where 90% of the capacity must be quickly recharged within 3 minutes, Li should be deposited at a current density of 40 mA cm^{-2}. On the other hand, in the case of low-rate charging for example by utilizing nighttime electricity, the battery may be charged at a very low current density of less than 1/100. That is, it is indispensable to understand Li deposition behavior, especially the dendritic growth behavior, from lower to higher current densities.

The relationship among dendrite growth rate, concentration boundary layer thickness and electrode surface roughness in metal electrodeposition in aqueous solution has been discussed with an interferometry by Ibl & Muller [5], Fukunaka et al. [6-7] and Argoul et al. [8], Chazaviel & Rosso [9].

It is essential to comprehend the coupled phenomena between dendrite growth and mass transfer rate at Li metal negative electrode under practical operations for rapid charging-discharging operation. Since Li dendrite growth phenomena should be considered from the viewpoint of nucleation and growth process, our study was divided into two parts. $0.028\,\mathrm{mAh\,cm^{-2}}$ ($100\,\mathrm{mC\,cm^{-2}}$) from the beginning of electrolysis covers a two-stage diffusion process in the SEI layer and organic electrolyte [10]. The diffusivity in the SEI layer was reasonably adjusted to represent the measured potential variations. Now, Chapter 3 covers 0.028 to $2.22\,\mathrm{mAh\,cm^{-2}}$ (100 to $8000\,\mathrm{mC\,cm^{-2}}$) during dendrite arm growth. It is straightforward to suppose that the microscopic morphology mainly composed of filament-like or columnar dendrite primary arm in the initial stage influences the subsequent morphology development probably accompanying secondary arm evolution. This study was conducted to investigate how the Li morphology develops on a macroscopic level at different current densities.

3.2 Experimental

The electrolyte composed of lithium bis (trifluoromethanesulfonyl) imide (LiTFSI) and PC was used. All chemical reagents were the same as those used in in the previous report [10] described in Chapter 2 of this thesis. Moisture content in the electrolyte was confirmed to be less than 20 ppm with a Karl Fischer titrator before use.

Chronopotentiometry (CP) and linear sweep voltammetry (LSV) were performed simultaneously with optical observation of Li electrodeposition behavior using the experimental system illustrated in Figure 3-1. Analogous to Chapter 2, the working electrode (W.E.) was Ni wire with a diameter of 500 μm. It was covered with FEP tube so that the contact part with the

electrolyte was 10 mm in length. The counter electrode (C.E.) and the reference electrode (R.E.) were similarly Li foil. The electrolytic cell was the same one used in Chapter 2. The screw cap of the glass sample tube was sealed air-tightly with Teflon seal tape to prevent moisture contamination from the atmosphere. The electrolytic cell was set in a special aluminum block fabricated to just fit the size of the cell. Thermal medium was circulated through a circulator bath inside the aluminum block to maintain a constant temperature. The slit cleaved in aluminum block to in-situ observe the working electrode surface with a digital optical microscope VHX-5000 (KEYENCE Corp.) was additionally designed. CP and LSV measurements were performed using HZ7000 (Hokuto Denko Corp.).

3.3   Results and Discussion

3.3.1   Optical observation of Li electrodeposition behavior

The Li deposition behavior in 1 M LiTFSI/PC electrolyte at galvanostatic electrolysis from 0.2 to 60 mA cm^{-2} up to 2.22 mAh cm^{-2} was observed by optical microscope as shown in Fig. 3-2 (see Appendix A for 2, 20 and 50 mA cm^{-2}). As seen in the appearance of the Ni substrate at 0.2 mA cm^{-2}, a non-uniform morphology is observed at 0.5 mAh cm^{-2}. Those deposits are presumably composed of filament-like deposits as clearly observed in Chapter 2. Hereinafter it will be referred to as filament-like deposits for simplicity. The appearance at 1 and 2 mA cm^{-2} became smoother compared to 0.2 mA cm^{-2}. It turned to fine deposits after a certain period, which implies the initial formation of dendrites at 1.33 mAh cm^{-2}. At 8 mA cm^{-2}, the electrode surface turned more uniform and no dendrites were observed up to 2.22 mAh cm^{-2}. At 20 mA cm^{-2}, such a smooth appearance accompanied some roughness from approx. 1.08 mAh cm^{-2} followed by fuzzy appearance at around 1.89 mAh cm^{-2}. In the case of 40 - 60 mA cm^{-2}, a slight roughness began to appear between 0.36 and 0.61 mAh cm^{-2}. It was followed by a typical dendrite morphology after a short period.

The effect of Li salt concentration was also examined. Fig. 3-3 shows the Li electrodeposition behavior in 0.1 M LiTFSI/PC at current densities of 0.2, 1, 2, 4 and 8 mA cm^{-2}.

The electrode surface at 0.2 mA cm^{-2} in 0.1 M appears inhomogeneous and coarse, though not as clear as in 1 M. At 1 and 2 mA cm^{-2}, relatively homogeneous and smooth deposition proceeds. It should be mentioned that a smoother surface was obtained at lower electrolyte concentrations. The heterogeneous surface chemistry characteristics of the SEI layer formed at a lower current density might introduce such a difference. Above 4 mA cm^{-2}, rapid dendrite development is observed even at 0.5 mAh cm^{-2}. The situation tends to approach to the case in the concentrated solution. As easily expected, the electrodeposition in less concentrated electrolytes introduces a significant dendrite growth mode.

3.3.2 *Dendrite growth process*

It was not possible to measure individual dendrite length due to the experimental difficulty caused by dendrite arm images overlapping each other along with the optical path. Thus, the electrode diameter was measured under the assumption that its variation corresponded to the average growth rate of deposits' bundle. This paper uses two kinds of electrode diameters. One is the apparent electrode diameter, which is the electrode diameter when the optical microscope images show a smooth deposition morphology. The other is the substrate electrode diameter. Since the regions indicated by the red dashed lines in Figs. 3-2 and 3-3 had a smooth deposition morphology, the apparent electrode diameters were measured using image processing software (Image-J). Fig. 3-4 demonstrates the electrode radius variations with the square root of time. When dendrites develop rapidly at higher current densities, it is no longer possible to apparently define the electrode diameter. Since such circumstances were encountered at 40 - 60 mA cm^{-2} in 1 M and 1 - 8 mA cm^{-2} in 0.1 M. Moreover, non-uniform deposits' growth probably stems from inhomogeneous surface SEI chemistry on Ni substrate was observed in the very early stage at 0.2 mA cm^{-2} in both 1 M and 0.1 M. Both cases were excluded from the measurement. Two-step linearity was observed except for the case of 8 mA cm^{-2} in 1 M. It suggests two growth modes similar to Li dendrites in ionic liquid [11].

During Li electrodeposition up to 2.22 mAh cm^{-2}, three characteristic times are defined. First, a slight roughness or unevenness begins to appear on the electrode surface at the time t_{app}. Then, the growth rate of the electrode diameter changes at t_L around or a little later at t_{app}, as demonstrated with an arrow symbol in Fig. 3-4. During Li deposition up to 0.028 mAh cm^{-2}, the dendrite primary arms less than a few μm in length were observed by SEM [10]. Considering that the resolution power of optical microscopy is at most a few to 10 μm, the appearance of slight unevenness or roughness on the electrode surface and the two-step linearity might be related to the growth process of dendrite primary arms followed by the appearance of something like secondary arms or branches. Then, at 40 - 60 mA cm^{-2} in 1 M and 1 - 8 mA cm^{-2} in 0.1 M, so-called dendrites of complex or fractal-shaped deposits suddenly appear to rapidly develop at t_ε.

The characteristic times of t_{app}, t_L and t_ε are defined as follows and summarized in Table 3-1 for each electrolyte along with the coulomb quantity.

t_{app}: The time when roughness or unevenness begins to appear on the smooth electrode surface. Note that the resolution of the optical microscope image is from a few to 10 μm.

t_L: The time when the growth rate of the apparent electrode diameter changes as represented by the arrow mark in Figure 3-4.

t_ε: The time when protrusions larger than 10 μm can be identified as dendrite initiation.

In addition, the calculated time (t_z) at which the electrode surface concentration of Li$^+$ reaches zero is also listed in Table 3-1 (see Appendix B). It was calculated with a transient diffusion model on a smooth electrode surface neglecting the unevenness less than a few μm range.

3.3.3 Potential variation behavior during galvanostatic Li electrodeposition

Fig. 3-5 shows the time variation of potential during galvanostatic electrolysis in the upper row and the calculated surface concentration based on a one-dimensional diffusion model. ((a) and

(c): 1 M LiTFSI/PC and (b) and (d): 0.1 M LiTFSI/PC electrolytes; Moreover, q_z, q_{app}, q_ε and q_L in Table 3-1 are indicated by the notations like ○, ●, × and arrow marks in Fig. 3-5, respectively.)

At 0.2 to 2 mA cm^{-2}, the potential increases monotonically until 0.275 mAh cm^{-2} and then remains relatively stable in 1 M electrolyte (Fig. 3-5(a)). Although the surface concentration should not be depleted during electrolysis up to 2.22 mAh cm^{-2} (Fig. 3-5(c)), filament-like deposits were recognized. The lower the current density in the 1 M case, the earlier the time (t_{app}) at which filament-like morphology begins to appear. The heterogeneous surface chemistry characteristics of the SEI layer formed at the lower current density should be responsible for such morphological variations as described in Chapter 2.

At much higher current densities of 8 - 60 mA cm^{-2} in 1M, the second minimum is seen around 0.0042 mAh cm^{-2} as illustrated in the inset of Fig. 3-5(a). This behavior may reflect the growth process of the deposits from the SEI into the electrolyte, that is, the "sprouting" behavior described in Chapter 2. At 8 mA cm^{-2}, the electrode potential slowly rises toward 0.55 mAh cm^{-2} and subsequently remains stable. The third minimum appears at around 0.275 mAh cm^{-2} followed by a slow increase to 1.11 mAh cm^{-2} at 20 mA cm^{-2}. The potential reaches clearly the third minimum between 0.275 and 0.5 mAh cm^{-2} and increases monotonously afterwards at 40 - 60 mA cm^{-2}. The similar tendency of potential change appears in the case of 0.1 M as shown in Fig. 3-5(b).

Figs. 3-5(c) & (d) indicate the calculated surface concentration depicted with the solid line. Li$^+$ ion concentration substantially depleted above 20 mA cm^{-2} in 1 M(c) and above 2 mA cm^{-2} in 0.1 M(d). (Note that a dot & dashed line in 1 M represents the time variation curve dare to be extrapolated over a significant dendritic growth stage. Such applicability with extrapolation is rather questionable under the significant growth of Li dendrite arm length greater than 10 μm. In the case of 0.1 M, the calculated surface concentrations are drawn by solid curves due to arm length less than a few to 10 μm.) Soon after the time when Li$^+$ ion concentration has been depleted, mesoscopic-sized deposits are recognized on the electrode surface at t_{app}. Then, the significant growth of dendrites begins to be visible at t_ε after a further delay. The appearance of the third

minimum inflection point may be related to an increase in concentration overpotential as well as an enlarged surface area under dendrite growth.

At lower current densities below 2 mA cm^{-2} in 1.0 M and 0.2 mA cm^{-2} in 0.1 M, Li electrodeposition behavior is strongly influenced by the heterogeneous chemical properties inherent to the SEI layer. It looks to develop under the growth mode controlled by such surface chemistry. Much more sophisticated instrumentation analysis including in-situ TEM [12] or synchrotron X-ray microscope [13] is mandatory to understand this growth mode.

At higher current densities accompanying a significant mass transfer overpotential, the measured potential variation corresponds well with the appearance of morphological variations in both solutions. At above 20 mA cm^{-2} in 1.0 M and above 1 mA cm^{-2} in 0.1 M, it may be suggested that the electrode surface concentration is closely related to the transition in dendrite growth mode to probably induce the appearance of dendrite secondary arms.

3.3.4 Estimation of limiting current density

At lower current densities, the local current concentration associated with non-uniform Li deposition is considered to affect the Li growth behavior. Extremely intensive research from this perspective is currently underway [14-15]. On the other hand, the electrode potential and deposition behavior are strongly influenced by the electrode surface concentration under higher current density operation, which is important from the viewpoint of rapid charging-discharging operation for EV batteries. The coupling phenomena between mass transfer rate and morphological variation should be understood.

LSV measurements with different concentrations of 0.1, 0.25, 0.5 M and 1.0 M in the LiTFSI/PC electrolyte are shown in Fig. 3-6. The lower the electrolyte concentration, the earlier the saturated current density condition, that is, so-called a limiting current density appeared. In 0.1 M and 0.25 M, the current plateau is clearly visible, but it becomes more unclear as the concentration increases from 0.5 M to 1.0 M. Such a concentration dependence of limiting current

density has been well known in aqueous electrolyte system since the pioneering work by C. Wagner in 1949. The electrode surface during LSV measurement was observed by using a video image attached to an optical microscope. The points at which dendrites begin to be visible are indicated by a solid circle. In each of the electrolytes, the dendrites begin to appear when the limiting current is attained. Moreover, the upward movement of suspended solids was occasionally observed at higher current density. It is straightforward to imagine the upward natural convection is induced along a vertical Ni wire electrode immersed in a stagnant organic electrolyte.

The whisker-like or rod-like morphology described in Chapter 2 is based on SEM observations with a resolution of about 100 nm. On the other hand, the resolution in this chapter is a few to 10 μm at most. Moreover, the field of view is extremely macroscopic across the dendrite growth layer. Therefore, the measured characteristic times related to dendrite evolution and growth may be slightly delayed compared to those in Chapter 2.

In lower concentration electrolytes, limiting current conditions are achieved quickly, hence generated dendrites develop significantly. On the other hand, relatively uniform deposition is underway by the time when the limiting current situation is reached in concentrated solutions. Consequently, even if dendrites begin to grow, they may not be fully developed by the end of electrolysis compared to the lower-concentration case. Looking at the morphological variations along Ni electrode height in 1 M, dendrite growth is more dominant at the tip as demonstrated in IV, Fig. 3-6. (Note that a considerable amount of deposit fell away due to weak mechanical property.) As a concentration gradient is formed in the vicinity of the cathode, upward natural convection is surely induced along Ni wire electrode. The dendrite growth is thus enhanced in the upper part with lower concentration, resulting in the current density distribution along the electrode height in a stagnant electrolyte. The current density distribution along electrode height is formed in a semi-infinite electrolyte layer.

Then, the limiting current density for Li galvanostatic electrodeposition in the organic electrolyte was tried to estimate using the regression equations (1) to (4) based on the interferometry measurements. For simplicity, the existence of the counter electrode was neglected.

Ignoring the SEI formation process, the plane electrodes are assumed to be placed in a semi-infinite electrolyzer and the similarity principle [16-18] is valid even though Ra is out of the applicable range.

$$Sh_x = 0.499(Ra_x)^{0.25} \tag{3-1}$$

$$Ra_x = ScGr_x \tag{3-2}$$

$$Gr_x = g(\rho^* - \rho^s)(\rho^*)^2 x^3 / ((\rho^s)\eta^2) \tag{3-3}$$

$$Sh_x = i_L(1-t^*)x / (zFD\Theta_1) \tag{3-4}$$

Sh_x: Sherwood number, Ra_x: Rayleigh number, Sc: Schmidt number, Gr_x: Grashof Number, Gravitational acceleration; $g = 981$ cm s^{-2}, Density of the electrolyte; ρ^* (g cm^{-3}), Density of the solvent; $\rho^s = 1.20$ (g cm^{-3}) for PC, viscosity; η (mPa s), electrode height; x (cm), Diffusion constant; D (cm^2 s^{-1}), Transference number; t^*, Limiting current density; i_L (mA cm^{-2}), Valence number; $z = 1$, Faraday constant; $F = 96485$ (C mol^{-1}), Concentration difference between bulk of the electrolyte (c_0) and the electrode surface (c_s); $\Theta_1 = c_0 - c_s = 10^{-3}$ (mol cm^{-3}). ρ^*, η, t^* and D are included in Appendix C.

Calculating the natural convection formed around a vertically installed Ni wire with 500 μm in diameter and 10 mm height using the above relation, the limiting current density for 1 M LiTFSI/PC can be obtained as $i_L = 44$ mA cm^{-2}. As for the different electrolyte concentrations, the same procedure was repeated. The calculated results agree well with the LSV measurements as presented in Table 3-2.

3.3.5 Change in the growth rate of Li deposits

Bazant et al. [19-20] observed Li electrodeposition behavior on Li metal using a two-electrode Li symmetric capillary cell. The results with a Li three-electrode cell were reported by Akolkar et al. [21].

The specific time (capacity) of $t_z(q_z)$ in Table 3-1 corresponds to Sand Time (Sand Capacity) and q_ε does to the transition point to Dendritic growth mode. There is a time lag between q_z and q_ε. Bazant et al. showed a transition from Mossy to Dendritic growth when Sand Capacity is reached. They identified a transition point even at current densities as low as 1 mA cm^{-2} in 1 M electrolyte, where mossy deposits reach about 300 - 400 μm regardless of the current density. In the present study, the electrode diameter at q_ε in Table 3-1 changed only about 20-35μm from the start of electrolysis.

These differences may be caused by the electrolytic cell configuration. Moreover, Ni substrate was immersed in LiTFSI/PC in this study, but Li substrate in LiPF$_6$/EC+DMC in the papers [20, 21]. Akolkar et al. showed that t$_{onset}$ varied considerably depending on the immersion time before starting the electrolysis. That is, SEI characteristics may be referred to such differences even under the same current density.

The top and side views of the electrode surface after Li electrodeposition at 20 mA cm^{-2} are demonstrated in Fig. 3-7(a). At 0.028 mAh cm^{-2}, the top view shows rod-like deposits uniformly deposited over the electrode surface. Rod-like microdeposits probably several hundred nanometers in length without branching are seen in the side view.

At 0.5 mAh cm^{-2}, the rod-like deposits at 0.028 mAh cm^{-2} turned into a filament-like structure with an intricate morphology. The swelled tip of the filament can be seen in the top view. Most filaments appear to grow perpendicularly to the substrate or partially bent. A side view shows that some of the filaments exhibit a bending characteristics, i.e., suggesting the possible induction of a secondary arm or branches, which may be possibly related to the change in the growth rate of deposits as shown in Fig. 3-7(b).

Although the SEI formation process is the key to dendrite suppression [22-23], the coupling phenomena should be also well understood simultaneously in order to challenge the charging operation at higher current densities. Many approaches have been taken to adjust electrolyte types and their compositions to form the desired robust SEI. For example, the high cycle efficiency of Li metal negative electrode has been reported due to the suppression of solvent decomposition in concentrated electrolytes and the formation of LiF-rich SEI [22]. Meng et al. reported that a new electrolyte made of liquefied fluoromethane and salt of LiTFSI successfully produced extremely smooth and dense Li deposition in the temperature range from - 60 to 20 °C [23]. Highly efficient Li deposition and dissolution over 0.1 to 10 mA cm^{-2} were achieved. The formed SEI is confirmed to be a dense, uniform and inorganic structure containing rich LiF and Li_2CO_3. It is assumed that SEI is required to be dense and uniform but not brittle and to have rigidity so as not to be easily deformed even if stress is generated under SEI due to the formation of the Li phase. On the other hand, the transport of Li^+ both in the electrolyte and in the SEI must be smooth so that non-uniform growth does not occur due to local depletion of Li^+. When the electrolyte composition changes, SEI characteristics and Li deposition morphology will be inevitably affected. By performing fundamental Li electrodeposition experiments, it is possible to predict the internal behavior of Li metal batteries based on the morphological changes of electrodeposited Li in conjunction with potential changes. The limiting current density is one of the most important threshold values for predicting battery failure modes and for designing safe batteries.

3.4 Conclusions

Galvanostatic Li electrodeposition was performed in 1 M and 0.1 M LiTFSI/PC electrolyte at different applied current densities, from 0.2 mA cm^{-2} to 60 mA cm^{-2}, to different levels of charge, from 0.028 to 2.22 mAh cm^{-2}, while optically imaging the cylindrical electrode. At lower current densities, a non-uniform standalone or stochastic deposition containing filament-like or columnar type deposition was observed. Such a deposition behavior should be referred to the inhomogeneous

SEI characteristics. On the other hand, the morphological variation mode was shifted to macroscopically smooth curved surface enveloping the numerous tips of similar sized rod-like or columnar deposits at higher current density. The growth process further changed into a rapid dendrite formation mode after a certain period. The electrode potential variations were strongly influenced by the electrode surface concentration.

The two-step linearity in the relationship between electrode diameter variation and the square root of duration period suggests the growth mode transitions. The induction of natural convection along a vertical cathode was also recognized at higher current densities. Calculating the limiting current density in 1 M LiTFSI/PC electrolyte along a vertical Ni cathode considering the effect of natural convection was estimated to be $i_L = 44$ mA cm^{-2} with the similarity principle. The calculation agreed well with LSV measurements. Although the limiting current density should vary depending on the electrolyte chemistry, battery shape, charge-discharge conditions and operating environment, it is extremely important to consider the limiting current density in the practical application of Li metal negative electrodes from the viewpoint of dendrite control.

The coupling phenomena in PC organic electrolyte should be understood not only during the very initial stage to 0.028 mAh cm^{-2} but also over 2.22 mAh cm^{-2} which probably governs the initiation of secondary arms.

References

[1] H.S. Das, M.M. Rahman, S. Li and C.W. Tan, Electric vehicles standards, charging infrastructure, and impact on grid integration: A technological review, Renewable and Sustainable Energy Reviews, 120, 109618 (2020).

[2] H.Zhang, G. G. Eshetu, X. Judez, C. Li, L. M. Rodriguez-Martínez and M. Armand, Electrolyte Additives for Lithium Metal Anodes and Rechargeable Lithium Metal Batteries: Progress and Perspectives, Angew. Chem. Int. Ed., 57, 15002-15027 (2018).

[3] H. Zhang, U. Oteo, X. Judez, G. G. Eshetu, M. Martinez-Ibañez, J. Carrasco, C. Li and M. Armand, Designer Anion Enabling Solid-State Lithium-Sulfur Batteries, Joule, 3, 1689-1702 (2019).

[4] M. Rosso, C. Brissot, A. Teyssot, M. Dollé, L. Sannier, J. M. Tarascon, R. Bouchet and S. Lascaud, Dendrite short-circuit and fuse effect on Li/polymer/Li cells, Electrochim. Acta, 51, 5334-5340 (2006).

[5] N. Ibl and R.H. Muller, Studies of Natural Convection at Vertical Electrodes, J. Electrochem. Soc., 105, 346 (1958).

[6] Y. Fukunaka, T. Yamamoto and Y. Kondo, Electrodeposition of Silver under Direct and Pulsed Current, J. Electrochem. Soc., 136(11), 3278&3630 (1989).

[7] Y. Fukunaka, T. Yamamoto and Y. Kondo, Ionic mass transfer associated with electrocrystallization of silver, Electrochim. Acta, 34(10), 1393-1400 (1989).

[8] J. Elezgaray, C. Léger and F. Argoul, Linear Stability Analysis of Unsteady Galvanostatic Electrodeposition in the Two‐Dimensional Diffusion‐Limited Regime, J. Electrochem. Soc., 145, 2016 (1998).

[9] C. Brissot, M. Rosso, J.-N. Chazalviel and S. Lascaud, In Situ Concentration Cartography in the Neighborhood of Dendrites Growing in Lithium/Polymer‐Electrolyte/Lithium Cells, J. Electrochem. Soc., 146, 4393 (1999).

[10] T. Nishida, Y. Fukunaka, T. Homma and T. Nohira, Galvanostatic Li Electrodeposition in LiTFSI-PC Electrolyte: Part I. Effects of Current Density in Initial Stage, J. Electrochem. Soc., 169, 100548 (2022).

[11] T. Nishida, K. Nishikawa, M. Rosso and Y. Fukunaka, Optical observation of Li dendrite growth in ionic liquid, Electrochim. Acta, 100, 333-341 (2013).

[12] P. M. Vereecken, A. Radisic and F. M. Ross, Differential Inhibition during Cu Electrodeposition on Ru:Combined Electrochemical and Real-Time TEM Studies, J. Electrochem. Soc., 166, D3129 (2019).

[13] Hongyi Pan, Tianyu Fu, Guibin Zan, Rusong Chen, Chunxia Yao, Quan Li, Piero Pianetta, Kai Zhang, Yijin Liu, Xiqian Yu and Hong Li, Fast Li Plating Behavior Probed by X-ray Computed Tomography, Nano Lett., 21(12), 5254-5261 (2021).

[14] A. Kushima, K. So, C. Su, P. Bai, N. Kuriyama, T. Maebashi, Y. Fujiwara, M. Bazant and J. Li, Liquid cell transmission electron microscopy observation of lithium metal growth and dissolution: Root growth, dead lithium and lithium flotsams, Nano Energy, 32(2), 271-279 (2017).

[15] J. Steiger, D. Kramer and R. Mönig, Mechanisms of dendritic growth investigated by in situ light microscopy during electrodeposition and dissolution of lithium, J. Power Sources, 261, 112-119 (2014).

[16] N. Ibl and R. Muller, Optische Untersuchungen der Diffusionsschicht und der hydrodynamischen Grenzschicht an belasteten Elektroden, Zeitschrift fur Elektrochemie, 59(7-8), 671-676 (1955).

[17] K. Denpo, T. Okumura, Y. Fukunaka and Y. Kondo, Measurement of Concentration Profiles of Cu^{2+} Ion and H^+ Ion near a Vertical Cathode by Two-Wavelength Holographic Interferometry, J. Electrochem. Soc., 132, 1145 (1985).

[18] Y. Fukunaka, T. Minegishi, N. Nishioka and Y. Kondo, Transient Natural Convection near a Plane Vertical Electrode Surface after Reversing the Electrolytic Current, J. Electrochem. Soc., 128(6), 1274-1280 (1981).

[19] P. Bai, J. Guo, M. Wang, A. Kushima, L. Su, J. Li, F. R. Brushett and M. Z. Bazant, Joule, 2, 2434–2449 (2018)

[20] P. Bai, J. Li, F. R. Brushett and M. Z. Bazant, Interactions between Lithium Growths and Nanoporous Ceramic Separators, Energy Environ. Sci., 9, 3221-3229 (2016).

[21] A. Maraschky and R. Akolkar, Mechanism Explaining the Onset Time of Dendritic Lithium Electrodeposition via Considerations of the Li^+ Transport within the Solid Electrolyte Interphase, J. Electrochem. Soc., 165(14), D696-D703 (2018).

[22] J. Qian, W. A. Henderson, W. Xu, P. Bhattacharya, M. Engelhard, O. Borodin and J. G. Zhang, High rate and stable cycling of lithium metal anode, Nat. Commun., 6, 6362 (2015).

[23] Y. Yang, D. M. Davies, Y. Yin, X. Wang, C. S. Rustomji and Y. S. Meng, Liquefied gas electrolytes for wide-temperature lithium metal batteries, Joule, 3, 1-15 (2019).

[24] T. Nishida, K. Nishikawa, Y. Fukunaka, Diffusivity Measurement of $LiPF_6$, LiTFSI, $LiBF_4$ in PC, ECS Transactions, 6(18), 1-14 (2008).

[25] K. Hayamizu, Direct relations between ion diffusion constants and ionic conductivity for lithium electrolyte solutions, Electrochim. Acta, 254, 101–111 (2017).

Table 3-1. The specific times t_z, t_{app}, t_L and t_ε (s) and the corresponding coulomb quantities q_z, q_{app}, q_L and q_ε (mAh cm^{-2}) during galvanostatic electrolysis at the current densities from 0.2 mA cm^{-2} to 60 mA cm^{-2} in 1M LiTFSI/PC and 0.1 M LiTFSI/PC electrolyte.

1M LiTFSI/PC

i	t_z	q_z	t_{app}	q_{app}	t_L	q_L	t_ε	q_ε
mAcm^{-2}	s	mAh cm^{-2}	s	mAh cm^{-2}	s	mAh cm^{-2}	s	mAh cm^{-2}
0.2	1710000	95	1500	0.08	—	—	—	—
1	68500	19	4800	1.33	4800	1.33	—	—
2	17100	9.5	2580	1.43	2700	1.50	—	—
8	1070	2.38	—	—	—	—	—	—
20	171	0.95	193	1.07	196	1.09	342	1.90
40	43	0.48	54	0.60	59	0.66	120	1.33
50	27	0.38	32	0.44	36	0.50	54	0.75
60	19	0.32	22	0.37	22	0.37	35	0.58

0.1M LiTFSI/PC

i	t_z	q_z	t_{app}	q_{app}	t_L	q_L	t_ε	q_ε
mAcm^{-2}	s	mAh cm^{-2}	s	mAh cm^{-2}	s	mAh cm^{-2}	s	mAh cm^{-2}
0.2	21000	1.17	6600	0.37	—	—	—	—
1	840	0.23	1280	0.36	1440	0.40	4080	1.13
2	210	0.12	240	0.13	289	0.16	2400	1.33
4	52	0.058	63	0.070	81	0.090	176	0.20
8	13	0.029	22	0.049	25	0.056	37	0.082

t_z / s : Calculated time when the surface concentration of Li$^+$ becomes zero

q_z / mAh cm^{-2} : The coulomb quantity at t_z

t_{app} / s : The time when roughness or unevenness begins to appear on the smooth electrode surface.

q_{app} / mAh cm^{-2} : The coulomb quantity at t_{app}

t_L / s : The time when the growth rate of the apparent electrode diameter changes.

q_L / mAh cm^{-2} : The coulomb quantity at t_L

t_ε / s : The time when protrusions larger than 10 μm can be identified as dendrite initiation.

q_ε / mAh cm^{-2} : The coulomb quantity at t_ε

Table 3-2. Comparison between estimated and measured values for limiting current density of Li electrodeposition in LiTFSI/PC electrolyte.

	Salt concentration / mol L^{-1}			
	0.1	0.25	0.5	1
Estimated value / mA cm^{-2}	4	12	25	44
Measured value / mA cm^{-2}	4	11	23	43
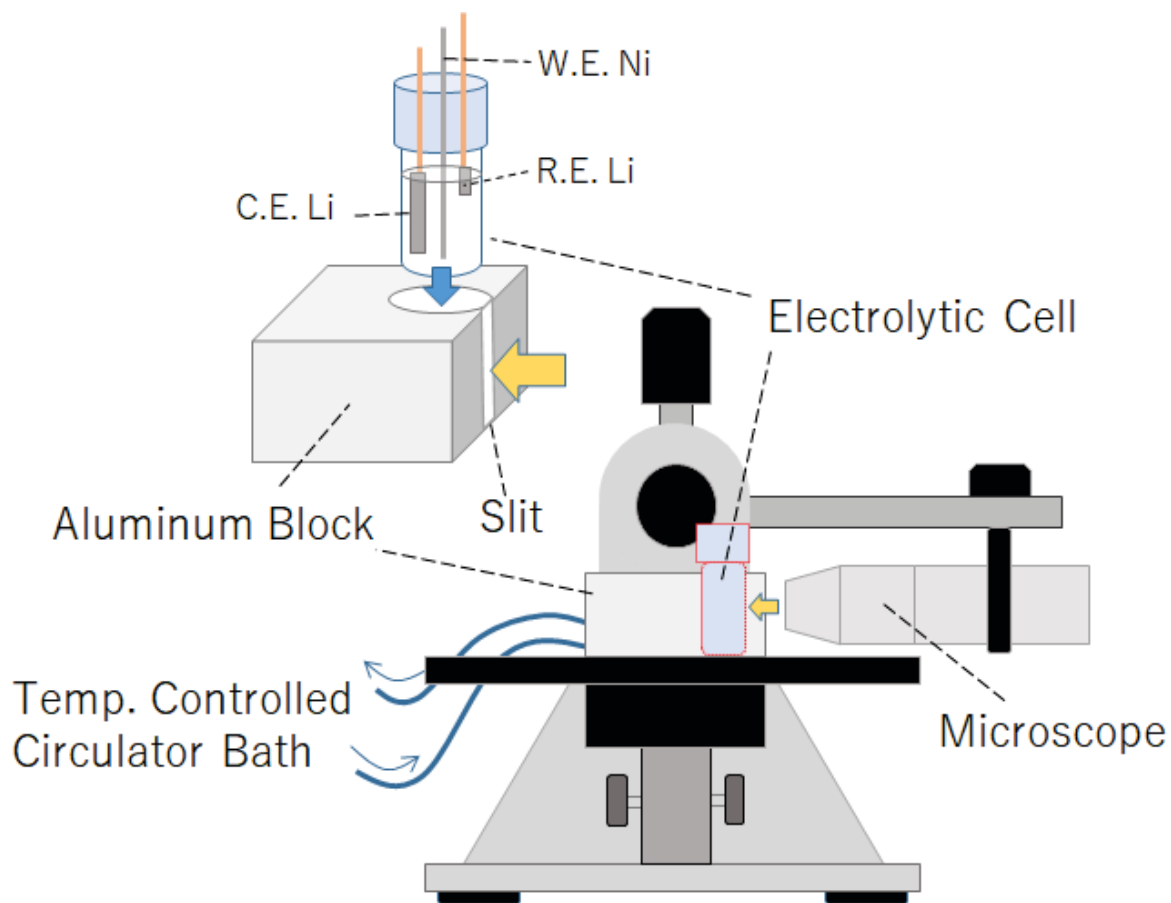
Figure 3-1. Schematic diagram of observation system and the electrolytic cell.
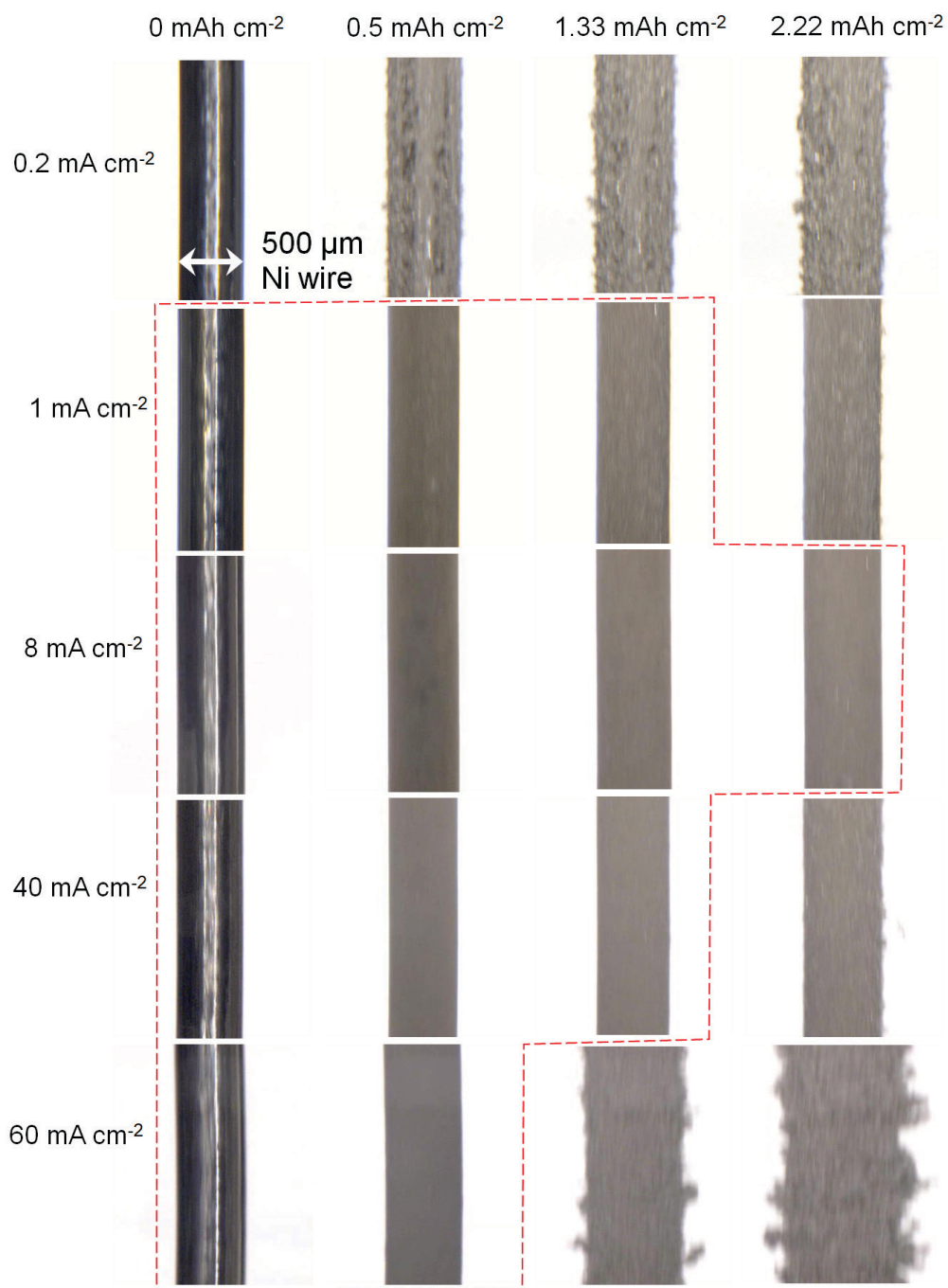
Figure 3-2. Transient variations of Li metal morphology electrodeposited in 1.0 M LiTFSI/PC at 0.2, 1, 8, 40 and 60 mA cm^{-2} (25 °C). The red dotted line represents the region of smooth deposition morphology to be measured in Figure 3-4 for the electrode diameter.
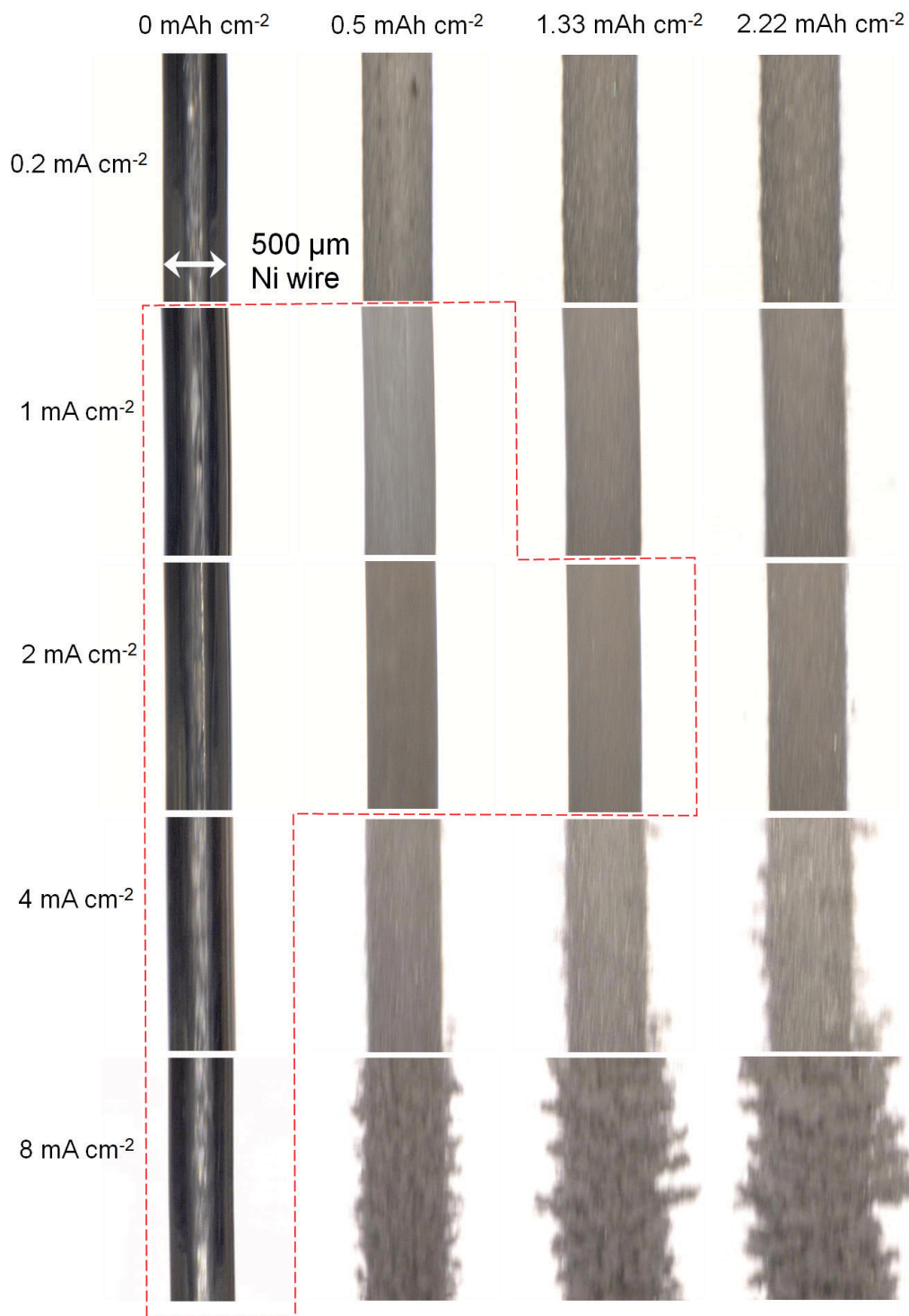
Figure 3-3. Transient variations of Li metal morphology electrodeposited in 0.1 M LiTFSI/PC at 0.2, 1, 2, 4 and 8 mA cm^{-2} (25 °C). The red dotted line is the same as in Figure 3-2.
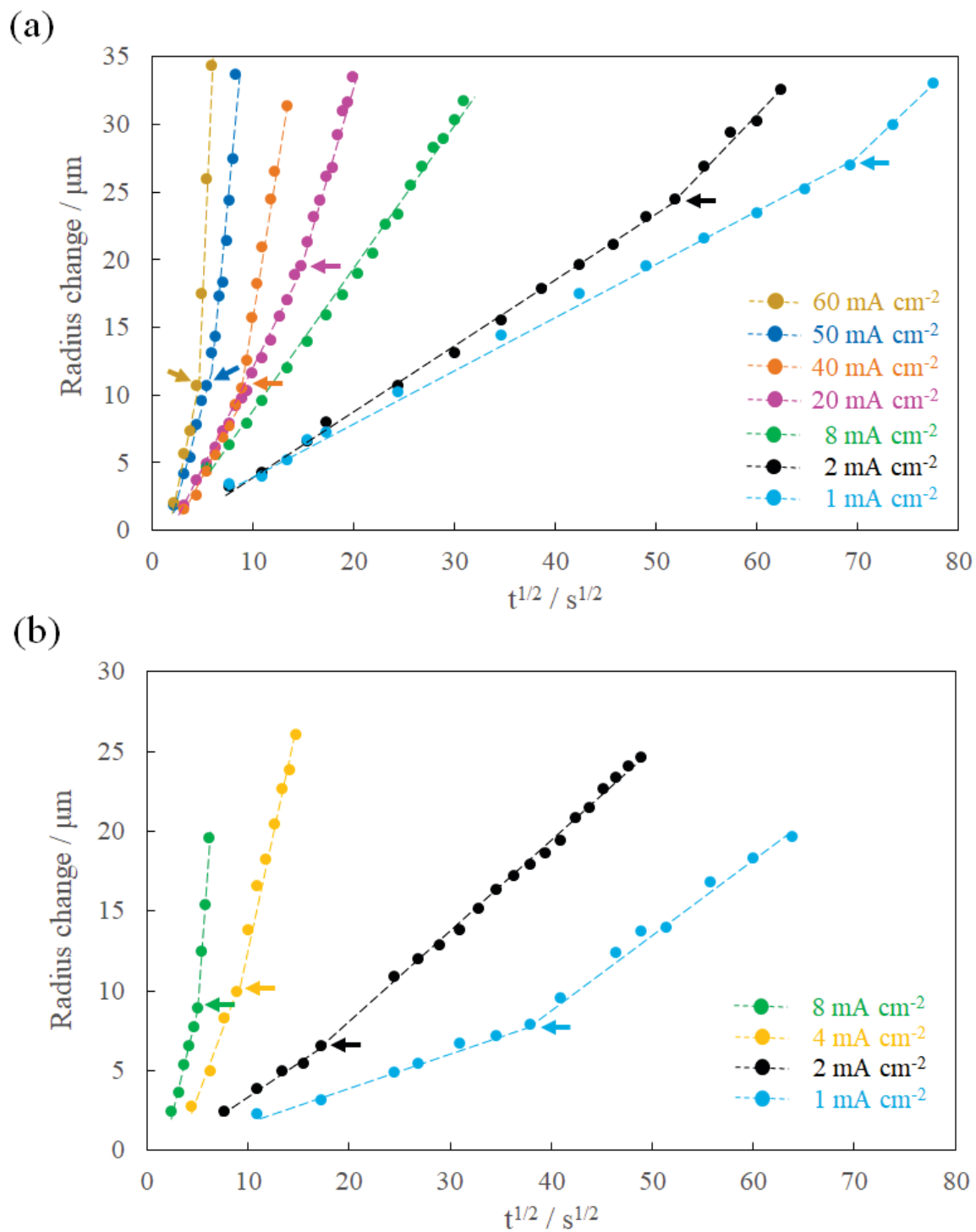
Figure 3-4. Relationships between the radius change of the Ni wire electrode and $t^{1/2}$ after starting electrolysis in (a) 1 M LiTFSI/PC and (b) 0.1 M LiTFSI/PC.
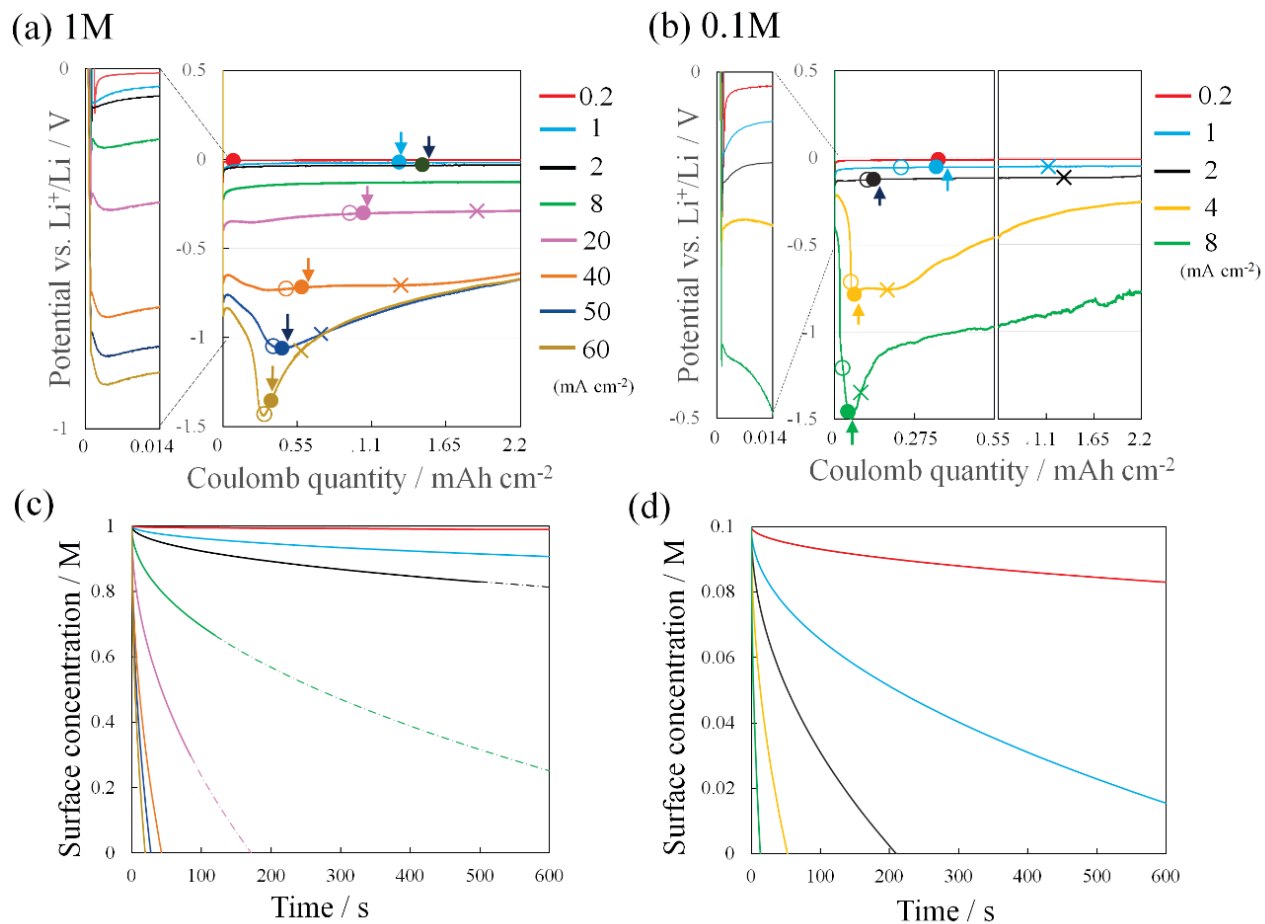
Figure 3-5. (Upper) Chronopotentiograms and (Lower) calculated surface concentration of Li^+ at different current densities on Ni Wire (φ0.5 mm × L10 mm) in 1 M LiTFSI/PC ((a) and (c)) and 0.1 M LiTFSI/PC ((b) and (d)). Open circle, solid circle, arrow and cross indicate the points at the coulomb quantities of q_z, q_{app}, q_L and q_ε listed in Table 3-1, respectively.
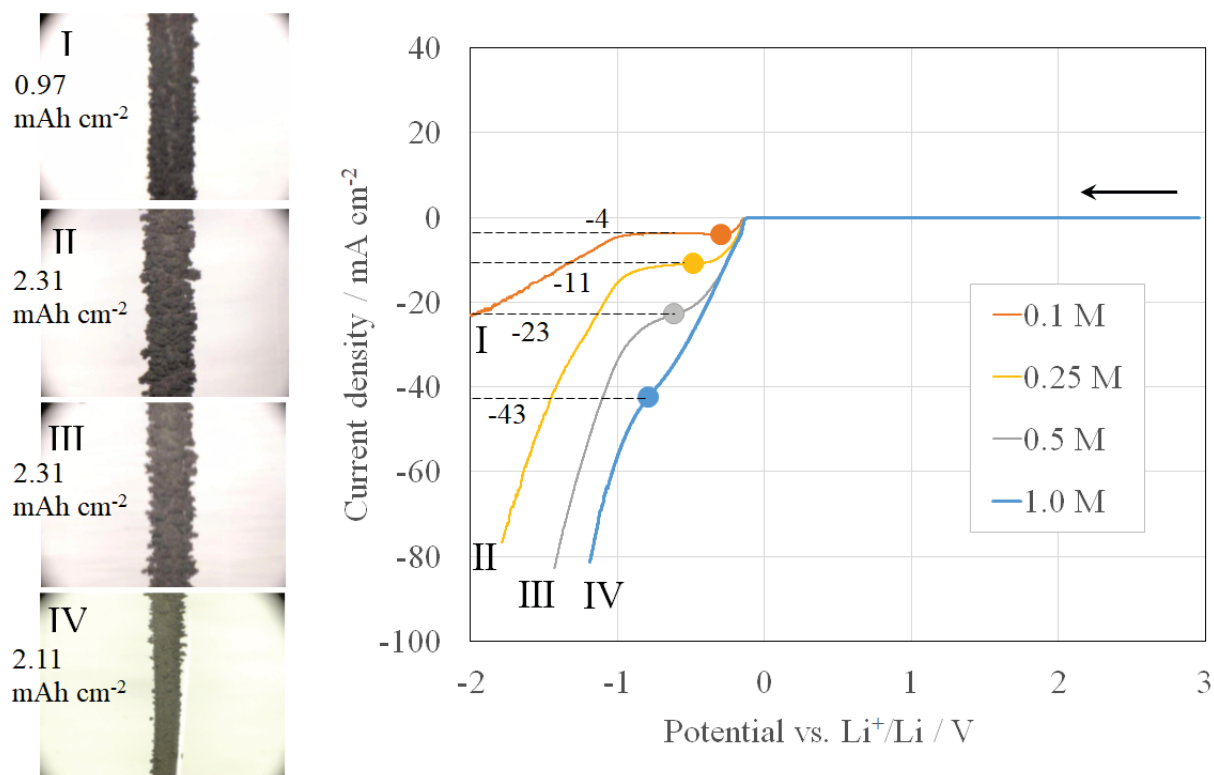
Figure 3-6. Linear sweep voltammograms at scan rates of 1 mV s⁻¹ from OCV for different salt concentrations of 0.1 M, 0.25 M, 0.5 M and 1.0 M in LiTFSI/PC electrolyte. The photos on the left show the electrode surfaces at the particular quantity of electricity in I - IV on the LSV, respectively. Solid circles on the LSV indicate the points where dendrites became visible on the video image.
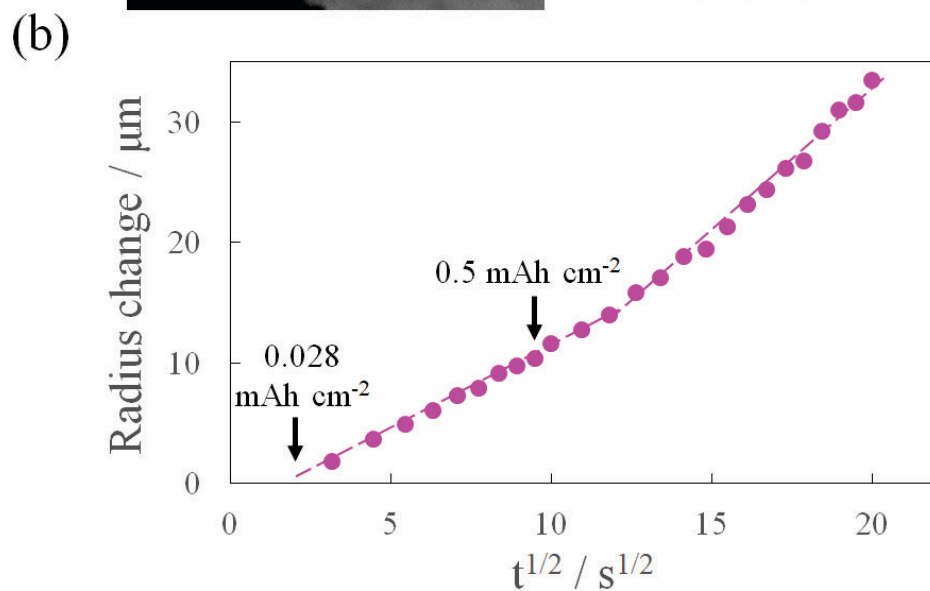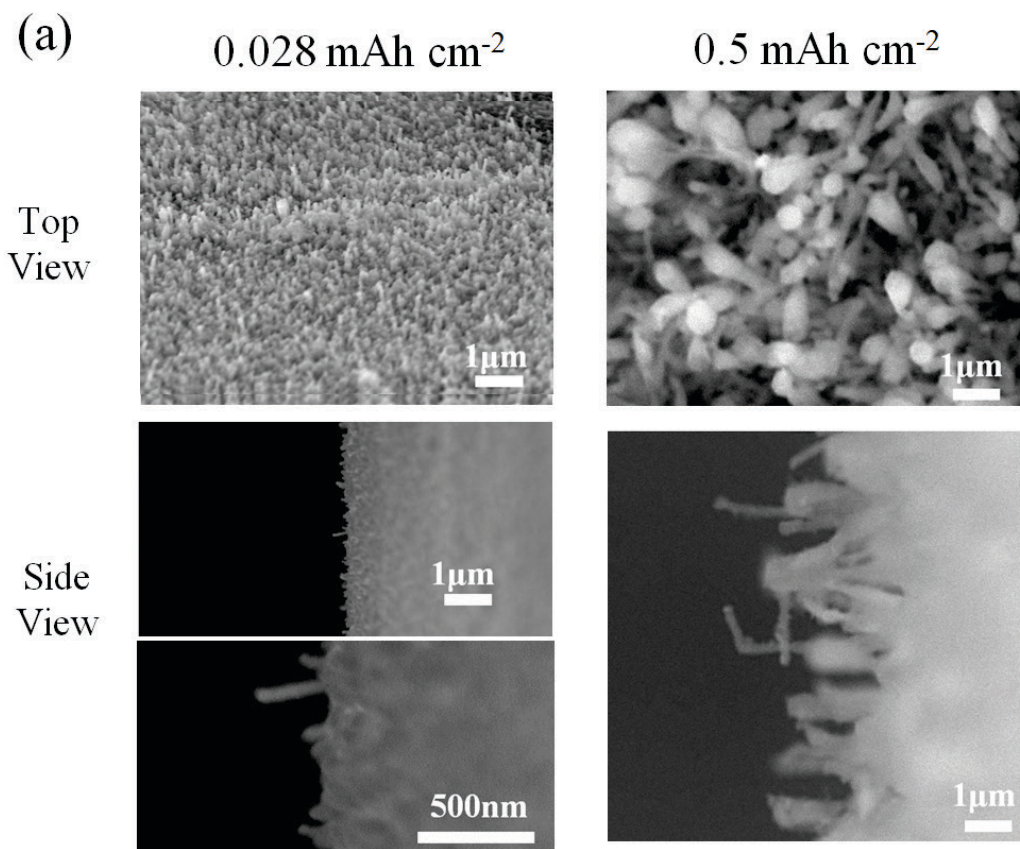
Figure 3-7. (a) SEM images taken from the top and side view of the electrode surface after electrolysis of 0.028 mAh cm^{-2} and 0.5 mAh cm^{-2} at 20 mA cm^{-2}. (b) Relation between electrode radius variation and t$^{1/2}$ at 20 mA cm^{-2}. The points corresponding to the above SEM images are indicated by arrows.

Appendix A
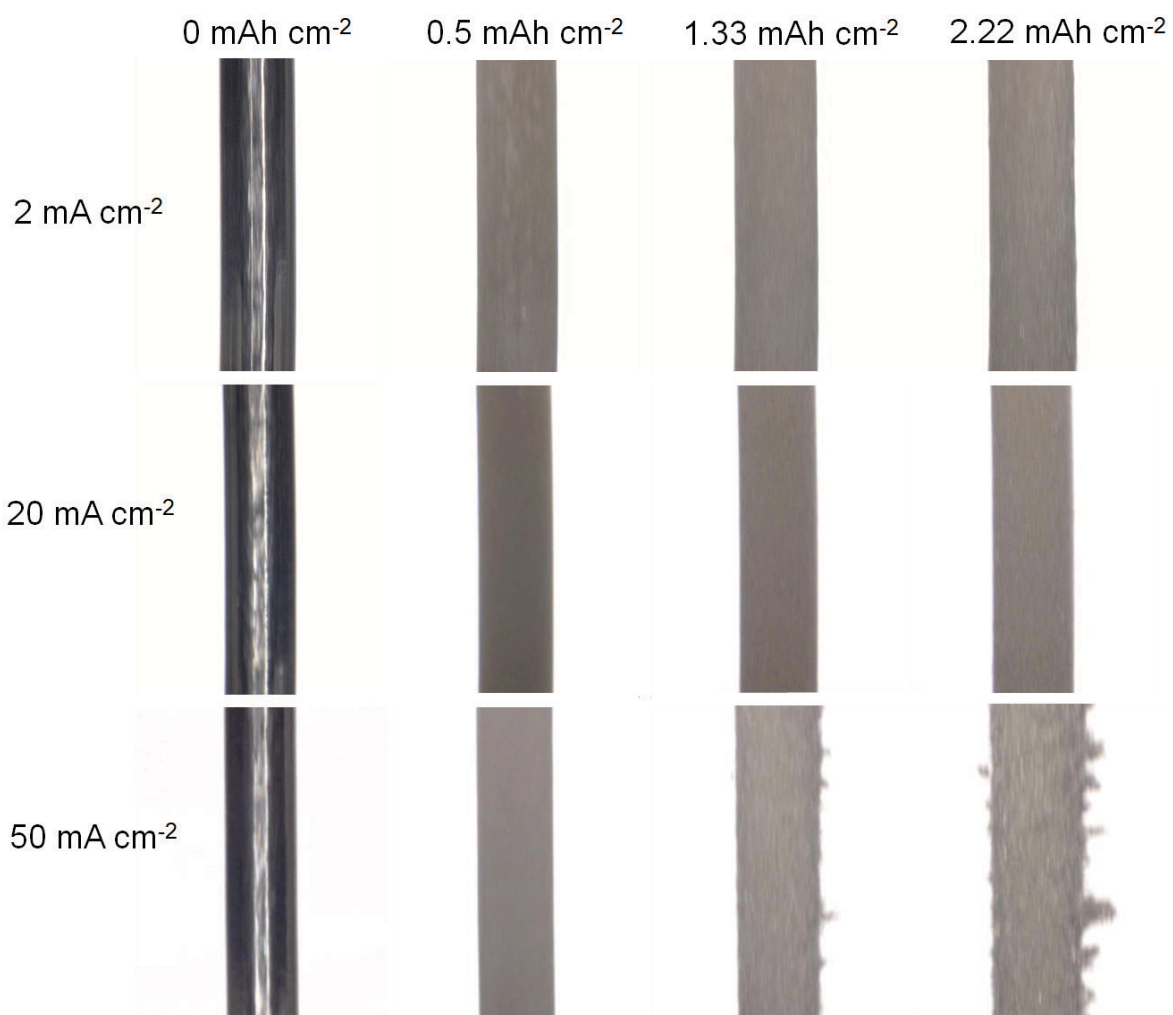
Figure 3-A1. Transient variations of Li metal morphology electrodeposited in 1.0 M LiTFSI/PC at 2, 20 and 50 mA cm^{-2} (25 ℃).

Appendix B

Assuming a one-dimensional transient diffusion equation with a boundary condition of the geometrically flat electrode surface, the transient surface concentration can be described as below. The time t_z at which $c_s = 0$ can be determined from the equation.

$$c_s = c_0 - \frac{2i(1-t^*)}{zF(\pi D)^{1/2}}t^{1/2}$$

(3-A1)

c_s is electrode surface concentration of Li$^+$, c_0 is bulk concentration, i is current density, t^* is transference number, z is valence number, F is faraday constant and D is diffusivity.

In the calculation of electrode surface concentration, the effect of natural convection was neglected. Let us now review the influence of natural convection. From the similarity law between heat conduction and mass transport, it is known that the effect of natural convection can be neglected when the value of the dimensionless number expressed as $T = [Dt/\delta^2)]$ is smaller than 0.1 and the induced natural convection attains the steady state after $T > 0.4$ in a semi-infinite electrolyte [16]. (δ; Averaged boundary layer thickness, t; Time)

$$Sh_x = \frac{x}{\delta} = 0.628(Ra_x)^{0.2} \quad (10^8 < Ra_x < 10^{13})$$

(3-A2)

$$Sh_x = \frac{i(1-t^*)x}{zFD\Theta}$$

(3-A3)

$$Ra_x = Sc \times Gr_x = \frac{v}{D} \times \frac{g\alpha i(1-t^*)x^4}{zFDv^2}$$

(3-A4)

$$v = \frac{\eta}{\rho}$$

(3-A5)

Sh_x: Sherwood number, Ra_x: Rayleigh number, Sc: Schmidt number, Gr_x: Grashof Number, Transference number; $t^* = 0.43$, Electrode height; x(cm), Faraday constant; $F = 96485$(C mol⁻¹), Diffusion constant; $D = 2.94 \times 10^{-6}$(cm² s⁻¹), Viscosity; $\eta = 8.52$(mPa s), Density; $\rho = 1.315$(g cm³), Densification coefficient; $\alpha = 90.5$(cm³ mol⁻¹), v; Kinematic viscosity.

The concentration boundary layer thickness and the time satisfying $T<0.4$ in which natural convection effects can be neglected are calculated for each current density and the results are shown in Table 3-A1. After the time satisfying $T < 0.4$, the decrease in the electrode surface concentration should be actually delayed due to the superposition of the mass transfer rate of natural convection. The time t_z at lower current densities below 8 mA cm⁻² in Table 3-1 is considerably larger than the time satisfying $T < 0.4$. Therefore, in this case, the actual point at which the electrode surface concentration reaches zero should be regarded as being later than the calculated result. On the other hand, at higher current densities above 20 mA cm⁻², it can be regarded that the effect of natural convection is negligible or its effect was small.

Table 3-B1. Concentration boundary layer thickness and specific time satisfying $T<0.4$ for each current density.

Current density	Concnetration boundary layer thickness	Specific time for $T<0.4$
/ mA cm⁻²	/ μm	/ s
1	256	89
2	223	67
4	194	51
8	169	39
20	140	27
40	122	20
50	117	19
60	113	17

Appendix C

The concentration dependence of diffusion coefficients measured in 0.5 M -1.0 M LiTFSI/PC diffusion couple by the Moiré method [24] was used in this study (Figure 3-B1).

$$D = -1.542\ C + 4.48\ /\ \times 10^6\ \text{cm}^2\ \text{s}^{-1}\ (C:\ \text{mol L}^{-1}) \tag{3-B1}$$

The transference number was calculated from $D = D_{\text{Li}+} / (D_{\text{Li}+} + D_{\text{TFSI}-})$ based on the self-diffusion coefficient measured using magnetic field gradient NMR by Hayamizu et al. [25]. In the concentration range of 0.1 M - 1.0 M, the transference number of 0.39 - 0.43 were used. The measurement results of viscosity and density of LiTFSI/PC electrolyte at different concentrations are shown in Figure 3-B2.
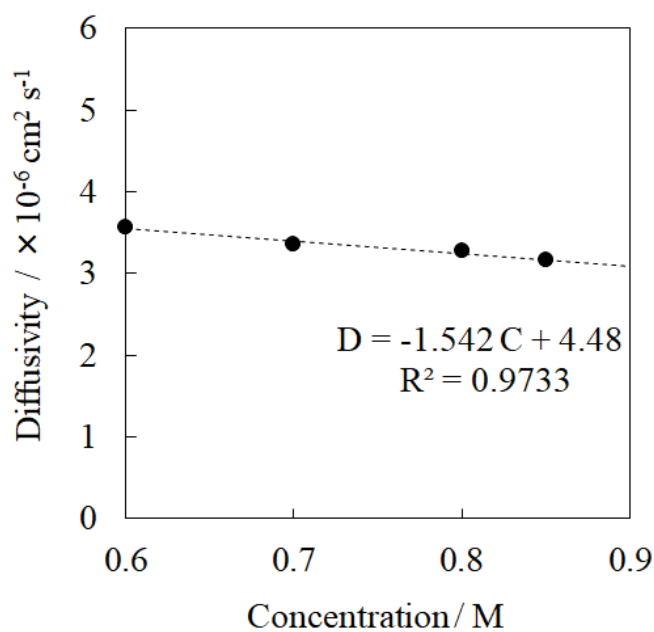
Figure 3-C1. Concentration dependence of diffusion coefficients measured in 0.5 M - 1.0 M LiTFSI/PC diffusion couple by Moiré technique.
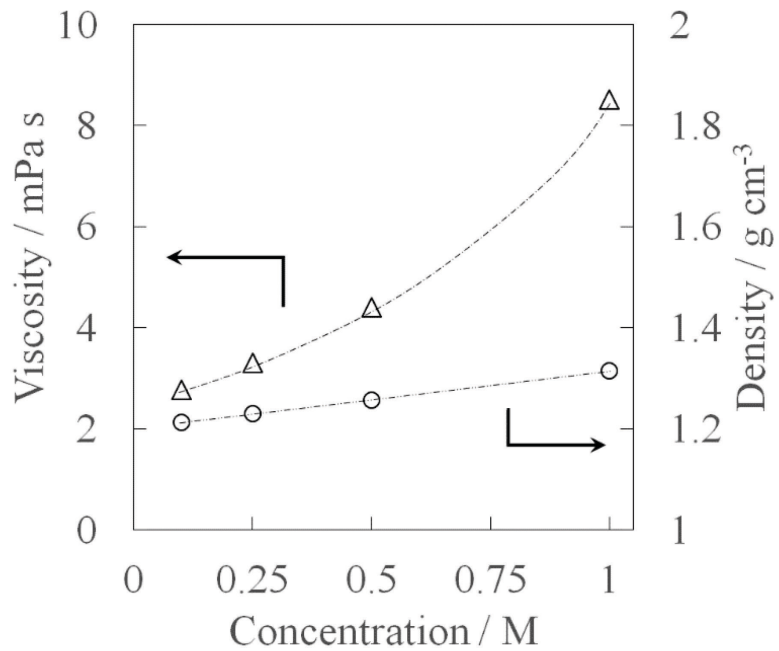
Figure 3-C2. The concentration dependence of viscosity and density of LiTFSI/PC electrolyte.

Chapter 4

Galvanostatic Li Electrodeposition in LiTFSI-PC Electrolyte: Part III. Nucleation Behavior

4.1 Introduction

The market for BEVs (battery electric vehicles) is expanding rapidly against the background of stricter environmental regulations. Rechargeable batteries are being intensively developed to replace conventional Li-ion rechargeable batteries, such as Li-O_2 batteries, Li-S batteries and lithium metal batteries combined with ternary oxide positive electrodes, which are lighter and have higher capacity [1-2]. Due to the energy density of lithium metal, a dramatic improvement in capacity can be expected if it can be used as an active material in the negative electrode. However, non-uniformity and dendrite formation in the lithium deposition process [3-4] have been standing barriers to the practical application of lithium metal negative electrodes as well as anode-less lithium metal batteries [5-6]. Short circuits may cause serious safety issues and significantly affect battery life by lowering coulomb efficiency. From this perspective, controlling morphology of electrodeposited Li is extremely important. Li electrodeposition in organic electrolyte is inherently different from metal electrodeposition in aqueous solution in that it accompanies SEI formation. In order to precisely control the morphology of electrodeposited lithium, it is necessary to consider the growth process back to the initial stage, which is consistent with the existing studies on metal electrodeposition. In previous report, the author has focused on the early stage of Li electrodeposition up to 100 mC cm^{-2} after the start of electrolysis [7]. Depending on the current density, differences were observed in the SEI formation process and in the Li deposition behavior. It was suggested from the deposit morphology and potential change that the nucleation and growth of Li at lower current densities are strongly influenced by the surface properties including SEI,

while the influence of mass transport properties becomes dominant over the influence of surface properties at higher current densities. Under the higher current density of 20 mA cm^{-2}, SEI was observed to form roughly up to 5 mC cm^{-2}, followed by the formation of nanoscale precipitates that appeared to be Li nuclei underneath the SEI up to 10 mC cm^{-2}, which grew in the SEI and penetrated into the electrolyte over 20 mC cm^{-2}.

Cui et al. reported the growth behavior of galvanostatically electrodeposited Li from 0.5 to 5 μm in size on Cu substrates up to 90 to 1080 mC cm^{-2} in 1M LiTFSI+1 wt% LiNO$_3$/DOL+DME (1:1 v/v) electrolyte. It is easy to imagine that the formation behavior of Li seed behind the particle-like Li precipitates few-μm in size influences the subsequent precipitation morphology and the observed particle-like Li precipitates correspond to the growing nuclei that have survived the growth competition. It was found that conventional nucleation and growth theory can be applied to Li nucleation under certain conditions, although it is essentially different from metal electrodeposition in aqueous solution due to the presence of SEI.

In this chapter, the author will focus on the initial electrodeposition process up to $10\,\mathrm{mC\,cm^2}$ and investigate the nucleation and growth behavior of Li underneath SEI, referring to the classical nucleation and growth theory established so far while recognizing the difference from the metal electrodeposition in aqueous solution.

4.2 Experimental

The electrolyte composed of lithium bis (trifluoromethanesulfonyl) imide (LiTFSI) and PC was used. Moisture content in the electrolyte was confirmed to be less than 20 ppm with a Karl Fischer titrator before use. The working electrode was Ni wire with a diameter of 500 μm and 10 mm in length of the exposed portion to the electrolyte. The counter electrode and the reference electrode were Li foil. All chemical reagents and the electrochemical experimental system were the same as those used in Chapter 2 [7]. Then, the electrode surface was observed using SEM

(JSM-7800F; JEOL) in the same manner described in Chapter 2. The deposits on SEM images were analyzed using image-processing software Image-J.

4.3 Results and Discussion

4.3.1 Potential variations

Fig. 4-1 shows the potential variation up to 10 mC cm^{-2} during galvanostatic electrolysis in 1M LiTFSI/PC at current densities from 0.04 to 60 mA cm^{-2} and a magnified view up to 0.4 mC cm^{-2}. As previously reported, there appears to be a boundary in potential variation and deposit morphology around 4 mA cm^{-2}. At any current density, the potential reaches a minimum after 4 to 8 mC cm^{-2}. At lower current densities up to 4 mA cm^{-2}, coulomb quantity required to reach a minimum decrease with increasing current density, but above 4 mA cm^{-2}, it does not change much with respect to changes in current density.

As soon as electrolysis begins, the potential changes rapidly over coulomb quantity of 0.2 mC cm^{-2}. There is a jump from an OCV around 3 V to +1.8 ~ 0.6 V. The higher the current density, the greater the change from the OCV. After that, a gradual change in potential can be observed over 0.4 mC cm^{-2}. In a previous report, it was considered that the coulomb quantity immediately after the start of electrolysis was derived from LiF formation based on XPS analysis [7]. The potential at 0.4 mC cm^{-2} plotted against current density is shown in Fig. 4-2. Different linearities between the potential and the current density are observed in the lower current density range of 0.04 to 4 mA cm^{-2} and in the higher current density range of 4 mA cm^{-2} to 60 mA cm^{-2}. If the potential plateau seen over 0.4 mC cm^{-2} originates from the same reaction, Fig. 4-2 should show a straight line as that below 4 mA cm^{-2}. It is suggested that two different resistive components depending on the current density are involved in the behavior of the potential immediately after the start of electrolysis. Ohmic drop may include electrolyte resistance, native oxide film on the Ni electrode surface and the effects of the SEI film formed immediately after the start of

electrolysis. If there exists a natural oxide film of ca. 10 nm thickness on Ni (estimated from XPS depth analysis), an ohmic loss of ca. 200 mV will be generated by applying $20\,\mathrm{mA\,cm^{-2}}$ assuming the resistivity of NiO film as 1.0×10^7 Ω cm[9]. Calculating the amount of LiF produced by 0.4 mC cm^{-2} yields 1.08×10^{-7} g cm^{-2}. Considering the density of LiF to be 2.639 g cm^{-3}, the uniform formation of LiF would result in a thickness of 4.08×10^{-8} cm (4 Å). Then, LiF will be produced roughly with the thickness of the lattice constant of 4.0173 Å.

4.3.2 SEM observation

Fig. 4-3 shows the SEM observation results for the electrode surface after electrolysis up to 10 mC cm^{-2} at each current density. At any current density, nanoscale precipitates ranging from several tens to 100 nm in size are formed. Their size looks slightly smaller and the number seems to increase with increasing current density. The precipitation morphology at lower current densities of 0.2 and 2 mA cm^{-2} is non-uniform as indicated by the formation of filament-like precipitates, while the deposition behavior appears more uniform at higher current densities of 8, 20 and 50 mA cm^{-2}.

The number and size of precipitates were analyzed from the SEM images using image processing software (Image-J). The size of the deposit was defined as the radius of a circle having the same area. First, the number and size of precipitates were counted and measured manually one by one for the SEM image of 10 mC cm^{-2} at 20 mA cm^{-2}. The results were compared with the results of the image processing. Those results are shown in Appendix A. There are some differences between them, but the results are relatively close. Therefore, image processing was performed on SEM images of arbitrary 8 fields of view for each current density. The current density dependence of the number of precipitates and average particle size is shown in Fig. 4-4 (SEM images of 8 fields of view for each current density and image processing results are shown in Appendix B). The number distribution of precipitates in Fig. 4-4(a) shows that there appears to be non-uniformity at lower current densities characterized by the presence of large particles while

being biased toward small particles. In comparison, a peak shape appears at higher current densities, which seems to reflect a more uniform depositing behavior. Fig. 4-4(b) shows that the number of precipitates at 10 mC cm^{-2} increased with current density from 2×10^{10} to 4.5×10^{10} particles cm^{2}, and the average particle size slightly decreased from ca. 19 nm to ca. 15 nm. At current densities of 0.2 mA cm^{-2} and 2 mA cm^{-2}, inhomogeneous deposition has already been observed at 10 mC cm^{-2} as characterized by the appearance of large filament-like precipitates, suggesting that localized growth is progressing. At higher current densities, more uniform nucleation and growth appears to be occurring compared to that at lower current densities. It should be noted that the precipitation morphology at lower current densities of 0.2 mA cm^{-2} and 2 mA cm^{-2} includes the effects of inhomogeneity even in the very early processes of 10 mC cm^{-2}.

The distribution of nanoscale precipitates on the substrate during the initial process is important for the subsequent growth process. The analysis results of the nearest neighbor distance of the nanoscale precipitates are shown in Fig. 4-5. Fig. 4-5(a) shows that the distribution of the nearest neighbor distances are relatively close to the Poisson distribution [10] represented by the dashed line at 2 and 8 mA cm^{-2}, but there is a divergence at 20 and 50 mA cm^{-2}. As shown in Fig. 4-5(b), the nearest neighbor distance decreases with current density, reflecting the tendency seen in Fig. 4-4(b) where the number of nuclei increases and their size decreases with increasing current density. The average grain size of the precipitates and the first nearest distance are getting closer as the current density increases. It is assumed that neighboring precipitates are very close to each other or agglomerated. The deviation from the Poisson distribution observed in the case of 50 mA cm^{-2} may be due to the agglomeration phenomenon of the nuclei.

4.3.3 Nucleation behavior

The potential profiles up to 4 mC cm^{-2} at 4 to 50 mA cm^{-2} appear to have similar potential profiles except for the potential drop derived from ohmic losses due to such as electrolyte resistance, native oxide film on Ni electrode and the generated SEI film. In other words, in Fig. 4-

1, the potential profile for current density higher than 4 mA cm^{-2} appears as if the potential profile for 4 mA cm^{-2} is shifted to the negative direction by the ohmic drop. Figure 4-6 shows the potential transients after each potential from 8 to 50 mA cm^{-2} is corrected in the positive direction for the potential difference relative to 4 mA cm^{-2} at 0.4 mC cm^{-2}. The corrected potential profiles at 4 to 50 mA cm^{-2} are in good agreement. Under higher current densities of 4 to 50 mA cm^{-2}, a similar SEI formation process is assumed to be taking place up to 4 mC cm^{-2}.

As confirmed by LSV measurements in a previous report [7], the potential at which the Li^{+} reduction reaction begins to occur was -25 mV. If the author sets -25 mV and its time as the zero point, an η-t curve for lithium deposition can be drawn as shown in Fig. 4-7(a). In any current densities, the overpotential η decreases linearly with respect to time and then reaches a minimum value. Kashchiev described the potential change immediately after the start of electrodeposition on a foreign substrate in aqueous solution as shown in Fig. 4-7(b) [11]. At first, charging of the electric double layer and a formation of adatom occur between time 0 and t_1, and the adatoms form clusters with a critical radius or less. When the potential exceeds η_c at the time t_1, nucleation begins and the overpotential begins to deviate from its linear variation to that point. Due to the increase in electrode area associated with nucleation and the precipitation on the same metal, the overpotential decrease. When nuclear growth becomes more dominant than nucleation, the potential reaches a minima of η_m at t_m and then begins to increase. At time t_2, the potential passes through η_c again and nucleation stops at a potential higher than η_c. After the time t_2, nuclear growth proceeds. As reported in a previous report, since nuclei generated in SEI immediately start to grow at higher current densities, the potential is expected to reach a maximum at t_3 before t_2 appears and then decrease again, as shown in Fig. 4-7(c).

Since the current associated with nucleation does not run until nucleation, the current i (A cm^{-2}) during galvanostatic electrolysis can be described as follows, where i_d (A cm^{-2}) is the current associated with charging of the electric double layer, i_L (A cm^{-2}) is the current associated with the Li^{+} reduction reaction, η (V) is the overpotential for Li deposition, C_d (F cm^{-2}) is the electrostatic

capacity of the electric double layer, Γ (cm^{-2}) is the concentration of adatom on the electrode surface, and e is the elementary charge (C).

$$i = i_d + i_L = C_d \frac{d\eta}{dt} + e\frac{d\Gamma}{dt} \tag{4-1}$$

Assuming a diffusion rate-limiting process under higher current densities, η is expressed as follows;

$$\eta = \frac{kT}{e} ln \frac{c_0}{c_s} \frac{\Gamma}{\Gamma_0} \qquad \left(\Gamma = \Gamma_0 \frac{c_s}{c_o} exp\left(\frac{e}{kT}\eta\right)\right) \tag{4-2}$$

where c_s: Li$^+$ concentration at electrode surface (cm^{-3}), c_0: Li$^+$ concentration in bulk (cm^{-3}), k: Boltzmann constant (J K^{-1}), T: temperature (K).

$$\frac{d\eta}{dt} = \frac{i}{C_d + ef\Gamma_0 \frac{c_s}{c_0} exp\left(\frac{e}{kT}\eta\right)} \tag{4-3}$$

From $t\rightarrow0$, $\eta\rightarrow0$, $c_s\rightarrow c_0$,

$$\Gamma_0 = \frac{kT}{e^2}\left(\frac{i}{\frac{d\eta}{dt}\big|_{t=0}} - C_d\right) \tag{4-4}$$

From $k = 1.38\times10^{-23}$ (J K^{-1}), $T = 298$ (K), $e = 1.60\times10^{-19}$ (C), $\frac{d\eta}{dt}\big|_{t=0}$ read from Fig. 4-7 and C_d $=7\times10^{-5}$ (F cm^{-2}), Γ_0 can be obtained.

Adatom and cluster formation on the electrode surface eventually leads to nucleation. From the Volmer-Weber equation [12] for three-dimensional nucleation, the nucleation rate and the number of nuclei are expressed as follows;

$$J = K_1 exp(-K_2/\eta^2) \tag{4-5}$$

$$N_0 = s \int_{t_1}^{t_2} J(\eta, t)\, dt \tag{4-6}$$

$$K_1 = \frac{2N_0 v i_0}{ze} \left(\frac{\sigma}{2kT}\right)^{1/2} \tag{4-7}$$

$$K_2 = \frac{8\pi\sigma^3 v^2}{3z^2 e^2 kT} \tag{4-8}$$

At time t_1, the first nucleus is generated from the clusters that have been formed on the electrode surface up to that point, so K_1 and K_2 are determined from the experimentally obtained η-t curve so as to satisfy the following equation.

$$1 = K_1 \int_0^{t_1} exp\left(-\frac{K_2}{\eta^2}\right) dt \tag{4-9}$$

where σ: surface energy of Li (J cm^{-2}), i_0: exchange current density (A cm^{-2}), N_0: number of nucleation sites (cm^{-2}), and v: atomic volume (cm^3).

Once the surface energy σ is determined so that the above relationship as well as the potential variation is satisfied, the value of r_c can be estimated from the relation $\eta_c = 2\sigma v/zer_c$ as $N_0 = 1\times10^{15}$ (cm^{-2})[13], $v = 2.16\times10^{-23}$ (cm^3), $i_0 = 0.01$ (A cm^{-2})[14], $z = 1$, $k = 1.38\times10^{-23}$ (J K^{-1}), $T = 298$ (K).

The values of Γ_0, σ, r_c, and N obtained from the η-t curve in Fig. 4-7(a) at higher current densities than 4 mA cm^{-2} are summarized in Table 4-1. The surface energy of Li is somewhat smaller than that calculated by Perdew et al. to be 2.0 - 4.3$\times10^{-5}$ (J cm^{-2}) [15]. Compared to the number of nanoscale precipitates in Fig. 4-4(b), the number of nucleation N shows close value.

4.4. Conclusions

The nucleation and growth behavior of Li was investigated from SEM images obtained during galvanostatic electrodeposition up to 10 mC cm^{-2} in 1M LiTFSI/PC electrolyte by changing the current density from 0.2 to 60 mA cm^{-2}. Nanoscale precipitates with sizes ranging from several tens to 100 nm were formed at every current density, and the number of precipitates and their sizes were analyzed using image analysis software. The number of precipitates at 10 mC cm^{-2} increased with current density from 2 to 4.5×10^{10} particles/cm^2, and the average particle size slightly decreased from ca. 19 nm to ca. 15 nm. Analysis of the nearest neighbor distances of the precipitates showed a deviation from the Poisson distribution at higher current densities, suggesting the influence of agglomeration between neighboring precipitates.

The potential profiles up to 4 mC cm^{-2} at 4 to 50 mA cm^{-2} appear to have similar potential profiles except for the potential drop derived from ohmic losses. At higher current densities above 4 mA cm^{-2}, the number of nucleation obtained by analyzing the potential transient behavior ranged from 1.2 to 4.5×10^{10} nuclei/cm^2 depending on the current density, which is relatively in good agreement with the results of the SEM image analysis. It was suggested that conventional nucleation and growth theory can be applied some extent to Li nucleation under certain conditions, although it is essentially different from metal electrodeposition in aqueous solution due to the presence of SEI.

References

[1] H.Zhang, G. G. Eshetu, X. Judez, C. Li, L. M. Rodriguez-Martínez and M. Armand, Electrolyte Additives for Lithium Metal Anodes and Rechargeable Lithium Metal Batteries: Progress and Perspectives, Angew. Chem. Int. Ed., 57, 15002-15027 (2018).

[2] H. Zhang, U. Oteo, X. Judez, G. G. Eshetu, M. Martinez-Ibañez, J. Carrasco, C. Li and M. Armand, Designer Anion Enabling Solid-State Lithium-Sulfur Batteries, Joule, 3, 1689-1702 (2019).

[3] X. Zhang, A. Aoxuan, X. Liu and J. Luo, Dendrites in lithium metal anodes: Suppression, regulation and elimination, Acc. Chem. Res., 52, 3223-3232 (2019).

[4] D. Lin, Y. Liu and Yi Cui, Reviving the lithium metal anode for high-energy batteries, Nature Nanotechnology, 12, 194–206 (2017).

[5] S. H. Park, D. Jun, G. H. Lee, S. G. Lee and Y. J. Lee, Toward high-performance anodeless batteries based on controlled lithium metal deposition: a review, J. Mater. Chem. A, 9, 14656 (2021).

[6] S. Nanda, A. Gupta and A. Manthiram, Anode-free full cells: A pathway to high-energy density lithium-metal batteries, Adv. Energy Mater, 11, 2000804 (2021).

[7] T. Nishida, Y. Fukunaka, T. Homma and T. Nohira, Galvanostatic Li Electrodeposition in LiTFSI-PC Electrolyte: Part I. Effects of Current Density in Initial Stage, J. Electrochem. Soc., 169, 100548 (2022).

[8] A. Pei, G. Zheng, F. Shi, Y. Li and Y. Cui, Nanoscale nucleation and growth of electrodeposited lithium metal, Nano Lett., 17, 1132–1139 (2017).

[9] A. Matsuda, S. Akiba, M. Kasahara, T. Watanabe, Y. Akita and M. Yoshimoto, Anisotropic electric conduction derived from self-organized nanogroove array on Li-doped NiO epitaxial film, Appl. Phys. Lett., 90, 182107 (2007).

[10] M. Morisue, Y. Fukunaka, E. Kusaka, R. Ishii and K. Kuribayashi, Effect of gravitational strength on nucleation phenomena of electrodeposited copper onto a TiN substrate, Journal of Electroanalytical Chemistry, 559, 155-163 (2003).

[11] D. Kashciev, Kinetics of the initial stage of electrolytic deposition of metals III. Galvanostatic conditions, Thin Solid Films, 29, 193-209 (1975).

[12] M. Volmer and A. Weber, Nucleus Formation in Supersaturated Systems, Z. Phys. Chem., 119, 227 (1926).

[13] Milchev, A. In Electrocrystallization Fundamental of Nucleation and Growth; Kluwer Academic Publishers: New York, 2002; Vol 1; pp 95−98

[14] X.-M. Wang, T. Nishina and I. Uchida, Application of the microelectrode technique to the kinetic study of lithium deposition/dissolution and alloying in organic solutions, J. Power Sources, 68, 483-486 (1997).

[15] J. P. Perdew, H. Q. Tran and E. D. Smith, Stabilized jellium: Structureless pseudopotential model for the cohesive and surface properties of metals, Phys. Rev. B: Condens. Matter Mater. Phys., 42, 11627-11636 (1990).

Table 4-1. The specific time value t_1, t_2 and t_3 read from Fig. 4-6 and analytical value of Γ_0, σ, r_c and N.

mA cm^{-2}	t_1 /s	t_2 /s	t_3 /s	Γ_0 /10^{-14}cm^{-2}	σ /10^{5}J cm^{-2}	$2r_c$ /nm	$N(t_{2\,or}\,t_3)$ /10^{-10}cm^{-2}
0.2	1.02	2.94	—	4.6	1.6	1.3	0.77
2	0.093	—	0.27	3.4	1.8	1.1	0.97
4	0.06	—	0.18	3.4	1.9	1.1	1.2
8	0.028	—	0.1	3.8	2.0	1.1	1.5
20	0.0066	—	0.051	3.6	1.2	1.4	4.0
40	0.004	—	0.018	3.5	1.5	1.3	4.5
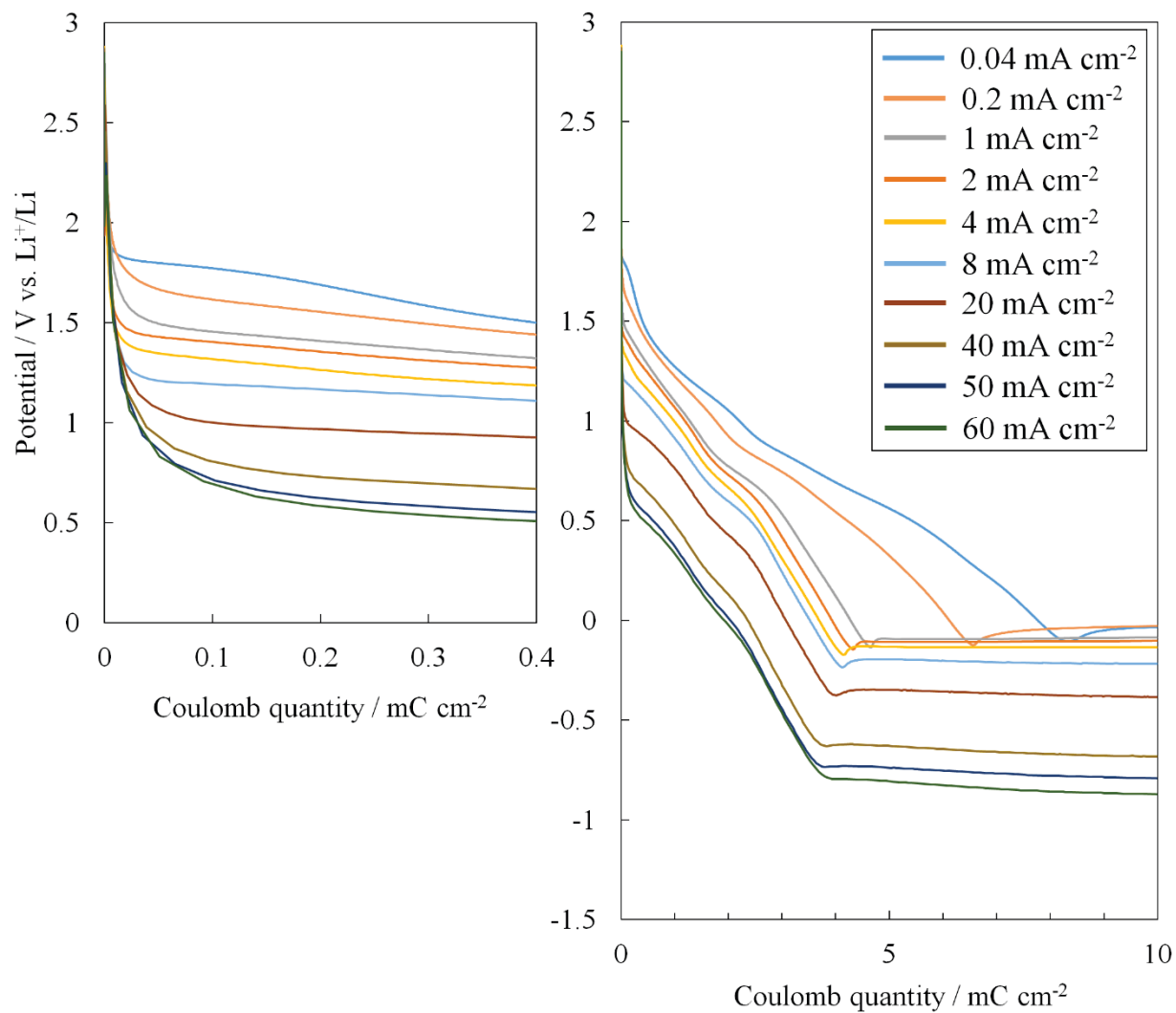
Figure 4-1. Chronopotentiograms after the start of electrolysis at the current density from 0.04 mA cm^{-2} to 60 mA cm^{-2} for the coulomb quantity of 0 - 0.4 mC cm^{-2} (left) and 0 - 10 mC cm^{-2} (right) in 1.0M LiTFSI/PC at 25°C.
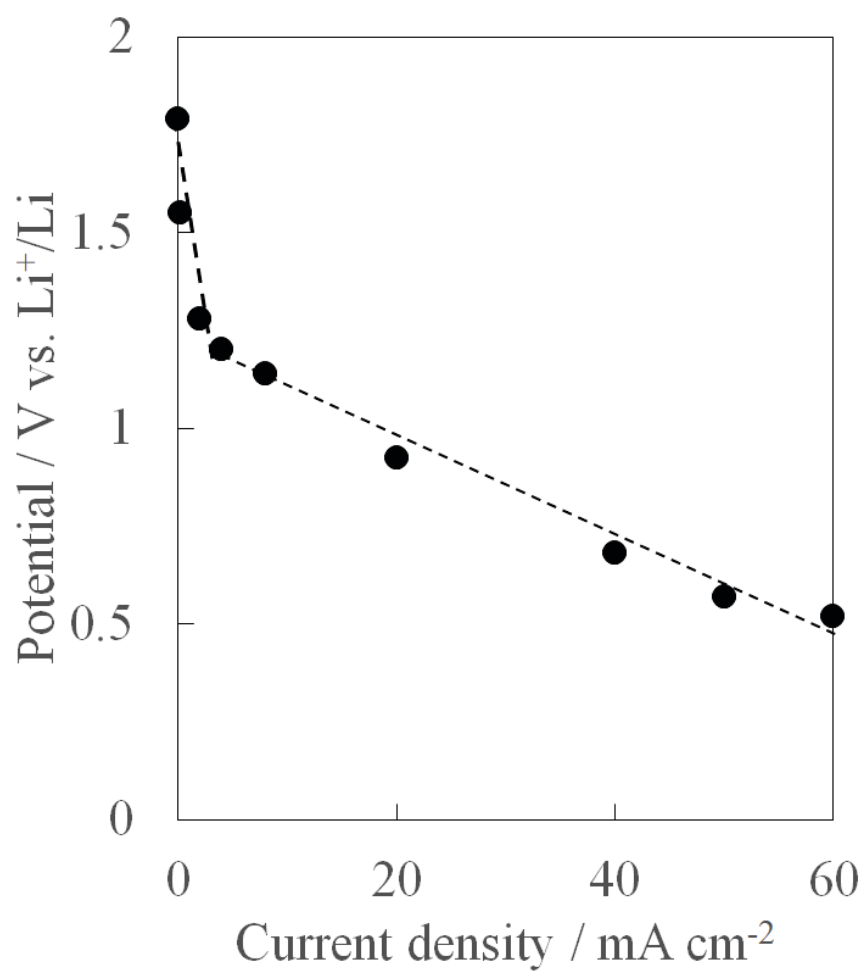
Figure 4-2. Relation between potential and current density at 0.4 mC cm^{-2} after the start of electrolysis.
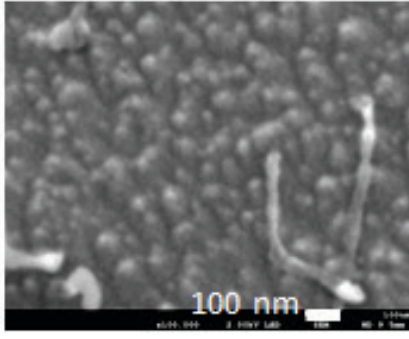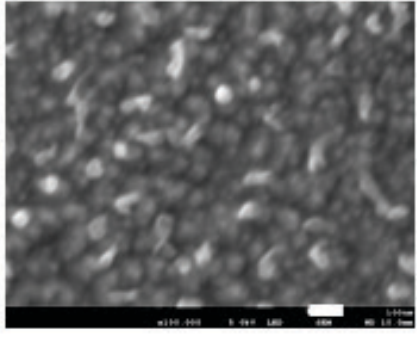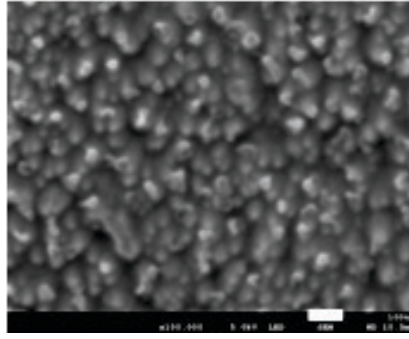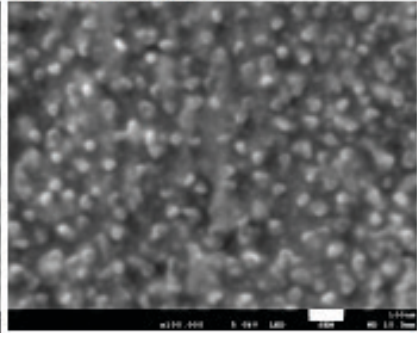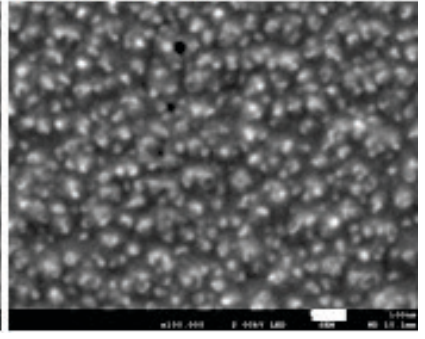
Figure 4-3. SEM images of Ni electrode surface after electrolysis up to 10 mC cm^{-2} at current densities of 0.2, 2, 8, 20 and 50 mA cm^{-2}.

(a)

0.2 mA cm^{-2} 2 mA cm^{-2} 8 mA cm^{-2} 20 mA cm^{-2} 50 mA cm^{-2}

Number / $\times 10^8$ cm^{-2}

Radius / nm

(b)

Number / $\times 10^{10}$ cm^{-2}

Radius / nm

Current density / mA cm^{-2}
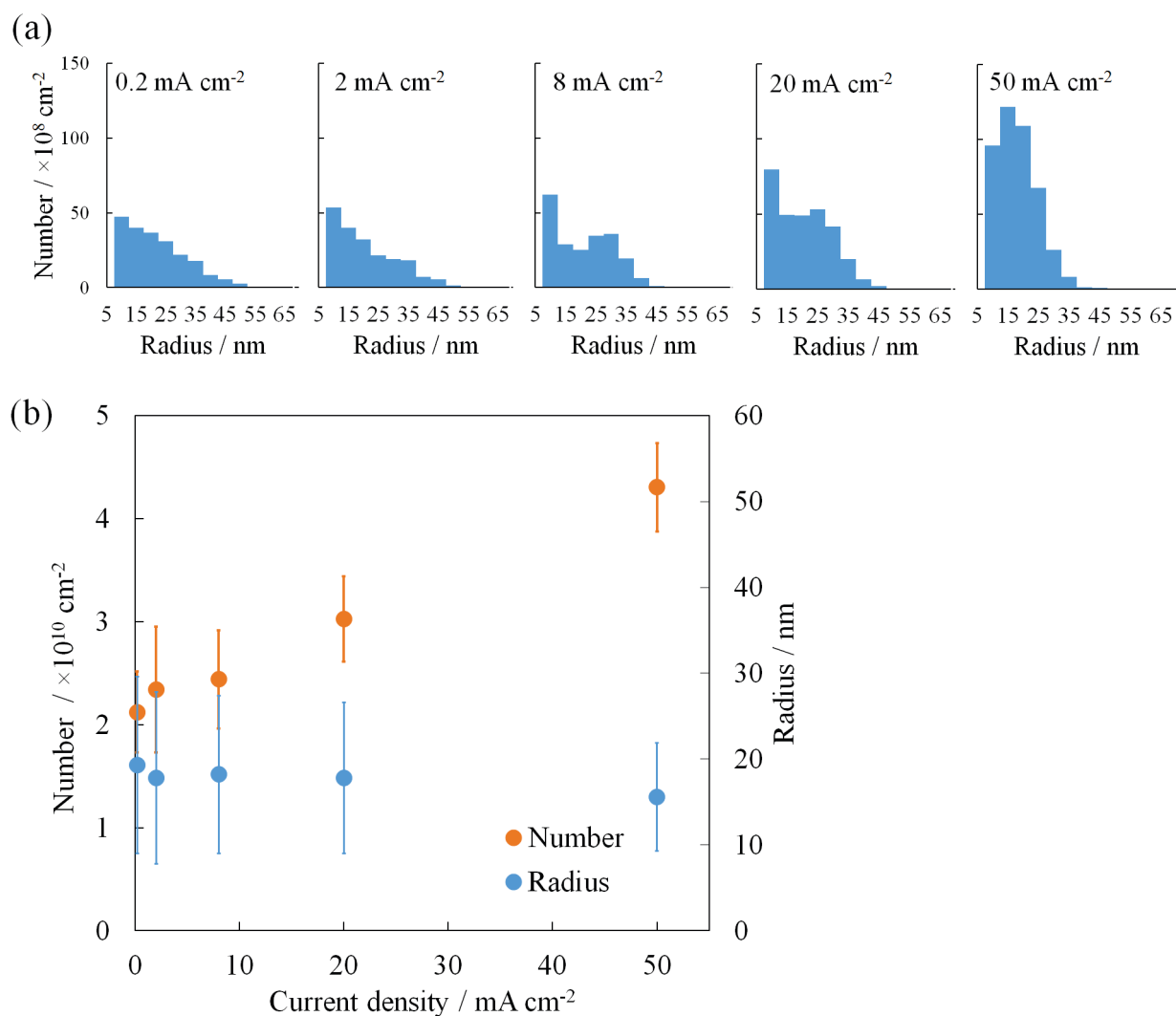
● Number
● Radius

Figure 4-4. (a) Effect of applied current density on electrodeposited Li size distribution after electrolysis up to 10 mC cm^{-2}. (b) Applied current density dependences of average number and radius of Li precipitates for 10 mC cm^{-2}.
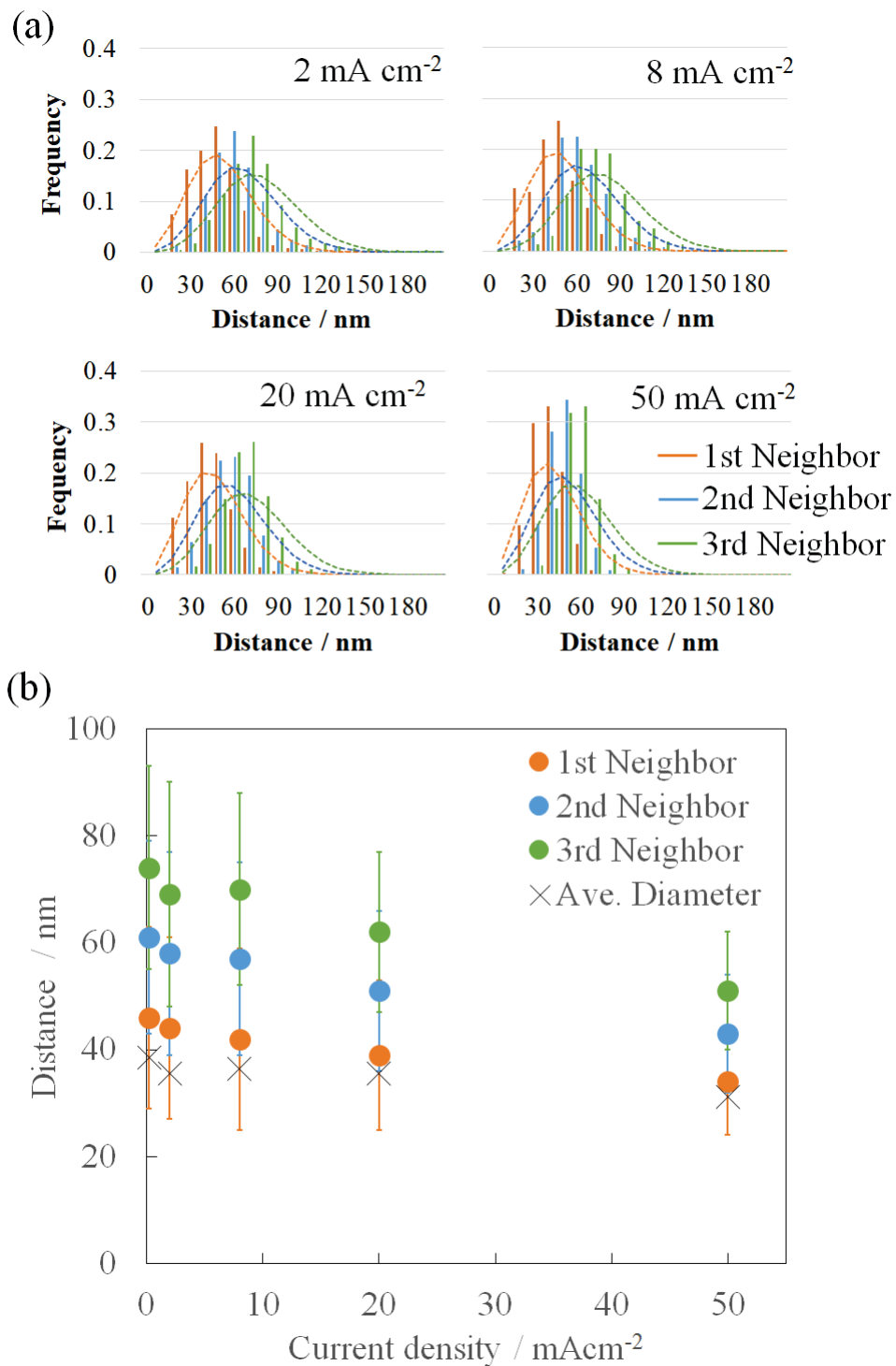
Figure 4-5. (a) Distribution of nearest neighbor distance of Li deposits after electrolysis up to 10 mC cm^{-2} at 2, 8, 20 and 50 mA cm^{-2}. (b) Applied current density dependences of nearest neighbor distance of Li deposits.
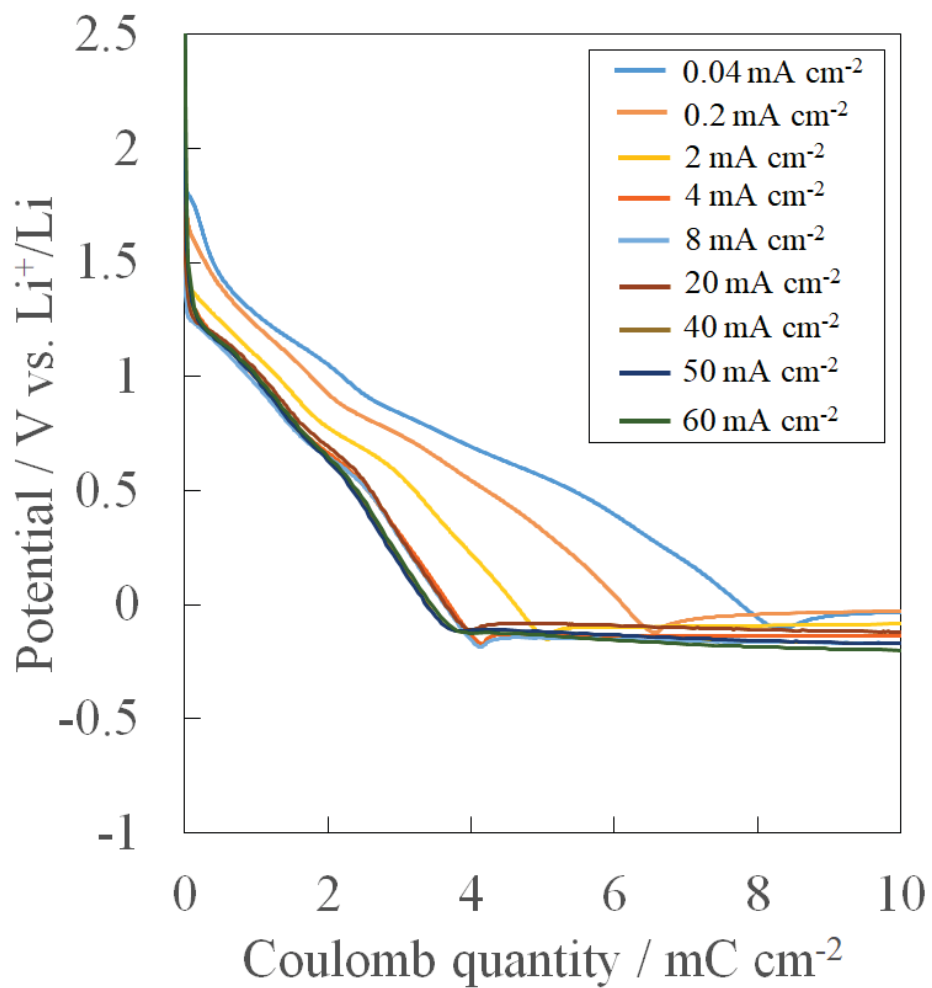
Figure 4-6. Chronopotentiograms after correction of potential for the current densities of 4, 8, 20, 40 and 50 mA cm⁻².
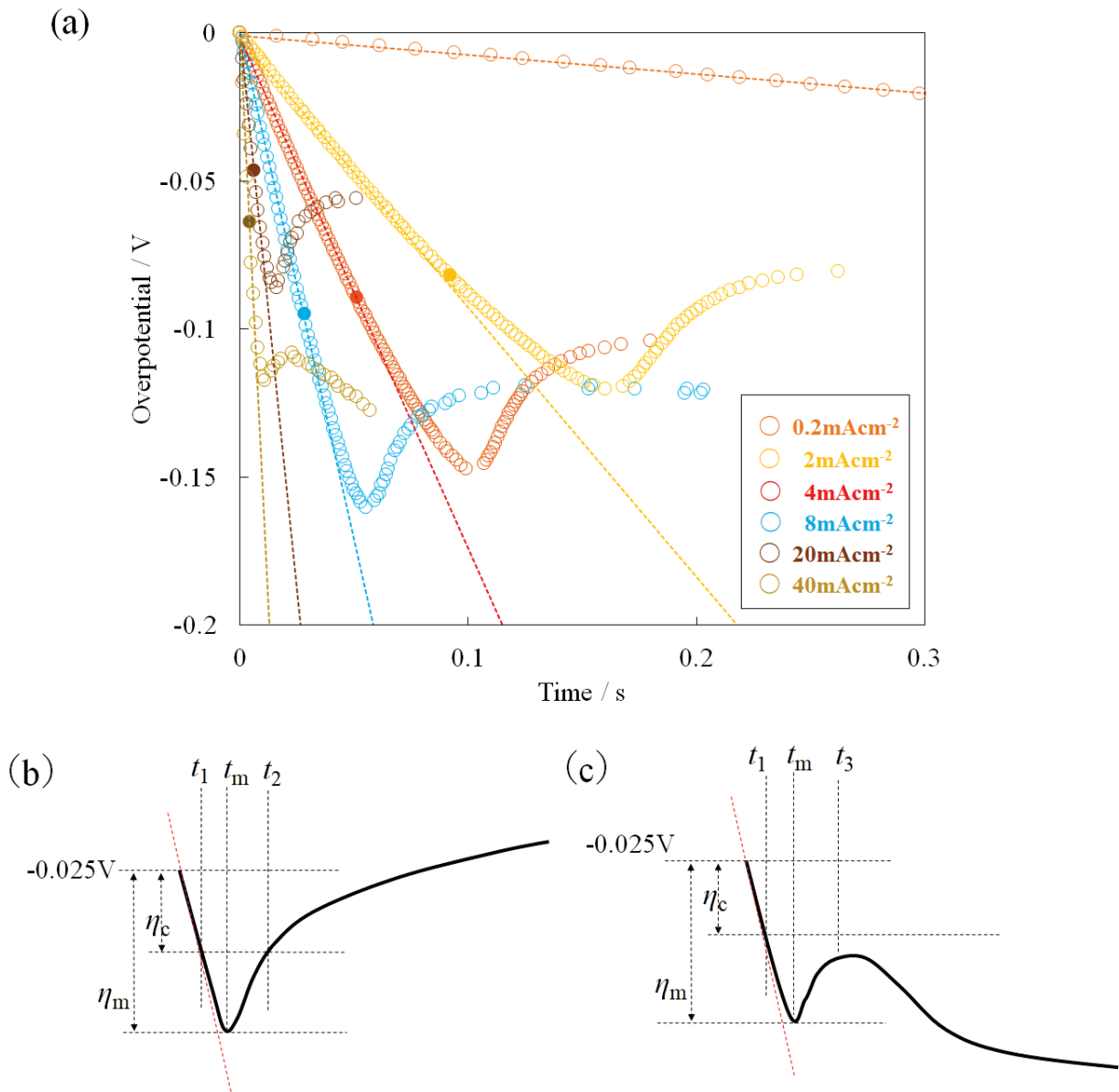
Figure 4-7. (a) Time variation of the potential when -25 mV and its time in Fig. 4-6 is corrected to 0 point. The ● mark indicates time t_1 in Figures (b) and (c). Figures (b) and (c) show schematic diagrams of the potential change during nucleation at lower and higher current densities, respectively.

Appendix A
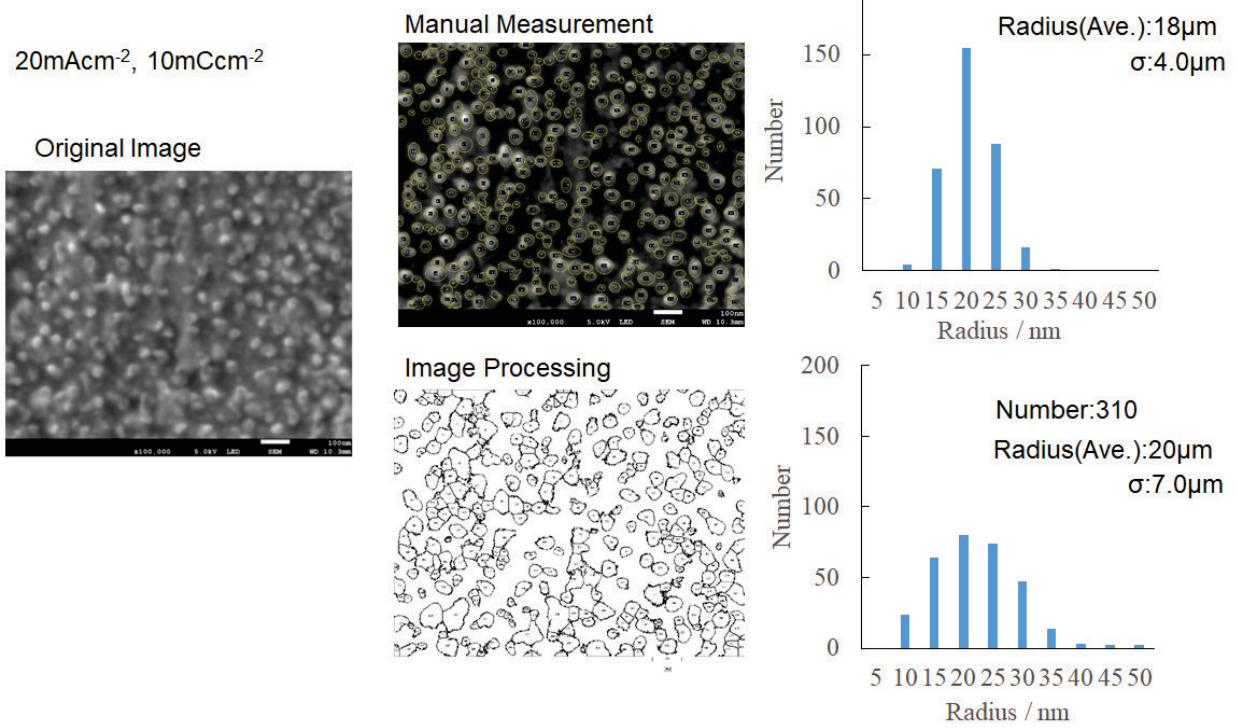
Figure 4-A. Comparison of visual measurement and image processing of deposits number and size in SEM images for 10 mC cm^{-2} at 20 mA cm^{-2}.

Appendix B

(a)
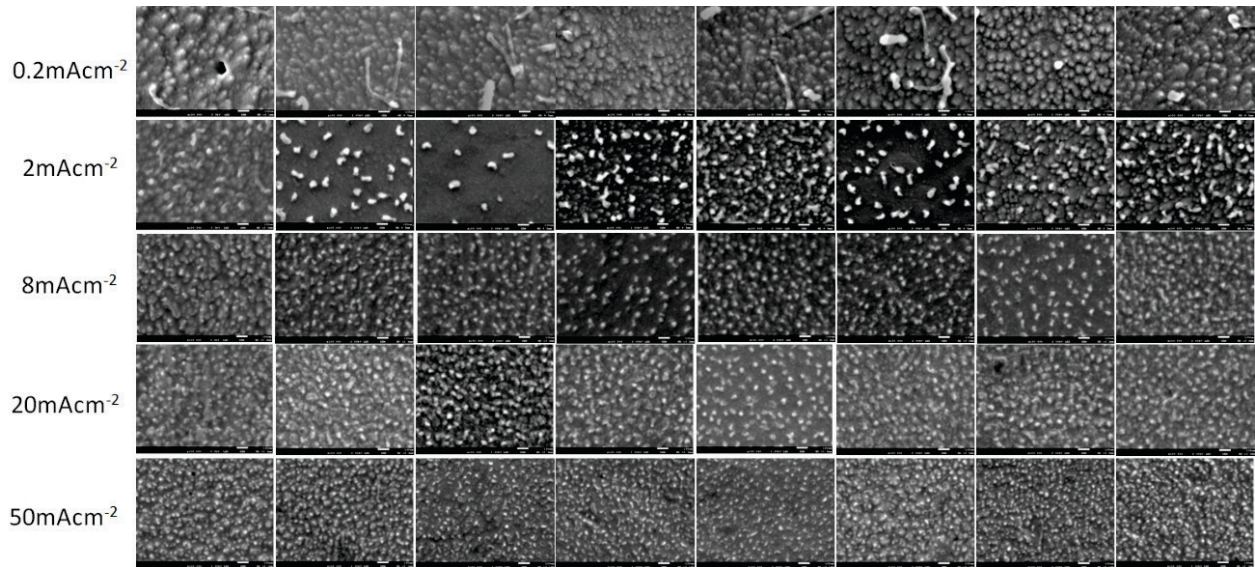
(b)

Figure 4-B. (a) SEM images for arbitrary eight fields of view for each current density and (b) the results of the image processing.

Chapter 5

Potentiostatic Li Electrodeposition in LiTFSI-PC Electrolyte

5.1 Introduction

Although the road to the practical application of lithium metal negative electrode was once closed due to safety issues, it is again coming up on agendas as a promising material for next-generation batteries because of its high capacity, light weight and most negative working potential [1-2]. From the viewpoint of short circuit protection and lowering capacity loss, controlling the morphology of electrodeposited Li is an urgent issue for the practical application of the ultimate negative electrode. The evolution of LiBs is facing a big challenge, and research from various angles is being intensively conducted to suppress dendrites. Chemical or physical approaches such as additives [3-7], artificial SEI (solid electrolyte interphase) [8-10] and constraint pressure control [11-13] have been investigated. At the same time, it is very important to feedback basic information on Li deposition phenomena in order to establish material and battery designs.

Most of the reports on Li electrodeposition are generally based on galvanostatic conditions [14-16]. This is largely due to the fact that the actual LiB is charged and discharged under constant current conditions. The author has been conducting galvanostatic Li electrodeposition at different current densities to investigate the effects of current density and associated mass transfer properties on the deposition morphology [17-21]. The morphological variation of electrodeposited Li had already started from the nucleation and growth process up to 100 mC cm^{-2} and was considered to be closely related to the mass transport phenomena in SEI and in the electrolyte [20].

In metal electrodeposition in aqueous solution, studies on the nucleation and growth mechanisms have been conducted for a long time to precisely control the deposition morphology

[22-24]. Many efforts have been made to discuss the nucleation and growth mechanism, and derive the kinetic parameters. In this context, nucleation-growth models (S-H [25], S-M [26], BFT [27]) have been proposed to describe the current-time curve during constant potential electrolysis with/without accompanying electrode reactions such as hydrogen evolution [28-29]. Li deposition in organic electrolytes is accompanied by the SEI formation. Consequently, the Li deposition process from nucleation and growth to dendrite development is strongly influenced by the SEI characteristics, and at the same time, the complexity of the SEI makes it difficult to understand the Li electrodeposition phenomenon. Although the nucleation and growth theory established for metal electrodeposition in aqueous solution is essentially inapplicable, it is believed to be suggestive for understanding the Li electrodeposition phenomenon.

SEI will be formed prior to Li deposition under galvanostatic conditions, whereas SEI formation and Li deposition should occur simultaneously in potentiostatic operation. The author has conducted galvanostatic electrodeposition in LiTFSI/PC electrolyte to investigate the effect of current density on the morphological variation of electrodeposited Li. The larger the current density, the more instantaneous the potential changes during the initial process, which is expected to approach the potentiostatic condition. From this perspective, it is expected that there can be some differences in the initial process between galvanostatic electrolysis at lower current density and potentiostatic electrolysis under lower applied potential, and the subsequent deposition morphology also may be affected. In galvanostatic electrolysis, the potential immediately after the start of electrolysis shows a minimum lower than -100 mV even at a very low current density of 0.04 mA cm^{-2}. It is estimated that an overpotential of -100 mV is required for Li nucleation and growth to occur in the presence of SEI. Therefore, deposition morphology might change at the boundary around -100 mV in potentiostatic electrolysis. There have been few studies investigating the deposition morphology in detail under potentiostatic conditions and comparing them with galvanostatic conditions. The purpose of this study is to investigate Li deposition under constant potential conditions in detail to gain a better understanding of nucleation and growth behavior and to insight into its relation to dendrite formation. Li deposition behavior under constant potential

conditions was presented in detail by comparing deposition morphologies with the current transients during electrolysis.

5.2 Experimental

The experimental method was basically the same as the galvanostatic experiment described in the previous report [20-21] except for the potentiostatic operation, so refer to the previous report for details. The electrolyte composed of lithium bis (trifluoromethanesulfonyl) imide (LiTFSI) and propylene carbonate (PC) was used. The working electrode (W.E.) was Ni wire with a diameter of 500 μm. It was covered with fluorinated ethylene propylene (FEP) tube so that the contact part with the electrolyte was 10 mm in length. The counter electrode (C.E.) and the reference electrode (R.E.) were Li foil. Chronoamperometry (CA) under the constant applied potential from 0 mV to -1000 mV vs. Li$^+$/Li was performed simultaneously with an optical observation of Li electrodeposition behavior using the same electrolytic cell and experimental system as in the previous chapters. The more negative the applied potential, it is described as the larger the applied potential. On the other hand, the more positive toward 0 mV the applied potential, it is described as the smaller the applied potential. Digital optical microscope VHX-5000 (KEYENCE) and electrochemical measurement system HZ7000 (Hokuto Denko) were used. Then, the substrate was supplied to SEM (JSM-7800F; JEOL) observation of deposits without exposure to air.

Double pulse voltammetry in 1 M LiTFSI/PC electrolyte was also performed using the cell shown in Figure 5-1(a). The W.E. was made of Ni wire with a diameter of 1 mm coated with a fluororesin tube. Its cross section was used as W.E. as follows. The fluororesin tube (Hagitec Ltd.) has a double-layer structure with an inner layer of FEP and an outer layer of PFA. After inserting the Ni wire, the tube is heated with a heating tool so that only the inner layer of FEP melts and tightly contacts with the Ni wire. The cross section was polished with emery paper up to #2000 and then buff polished with 0.05 μm alumina abrasive. Li foil (200 μm thickness, Honjo Metal Co., Ltd.) was used as C.E. and R.E. Electrolysis was performed in an argon glove box (dew point

below -90 °C) with the electrolytic cell set in an aluminum block kept at 25 °C. As shown in Figure 5-1(b), the first applied potential (η_{on}) and the duration (t_{on}) were varied from 0 to -150 mV and from 0 to 5 s, respectively, while the second applied potential (η_{off}) was -15 mV and its duration (t_{off}) was varied from 0 to 1800 s. After electrolysis, the electrode surface was washed with dimethyl carbonate (DMC) and then vacuum dried, followed by SEM observation.

5.3 Results and Discussion

5.3.1 Optical observation

The electrolysis was performed at a constant potential up to 8000 mC cm^{-2} by varying the applied potential from 0 mV to -1000 mV. The observation results of the electrode surface using an optical microscope are shown in Fig. 5-2. No precipitates are visible at 0 mV. Local deposition and growth are observed at smaller applied potentials (-25 mV to -75 mV), while the rest of the electrode surface retains the texture of the original Ni electrode substrate. This is evident at -25 mV, and a similar trend is seen at -50 mV. For -100 mV, the precipitates are relatively homogeneous at 1800 mC cm^{-2}, but dendrites appear at 4800 mC cm^{-2} and their development can be seen by 8000 mC cm^{-2}. A boundary appears to exist around -100 mV. For the potentials positive than -100 mV, it is assumed that there is a growth competition among the discretely generated precipitates, and the surviving precipitates are preferentially growing. For -125 mV to -400 mV, the precipitation behavior appears to be uniform, dense and relatively smooth. For -1000 mV, it appears smooth up to 1800 mC cm^{-2}, but dendrites begin to be apparent at 4800 mC cm^{-2} and then dendrite development can be seen in the process up to 8000 mC cm^{-2}. Under larger applied potentials, such as 1000 mV, the effect of mass transport is likely to be significant because of the depletion of Li$^+$ concentration at the electrode surface.

5.3.2 Current transient during potentiostatic Li deposition

The chronoamperograms at applied potentials from 0 mV to -1000 mV in 1 M LiTFSI/PC are shown in Fig. 5-3. Fig. 5-3(a) shows the current profile with respect to the coulomb quantity from 0 to 8000 mC cm^{-2}. Fig. 5-3(b) shows an enlarged view from 0 to 10 mC cm^{-2} immediately after the start of electrolysis, and Fig. 5-3(c) shows an enlarged view from 0 to 50 mC cm^{-2}. Here, the larger the absolute value of the negative current, i.e., the larger the reductive current, denoted as the current decreases or reaches a minimum. On the other hand, the smaller the absolute value of the negative current, i.e., the smaller the reductive current, denoted as the current increases, rises or reaches a maximum. As shown in Figure 5-3(b), spike currents can be seen over 4 mC cm^{-2} immediately after the start of electrolysis in every case. The current reaches the first minimum of -100 to -180 mA cm^{-2} and then rapidly increases to the first maximum around 3 to 4 mC cm^{-2}. The more negative the applied potential, the larger the first minimum and the first maximum of the current. For -150 mV to -1000 mV, the current takes the first maximum, then decreases slightly and reaches the second minimum. For -1000 mV, the first maximum and second minimum are so close that the second minimum is not clear and appears as a shoulder. It then turns to increase and reaches the second maximum between 8 mC cm^{-2} and 12 mC cm^{-2}. Fig. 5-3(a) shows that the third minimum is reached again at about 100-200 mC cm^{-2} for -400 mV and -1000 mV. At -400 mV, the current rises to 800 mC cm^{-2} and then begins to slowly decrease again. At -1000 mV, the current rises as the coulomb quantity reaches 1000 mC cm^{-2}, then begins to slightly decrease again, and turns to decrease from about 3000 mC cm^{-2}. As for -125 mV, it also shows a sharp decrease in current after the first maximum, followed by a monotonic decrease in current without the second minimum. The higher the applied potential above -100 mV, the smaller the first maximum and the slower the subsequent decrease in current.

5.3.3 SEM observation

Fig. 5-4 shows SEM images of the electrode surface at (a) 10 mC cm^{-2} and (b) 50 mC cm^{-2} during potentiostatic electrolysis by changing the applied potential -25, -50, -100 and -150 mV. At

10 mC cm^{-2}, numerous nanoscale precipitates of several tens of nm in size are formed at every applied potential. At 50 mC cm^{-2}, there is a considerable difference in the deposition morphology depending on the applied potential. At -25 mV, locally formed precipitates with complex shapes are observed. At -50 mV, localized island precipitates are formed. At -100 mV, filament-like precipitates of a few μm in length and granular precipitates 300-400 nm in size are found in the mixture. At -150 mV, a numerous number of very fine filament-like precipitates with a length of several hundred nm are formed. Compared to the -25 mV and -50 mV, the -100 mV and -150 mV clearly show a change in the precipitation morphology and an increase in the number of deposits.

Fig. 5-5 shows (a) the time variation of the current during the potentiostatic electrolysis at -100 mV and (b) SEM images of the electrode surfaces at the point I through VI corresponding to 2, 4, 10, 25, 50 and 100 mC cm^{-2}, respectively. (I) 2 mC cm^{-2} corresponds to the point in Fig. 5-3(b) where the current has passed the first minimum of ca. -100 mA cm^{-2} and has increased to ca. -50 mA cm^{-2}. The SEM image shows the formation of nanoscale precipitates of several tens of nm in size already on the electrode surface where Ni crystal grains (several μm in diameter) can be seen. (II) The current density increases to ca. -0.5 mA cm^{-2} at 4 mC cm^{-2}, then reaches a first maximum of -0.2 mA cm^{-2} at ca. 4.5 mC cm^{-2}, after which the current slowly decreases again. At 4 mC cm^{-2}, the nanoscale precipitates appear to be slightly larger than at 2 mC cm^{-2}, and their contours are getting more distinct. (III) At 10 mC cm^{-2}, the precipitates begin to show a distribution in size compared to that at 4 mC cm^{-2}. The larger precipitates appear to be raised from the surface.

The appearance of the electrode surface changes drastically between (III) 10 mC cm^{-2} and (IV) 25 mC cm^{-2}. It can be seen that granular precipitates 100 to 300 nm in size and filament-like precipitates are beginning to grow, which were not seen at 10 mC cm^{-2}. This morphological change corresponds well with the trend in Fig. 5-5(a) from (II) 4 to (IV) 25 mC cm^{-2}, where the current once shows a maximum but decreases again. II→III→IV may reflect nucleation and growth in SEI and the growth process of nanoscale precipitates breaking through the SEI layer. (V) At 50 mC cm^{-2}, the situation is similar to that at 25 mC cm^{-2}, but the number of granular precipitates and filament-like precipitates has increased. (VI) At 100 mC cm^{-2}, the granular precipitates grow to

500-800 nm in size, and a horsetail-like structure with grain precipitates at the tips of the filament can be observed.

In potentiostatic electrolysis, SEI formation and Li deposition occur simultaneously unlike galvanostatic electrolysis. The charging of the electric double layer, SEI formation by electrolyte decomposition, reduction of the native oxide and Li deposition reactions should progress competitively on the Ni electrode immediately after the start of electrolysis. After the first minimum, SEI growth decelerates to the first maximum of 4.5 mC cm^{-2}, during which Li atoms and Li clusters are expected to be formed on the Ni substrate along with the SEI. Underneath the SEI, Li precipitation on the generated Li and new Li nucleation on the Ni substrate are possible. The latter is similar to the nucleation phenomenon in the presence of SEI in galvanostatic electrolysis. When the applied potential is small, the growth point is localized because new nucleation cannot occur in the presence of SEI, but when the applied potential is large, Li can nucleate and grow through SEI, which is assumed to result in a more uniform deposition behavior. In order to further investigate the morphological changes of nucleation and growth in the SEI layer during the above 10-50 mC cm^{-2} region, double pulse voltammetry was conducted.

5.3.4 *Double pulse voltammetry*

The time variation of the current accompanied with the double-pulse method and SEM images after the electrolysis are shown in Fig. 5-6. The double-pulse method was performed as shown in Fig. 5-1(b) of the Experimental section, where the first potential (η_{on}) of -100 mV was applied for t_{on} = 5 s and the second potential (η_{off}) of -15 mV was applied for t_{off} = 0, 600, 1200, and 1800 s. Coulomb quantity of about 5 mC cm^{-2} passes during applying the first potential of -100 mV for 5 s, and a weak current of about -0.2 mA cm^{-2} flows until around 400 s after switching to η_{off} = -15 mV, followed by a gradual decrease in current. Precipitates cannot be seen when the second potential is not applied i.e., t_{off} = 0 s. At t_{off} = 600 s, a small number of microscopic precipitates are formed, and then granular and distinct precipitates can be seen at t_{off} = 1200 s. At t_{off} = 1800 s, the

number of the precipitates is increasing, and some of them are filament-like. Next, the duration of the first potential of -100 mV was varied from 0, 1, 3 and 5 s, while the second potential and the duration were fixed to -15 mV and 1800 s, respectively. The time variations of the current and SEM images of the electrode surface are shown in Fig. 5-7. When η_{on} is applied for $t_{on} = 1, 3$ and 5 s, a weak current of about -0.2 mA cm^{-2} is observed, followed by an increase in current in a similar manner as in Fig. 5-6. The period before the current begins to increase during the application of the second potential becomes longer with the shorter time of the first potential application. There is no increase in current during the second potential application when η_{on} is not applied. Subsequently, the first potential varied between -15 and -150 mV was applied for 5 s, while the second potential and the application time were left unchanged ($\eta_{off} = -15$ mV, $t_{off} = 1800$ s). The results are similarly shown in Fig. 5-8. A sudden change in current appears immediately after the spike current during t_{on} when the first applied potential is between -100 mV and -150 mV. At -100 mV, the change is small, but as the applied potential becomes larger to -125 mV and -150 mV, the reductive current is more rapidly turning from decrease to increase. After switching to the second potential, the reductive current still increases again after an incubation period. The incubation period is almost the same when η_{on} is between -100 mV and -150 mV, while becomes longer as more positive η_{on} of -75 mV and -50 mV is applied. It is suggested that the reductive current increase after the incubation period is related to the growth process of the generated nuclei from the SEI into the electrolyte. When η_{on} was the same as η_{off} at -15 mV, nothing could be seen on the electrode surface. At -50 mV and -75 mV, a tiny amount of precipitates was observed. At -100 mV or less, distinct granular precipitates can be seen. At 100 mV, the number of precipitates is somewhat fewer and their size appears a little larger than at -125 mV and -150 mV. By varying the first potential to generate nuclei and keeping the second potential constant at which the nuclei grow, the deposition behavior can be regarded as reflecting the difference in nucleation behavior at the first potential. The behavior of nucleation seems to differ at the boundary of potential around -100 mV. At potentials positive than -100 mV, the driving force for precipitation is small, so it is expected that local Li precipitation occurs only at energetically favorable locations on the electrode

strongly influenced by surface properties such as native oxide and SEI on the electrode. On the other hand, at lower potentials below -100 mV, the influence of surface properties can be overcome. It is believed that more uniform nucleation and growth occurs because Li electrodeposition can take place even in areas where it was not possible to deposit at the more positive potentials.

5.3.5   Lower applied potential

In constant potential electrolysis, Li deposition and SEI formation are considered to proceed competitively irrespective of the applied potential. When the applied potential is small, the SEI is expected to grow relatively faster due to the slower Li deposition rate. The situation is similar to that of Li precipitation in the presence of SEI, apparently analogous to galvanostatic deposition at lower current density. However, as we have seen in the previous chapters, the nucleation behavior changes with a boundary potential around -100 mV. Even very low current densities, such as 0.04 mA cm^{-2}, Li electrodeposition experience potentials lower than -100 mV in galvanostatic electrolysis, but naturally the potential does not exceed it in potentiostatic electrolysis when the applied potential is more positive than -100 mV. If an overvoltage of -100 mV is required for nucleation and growth in the presence of SEI, then potentiostatic electrolysis at the potential more positive than -100 mV should have a different nucleation and growth mechanism from that of galvanostatic electrolysis. Fig. 5-9 shows the current-overpotential curves at (a) 50 mC cm^{-2}, 100 mC cm^{-2} and (b) 4000 mC cm^{-2} for galvanostatic and potentiostatic electrodeposition, respectively. In the early stages of electrolysis at 50 and 100 mC cm^{-2}, differences are observed in the positive potential region above -100 mV. At negative potentials below -125 mV, both the galvanostatic and potentiostatic current-overpotential curves approach each other when the reductive current is greater than 4 mA cm^{-2}. The difference in the current-overpotential curves at 4000 mC cm^{-2}, where electrolysis has progressed, is negligible between galvanostatic and potentiostatic condition.

Fig. 5-10 shows the optical microscope images (upper panel) and the time evolution of the current and potential (lower panel) when Li was deposited up to 8000 mC cm^{-2} under (a) galvanostatic condition of -2 mA cm^{-2} and (b) potentiostatic condition of -50 mV, respectively, as reported in the previous report. (a) galvanostatic electrolysis at -2 mA cm^{-2} shows the potential progressing around -35 mV, and (b) potentiostatic electrolysis at -50 mV shows the current transitioning from -2 to -4 mA cm^{-2}. It corresponds to the current and potential conditions in the region where the differences were observed in Fig. 5-9, and the differences in the initial process of electrolysis are considered to cause such a change in the deposition morphology. There seems to be a difference between the nucleation and growth process in the presence of SEI and that in the case of simultaneous SEI formation and Li deposition. The difference is more pronounced at lower applied potentials. Investigation of the influence of electrodeposition conditions on the structure of SEI and Li deposition behavior in SEI is a subject for future work.

5.3.6 *Higher applied potential*

At larger applied potential more negative than -100 mV, Li deposition is possible even in the presence of SEI, as in the case of galvanostatic electrolysis, and it is thought that Li deposition becomes more uniform as the potential becomes more negative. Furthermore, it is assumed that the influence of mass transport properties becomes dominant at even larger applied potentials. As schematically shown in Fig. 5-11, the *i-t* curve at -400 mV exhibits complex behavior. This section discusses what phenomena each current change corresponds to. For comparison, *V-t* curves obtained in previous galvanostatic experiments are also shown.

In the initial stage P-I, which shows a peak profile over 3.5 mC cm^{-2}, nanoscale Li precipitates are formed along with SEI formation as seen in the SEM observations. To eliminate the influence of the double-layer charging current and the current related to SEI generation as much as possible, the current at an applied potential of 0 mV was subtracted from the current at each applied potential. The results are shown in Fig. 5-12. The peak was observed over 0.05 s at each potential, which is

considered to be the current associated with SEI formation and Li reduction reactions originating from the potential difference with 0 mV. At the moment of electrolysis initiation, Li deposition and SEI formation (including reduction of Ni native oxide film) occur simultaneously on the Ni electrode. Once SEI is formed, Li is immediately electrodeposited through SEI. The situation is very complicated unlike metal electrodeposition in an aqueous solution.

Stage P-II may reflect the nucleation and growth process of Li in SEI. Fig. 5-3(c) or Fig. 5-12 shows that when the larger potential (more negative than -125 mV) is applied, the nucleation and growth underneath SEI proceed immediately and the current rises again due to the effect of increased electrode area. For example, the current is rising again from 0.05 s at -400 mV. This is probably because Li cluster formation and aggregation of nuclei generated in SEI uniformly turn to growth due to the large applied potential. Thereafter, the current drops again with a second peak. That may reflect the effect of mass transport resistance in SEI. At -150 mV and -125 mV, the period before the current rises again becomes longer, to about 0.2 s and 0.4 s, respectively. This may be due to the smaller driving force for the reaction and the slower rate of Li deposition in SEI compared to the -400 mV case. As the applied potential becomes smaller, the precipitate grows preferentially in the areas where it is easy to precipitate, resulting in a non-uniform precipitation morphology. As a result, it is thought that the second peak does not appear clearly.

The current change in the second peak appearing in Stage II at -400 mV is considered to be due to the nucleation and growth of Li in SEI. Fig. 5-13 shows the result of plotting $(i/i_{max})^2$ against t/t_{max} for the peak area from 0.05 s in Fig. 5-12. Hwang et al [30] analyzed the nucleation behavior of preformed SEI on Cu foil at 20 mV (vs. Li^+/Li) followed by constant potential deposition of Li from -10 mV to -100 mV. Their current change behavior is similar to the results of Fig. 5-13. Instantaneous 3D nucleation and growth of Li in the SEI is expected to be in progress under diffusion control.

The Li nucleation growth phenomenon in the SEI layer must be based on the SEI layer thickness rather than a semi-infinite diffusion field. D'Ajello et al. [31] set up a hemispherical diffusion field of radius R instead of a semi-infinite diffusion field. Li et al. [32] extended this

model and described the Instantaneous 3D nucleation and growth process within a diffusion layer at a height of R above the electrode as follows.

$$i = zFc_0 D^{1/2}/\pi^{1/2}\left(\frac{(\pi D)^{1/2}}{R} + \frac{1}{t^{1/2}}\right)(1 - exp(-N\pi aDt)) \qquad (5\text{-}1)$$

Where, z:number of electron transferred, F: Faraday constant [mC mol^{-1}], D: Diffusion constant [cm^2 s^{-1}], ρ: Density of deposited metal [g cm^{-3}], M: Molecular weight [g mol^{-1}], c_0: bulk concentration in the electrolyte, N: Number density of active sites for nucleation [cm^{-2}], a: Numerical constant determined by experimental conditions [mol cm^{-2} s^{-1}] and R: diffusion distance [cm].

If the start time of nucleation growth described by this equation is t_0, equation (5-1) is written as follows (5-2) – (5-5). Fitting was attempted for peak currents in the 0.05 s to 0.30 s interval.

$$i = \left(k_0 + \frac{k_1}{(t-t_0)^{1/2}}\right)(1 - exp[-k_2(t - t_0)]) \qquad (5\text{-}2)$$

$$k_0 = zFc\frac{D}{R} \qquad (5\text{-}3)$$

$$k_1 = zFc\left(\frac{D}{\pi}\right)^{0.5} \qquad (5\text{-}4)$$

$$k_2 = N\pi aD \qquad (5\text{-}5)$$

Where, F: 96500×10^3 [mC mol^{-1}], D: Diffusion constant of Li$^+$ in SEI [cm^2 s^{-1}], ρ: Density of Li [g cm^{-3}], M: Molecular weight [g mol^{-1}], c: Li$^+$ concentration in the electrolyte, N_0: The density of active sites for nucleation [cm^{-2}], N: The steady-state nucleation rate constant [s^{-1}], $z_{SEI}F$: Molar

charge transferred for the SEI formation reaction, k_{SEI}: The rate constant for SEI formation reaction [mol cm^{-2} s^{-1}]

Fitting results showed relatively good agreement with experimental values as shown in Fig. 5-14. Table 5-1 summarizes the various parameters obtained as a result of the fitting. The diffusion coefficient in SEI was calculated to be about 3.3×10^{-10} /cm^2 s^{-1}. The result is somewhat different from the value (8×10^{-10} /cm^2 s^{-1} at 20 mA cm^{-2}) estimated from the potential profile of galvanostatic electrodeposition in Chapter 2. Since the thickness of SEI was assumed to be 30 nm in the previous chapter, recalculating on the basis of SEI thickness of 17 nm yields the diffusion coefficient of 4×10^{-10} / cm^2 s^{-1}, which is close to the value obtained in the present calculation.

Then, in Stage P-III, the current begins to decrease again from around 14 mC cm^{-2}. This is expected to reflect the phenomenon in which Li precipitates grown in SEI break through SEI and grow into the electrolyte. This behavior is considered to correspond to the sprouting observed in the early stages of galvanostatic electrolysis reported previously. The current decreases as Li precipitates project into the electrolyte, but gradually increases again from 200 mC cm^{-2} likely due to the concentration overpotential associated with a decrease in Li$^+$ concentration on the electrode surface. Thereafter, the current decreases again after reaching a maximum. This point probably corresponds to the time when dendrites begin to develop under an optical microscope. Fig. 5-11(a) shows that the current during potentiostatic electrolysis changes at roughly the same timing (coulomb quantity) as the potential during galvanostatic electrolysis, so that one increases the other decreases. As also shown in Fig. 5-11(b), the phenomena in P-I, P-II and P-III of the potentiostatic electrolysis correspond to those in G-I, G-II and G-III of the galvanostatic electrolysis. Therefore, there is a similarity between the behavior of potentiostatic electrolysis at larger applied potentials and that of galvanostatic electrolysis at higher current densities.

A schematic diagram comparing the initial stage of Li electrodeposition under galvanostatic and potentiostatic conditions is shown in Fig. 5-15. SEI is formed before Li deposition at galvanostatic electrolysis. As previously reported, it was expected that the Li deposition morphology would be affected by the difference in defect density of SEI depending on the current

density. In constant potential electrolysis, SEI formation and Li deposition occur competitively as soon as electrolysis starts, and Li clusters and Li atoms are thought to be formed at the interface between the SEI and the electrode. At potentials positive than -100 mV, these are considered to be the origin of growth, and it is assumed that no new nucleation is taking place in the presence of SEI. At applied potentials more negative than -100 mV, Li nucleation and growth occur even in the presence of SEI as well as Li clusters generated with SEI immediately after the start of electrolysis, leading to a more uniform deposition morphology.

5.4 Conclusions

Potentiostatic Li electrodeposition behavior up to 8000 mC cm^{-2} was observed under an optical microscope on Ni wire in 1M LiTFSI/PC with applied potentials from 0 mV to -1000 mV. The smaller applied potentials of -25 to -75 mV showed localized or discrete and non-uniform growth. Applying a potential more negative than -100 mV resulted in a transition to a more uniform and smooth deposition compared to the application of more positive potentials. For -1000 mV, the precipitation proceeds smoothly at first, but dendrites started to develop in the course of the deposition, suggesting the influence of mass transport.

A Comparison of SEM images obtained during potentiostatic electrolysis revealed significant differences in deposition morphology depending on the applied potential. At -25 mV and -50 mV, the precipitates grew very locally, while at -100 mV, filament and granular precipitates were relatively uniform, and at -150 mV, numerous very fine filament-like precipitates were formed over the electrode surface. A detailed study of the change in nucleation and growth morphology in the SEI layer by the double-pulse method showed that there is a very large difference in the uniformity of Li precipitates that appear at a boundary of -100 mV, suggesting that the change in precipitation morphology is affected by the potential.

It was assumed that at potentials positive than -100 mV, no nucleation and growth occurs on the Ni substrate in the presence of SEI and that the Li generated simultaneously with SEI

immediately after the start of electrolysis becomes the origin of subsequent growth, resulting in a non-uniform deposition morphology. The precipitation morphology was similar to that of galvanostatic electrolysis at higher current density, since Li nucleation and growth were considered to be possible even in the presence of SEI at larger applied potentials more negative than -100 mV, resulting in a uniform precipitation morphology. At larger applied potentials, Li nucleation and growth can be regarded as occurring in a uniform SEI, and analysis of the current-time variation at -400 mV showed relatively good agreement with the instantaneous 3D nucleation and growth model in the diffusion layer on the electrode. From the fitting results, the diffusion coefficient of Li^+ in SEI was estimated to be 3.3×10^{-10} cm^2 s^{-1} and the diffusion distance corresponding to the SEI layer thickness was estimated to be 17 nm. The diffusion coefficient estimated from the potential change during galvanostatic electrolysis at 20 mA cm^{-2} in the previous report was recalculated to be 4×10^{-10} cm^2 s^{-1} based on the SEI layer thickness of 17 nm, which is relatively close to the previous result.

References

[1] D. Lin, Y. Liu and Y. Cui, Reviving the lithium metal anode for high-energy batteries, Nature Nanotechnology, 12, 194–206 (2017).

[2] B. Liu, Ji-G. Zhang, and W. Xu, Advancing Lithium Metal Batteries, Joule, 2(5), 833-845 (2018).

[3] J. K. Stark Goodman and P. A. Kohl, Effect of Alkali and Alkaline Earth Metal Salts on Suppression of Lithium Dendrites, J. Electrochem. Soc., 161(9), D418-D424 (2014).

[4] Y. Zhang, J. Qian, W. Xu, S. M. Russell, X. Chen, E. Nasybulin, P. Bhattacharya, M. H. Engelhard, D. Mei, R. Cao, F. Ding, A. V. Cresce, K. Xu and Ji-G. Zhang, Dendrite-Free Lithium Deposition with Self-Aligned Nanorod Structure, Nano Lett., 14, 6889−6896 (2014).

[5] J. Qian, W. Xu, P. Bhattacharya, M. Engelhard, W. A. Henderson, Y. Zhang, Ji-G. Zhang, Dendrite-free Li deposition using trace-amounts of water as an electrolyte additive, Nano Energy, 15, 135-144 (2015).

[6] H. Zhang, G. G. Eshetu, X. Judez, C. Li, L.M Rodriguez-Martínez and M. Armand, Electrolyte Additives for Lithium Metal Anodes and Rechargeable Lithium Metal Batteries: Progress and Perspectives, Angew Chemie, 57(46), 15002-15027 (2018).

[7] W. Li, H. Yao, K. Yan, G. Zheng, Z. Liang, Yet-Ming Chiang and Yi Cui, The synergetic effect of lithium polysulfide and lithium nitrate to prevent lithium dendrite growth, Nature Communications volume, 6, 7436 (2015).

[8] Z. Liang, D. Lin, J. Zhao, Z. Lu, Y. Liu, C. Liu, Y. Lu, H. Wang, K. Yan, X. Tao and Y. Cui, Proc. Natl. Acad. Sci. USA, 113, 2862-2867 (2016).

[9] J. Luo, C.-C. Fang and N.-L. Wu, Adv. Energy Mater., 8, 1701482 (2018).

[10] Y. Guo, P. Niu, Y. Liu, Y. Ouyang, D. Li, T. Zhai, H. Li and Y. Cui, Adv. Mater., 31, 1900342 (2019).

[11] C. Fang, B. Lu, G. Pawar, M. Zhang, D. Cheng, S. Chen, M. Ceja, J.-M. Doux, H. Musrock, M. Cai, B. Liaw and Y. S. Meng, Pressure-tailored lithium deposition and dissolution in lithium metal batteries, Nature Energy, 6, 987–994 (2021).

[12] X. Zhang, Q. J. Wang, K. L. Harrison, K. Jungjohann, B. L. Boyce, S. A. Roberts, P. M. Attia and S. J. Harris, Rethinking How External Pressure Can Suppress Dendrites in Lithium Metal Batteries, J. Electrochem. Soc., 166, A3639 (2019).

[13] P. Barai, K. Higa and V. Srinivasan, Impact of External Pressure and Electrolyte Transport Properties on Lithium Dendrite Growth, J. Electrochem. Soc., 165, A2654 (2018).

[14] P. Biswal, S. Stalin, A. Kludze, S. Choudhury and L. A. Archer, Nucleation and Early Stage Growth of Li Electrodeposits, Nano Lett., 19, 8191−8200 (2019).

[15] Allen Pei, Guangyuan Zheng, Feifei Shi, Yuzhang Li and Yi Cui, Nanoscale Nucleation and Growth of Electrodeposited Lithium Metal, Nano Lett. 17, 1132−113 (2017).

[16] P. Bai, J. Li, F.R. Brushett and M.Z. Bazant, Transition of lithium growth mechanisms in liquid electrolytes, Energy Environ. Sci., 9, 3221 (2016).

[17] M. Ota, S. Izuo, K. Nishikawa, Y. Fukunaka, E. Kusaka, R. Ishii and J.R. Selman, Measurement of concentration boundary layer thickness development during lithium electrodeposition onto a lithium metal cathode in propylene carbonate, J. Electroanal. Chem., 559, 175-183 (2003).

[18] K. Nishikawa, Y. Fukunaka, T. Sakka Y. H. Ogata and J. R. Selman, Measurement of concentration profile during charging of Li battery anode materials in $LiClO_4$-PC electrolyte, J. Electrochem. Soc., 154(10), A943 (2007).

[19] K. Nishikawa, T. Mori, T. Nishida, Y. Fukunaka and M. Rosso, Li dendrite growth and Li^+ ionic mass transfer phenomenon, J. Electroanal. Chem., 661, 84–89 (2011).

[20] T. Nishida, Y. Fukunaka, T. Homma and T. Nohira, Galvanostatic Li Electrodeposition in LiTFSI-PC Electrolyte: Part I. Effects of Current Density in Initial Stage, J. Electrochem. Soc., 169, 100548 (2022).

[21] T. Nishida, Y. Fukunaka, T. Homma and T. Nohira, Galvanostatic Li electrodeposition in LiTFSI-PC Electrolyte: Part Ⅱ. Coupling Phenomena in Growth Process, Journal of The Electrochemical Society, 169, 090529 (2022).

[22] E. Budevski, G. Staikov and W. J. Lorenz, Electrocrystallization: Nucleation and growth phenomena, Electrochim. Acta, 45, 2559-2574 (2000).

[23] G. Gunawardena, G. Hills, I. Montenegro and B. Scharifker, Electrochemical nucleation: Part I. General considerations, J. Electroanal. Chem. and Interfacial Electrochem., 138(2), 225-239 (1982).

[24] M.E. Hyde and R.G. Compton, A review of the analysis of multiple nucleation with diffusion controlled growth, J. Electroanal. Chem., 549(5), 1-12(2003).

[25] B. Scharifker, G. Hills, Theoretical and experimental studies of multiple nucleation, Electrochim. Acta, 28, 879-889 (1983).

[26] J. Mostany, J. Mozota, B. Scharifker, Three-dimensional nucleation with diffusion controlled growth, J. Electroanal. Chem. Interfacial Electrochem, 177, 25-37 (1984).

[27]A. Bewik, M. Fleishmann and HR. Thrisk,Kinetics of the electrocrystalization of thin films of calomel., Faraday Soc., 58, 2200 (1962)

[28] M. Rezaei, S.H. Tabaian, D.F. Haghshenas, Electrochemical nucleation of palladium on graphene: a kinetic study with an emphasis on hydrogen co-reduction, Electrochim. Acta, 87, 381-387 (2013).

[29] M. Palomar-Pardave, B. Scharifker, E. Arce, M. Romero-Romo, Nucleation and diffusion-controlled growth of electroactive centers, Electrochim. Acta, 50, 4736-4745 (2005).

[30] B. Thirumalraj, T. T. Hagos, C.-J. Huang, M. A. Teshager, J.-H. Cheng, W.-N. Su and B.-J. Hwang, Nucleation and Growth Mechanism of Lithium Metal Electroplating, J. Am. Chem. Soc. 141, 46, 18612–18623 (2019)

[31] P. C. T. D'Ajello, M. A. Fiori, A. A. Pasa and Z. G. Kipervaser, Reaction-Diffusion Interplay in Electrochemical Deposition Processes A Theoretical Approach, J. Electrochem. Soc., 147(12), 4562 (2000)

[32] G. Luo, D. Li, G. Yuan and N. Li, Potentiostatic Current Transient for Multiple Nucleation: A Limited-Diffusion Process Description, J. Electrochem. Soc., 165(3), D147-D151 (2018).

Table 5-1. Kinetic parameters obtained by nonlinear fitting.

k_0	k_1	k_2	k_3	D	R
mA cm^{-2} s$^{1/2}$	s^{-1}	mA cm^{-2}	s^{-1}	cm^2 s^{-1}	nm
18.4	0.98	36.5	0.042	3.3×10^{-10}	17
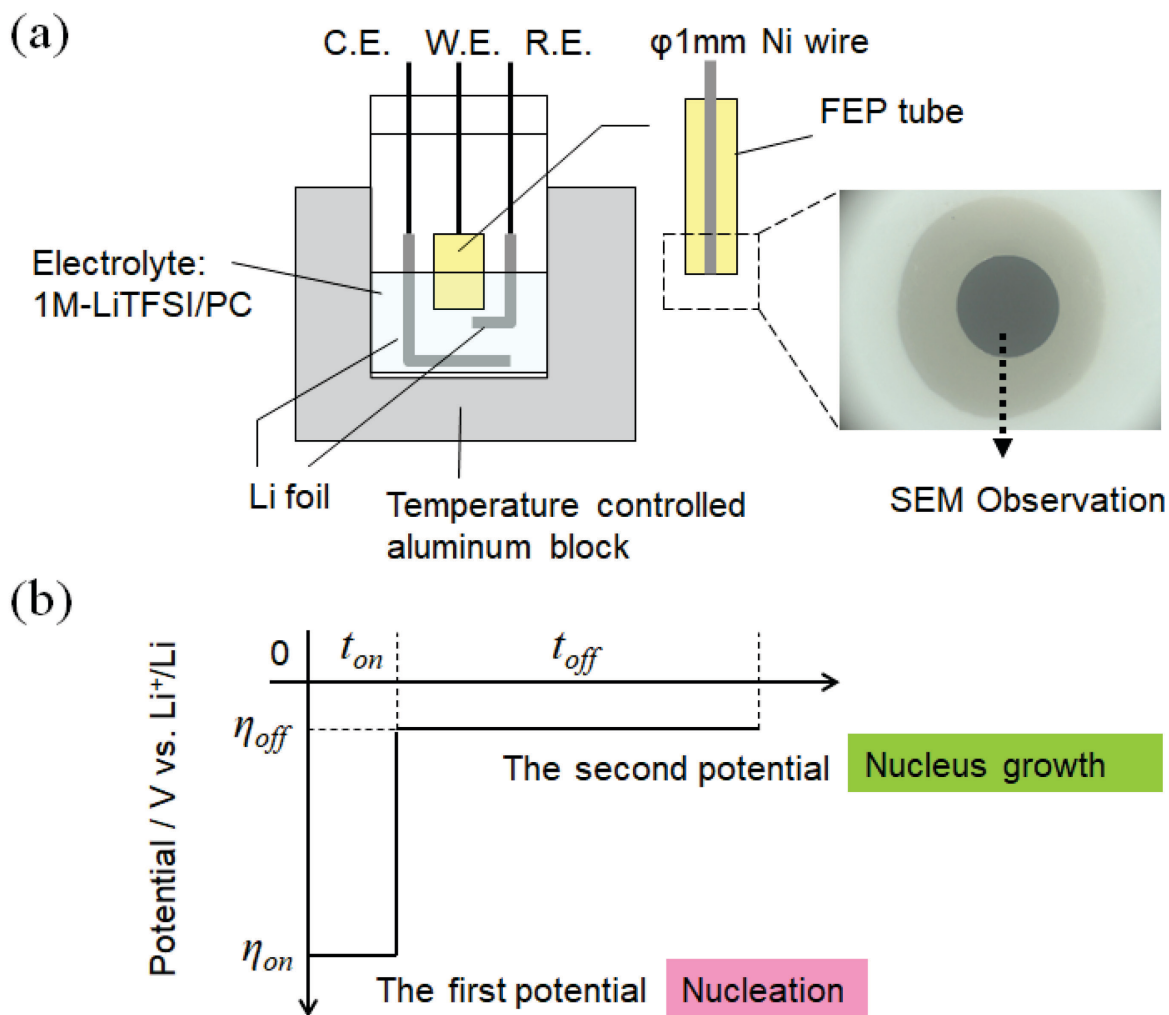
Figure 5-1. (a) Schematic diagram of the electrolytic cell for double pulse voltammetry. (b) Schematic diagram of applied potential and its duration for double-pulse voltammetry.
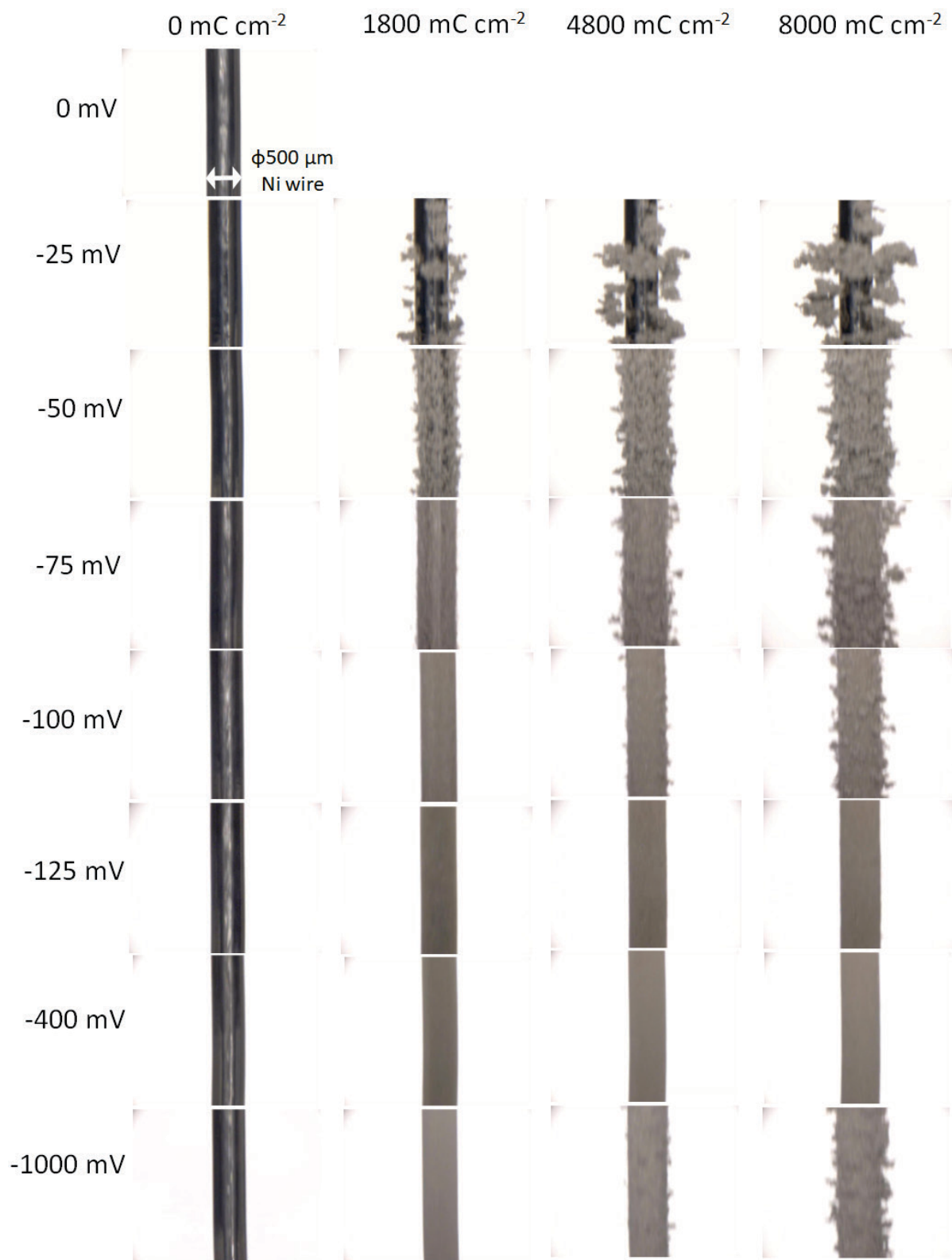
Figure 5-2. Time transient of the morphology of potentiostatically electrodeposited Li on Ni wire electrode in 1 M LiTFSI/PC at 0, -25, -50, -75, -100, -125, -400 and -1000 mV vs. Li$^+$/Li at 25 °C.
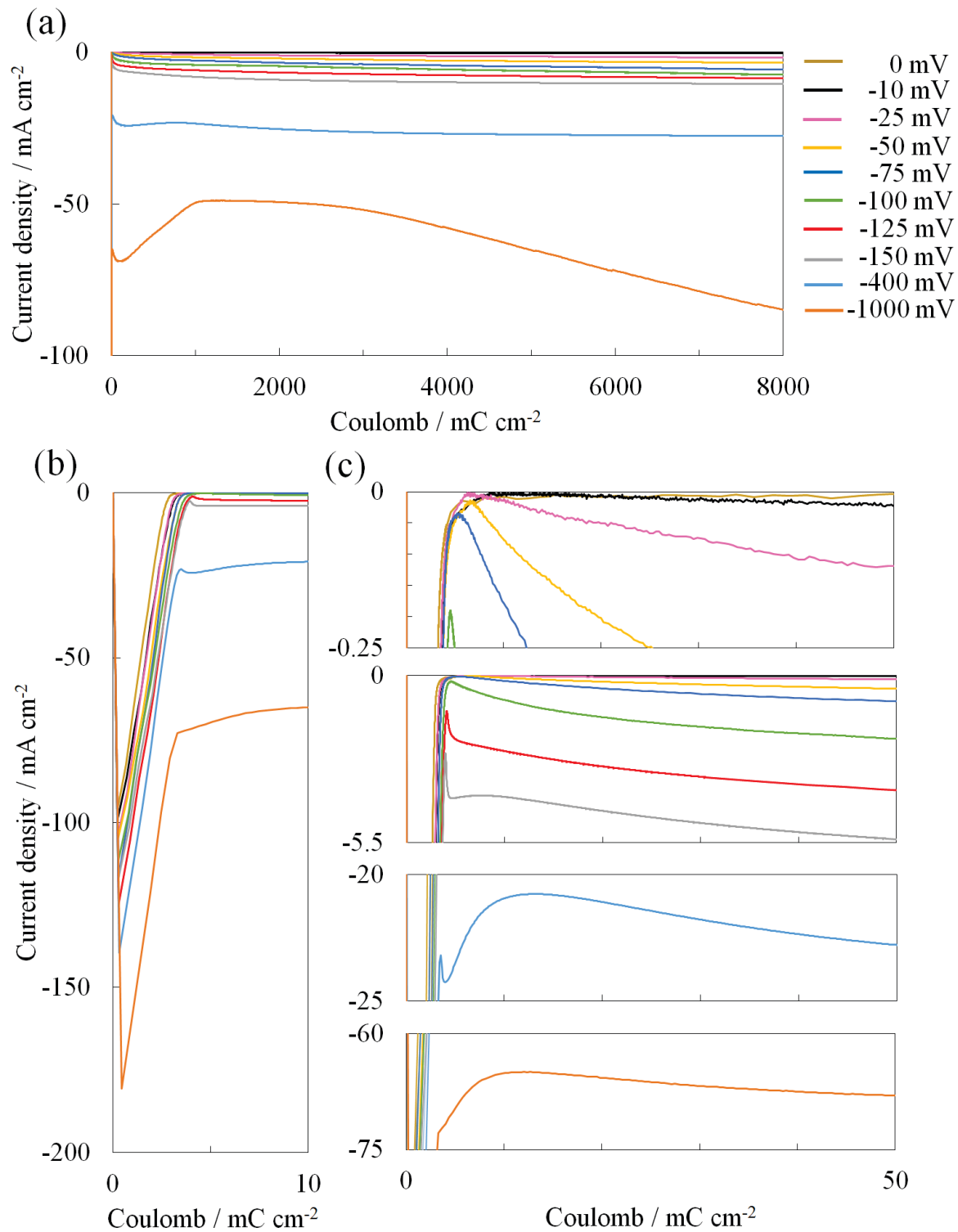
Figure 5-3. Chronoamperograms after the starts of electrolysis at the potential ranges from 0 mV to -1000 mV for the coulomb quantity of (a) 0 - 8000 mC cm^{-2}, (b) 0 - 10 mC cm^{-2} and (c) 0 - 50 mC cm^{-2} in 1.0M LiTFSI/PC at 25 ℃.
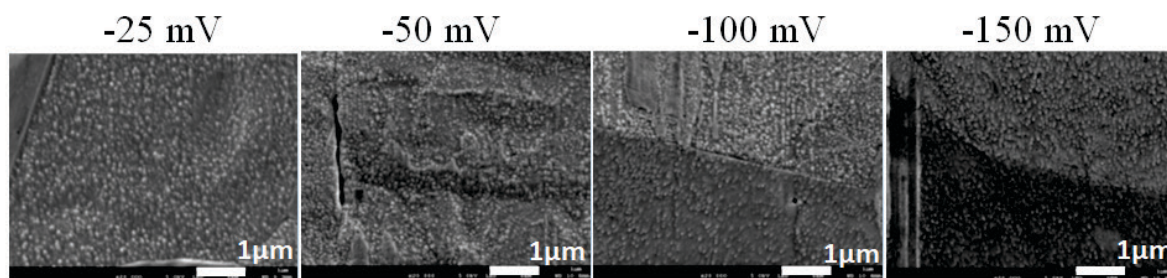
(a) 10 mC cm^{-2}

(b) 50 mC cm^{-2}
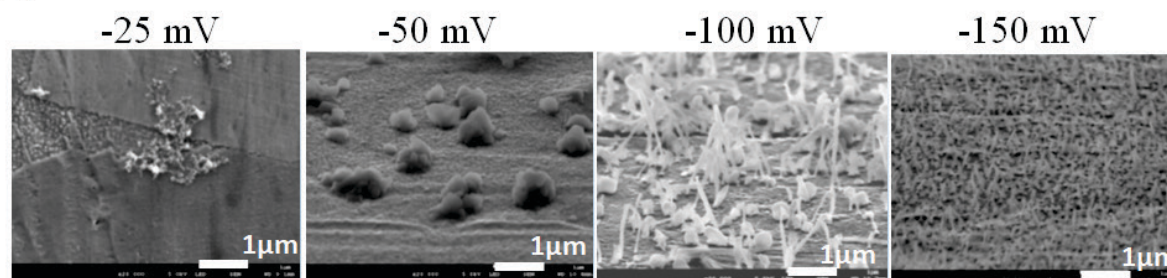
Figure 5-4. SEM images of the electrode surface after electrolysis at the applied potential of -25, -50, -100 and -150 mV. Coulomb quantity passed during deposition: (a) 10 mC cm^{-2} and (b) 50 mC cm^{-2}.
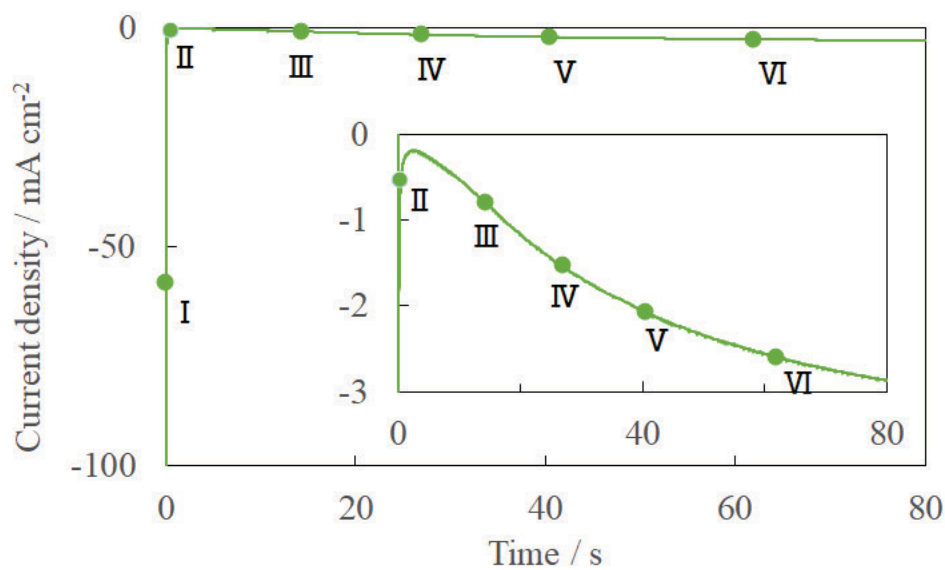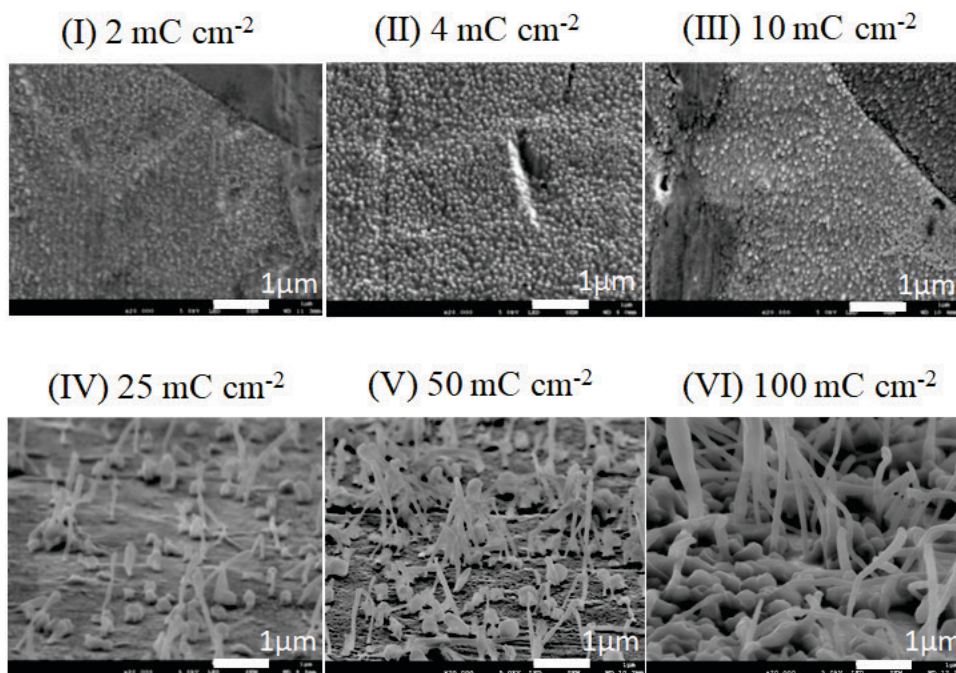
Figure 5-5. (a) Chronoamperogram of Li electrodeposition in 1M LiTFSI/PC at -100 mV vs. Li$^+$/Li. (b) SEM photographs of the electrode surfaces corresponding to the points (2, 4, 10, 25, 50 and 100 mC cm^{-2}) marked as I - VI in Figure (a).
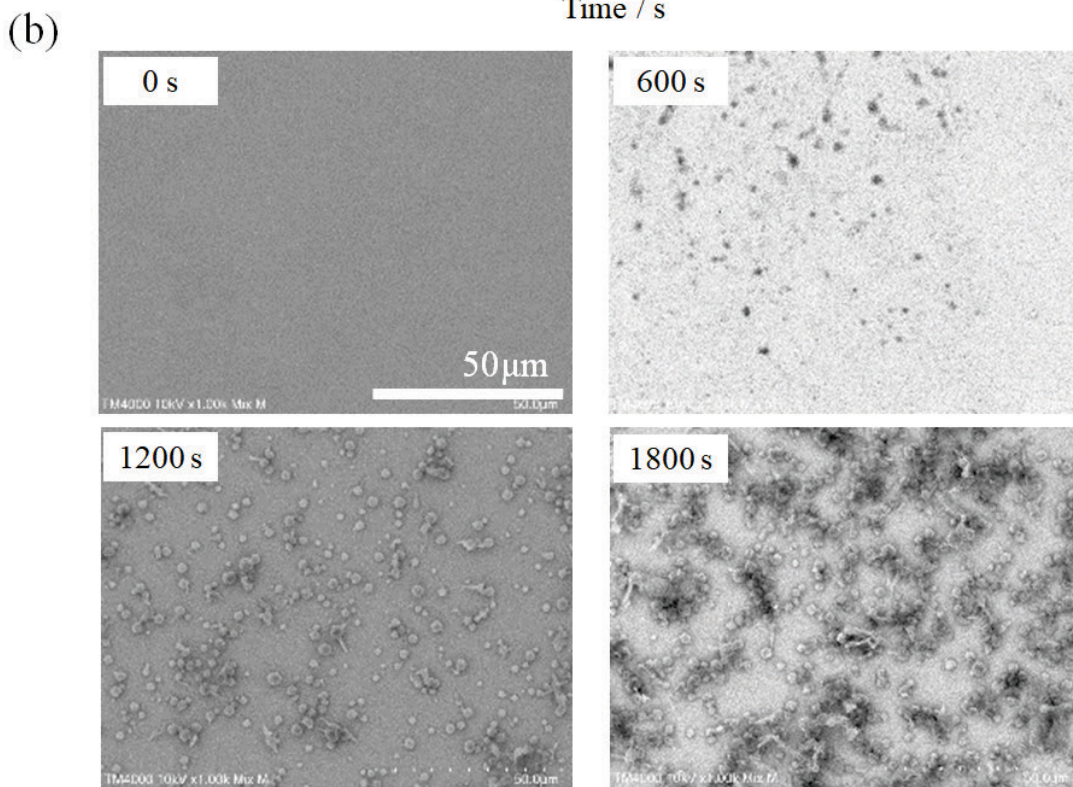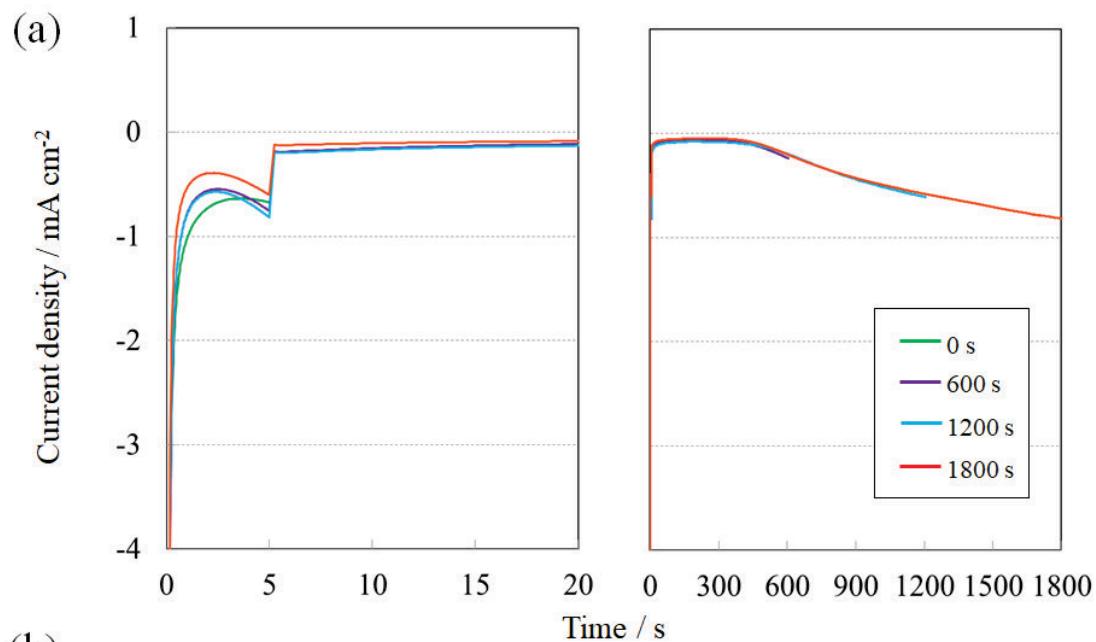
Figure 5-6. (a) Constant potential double pulse chronoamperograms of Li electrodeposition in 1M LiTFSI/PC on Ni electrode at the first potential of -100 mV vs. Li$^+$/Li for 5 s and the second potential of -15 mV vs. Li$^+$/Li for different four durations (0 s, 600 s, 1200 s and 1800 s). (b) SEM micrographs of Ni electrode surface after applying double pulse potential.

125
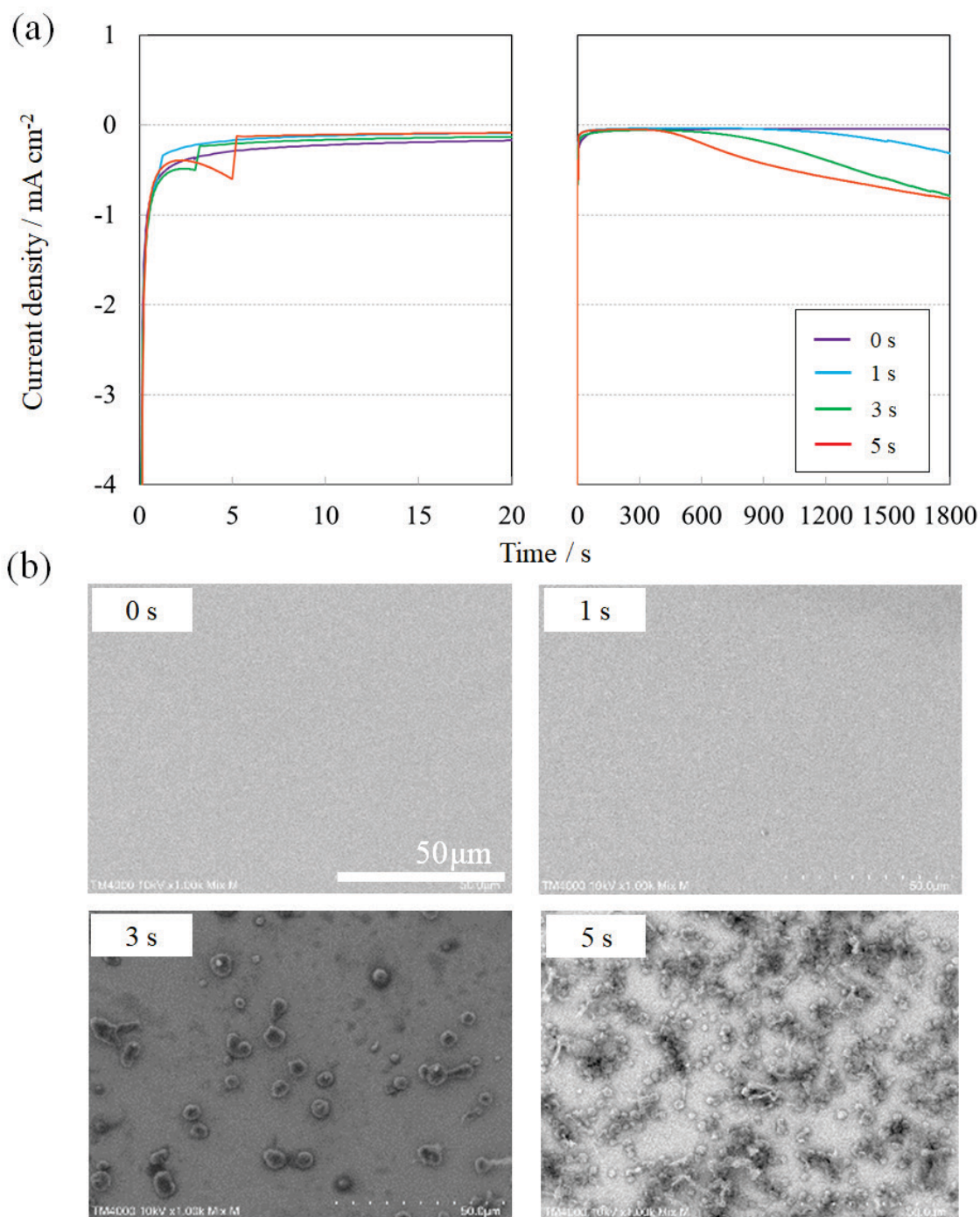
Figure 5-7. (a) Constant potential double pulse chronoamperograms of Li electrodeposition in 1M LiTFSI/PC on Ni electrode at the first potential of -100 mV vs. Li$^+$/Li for different four duration(0 s, 1 s, 3 s and 5 s) and the second potential of -15 mV vs. Li$^+$/Li for 1800 s.

(b) SEM micrographs of Ni electrode surface after applying double pulse potential.

126
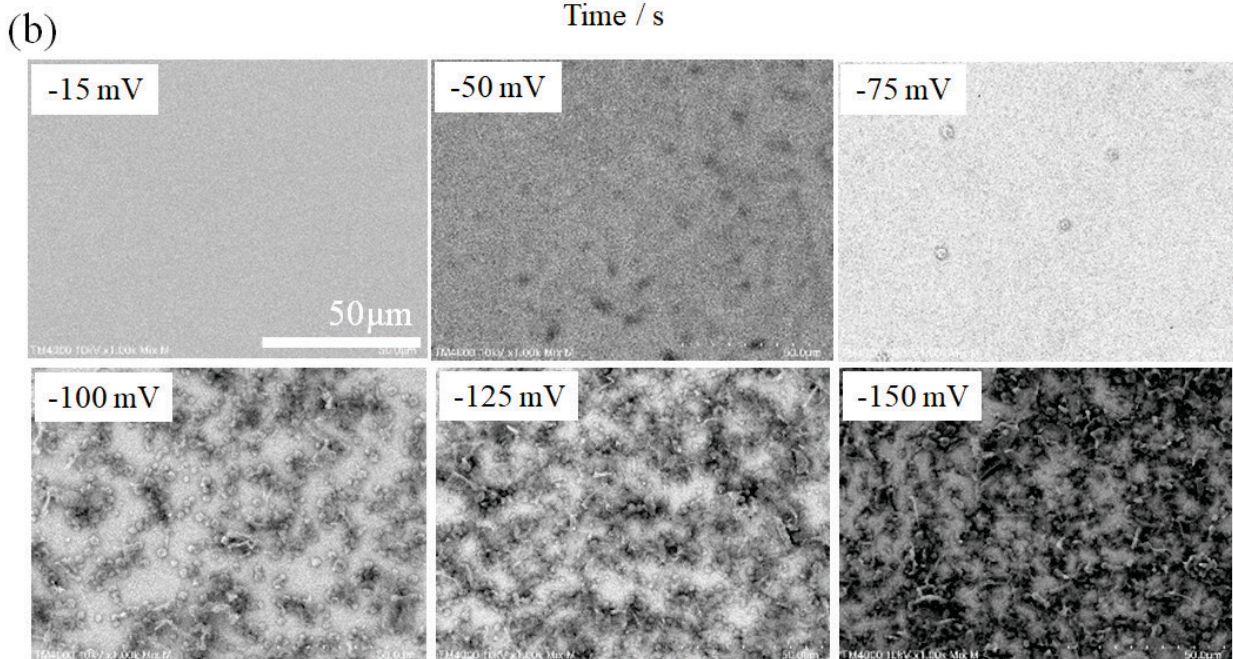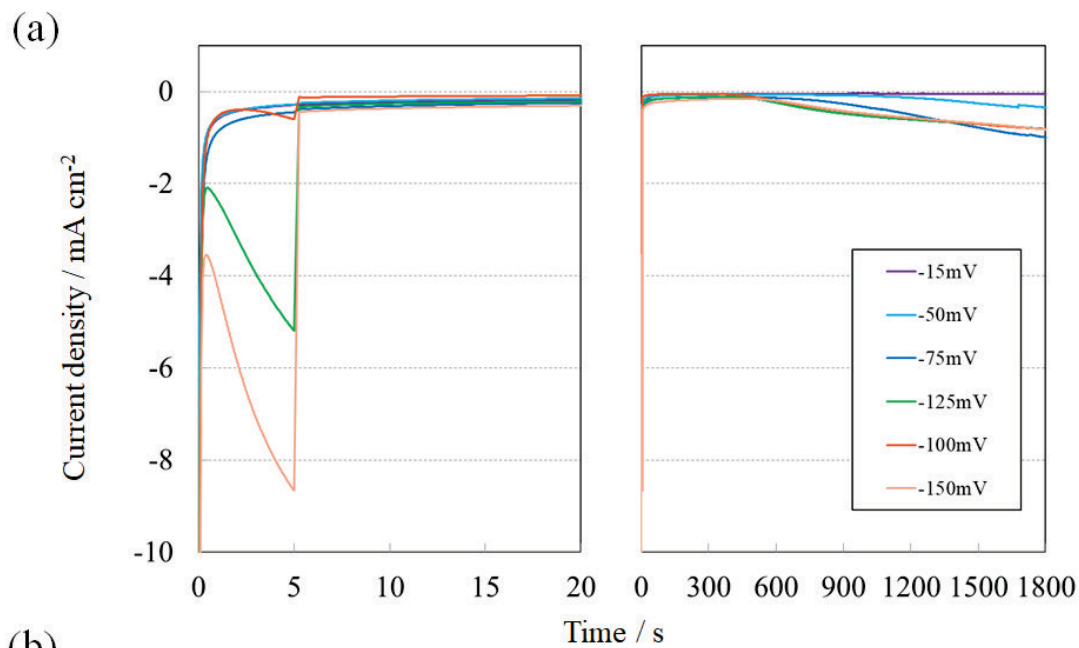
Figure 5-8. (a) Constant potential double pulse chronoamperograms of Li electrodeposition in 1 M LiTFSI/PC on Ni electrode at the first potential of different six potentials (-15 mV, -50 mV, -75 mV, -100 mV, -125 mV and -150 mV vs. Li$^+$/Li) for 5 s and the second potential of -15 mV vs. Li$^+$/Li for 1800 s. (b) SEM micrographs of Ni electrode surface after applying double pulse potential.
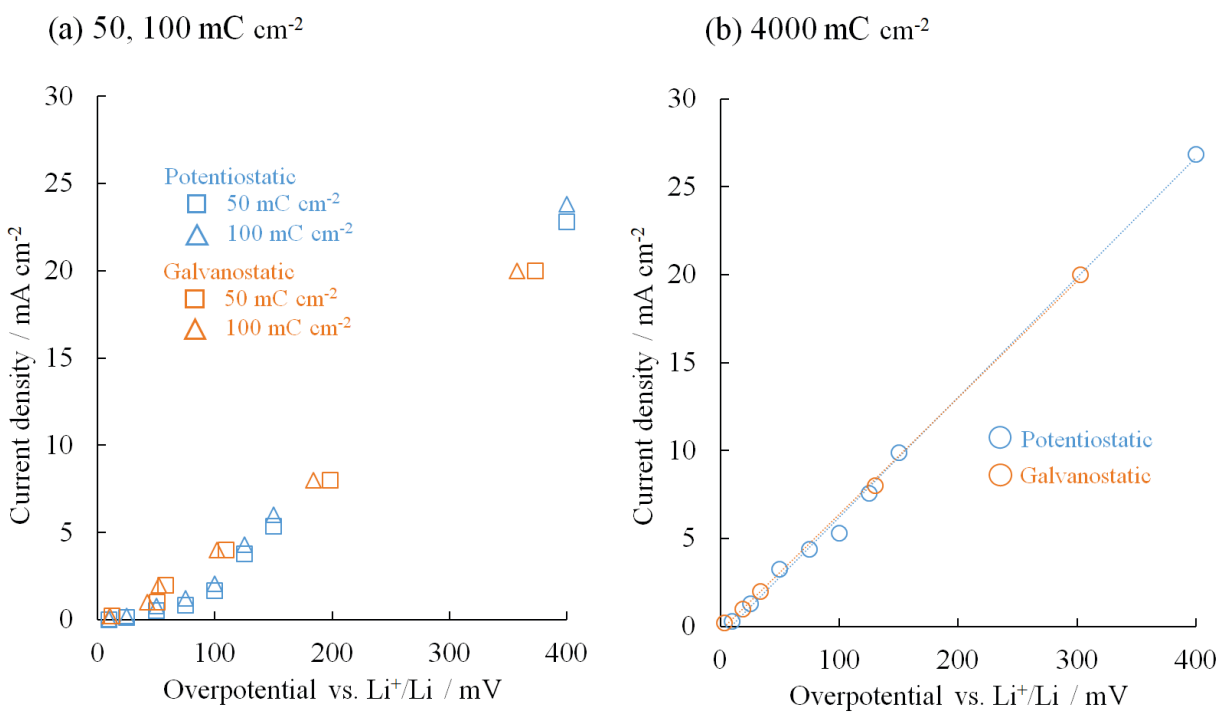
Figure 5-9. Current-potential curves at (a) 50 mC cm^{-2} and 100 mC cm^{-2} and (b) 4000 mC cm^{-2} during galvanostatic and potentiostatic Li electrodeposition in 1M LiTFSI/PC.
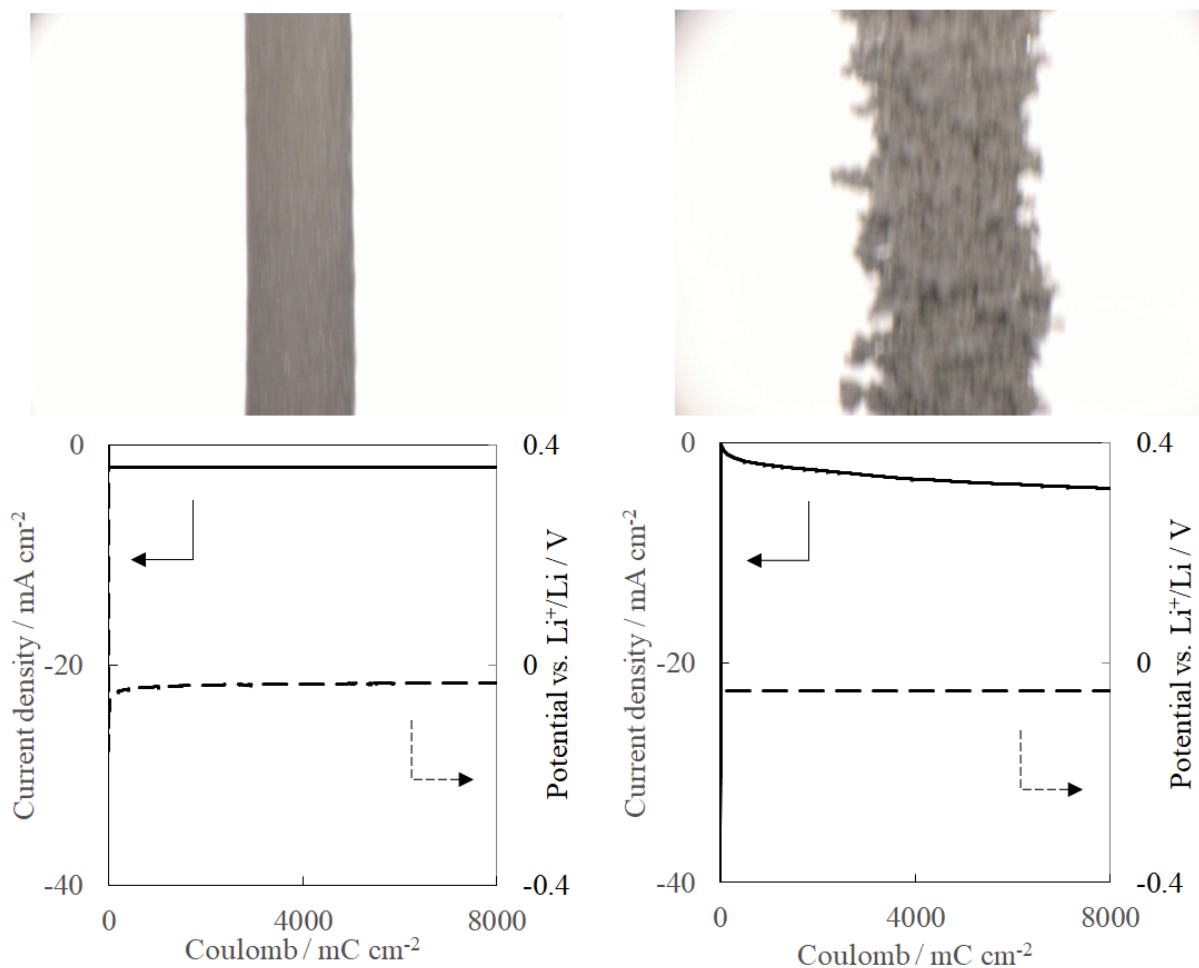
Figure 5-10. Optical microscope image of Li precipitates electrodeposited up to 8000 mC cm^{-2} (upper row) and time variation of current and potential (lower row) (a) under galvanostatic conditions of -2 mA cm^{-2} and (b) under potentiostatic condition of -50 mV.

(a)

(b)
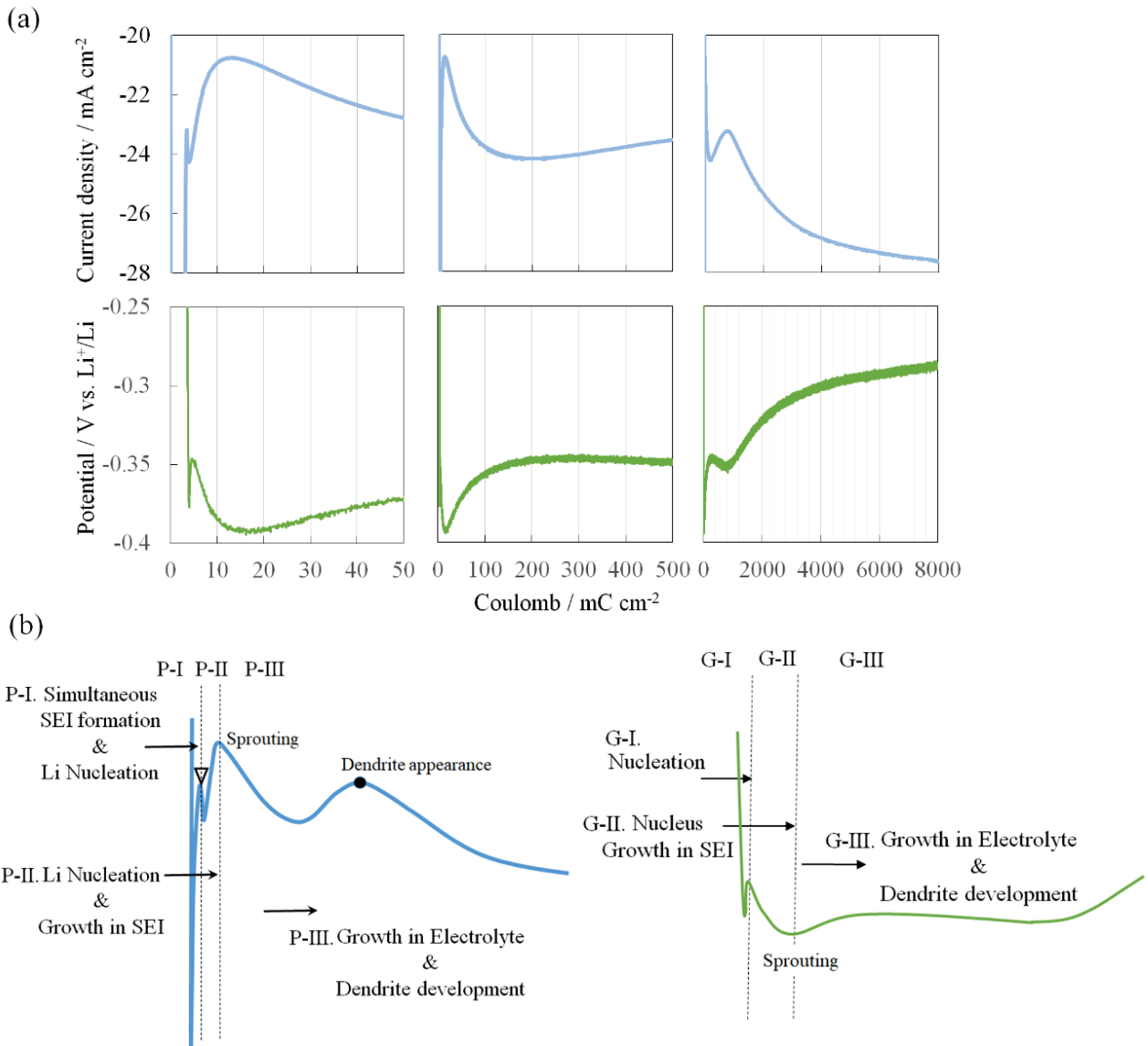
Figure 5-11. (a) Comparison between variation of current density during constant potential electrolysis at -400 mV (upper) and potential variation during galvanostatic electrolysis at -20 mA cm^{-2} (lower). (b) Schematic diagram of i-t curve during potentiostatic electrolysis at -400 mV (left) and V-t curve during galvanostatic electrolysis at -20mA cm^{-2} (right) and the estimated events responsible for each transition. The points marked with ∇ and $\bullet$ represent the point re-defined as zero point for current and time and the point where dendrites began to appear in the optical microscope observation, respectively.
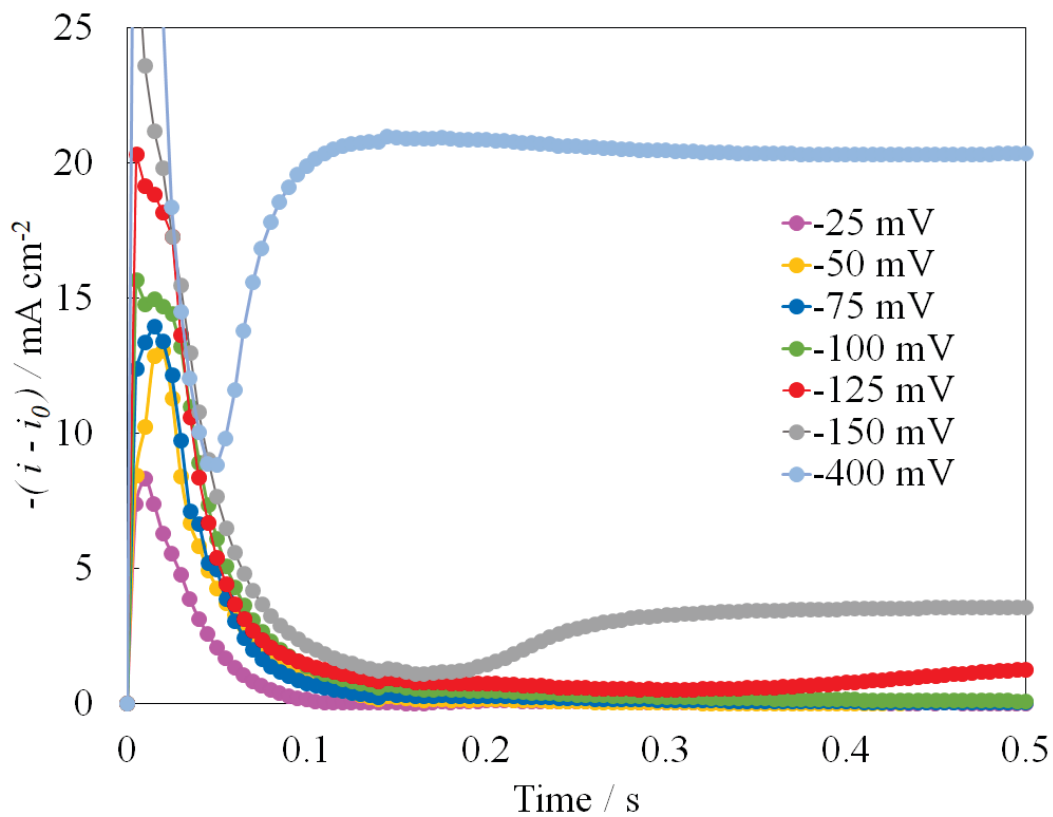
Figure 5-12. Time course changes of the current density during 0.5 s after the start of electrolysis subtracting the current density of the chronoamperogram at 0 mV from it at each set potential in Fig. 5-2
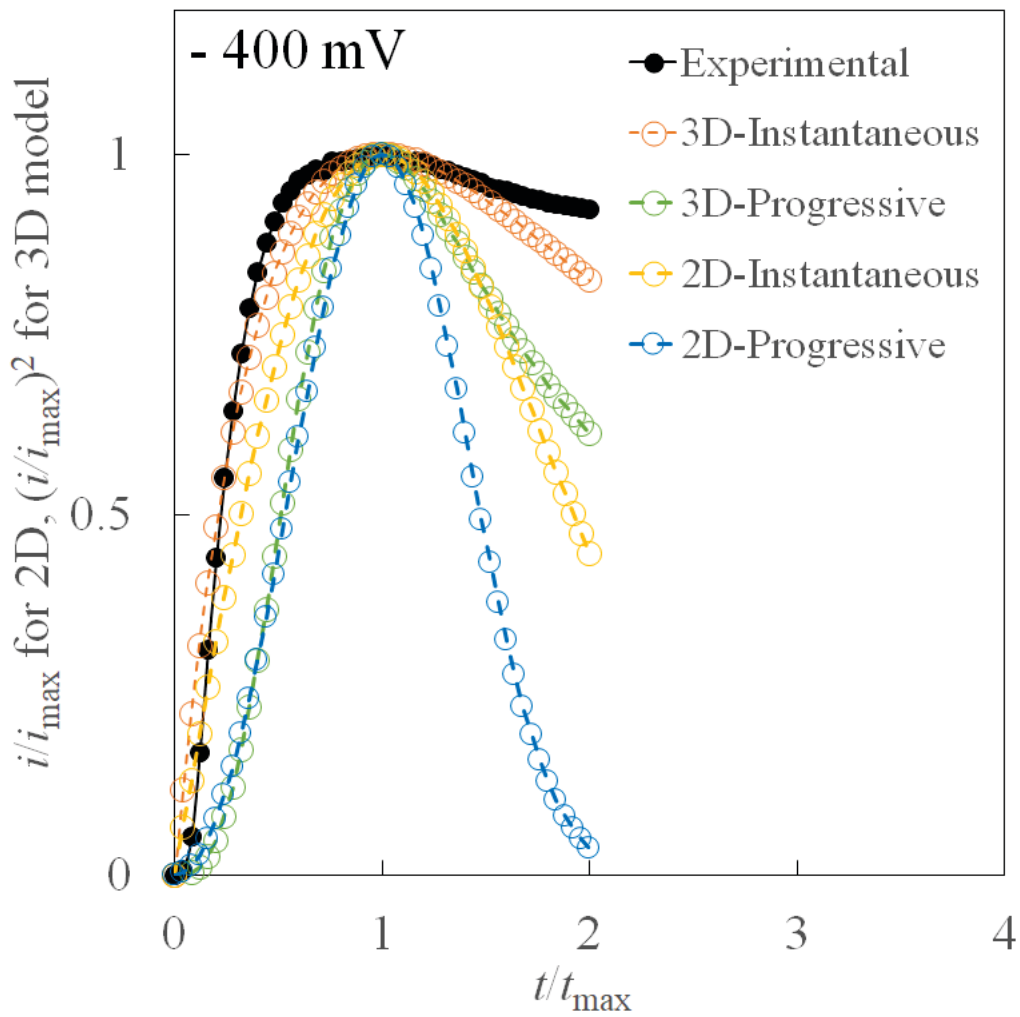
Figure 5-13. Comparison between experimental curve (solid circle) and the theoretical curves (open circle) of normalized current $(i/i_{max})^2$ for 3D model or (i/i_{max}) for 2D model vs. normalized time (t/t_{max}) obtained according to the Scharifker-Hills model for potentiostatic current transient at -400 mV.
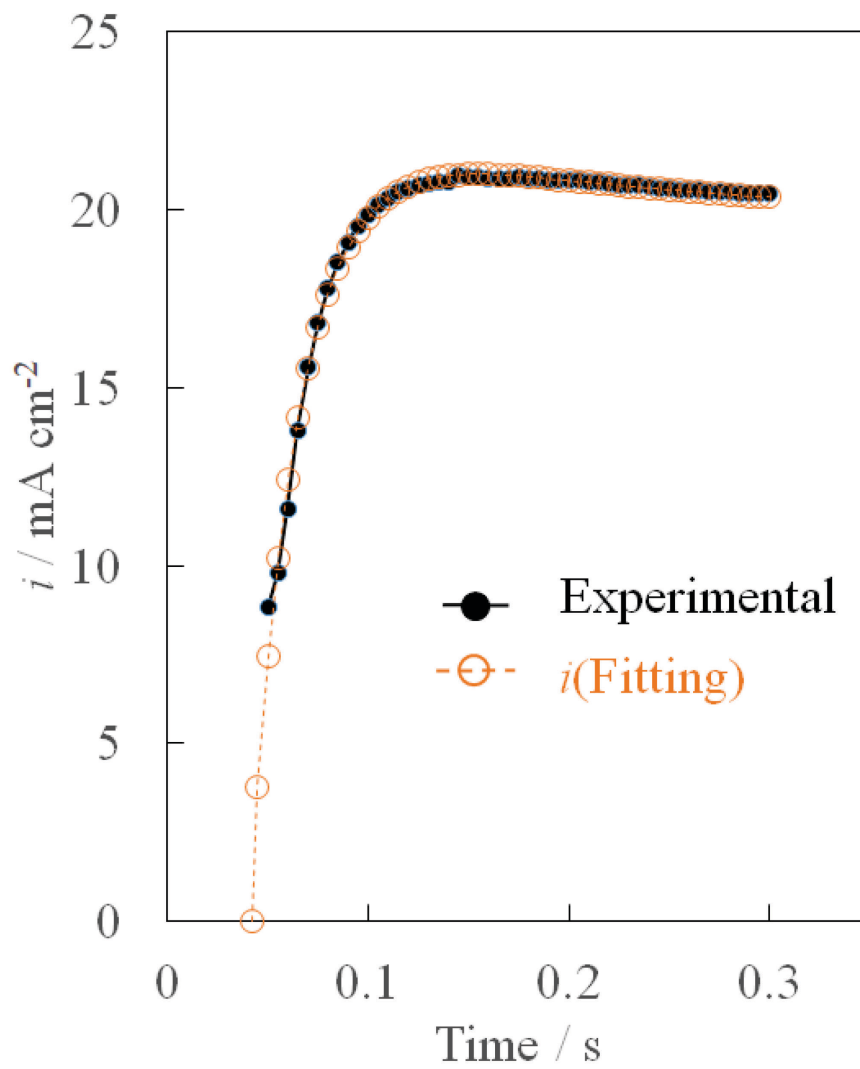
Figure 5-14. Time-course changes of experimental current density (filled circle) in the interval from 0.05 s to 0.3 s and the fitting result (open circle) calculated from the parameter listed in Table 5-1.

(a) Galvanostatic

(< 4 mA cm^{-2}) Low ⇐ Current density ⇒ High (≧ 4 mAcm^{-2})

Electrolyte

SEI

Ni   Ni

Discrete   Homogeneous

Li deposition in the presence of SEI
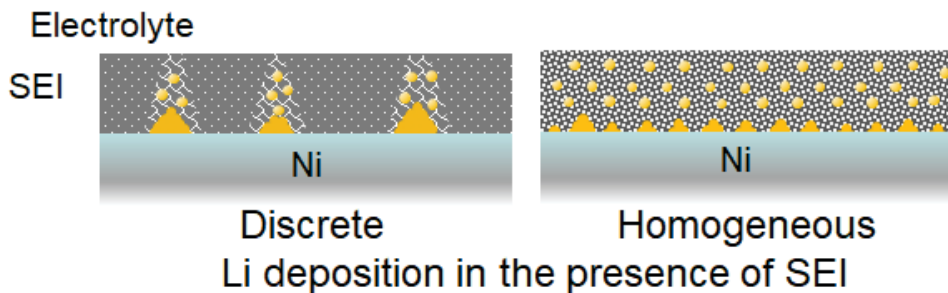
(b) Potentiostatic

(< 100 mV) Low ⇐ |Applied Potential| ⇒ High (≧ 100 mV)

Electrolyte

SEI

Ni   Ni

Localized   Uniform

Competitive SEI formation and Li deposition
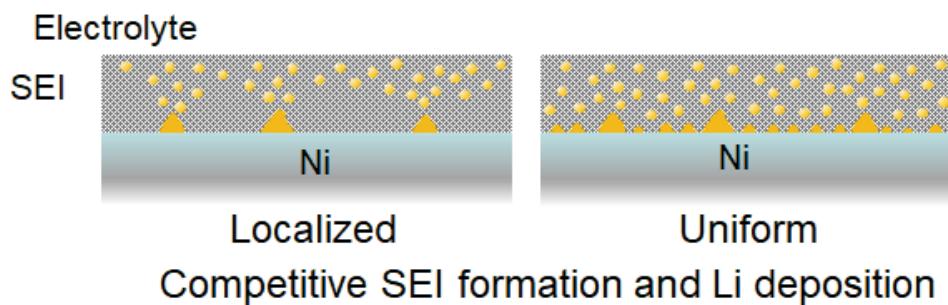
Figure 5-15. Schematic diagrams comparing the initial state of Li electrodeposition between under (a) galvanostatic condition and (b) potentiostatic condition.

Appendix

When analyzing nucleation & growth mechanisms and kinetic parameters based on the current response during constant potential electrolysis, the nucleation & growth model proposed by Scharifker and Hills [25-26] for metal electrodeposition in aqueous solution has been often adopted. The current response of nuclei generated in a disk or hemispherical shape during constant potential electrolysis to growing two-dimensionally or three-dimensionally under diffusion control, respectively, is theoretically predicted to be as follows. The nucleation and growth mechanism can be estimated by comparing the relation of the dimensionless $(i/i_{max})^2$ to (t/t_{max}) or (i/i_{max}) to (t/t_{max}) with these theoretical equations, based on the time variation of current experimentally obtained under potentiostatic conditions.

For 2D nucleation and growth,

(Instantaneous)

$$\frac{i}{i_{max}} = 1.6487 \left(\frac{t}{t_{max}}\right) exp\left[-0.5 \left(\frac{t}{t_{max}}\right)^2\right] \tag{5-A1}$$

(Progressive}

$$\frac{i}{i_{max}} = 1.9477 \left(\frac{t}{t_{max}}\right)^2 exp\left[-0.6667 \left(\frac{t}{t_{max}}\right)^3\right] \tag{5-A2}$$

For 3D nucleation and growth,

(Instantaneous)

$$\left(\frac{i}{i_{max}}\right)^2 = 1.9542 \left(\frac{t}{t_{max}}\right)^{-1} \left\{1 - exp\left[-1.2564 \left(\frac{t}{t_{max}}\right)\right]\right\}^2 \tag{5-A3}$$

(Progressive)

$$\left(\frac{i}{i_{max}}\right)^2 = 1.2254 \left(\frac{t}{t_{max}}\right)^{-1} \left\{1 - exp\left[-2.3367 \left(\frac{t}{t_{max}}\right)^2\right]\right\}^2 \qquad \text{(5-A4)}$$

Chapter 6

Optical Observation of Li Dendrite Growth in LiTFSI-Pyr(1,101)TFSI Ionic Liquid Electrolyte

6.1 Introduction

Li-ion batteries are received attention for large-scale application to energy sources for not only hybrid electric vehicles (HEVs) and electric vehicles (EVs) but also for space satellites and planetary exploration spacecrafts. Such applications demand high energy density and reliability. In order to increase the energy density, new negative electrode materials to replace graphite material are necessary. Li metal is an attractive negative electrode because it has the highest energy density (about 3600 mA h g^{-1}). However, the Li metal dendrite is easily formed during the charging/discharging repetition process corresponding to the electrodeposition / electrochemical dissolution of Li metal. This dendrite growth induces a loss of electrochemical reversibility as well as possibility of a short-circuiting phenomenon.

In order to suppress the dendrite growth, a small amount of additives to electrolyte is sometimes very effective because the additives can change the composition of the surface Solid Electrolyte Interphase (SEI) layer (1-5). Li dendrite arm starts to grow at the points where SEI layer is absent or thin. The qualitative and quantitative control of SEI layer on Li metal surface is therefore indispensable to suppress the dendrite growth.

Generally speaking, the electrodeposited metal is significantly influenced not only by the surface state of substrate but also by ionic mass transfer rate. That is, the coupling phenomenon between them has to be fully understood. However, there are only a few studies that focus on coupling between ionic mass transfer rate and electrodeposited surface morphology in Li electrodeposition system.

Our previous researches discussed the ionic mass transfer rate during the electrodeposition and electrochemical dissolution of Li metal in organic electrolyte (propylene carbonate) by applying the holographic interferometry (6-8). This optical technique successfully visualized the development of Li^+ concentration profile in agreement with the theoretical prediction, while an apparent incubation period was caused by a chemical reaction between the electrodeposited Li metal and chemical species in electrolyte in the initial stage of electrodeposition. It also demonstrated that steeper Li^+ ion concentration gradient field accompanied the Li dendrite arm growth front in $LiPF_6$-PC electrolyte. In addition to these optical measurements, the role of SEI dynamics during the dendrite growth phenomenon in $LiClO_4$-PC and $LiPF_6$-PC electrolyte was also tracked by laser scanning confocal microscope(LSCM) (8, 9).

Ionic liquids represent promising electrolyte candidates for next generation Li ion battery because non-flammability contributes to increased safety and reliability. It is absolutely indispensable for the vehicles for human being. Several researchers have investigated the basic property of this new type electrolyte for Li ion battery application (11-13). In this study, the author focused to the coupling relationship between the ionic mass transfer rate and the dendrite growth morphology during Li electrodeposition in ionic liquid. Similarly to our previous work in organic electrolyte (9), in-situ optical observation for Li dendrite growth were conducted.

6.2 Experimental

The ionic liquid, (*N*-methoxymethyl-*N*-methylpyrrolidinium) bis (trifluoromethane-sulfonyl) imide (Pyr(1,101)TFSI, referred to hereafter simply as IL), used in this study is described in Figure 6-1. It was supplied from Stellachemifa Corporation. The company reports the initial content of water contamination less than 30 ppm. Lithium bis (trifluoromethanesulfonyl) imide (LiTFSI) was purchased from Sigma-Aldrich. LiTFSI was dried for 24 h at 150 °C under a stream of nitrogen gas before use.

LiTFSI-IL solutions were prepared as follows. LiTFSI was weighed up in 10 mL measuring flasks so as to be adjusted to 0.5 M, 0.75 M, 1.0 M and 1.5 M in dry box purged with Nitrogen gas. Next, IL was weighed below the specified line of measuring flask, respectively. It is rather difficult to dissolve LiTFSI in IL. So the flask was heated at 60 °C on a hotplate placed in dry box. After LiTFSI dissolved completely in IL contained in the flask, IL was further added up to the measuring line accurately. The weight percentage concentration (c: %) and the weight-molar concentration (m: mol kg^{-1}) were derived. Then, the density of electrolyte solutions (ρ: kg L^{-1}) was measured by using density meter (Kyoto Electronics Manufacturing CO., Ltd; DA-130N) in temperature-controlled bath at 25 °C. The volume-molar concentration of the solutions (M: mol L^{-1}) was calculated from the m×ρ.

Figure 6-2 shows the relation between weight percentage concentration and volume-molar concentration. According to the regression line in Figure 6-2, LiTFSI-IL solution was adjusted to a given concentration. Water content in solutions was measured by Karl Fischer titration (Hiranuma Sangyo Co., Ltd.; AQ-7) and confirmed to be below 30 ppm. The conductivity of electrolyte solutions was measured by conductivity meter (Radiometer Analytical S. A.; CDM210). Measured solution was poured into a glass vessel and conductivity cell was immersed in it. The gap between the mouth of glass vessel and the conductivity cell was sealed air-tightly with parafilm to prevent moisture contamination from the atmosphere. The above assembled conductivity cell was immersed in a thermostatic bath and the conductivity was measured at a given temperature. Assembling the conductivity cell was performed in a dry box purged with Nitrogen gas, while the measurement was conducted outside the dry box. Conductivity measurement cell (Radiometer Analytical S.A.; XE100) was calibrated using a standard solution of 0.1D KCl (Radiometer Analytical S.A., 12.85 mS cm^{-1}). The cell constant was 1.116.

The viscosity of ionic liquid solutions was measured using a viscosity meter (Brookfield; LVDV-I+). The viscosity meter was placed in the dry box to avoid moisture contamination. The cell temperature was controlled using a circulator temperature-controlled bath.

Electrochemical measurements of cyclic voltammetry and chronopotentiometry were performed. Cyclic voltammetry was conducted by using a usual three-electrode cell. The working electrode was 5 mm square Ni sheet with 100 μm thickness (Nilaco Corp.). The counter electrode and the reference electrode were made of Li foil with 200 μm thickness (Honjo Metal Co., Ltd.). A glass container used as a cyclic voltammetry cell was wholly installed into an aluminum block of Peltier temperature control unit (Nissin Electric; NDC-100) to keep constant temperature conditions. Cyclic voltammetry was carried out in an argon glove box (Takasugi Seisakusho; G65MVAV) maintained with dew point below -70 ℃.

Chronopotentiometry was simultaneously performed with optical observation of Li metal dendrite growth. The configuration of electrolytic cell for in-situ optical observation is illustrated in Figure 6-3. The working electrode is Ni wire of 100 μm in diameter (Nilaco Corp.). Ni wire and stainless needles of disposable syringes are passed through an o-ring. The counter electrode and reference electrode are similarly made of Li foil with 200μm thickness (Honjo Metal Co., Ltd.) crimped on stainless steel needles. The o-ring is sandwiched by slide glasses and clipped. Ionic liquid electrolyte is slowly injected by syringe from this needle.

The in-situ dendrite growth behavior was observed by digital optical microscope and the video image was stored on a personal computer. Assembling the electrolytic cell was conducted in a glove box (Takasugi Seisakusho, model) filled in argon gas. Dew point of the glove box was always maintained below -70 ℃. Electrochemical measurement and optical observation was conducted in a temperature-controlled bath (Espec corp.; PWL-3KP. Nitrogen gas was purged into the bath so as to eliminate the influence of moisture from the atmosphere as much as possible. The galvanostatic electrodeposition of Li metal was conducted by using an electrochemical measurement system (Hokuto Denko Co., Ltd; HZ-3000). Imposed current density was varied galvanostatically from 0.1 to 5.0 mA cm^{-2}.

6.3   Results and Discussion

6.3.1   *Optical observation of Li dendrite growth*

Before performing the observation of dendrite growth, ionic conductivity and viscosity were measured in order to understand the fundamental characteristics of the solution consisted of LiTFSI and the ionic liquid. As well known, ionic liquid becomes viscous and the conductivity decreases with decreasing in temperature as well as with the addition of LiTFSI demonstrated in Figures 6-4 and 6-5.

Some papers discussed possible application of ionic liquid into electrolyte for lithium ion battery electrolyte. As illustrated in Table 6-1, the aliphatic ammonium type ionic liquid was selected among various kinds of ionic liquid from the viewpoints of reductive electrochemical stability and conductivity in the present work. The reversibility of Li electrodeposition in the ionic liquid was checked by usual cyclic voltammetry. Figure 6-6 shows the cyclic voltammogram of lithium electrodeposition. Ten cycles were performed and reversible deposition and dissolution of Li was observed within the applied potential range (above -0.2 V vs. Li^+/Li). Small leakage current has been observed from around +1.5 V in the inset, which is gradually reduced with cycles. The leak current may be caused by the reduction of very thin surface oxide layer on Ni electrode, followed by resultant formation of the SEI layer which stems from the unavoidable reaction between reduced Li metal and electrolyte solution. In this study, the initiation and growth of Li dendrite in 1.0 M LiTFSI-ionic liquid (IL) are focused from the viewpoint of Li^+ ionic mass transfer rate in the vicinity of the dendrite.

Figure 6-7 (a) demonstrates the time transient behavior of electrode potential in the initial stage of galvanostatic electrodeposition of the Li metal on nickel wire. The higher the current density, the larger the overpotential of Li metal electrodeposition. At 5 mA cm^{-2}, the electrode potential quickly drops to the negative direction against Li^+/Li potential only a few seconds after the electrolysis starts. At smaller current density, the period when the potential keeps positive against Li^+/Li potential is extended. This potential shifts start from around +0.9 - +1.4V, which

roughly corresponds to the potential of the beginning of the leak current in Figure 6-5. It slowly relaxes toward the Li^+/Li potential and gradually approaches steady-state. Open circle symbol assigns the time when precipitates were at first visible on video image. It may apparently correspond to the phenomenon which Li dendrite precursor starts to grow. Figure 6-7 (b) shows the electrode potential variations with the amount of electricity passing. Before precipitates are evident on video image, 8 mC cm^{-2} ～20 mC cm^{-2} are consumed. These apparent initiation periods and potential transition phenomena may relate to the reduction of surface oxide layer of Ni, small amount of impurities in the electrolyte, SEI formation and Li nucleation and so on.

The onset and appearance of dendrite growth was carefully observed by video image. Figure 6-8 shows the time transient of morphological variations of electrodeposited Li metal on Ni wire in 1.0M LiTFSI-IL at 0.1, 0.2, 0.5, 2.0 and 5.0 mA cm^{-2}. The electrolysis was terminated at 900 mC cm^{-2}.

Our previous paper described the growing dendrite arm accompanied by dynamically swinging movement in LiPF$_6$-PC electrolyte solution observed with holographic interferometry (8) as well as LiClO$_4$-PC with LSCM (9). In the case of LiClO$_4$-PC electrolyte solution, the frequency and amplitude of dendrite movement were dependent on the salt concentration, but independent on applied current density. Yamaki et al. reported the dynamic movement of the Li metal dendrite observed by optical microscope (10). The motion of the whisker-like dendrite was attributed to the pressure difference induced by variations of the surface tension around electrodeposited Li metal tip, and the calculation results based on the surface curvature concept agreed with the experimental results.

The dynamic swinging movement is also observed in the present ionic liquid experiment. The dendrite movement seems to be dependent on the applied current density in the present case (Fig. 6-8). At lower current densities less than 0.2 mA cm^{-2}, needle-like deposits develop with the progress of electrodeposition. Many long, sharp whisker deposits are observed. These begin to be evident after 150 mC cm^{-2} at 0.1 mA cm^{-2}. Above 0.5 mA cm^{-2} the needle-like dendrite growth

does not appear, rather a complex dendritic form similar to seaweed emerges. In this case a relatively smooth surface is maintained until 300 mC cm^{-2} is passed.

At 300 mC cm^{-2}, needle-like deposits appear at 0.1 and 0.2 mA cm^{-2}, while no clear morphological variations are observed at higher current density. There seems to be a transition in morphology between 0.2 mA cm^{-2} and 0.5 mA cm^{-2}. At 600 mC cm^{-2} and 900 mC cm^{-2}, the morphological difference introduced by applied current density becomes more distinguished. Although dendrite structure below 0.2 mA cm^{-2} is kept in the form of needle-like morphology, morphology with a lower aspect ratio consisting of aggregated dendrite arms appears to develop above 0.5 mA cm^{-2}.

The dendrite swinging movement behavior is also influenced by applied current density. The video image reveals enhanced dendrite movement with the applied current density. In the case of 5 mA cm^{-2}, the surface of Ni wire electrode appears to swell soon after starting electrolysis. Some deposits begin to loom on the outer surface of Ni wire electrode 4 s after the initiation (after the passage of 20 mC cm^{-2}), and the whisker-like deposits starts to appear along with gradual apparent expansion of the diameter of the Ni electrode. During this period (150 mC cm^{-2}～300 mC cm^{-2}), whisker-like deposits swing sporadically interfering with the growth of neighboring deposits. They begin to ramify as they grow in length and swing slowly in a chaotic pattern taking on the appearance of flowing sea grass in a sea (300 mC cm^{-2}～600 mC cm^{-2}). Subsequently, a part of deposits come to expand dendritically and begin to flutter.

For the case of 2.0 mA cm^{-2} and 0.5 mA cm^{-2}, the transition from whisker-like deposits to dense dendritic aggregates appear later compared to the case of 5 mA cm^{-2}. Below 0.2 mA cm^{-2}, expanded-dendritic growth is not observed, but only whisker deposits grow up to spiny morphology. Likewise, a much slower swinging motion of the whisker or spiny deposits is observed under these conditions.

The temperature dependence of Li metal electrodeposition is shown in Figure 6-9. No substantial temperature dependence of morphological variations is seen at 150 mC cm^{-2}, while a small indication of preferential growth of needle-like deposit is recognized at 40 °C. Such a

transition from smooth surface to needle-like deposit occurs at 300 mC cm^{-2} in the case of 25 °C. With increasing temperature and charge, the needle-like deposit becomes preferentially predominant with coagulation each other.

The effect of Li salt concentration of growth morphology was also investigated as shown in Figure 6-10. Ionic liquid with five different LiTFSI concentrations from 0.5 M to 1.5 M were used. The dendrite growth behavior is very different between 0.75 M and 1.0 M. Below 0.75 M, dense dendrite aggregate are evident, while needle-like deposits develop above 1.0 M. The differences in morphology introduced by variation of the LiTFSI concentration are already evident even at 300 mC cm^{-2}. In 1.25 M solution, needle-like deposits appear preferentially compared to 1.0 M, although such morphological variations are somewhat restricted above 600 mC cm^{-2} in the case of 1.5 M.

6.3.2   *Measurement of dendrite length*

The dendrite primary arm length was measured at several locations along a cathode surface which was divided into eight sections for each image. A representative dendrite arm was selected to be measured in each section. Each plot and error bar mean the averaged length and the standard deviation calculated with these eight dendrite arms. Figure 6-11 demonstrates the time variations of averaged arm length, the variance and the surface concentration of Li$^+$ ion. Neglecting the possible induction of electrolyte natural convection, a transient diffusion model was used to predict the transient variation of Li$^+$ ion surface concentration at Ni wire cathode in LiTFSI-IL system illustrated by dotted lines (see Appendix).

Dendrite arm length grows proportionally with the square root of time. Similarly to the case in propylene carbonate organic electrolyte solution, two stages with different dendrite growth rates are clearly recognized at five current densities. In the initial stage, the dendrite arm growth rate is relatively slow, followed by faster growth rate region. Such a growth rate transition appears when the averaged arm length reaches a critical value of a few or at most 10 μm in the present optical

arrangement. The resolution power of optical microscope is at most a few micrometers. Thus, the calculated result of the surface concentration is no longer available once dendrite arm length exceeds such optical resolution power. That is, the mass transfer rate can be discussed based on such a model in the beginning of initial stage, but no longer applied in the later stage close to the growth rate transition.

Li^+ surface concentration corresponding to the critical arm length is about 0.98, 0.98, 0.95, 0.89 and 0.82 M depending on each current density varied from 0.1 to 5.0 mA cm^{-2}. Examining the video images, the initial growth period roughly corresponds to the region when whisker-like or fuzzy deposit gently grows dominantly, followed by the second period when dendritic or spiny deposits develop with swinging movement.

Such a sequence of dendrite growth process is schematically illustrated in Figure 6-12. Looking at the early stage of Li electrodeposition in Figure 6-8, the number of the electrodeposition site is quite limited at lower current density. It may be partly caused by smaller electrochemical overpotential as well as by heterogeneous surface active site caused by non-uniformity of SEI layer. Moreover, it is expected for Li^+ ion to more easily electrodeposit onto Li surface than Ni surface. These aspects introduce more non-uniform current density distribution which results in much higher local current density distribution around the growing dendrite at apparent lower current density. This causes Li^+ ion depletion and significantly accelerates the whisker dendrite growth locally.

The current density distribution in the initial stage of electrodeposition becomes more uniform with increase in current density above 0.5 mA cm^{-2}. Because dendrite movements are relatively moderate in the initial stage, Li metal nucleation and growth process is controlled mainly by diffusive mass transfer rate. Electrochemically nucleated Li metal forms many small dendrite precursors. Once such Li metal precursors are grown, typical dendrites start to grow with competition among dendrite arms. Dynamically swinging movement becomes active as the competition for growth proceeds. Such a dendrite movement induces the electrolyte convective

flow or vortex adjacent to the electrode. Fresh electrolytic solution is supplied by the disturbed electrolyte flow and the dendrite arm growth rate is further accelerated as shown in Figure 6-12.

The good linearity shown in Figure 6-11 suggests that Li^+ ionic mass transfer rate affects the dendrite growth once the dendrite precursor growth starts, as was previously reported in $LiClO_4$-PC system (9). Open markers in Figure 6-11 demonstrate the points where the precursors can be visible in the video image. They are 4 s at 5 mA cm^{-2}, 9 s at 2.0 mA cm^{-2}, 25 s at 0.5 mA cm^{-2}, 4 s at 0.2 mA cm^{-2} and 140 s at 0.1 mA cm^{-2} respectively. The critical surface concentration at these apparent initiation periods is estimated to be 0.82 M at 5 mA cm^{-2}, 0.89 M at 2.0 mA cm^{-2}, 0.95 M at 0.5 mA cm^{-2}, 0.98 M at 0.2 mA cm^{-2} and 0.98 M at 0.1 mA cm^{-2}. Initiation periods for dendrite precursors to start to grow are also estimated independently by the extrapolating the inclination line to zero length. Apparent initiation periods (t_{app}) and initiation periods (t_{ex}) determined by extrapolation method are summarized in Table 6-2. Above 0.5 mA cm^{-2}, (t_{ex}) is substantially identical to (t_{app}). Below 0.2 mA cm^{-2}, (t_{ex}) is longer than that recognized in video image (t_{app}). Such a discrepancy seems to be caused by the significant non-uniform current distribution, as mentioned above. The surface chemistry on Li metal also affects to the dendrite initiation as well as the residual stress accumulated inside a critical thickness of deposited Li metal film or deposit.

The two-stage growth process is also seen at four different temperatures as shown in Figure 6-13. At 40 °C, the growth rate in the first stage seems to be faster and critical dendrite length reaches about 20 μm, while for temperature below 25 °C no substantial temperature dependence in the first stage is noticed and critical length stays around 10 μm. The growth rate in the second stage seems slow at -5 °C. The temperature effect is more clearly demonstrated in the potential variations shown in Figure 6-14. The potential shift is considerably retarded at higher temperature till the coulomb quantity reaches roughly 6 to 13 mC cm^{-2}. It may suggest that the thicker SEI layer is formed when the higher temperature is applied, because the mass transfer rate of impurity species is enhanced followed by the retarded precipitation of Li metal.

The concentration dependence of dendrite arm growth rate is demonstrated in Figure 6-15. For 0.5 M and 0.75 M, dendrite growth rate is almost constant, while two-stage growth mode is observed only in 1.0 M, 1.25 M and 1.5 M. In spite of such a significant growth mode transition, no characteristic difference is noticed in the potential variation curve till roughly 5 mC cm^{-2} (roughly corresponds to 25s) in Figure 6-16. As for 1.0 M, 1.25 M and 1.5 M, the extrapolation point t_{ex} in the first step is lower than the apparent initiation period t_{app} as illustrated in Table 6-2. In the case of 0.5 M and 0.75 M showing a single stage in Fig. 6-15, the extrapolated point is faster than apparent initiation period. This tendency can't be understood at the present stage. Further research on the interaction between lithium ion and the ionic liquid and the microscopic structure between the electrode and electrolyte interface must be further examined.

6.4 Conclusions

The in-situ observation of electrodeposited of Li metal in ionic liquid (*N*-methoxymethyl-*N*-methylpyrrolidinium) bis (trifluoromethanesulfonyl) imide was conducted by optical microscope. The time variation of dendrite morphology and dendrite motion behavior is different according to the current density, temperature and salt concentration. Not only the electrode surface state but also the Li$^+$ ionic concentration in the vicinity of the electrode surface must be one factor for the dendrite initiation. After the dendrite starts to grow, Li$^+$ ionic mass transfer rate also affects the dendrite growth of the electrodeposited Li metal significantly. It is necessary to couple the surface chemistry of the Li metal with Li$^+$ ionic mass transfer rate near the electrode surface in order to reveal the detailed mechanism of dendrite growth of Li metal in the future study.

References

[1] K. Kanamura, S. Shiraishi, Z. Takehara, Electrochemical Deposition of Very Smooth Lithium Using Nonaqueous Electrolytes Containing HF, J. Electrochem. Soc., 143, 2187 (1996).

[2] S. Shiraishi, K. Kanamura, Z. Takehara, Study of the Surface Composition of Highly Smooth Lithium Deposited in Various Carbonate Electrolytes Containing HF, Langmuir, 13, 3542 (1997).

[3] T. Osaka, T. Momma, T. Tajima, Y. Matsumoto, Enhancement of Lithium Anode Cyclability in Propylene Carbonate Electrolyte by CO_2 Addition and Its Protective Effect Against H_2O Impurity, J. Electrochem. Soc., 142, 1057 (1995).

[4] M. Ishikawa, Y. Takaki, M. Morita, Y. Matsuda, Improvement of Charge‐Discharge Cycling Efficiency of Li by Low‐Temperature Precycling of Li, J. Electrochem. Soc., 144, L90 (1997).

[5] M. Ishikawa, M. Kanemoto, M. Morita, Control of lithium metal anode cycleability by electrolyte temperature, J. Power Sources, 81, 217 (1999).

[6] M. Ota, S. Izuo, K. Nishikawa, Y. Fukunaka, E. Kusaka, R. Ishii, J. R. Selman, Measurement of concentration boundary layer thickness development during lithium electrodeposition onto a lithium metal cathode in propylene carbonate, J. Electroanal. Chem., 559, 175 (2003).

[7] K. Nishikawa, Y. Fukunaka, T. Sakka, Y. H. Ogata, J. R. Selman, Measurement of concentration profile during charging of Li battery anode materials in $LiClO_4$-PC electrolyte, Electrochim. Acta, 53, 218 (2007).

[8] K. Nishikawa, Y. Fukunaka, T. Sakka, Y. H. Ogata, J. R. Selman, Measurement of $LiClO_4$ Diffusion Coefficient in Propylene Carbonate by Moiré Pattern, J. Electrochem. Soc., 154, A943 (2007).

[9] K. Nishikawa, T. Mori, T. Nishida, Y. Fukunaka, M. Rosso, T. Homma, J. Electrochem. Soc. Submitted

[10] J. Yamaki, T. Toboshima, K. Hayashi, K. Saito, Y. Nemoto, M. Arakawa, A consideration of the morphology of electrochemically deposited lithium in an organic electrolyte, J. Power Sources, 74, 219 (1998).

[11] H. Sakaebe, H. Matsumoto, *N*-Methyl-*N*-propylpiperidinium bis(trifluoromethanesulfonyl)imide (PP13–TFSI) – novel electrolyte base for Li battery, Electrochem. Commun., 5, 594 (2003).

[12] P. C. Howlett, N. Brack, A. F. Hollenkamp, M. Forsyth, D. R. MacFarlane, Characterization of the Lithium Surface in *N*-Methyl-*N*-alkylpyrrolidinium Bis(trifluoromethanesulfonyl)amide Room-Temperature Ionic Liquid Electrolytes, J. Electrochem. Soc., 153, A595 (2006).

[13] S. Seki, Y. Ohno. Y. Kobayashi, H. Miyashiro, A. Usami, Y. Mita, H. Tokuda, M. Watanabe, K. Hayamizu, S. Suzuki, M. Hattori, N. Terada, Journal of The Electrochemical Society The Electrochemical Society, find out more Imidazolium-Based Room-Temperature Ionic Liquid for Lithium Secondary Batteries: Effects of Lithium Salt Concentration, J. Electrochem. Soc., 154, A173 (2007).

[14] H. Matsumoto, M. Yanagida, K. Tanimoto, M. Nomura, Y. Kitagawa, Y. Miyazaki, Highly Conductive Room Temperature Molten Salts Based on Small Trimethylalkylammonium Cations and Bis(trifluoromethylsulfonyl)imide, Chemistry Letters, 922 (2000).

[15] D. R. McFarlane, J. Sun, J. Golding, P. Meakin, M. Forsyth, High conductivity molten salts based on the imide ion, Electrochim. Acta, 45, 1271 (2000).

[16] H. Matsumoto, H. Sakaebe, K. Tatsumi, Preparation of room temperature ionic liquids based on aliphatic onium cations and asymmetric amide anions and their electrochemical properties as a lithium battery electrolyte, J. Power Sources, 146, 45 (2005).

Table 6-1. Melting point and conductivity of ionic liquids based on several aliphatic ammonium cations and bis (trifluoromethanesulfonyl) imide anion.
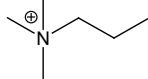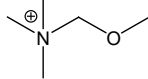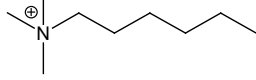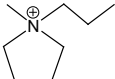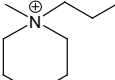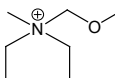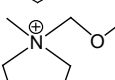
Cation	m.p. / °C	Conductivity/mS cm^{-1}	References
	17	3.3	[14]
	4.5	4.7	[14]
	—	0.43	[15]
	12	1.4	[15]
	8.7	1.51	[16]
	(-85)	2.2	[16]
	-21	5.4	This work

Table 6-2. Apparent initiation periods (t_{app}) when precipitates can be visible on video image and initiation period (t_{ex}) determined by extrapolating the inclination line of dendrite growth.

Effect of current density (j)			Effect of temperature (T)			Effect of Li salt concentration (c)		
j/mA cm^{-2}	t_{app}/ s	t_{ex}/ s	T / °C	t_{app}/ s	t_{ex}/ s	c/mol dm^{-3}	t_{app}/ s	t_{ex}/ s
5	4	4	40	67	210	1.5	40	91
2	9	10	25	43	69	1.25	71	84
0.5	25	23	10	60	100	1	43	69
0.2	43	69	-5	63	137	0.75	67	6
0.1	140	328				0.5	59	16
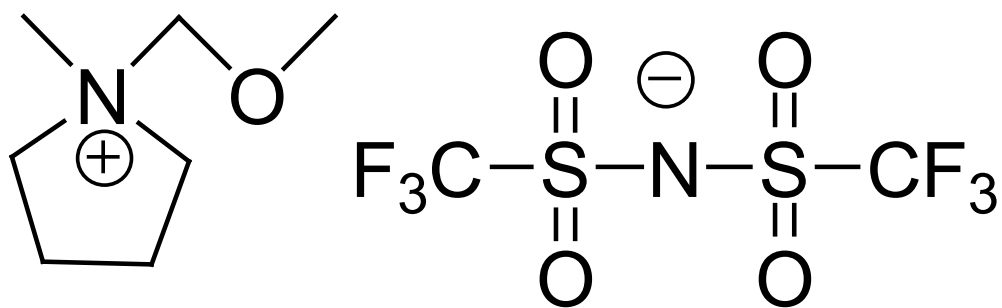
Figure 6-1. Schematic diagram of *N*-methoxymethyl-*N*-methylpyrrolidinium bis (trifluoromethanesulfonyl) imide ionic liquid.
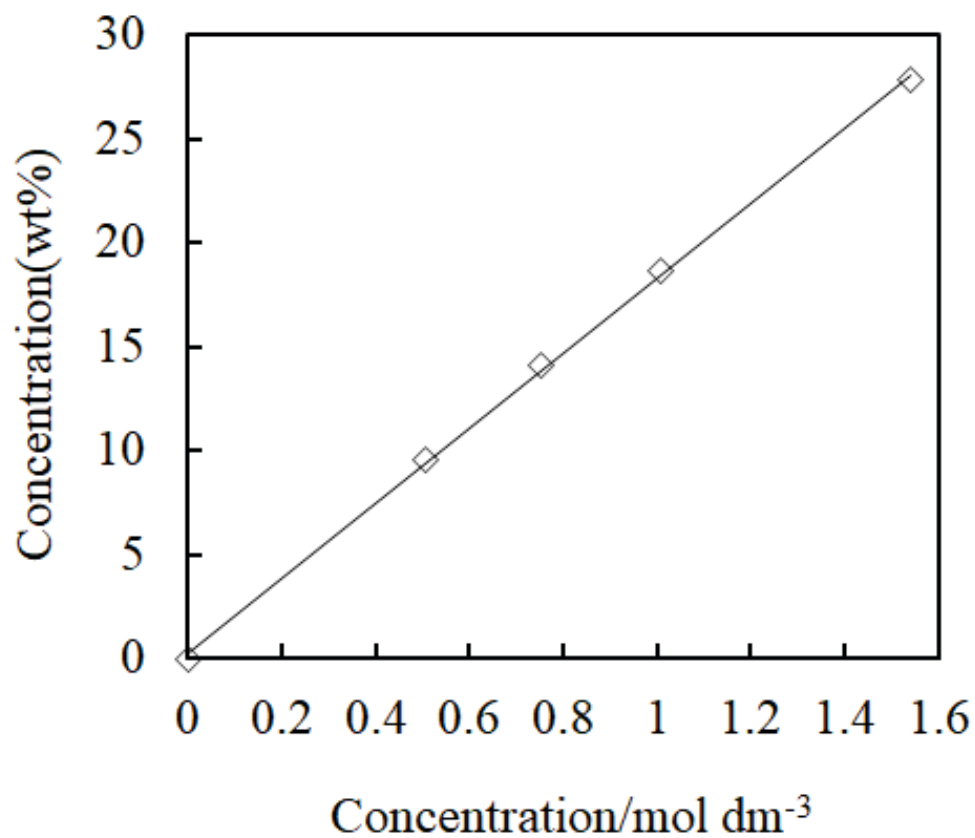
Figure 6-2. The relationships between molar concentration and weight concentration of LiTFSI-IL solutions.
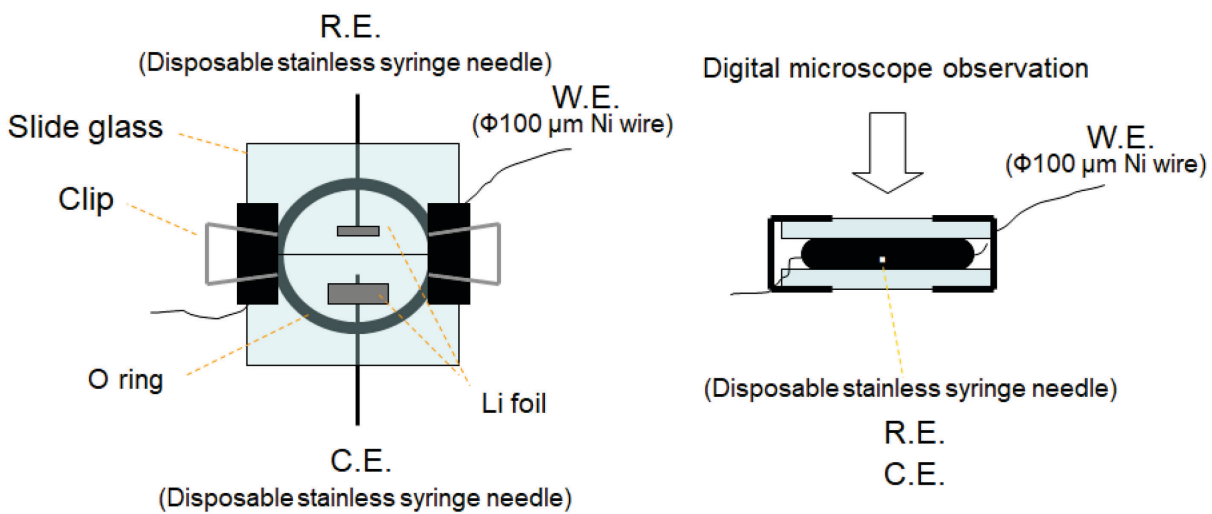
Figure 6-3. The schematic diagrams of electrolytic cell for in-situ optical observation
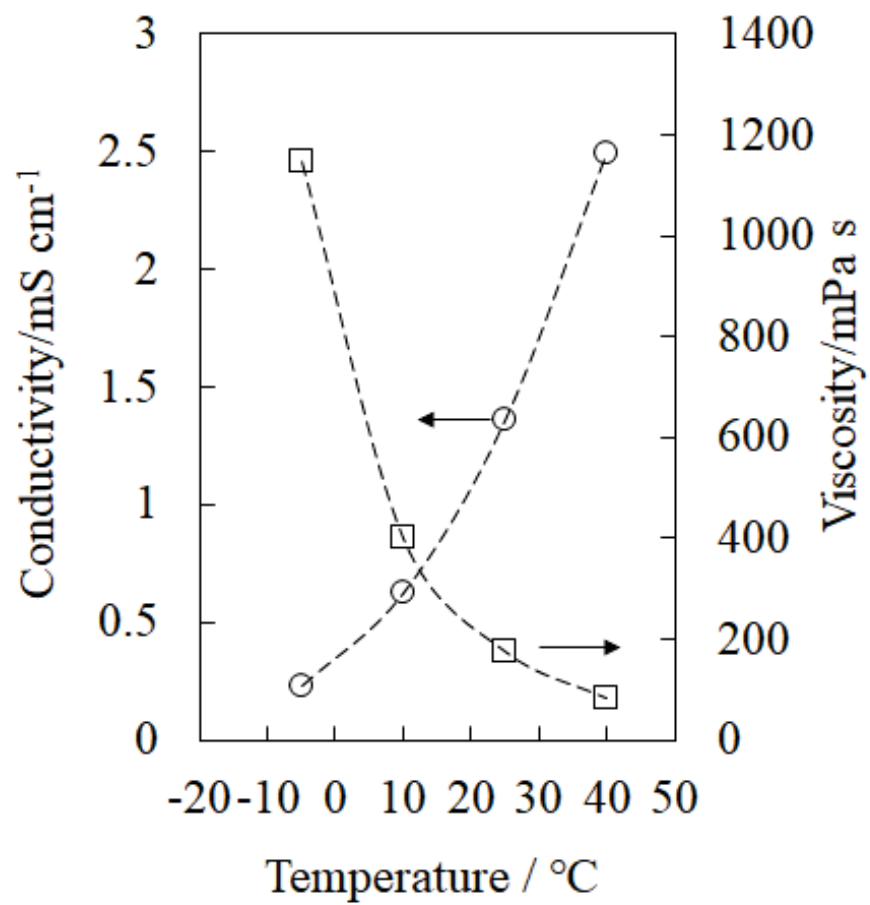
Figure 6-4. Temperature dependencies of conductivity and viscosity of the solution of 1.0 M LiTFSI-IL (○: Conductivity, □: Viscosity).
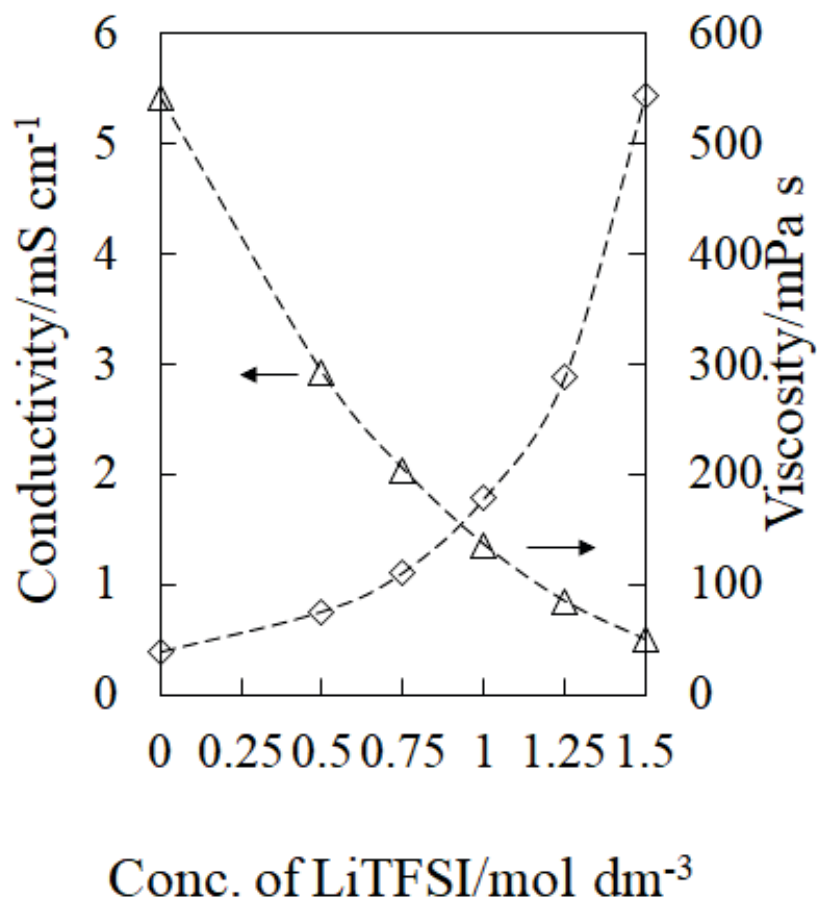
Figure 6-5. Concentration dependencies of conductivity and viscosity of the solutions of LiTFSI-IL at 25 °C (△: Conductivity, ◇: Viscosity).
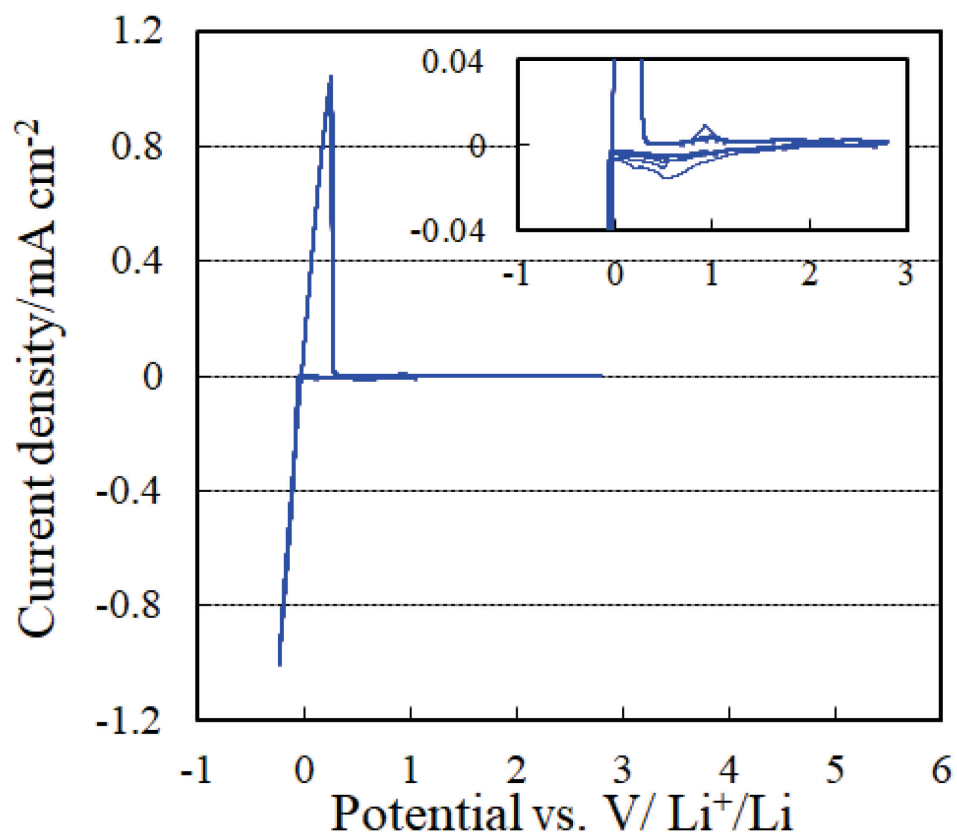
Figure 6-6. Cyclicvoltammogram of Li electrodeposition in 1.0 M LiTFSI-IL solution (W.E.: 5 mm×5 mm×0.5 mm Ni sheet, C.E. and R.E.: Li foil. Scan rate: 1 mV s^{-1}). The inset shows enlarged current density.
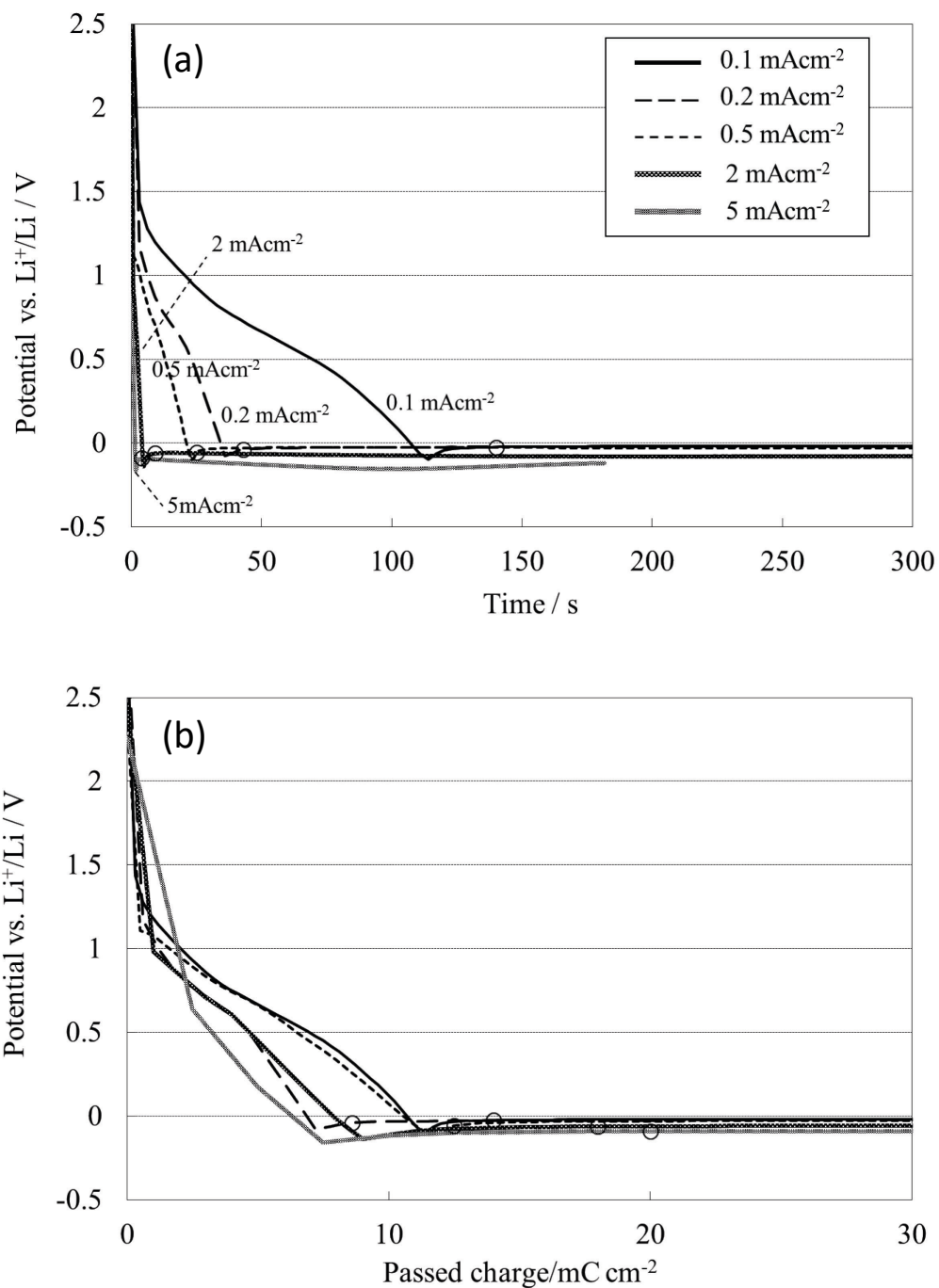
Figure 6-7. Chronopotentiometry after the starts of electrolysis depending on time (a) and coulomb quantity (b) in 1.0 M LiTFSI-IL at 25 °C.
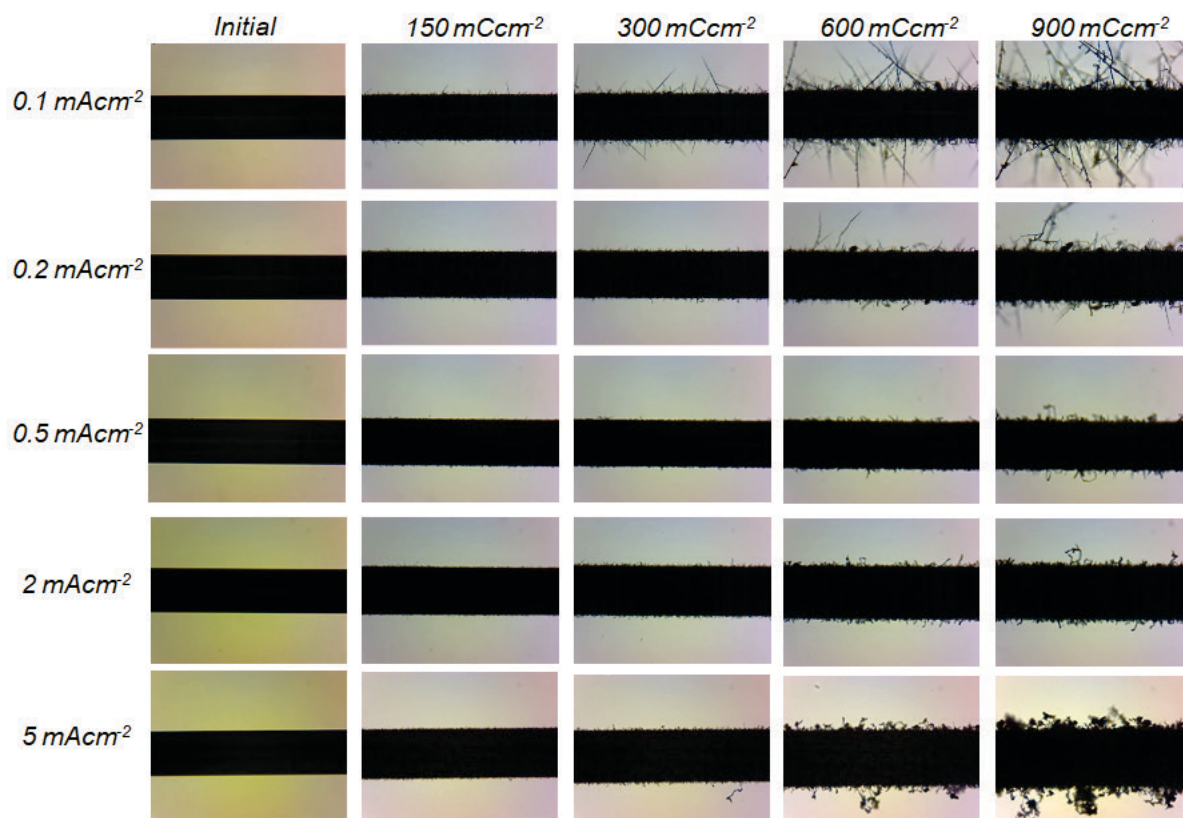
Figure 6-8. Time transients of the morphology of electrodeposited Li metal in ionic liquid at 0.1 mA cm^{-2}, 0.5 mA cm^{-2}, 0.5 mA cm^{-2}, 2.0 mA cm^{-2} and 5.0 mA cm^{-2} (LiTFSI concentration: 1.0 M, Temperature: 25 °C).
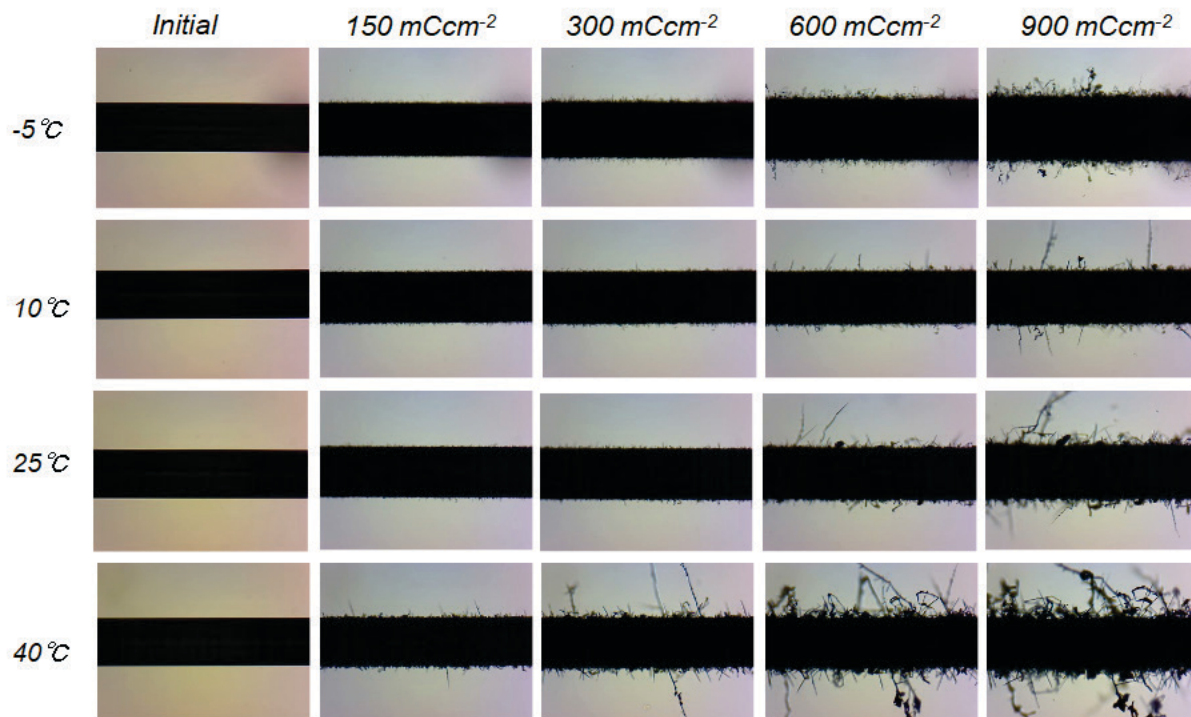
Figure 6-9. Time transients of the morphology of electrodeposited Li metal in ionic liquid solution at -5 °C, 10 °C, 25°C and 40 °C (Current density: 0.2 mA cm^{-2}, LiTFSI concentration: 1.0 M).
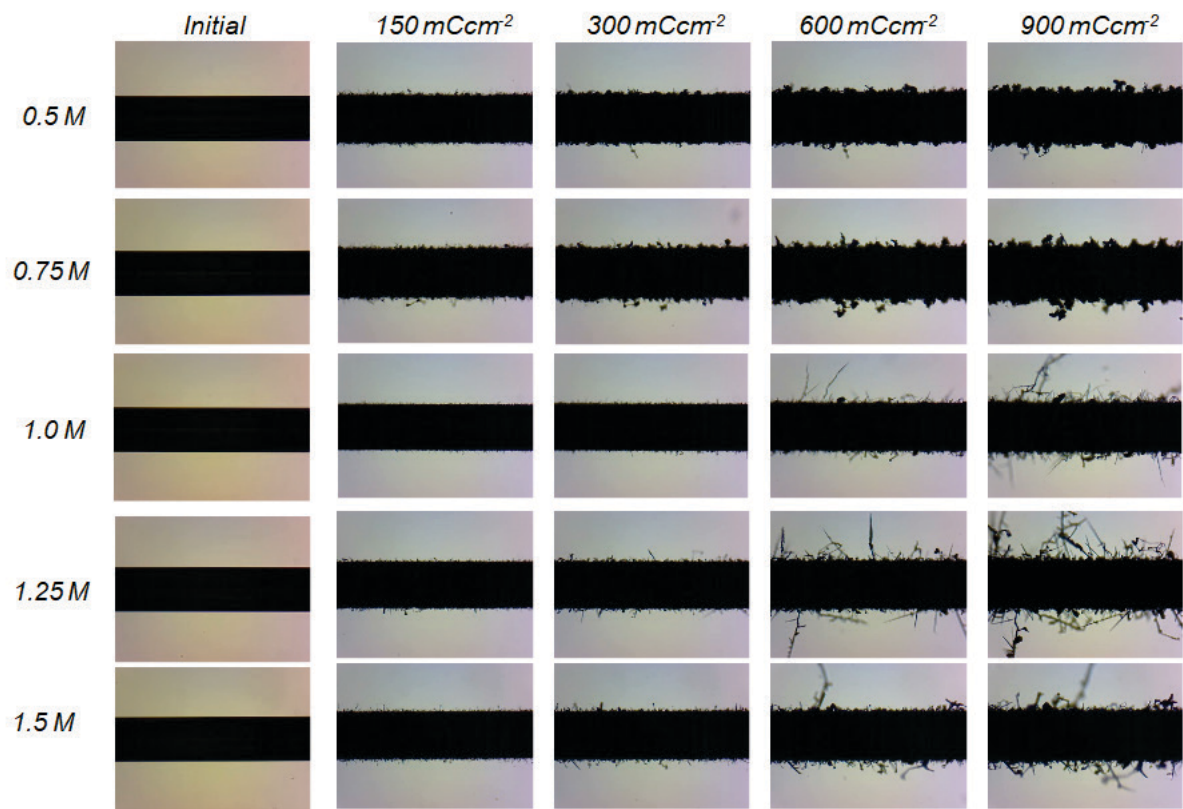
Figure 6-10. Time transients of the morphology of electrodeposited Li metal in ionic liquid solutions with LiTFSI concentrations of 0.5 M, 0.75 M, 1.0 M, 1.25 M and 1.5 M (Current density: 0.2 mA cm^{-2}, Temperature: 25 °C).
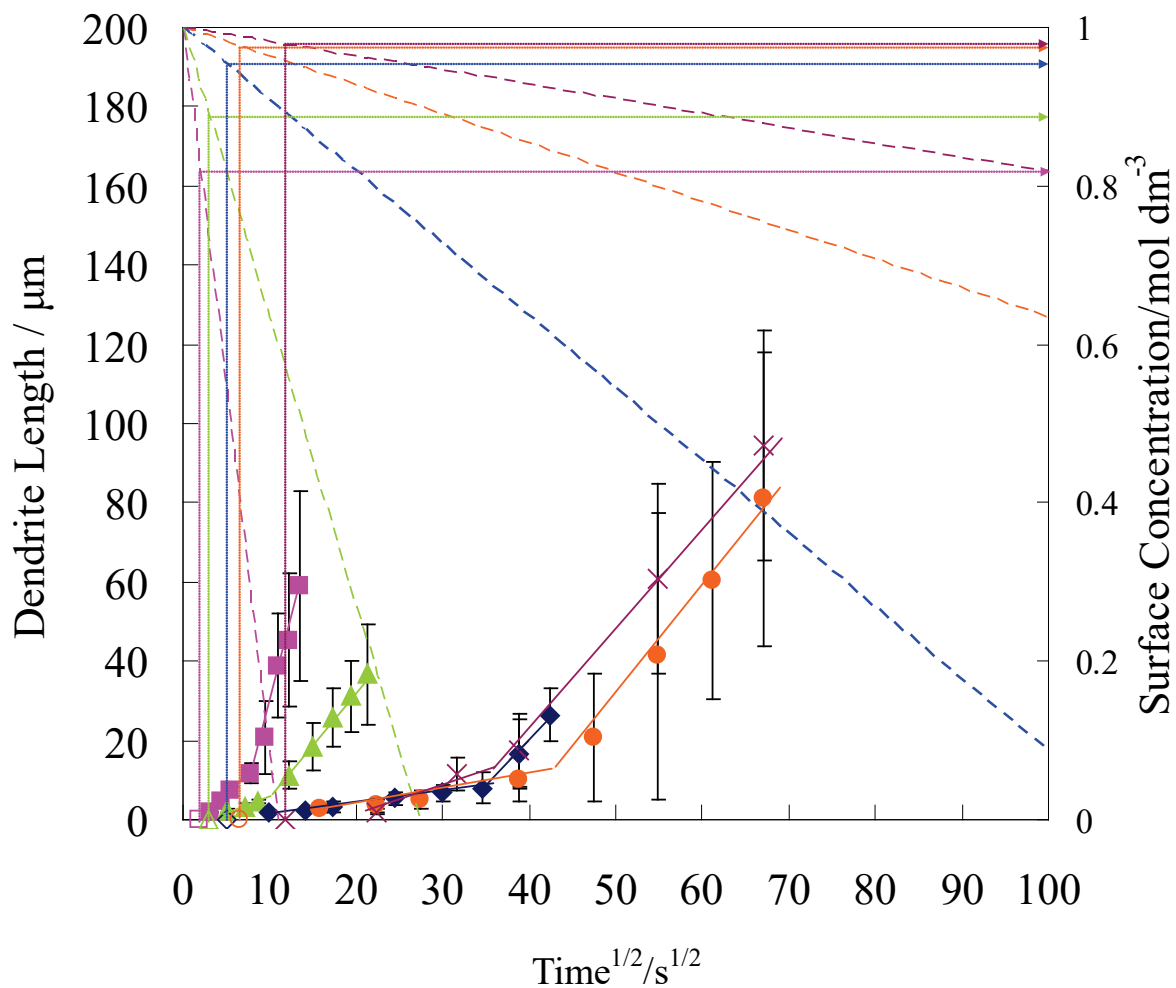
Figure 6-11. Time transient of Li dendrite length and calculated Li⁺ surface concentration with the square root of time. Solid markers represent the mean dendrite length at 5 mA cm⁻²(■), 2 mA cm⁻²(▲), 0.5 mA cm⁻²(◆) 0.2 mA cm⁻²(●) and 0.1 mA cm⁻²(×), respectively.
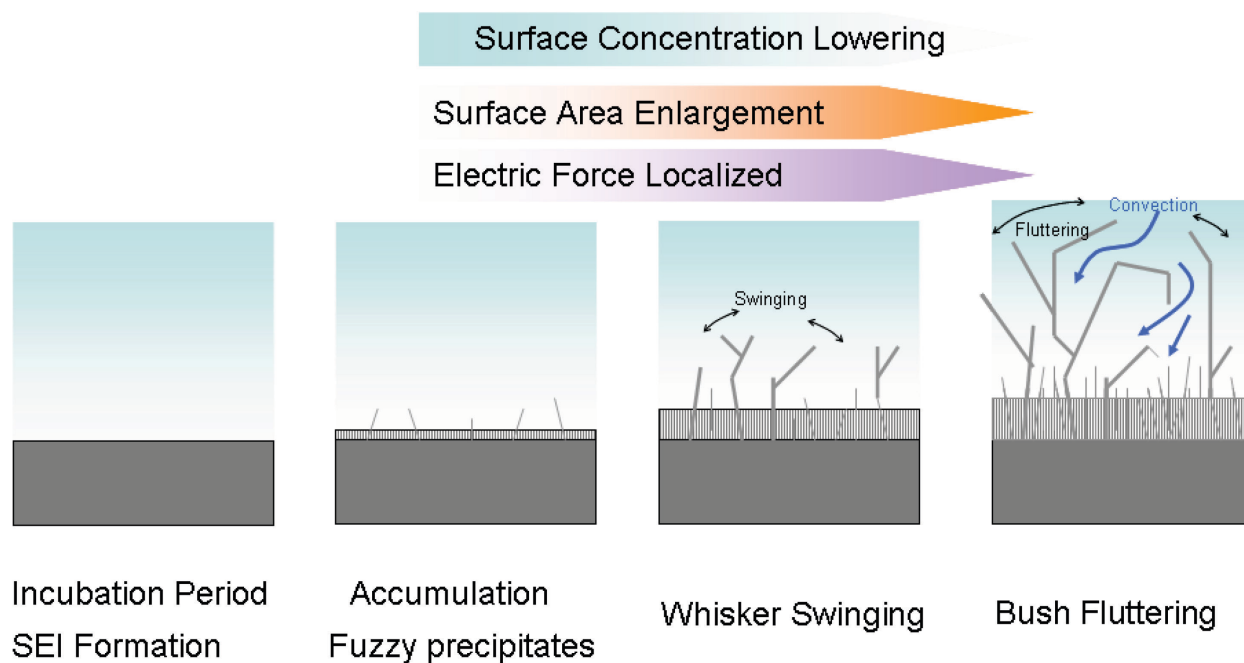
Figure 6-12. Schematic diagram of the sequence of dendrite growth.
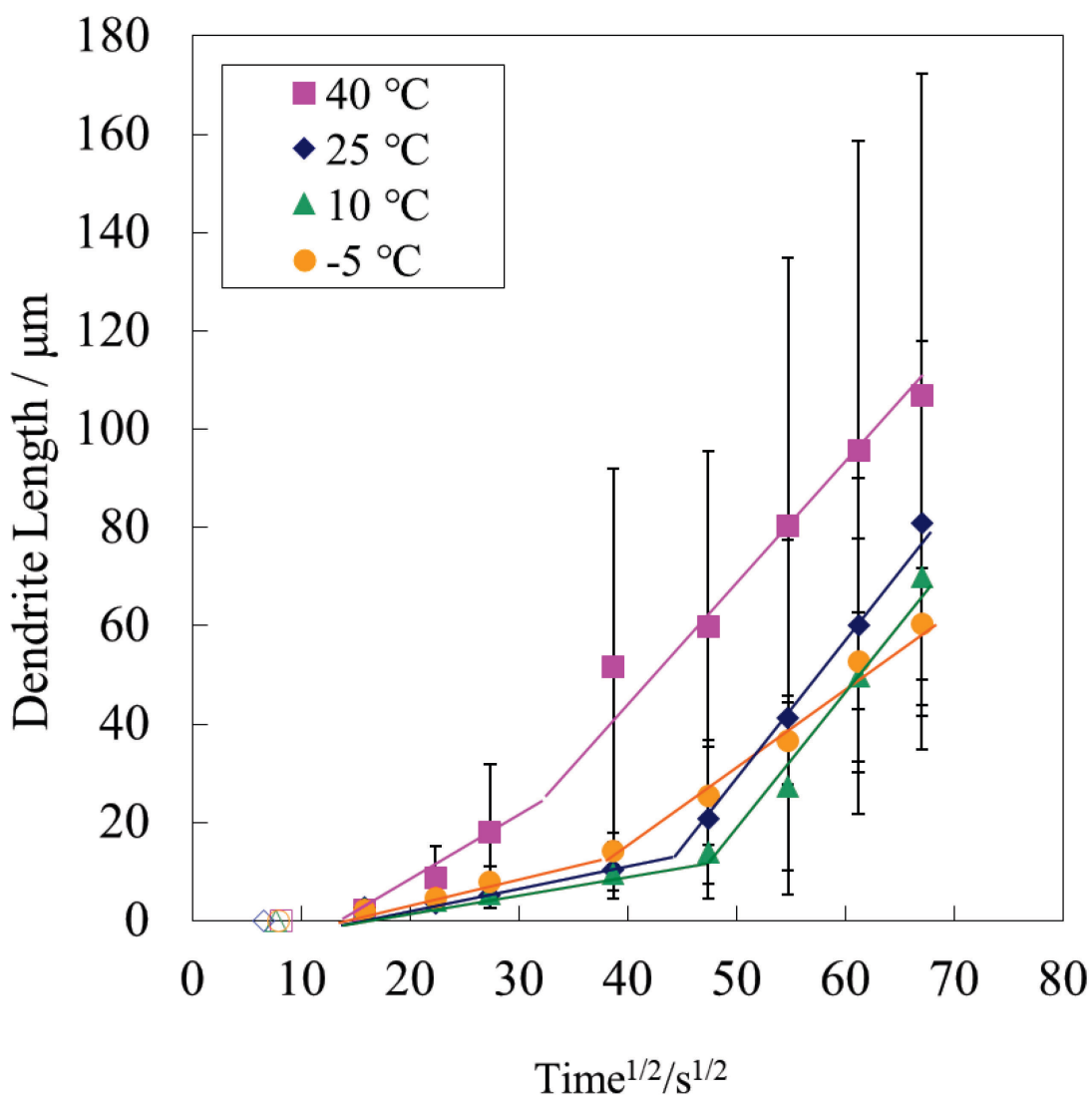
Figure 6-13. Temperature dependencies of dendrite growth rate of Li metal electrodeposited on Ni wire in 1.0 M LiTFSI-IL at 0.2 mA cm^{-2}.
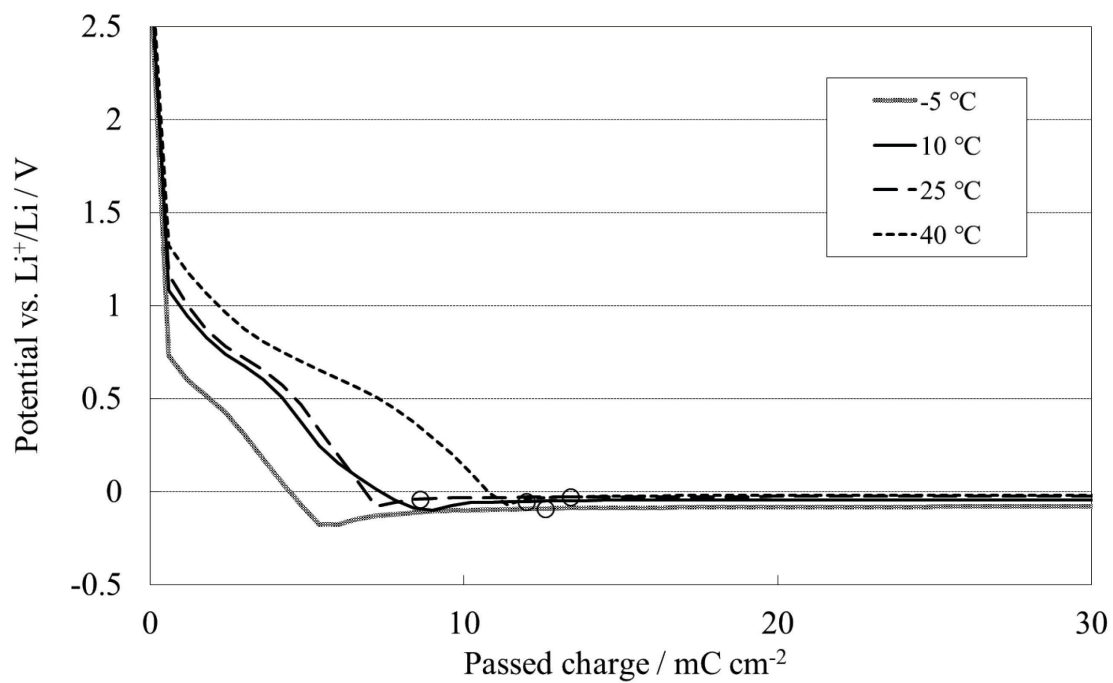
Figure 6-14. Temperature dependences of the electrode potential variations after electrolysis in 1.0 M LiTFSI-IL at 0.2 mA cm^{-2}.
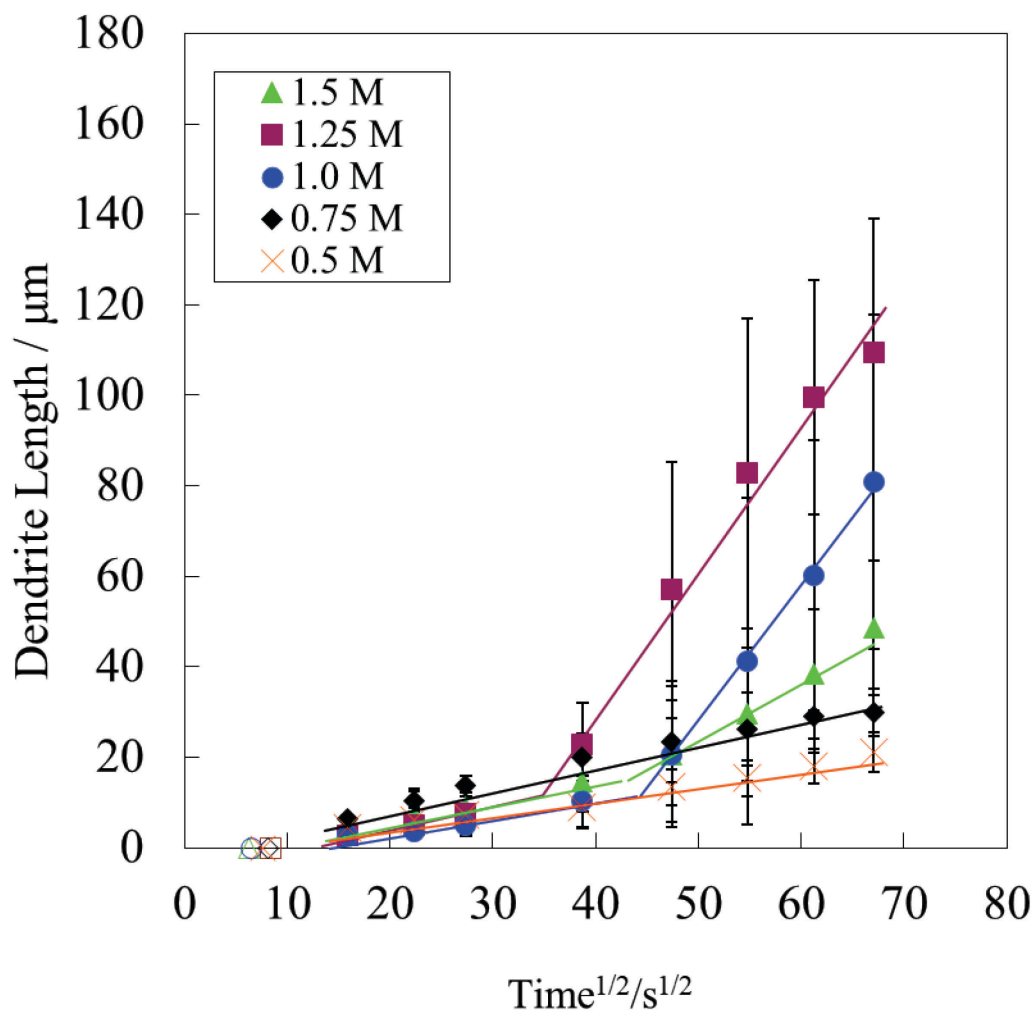
Figure 6-15. Concentration dependences of dendrite growth rate of Li metal electrodeposited on Ni wire at 0.2 mA cm^{-2} at 25 °C.
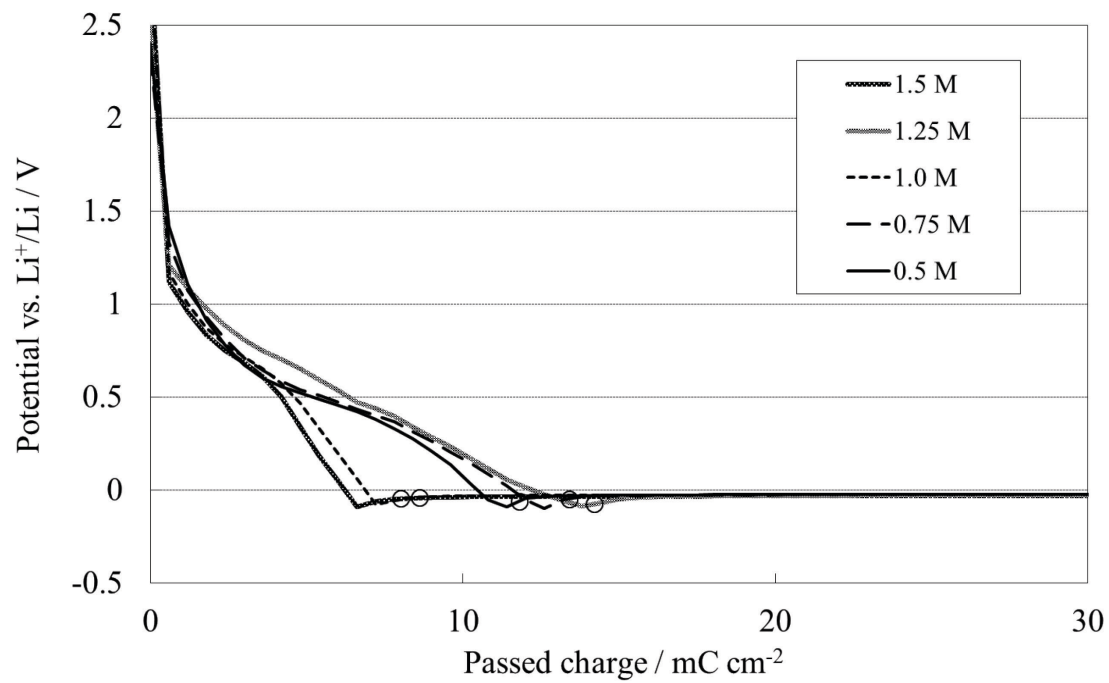
Figure 6-16. Concentration dependences of variations of the electrode potential after the starts of electrolysis at 0.2 mA cm^{-2} at 25 ℃.

Appendix

Li$^+$ ionic mass transfer rate must be considered to explain the dendrite growth phenomenon. For simplicity, the natural convection accompanied with the electrodeposition is not taken into consideration. Assuming one-dimensional transient diffusion equation with a boundary condition of geometrically flat electrode surface, the time transient of surface concentration can be described as below;

$$c_s = c_0 - \frac{2i(1-t^*)}{zF\sqrt{\pi D}}\sqrt{t} \qquad (6\text{-}A1)$$

c_s is electrode surface concentration of Li$^+$ ion, c_0 is bulk concentration, i is current density, t^* is transference number, z is valence number, F is faraday constant, and D is diffusion coefficient. The diffusion coefficient and transference number are assumed to be independent of Li$^+$ concentration. The dashed lines in Figure 6-11 represent this simplified calculation results. For example, Li$^+$ concentration depletes about 100, 680, 12000 s at 5, 2 and 0.5 mA cm^{-2}, respectively. Steeper concentration gradient is formed in the vicinity of cathode surface with increasing in current density.

Chapter 7

Development of Non-flammable Electrolyte for Lithium Metal Batteries using Phosphoric Ester with LiPO$_2$F$_2$ Salt

7.1 Introduction

From the viewpoint of energy density, lithium metal-based batteries, such as Li-S battery and Li-air battery, are the most attractive candidates for next-generation batteries. However, as the energy density of batteries increases and as batteries become larger, accidental events could lead to catastrophe. Therefore, safeguards for lithium metal batteries are imperative.

Various attempts are under way to increase their safety. One approach is to convert all flammable conventional carbonate ester electrolytes to all solid-state electrolytes [1-2]. However, there are problems such as how to stably and uniformly establish the electrode reaction interface, which has been formed at the solid-liquid interface, over a large area by solid-solid contact [1], and the problem of H$_2$S generation due to reaction with moisture [3]. Research is being conducted intensively to solve these problems toward the commercialization of all-solid-state batteries.

On the other hand, the simplest and clearest approach toward safety is to replace the flammable electrolyte with a non-flammable electrolyte, and there has also been vigorous research into flame-retardant electrolytes or additives from this strategy [4]. For example, ionic liquids and organophosphorus compounds are known. Since characteristics of ionic liquids can be modified by their combination of cations and anions, the applicability of various types of ionic liquids to lithium metal batteries has been studied [5]. However, ionic liquids still have challenges such as their high viscosity and cost. Various organophosphorus compounds have also been proposed,

including phosphoric esters [6-7], phosphoric amides [8], phosphites [9] and phosphazenes [10]. Among them, phosphoric esters such as trimethyl phosphate (TMP) and triethyl phosphate (TEP) well known as flame retardant additives for plastics are suitable for electrolyte solvents due to their high dielectric constant, high salts' solubility, relatively low viscosity and wide liquid temperature range, so there are many examples of studies using phosphoric esters.

The problem with phosphoric ester electrolytes is essentially the low reductive electrochemical stability and resultant low reversibility of Li deposition and dissolution [11-12]. Normally, favorable SEI formation is unlikely to be formed in phosphoric ester electrolytes. It has been reported that the additives (FEC, $LiNO_3$) [13-14] or concentrated electrolyte [15-16] improves the reversibility in phosphoric ester electrolytes. The author has previously investigated the effect of current density on the morphological variation of electrodeposited Li. Here, the author has confirmed that the SEI formed prior to Li deposition also exhibited different behavior depending on the current density and deduced the difference in defect density of SEI as one of the factors responsible for Li deposits' morphology [17]. Although it can be said that the key is the formation of SEI suitable for phosphoric ester electrolyte and the control of Li deposition morphology, there are few studies dealing with effects of current density on morphological change of Li electrodeposited in phosphoric ester electrolytes in detail.

It is well known that anions are involved in SEI formation. The author found that lithium difluorophosphate is relatively well soluble in phosphoric esters while it has only 1% solubility in ordinary carbonate ester solvents. This study presents the battery characteristics using the electrolytes based on $LiPO_2F_2$/TEP with/without ethylene carbonate (EC) as film-forming agent and $LiPF_6$ to supplement the conductivity as well as the results of a survey on the flame retardancy of the electrolyte.

7.2   Experimental

LiPF$_6$, LiTFSI (lithium bis(trifluoromethanesufonyl)imide) and LiPO$_2$F$_2$ were obtained from Stellachemifa corp. as test samples. LiTFSI was dried at 150 °C for 24 h under nitrogen flow before use. The electrolyte solvents of TMP and TEP were purchased from Tokyo Chemical Industry Co., Ltd. and battery-grade EC (ethylene carbonate) and PC (propylene carbonate) were purchased from Kishida Chemical. TMP and TEP were dehydrated by molecular sieves (ZMS LiX). EC and PC were used as received. The electrolyte solutions were prepared using 10 mL measuring flasks in an argon glove box (Takasugi Seisakusho; G65MVAV; dew point < -90 °C). The moisture value of each electrolyte was confirmed to be less than 30 ppm by Karl Fischer titrator (AQ-7, Hiranuma Sangyo Co., Ltd.). Conductivity was measured by using a conductivity meter (TOA-DKK corporation: CM-42X).

Electrospray ionization mass spectrometry (ESI-MS) measurements of the electrolyte were performed using LC-MS (Waters corporation; Acquity SQD2 LC-MS with H-Class UPLC). Cationic clusters and anionic clusters were analyzed in positive and negative modes, respectively. Each electrolyte solution was diluted 1/1000 times with acetonitrile. The cone voltage was set to 70 V and the desolvation temperature to 250 ℃.

Cyclic voltammetry (CV), linear sweep voltammetry (LSV) and chronopotentiometry (CP) were performed in an argon glove box using a three-electrode cell. As for CV and LSV, the working electrode was a 5 mm square Ni sheet with a thickness of 80 μm (Nilaco Corp.) and the counter and reference electrodes were lithium foil with a thickness of 200 μm (Honjo Metal Co., Ltd.). For CP experiments, the working electrode was Ni wire (Nilaco Corp.) 500 μm in diameter and lithium foil was used for the counter and reference electrode. Pretreatment of Ni electrodes was performed in the same way as described in the previous report [17]. Electrochemical measurements were performed using HZ7000 (Hokuto Denko).

After electrolysis, the electrodes were washed with dimethyl carbonate (DMC) and vacuum-dried in the pass box of the argon glove box, then analyzed by XPS (VersaProbe III; ULVAC PHI,

Inc.) and observed by SEM (JSM-7800F; JEOL). Transfer vessel was used for XPS analysis and SEM observation to prevent contact with atmosphere.

Cell characteristics were evaluated using CR-2032 type coin cells. NCM electrode sheet (design capacity; 1.5 mAh cm^{-2}, manufactured by Piotrek Co., Ltd.) was punched to φ11.30 mm (ca. 1 cm^2) for the positive electrode. The punched positive electrode sheets were placed in a transfer vessel and vacuum-dried at 100 °C for 12 h. For the negative electrode, a lithium foil (0.2 mm thick, Honjo Metal Co., Ltd.) punched to φ11 mm in an argon glove box was used. For the separator, a glass filter (Advantech Toyo, GC-50) with a thickness of 190 μm was punched to ⌀19 mm and vacuum-dried at 100 °C for 8 h. 100 μL of electrolyte was used for each coin cell. The parts of coin cell were purchased from Hosen corp. Charging and discharging tests were conducted using a BTS2004W (NAGANO Co., Ltd.). Both charging and discharging were performed at the same current density and the terminal voltages were 4300 mV and 3000 mV, respectively. Charging and discharging were performed up to 100 cycles in total.

Flame retardancy tests were conducted as follows. The electrolyte was soaked into a glass filter (Advantech Toyo, GC-50) pinched with metal tweezers and exposed to an open flame with an ignition rod for 1 s and the combustibility was captured by a video camera.

7.3   Results and Discussion

7.3.1   Electrolyte characteristics

Fig. 7-1 shows the concentration dependence of conductivity at 25 °C for the electrolytes consisted of LiPF$_6$, LiTFSI and LiPO$_2$F$_2$ as the salt and TEP or TMP as the solvent. LiPO$_2$F$_2$ is known as an additive for carbonate ester electrolytes [18-20], but it is hard to dissolve in carbonate ester solvents even at about 1%. Solubility of LiPO$_2$F$_2$ in phosphoric ester solvents were examined and found to be much easier to dissolve than in carbonate ester solvents. It was confirmed to dissolve up to about 2 M, although it became less soluble at higher concentrations. However, the

conductivity of $LiPO_2F_2$ electrolyte was about 0.5 mS cm^{-1} at 1 M, which was considerably lower than that of $LiPF_6$ and LiTFSI. This suggests that the dissolution phenomenon of $LiPO_2F_2$ is not due to salt dissociation, but may be related to another mechanism.

The results of LC-MS analysis of three electrolytes, 1 M $LiPF_6$/TEP, 1 M LiTFSI/TEP and 1 M $LiPO_2F_2$/TEP, are shown in Fig. 7-2. In the electrolyte with $LiPF_6$ and LiTFSI dissolved in TEP, clusters with one to three TEP molecules coordinating to lithium ions were mainly detected in the positive mode, while PF_6^- or TFSI$^-$ was detected as the main component in the negative mode. In addition, trace amounts of associated $LiPF_6$ or LiTFSI coordinated by their respective anions were also detected.

In the case of $LiPO_2F_2$, Li$^+$ solvated by one to three TEP molecules in the positive mode and the PO_2F_2 anion in the negative mode were detected similar to $LiPF_6$ and LiTFSI. However, difference from the case of $LiPF_6$ and LiTFSI is the prominence of clusters in which Li$^+$ or $PO_2F_2^-$ is coordinating to the associated $LiPO_2F_2$. This may be related to the fact that $LiPO_2F_2$ dissolves in TEP but has considerably lower conductivity than $LiPF_6$ or LiTFSI as indicated in Fig. 7-1. This means that the dissolution phenomenon of $LiPO_2F_2$ into TEP is thought to be caused not only by salt dissociation due to solvation of TEP molecules with Li$^+$ but also by the mechanism of cluster ion formation by coordination of dissociated Li$^+$ or $PO_2F_2^-$ to associated $LiPO_2F_2$. Therefore, such cluster ions are assumed to be responsible for the low conductivity of the $LiPO_2F_2$/TEP electrolyte.

Next, CV measurements were performed in order to investigate Li deposition and dissolution behavior in TEP electrolyte with $LiPF_6$, LiTFSI and $LiPO_2F_2$ and the results are shown in Fig. 7-3. Although TEP electrolytes using $LiPF_6$ or LiTFSI had good conductivity, the reversibility of lithium deposition and dissolution was poor. On the other hand, the use of $LiPO_2F_2$ electrolyte with poor conductivity showed an improvement in the reversibility. Although the applicability of phosphoric ester electrolyte to graphite or lithium metal negative electrode has been studied extensively, unfavorable reduction stability and lack of SEI formation capability of phosphoric ester solvents have been cited as problems [11-12]. It was suggested that lithium metal negative

electrode performance could be improved by incorporating $LiPO_2F_2$ into phosphoric ester electrolytes.

7.3.2 Li deposition behavior in TEP electrolytes

The LSVs at a scan rate of 1 mV s^{-1} on a Ni foil electrode (0.5 mm × 0.5 mm × 0.1 mm) in three different electrolytes of 1 M $LiPF_6$/TEP, 1 M LiTFSI/TEP and 1 M $LiPO_2F_2$/TEP are shown in Fig. 7-4 (a-I), (b-I) and (c- I), respectively. The potential was swept from OCV to 2 V, 1 V, 0 V and Li deposition potential. The results of XPS analysis after electrolysis are shown in Fig. 7-4 (a-II), (b-II) and (c-II).

In the case of $LiPF_6$ and LiTFSI, a weak current begins to pass at around 2.6 V vs. Li$^+$/Li, and then several peaks can be observed while sweeping the potential. The current gradually amplifies. On the other hand, in the case of $LiPO_2F_2$, a weak current begins to appear almost immediately after sweeping the potential from OCV to the negative direction and a distinctive large peak is observed at around 2 V. The current appears to be suppressed after the first large peak.

The XPS results show quite differences in the chemical species formed on the electrode surface depending on the salts. In the case of $LiPF_6$, the formation of LiF can be recognized by sweeping from OCV to 2 V and then LiF peak becomes more distinct as the potential sweeps down to lower direction. In (a-I), the current begins to increase rapidly when it reaches a potential lower than 0 V. Although the current is expected to be derived from Li deposition, it is not possible to clearly identify the signal attributed to the Li1s in (a-II). On the other hand, the presence of phosphate can be confirmed in P2p at 0 V or lower potential. Considering the poor reversibility of CV in Fig. 7-3, it can be inferred that the decomposition of phosphoric ester is not sufficiently suppressed.

In the case of LiTFSI, the current during sweeping up to 2 V is much lower than that of $LiPF_6$. In F1s, a weak peak originating from the CF_3 group and LiF can be recognized. These peaks become pronounced by sweeping down to 1 V and sulfate bonds can be ascribed from O1s and

S2p, implying that the TFSI anion is being decomposed. Furthermore, the sulfide bonding peak also can be seen in the sweep up to 0 V. At potentials lower than 0 V, the presence of Li can be clearly seen in Li1s, which was not seen in the case of $LiPF_6$. This is reflected on the improved reversibility in the LiTFSI electrolyte compared to that in the $LiPF_6$ electrolyte as shown in Fig. 7-3.

For $LiPO_2F_2$, a large peak current appears at 2 V. Presence of fluorophosphate groups along with LiF is distinctive for $LiPO_2F_2$ compared to the cases of $LiPF_6$ and LiTFSI. LiF formation becomes clearer and the presence of phosphate becomes more evident as the potential sweeps to 1 V and then to 0 V. It is presumed that the decomposition of PO_2F_2 anion is followed by the decomposition of the phosphoric ester. The presence of Li can be clearly confirmed when the potential is swept to lower than 0 V. Considering the improved reversibility of Li deposition and dissolution in Fig. 7-3, $LiPO_2F_2$ is expected to form favorable SEI for Li deposition accompanying with the decomposition of the phosphoric ester.

To investigate the origin of the low reversibility in $LiPF_6$/TEP electrolyte and LiTFSI/TEP electrolyte shown in the left figure of Fig. 7-3, chronopotentiometry (CP) was performed up to 1800 mC cm^{-2} at different current densities. Fig. 7-5 shows its coulomb efficiency for Li deposition and dissolution. Results in PC electrolyte are also shown as an example for a common carbonate electrolyte. Since EC is solid at room temperature, PC was chosen. The TEP electrolyte, whether the salt is $LiPF_6$ or LiTFSI, shows a high coulomb efficiency around 95% at low current densities of 0.04 to 0.2 mA cm^{-2}. However, the coulomb efficiency drops sharply when the applied current density is 0.4-0.5 mA cm^{-2}. On the other hand, PC-based electrolytes show the opposite trend, i.e., the lower the current density, the lower the coulomb efficiency.

The chronopotentiograms for Li deposition and dissolution in 1M LiTFSI/TEP at 0.4 mA cm^{-2} up to 1800 mC cm^{-2} are shown in Fig. 7-6(a). SEM images of the electrode surface at 100 mC cm^{-2}, 1000 mC cm^{-2}, 1800 mC cm^{-2} and after dissolution are shown in Fig. 7-6(b). At 100 mC cm^{-2}, deposits with a large aspect ratio of several tens to 100 nm in diameter and several μm to 10 μm in length are formed along with the electrode surface. After the electrolysis up to 1000 mC

cm^{-2}, it can be seen that this large aspect ratio deposit has further developed and intertwined fibrous deposits have begun to cover the electrode surface. At 1800 mC cm^{-2}, the formation of numerous granular deposits of 1 to 2 μm in diameter can be identified among the fibrous deposits. The SEM image after dissolution indicates that the granular deposits appear to shrink, suggesting the dissolution of the granular lithium. However, most of the fibrous deposits remain. Immediately after the start of dissolution, the fibrous deposits begin to dissolve due to many electrical contacts in the fibrous deposits' network. Since each deposit is very thin, it is easy to imagine that the electrical contact with the electrode substrate is easily lost at the root.

Fig. 7-7 also shows the results for SEM observation of Li deposits' morphology in 1M LiPF$_6$/TEP and 1M LiPO$_2$F$_2$/TEP at 0.4 mA cm^{-2}. As shown in Fig. 7-7(a), deposits with very large aspect ratios are also observed in 1M LiPF$_6$/TEP, the same as in the case of LiTFSI. Fibrous deposits did not appear under the very low current density, and perhaps because of this, the coulomb efficiency was rather good. On the other hand, in 1M LiPO$_2$F$_2$/TEP, the aspect looks slightly different from that of LiTFSI or LiPF$_6$ as shown in Fig. 7-7(b). In the case of LiPO$_2$F$_2$, dendrites appeared but fibrous deposits have not developed. Besides, the deposits seem to have a rigid structure compared to LiTFSI or LiPF$_6$. One of the reasons for the poor reversibility of lithium deposition and dissolution in the phosphoric ester electrolyte may be the fibrous morphology of Li that emerges above a certain current density when LiTFSI or LiPF$_6$ is used as a salt.

As an approach to improve the reversibility in the phosphoric ester electrolyte, the author attempted to combine LiPF$_6$ and LiPO$_2$F$_2$ as the salts and TEP and EC as the solvents, based on the results as demonstrated in Fig. 7-5 and in Fig. 7-7. From the viewpoint of SEI formation capability, EC was selected as the carbonate solvent instead of PC [21]. The results of the coulomb efficiency for LiPF$_6$, LiPO$_2$F$_2$ and a mixture of LiPF$_6$ and LiPO$_2$F$_2$ in the electrolytes with different ratios of TEP and EC are shown in Fig. 7-8. When EC:TEP=1:1 (v/v), they all show comparable coulomb efficiencies, but as the ratio of EC decreases, the coulomb efficiency drops rapidly for LiPF$_6$ only. When LiPO$_2$F$_2$ itself or a mixture of LiPO$_2$F$_2$ and LiPF$_6$ is used as the salts, the

coulomb efficiency enhances, especially in the range of high phosphoric ester ratios, indicating that the addition of $LiPO_2F_2$ suppresses the degradation caused by $LiPF_6$.

7.3.3 Coin cell evaluation

Next, coin cells were fabricated with only a Cu current collector as the negative electrode and Li foil as the positive electrode. Nine different electrolytes were used in the coin cell: $LiPF_6$, $LiPO_2F_2$ and $LiPF_6+LiPO_2F_2$ as salts and three different solvents with different ratios of EC and TEP (1:9, 2:8 and 3:7). The charge-discharge characteristics of the coin cells are shown in Fig. 7-9 when deposited lithium is equivalent to 3600 mC cm^{-2}(1 mAh cm^{-2}) at a current density of 0.5 mA cm^{-2}. When $LiPF_6$ is singly used as salt, regardless of the ratio of EC and TEP, the overvoltage during charging and discharging increases with cycles, resulting in capacity degradation. The degradation is more pronounced the lower the EC ratio. On the other hand, when $LiPO_2F_2$ is used singly or mixed with $LiPF_6$, the overvoltage during charging/discharging remains stably lower and there can be seen less degradation in capacity than the case of single use of $LiPF_6$. Fig. 7-10 (a) and (b) show the results of the cycle test at 0.33 C and 1.0 C of coin cells consisting of lithium foil as negative electrode and NCM as positive electrode, respectively, with the three electrolytes of EC:TEP=2:8 (v/v) that showed good characteristics in Fig. 7-9 (b). While significant degradation is observed in the case of $LiPF_6$ alone, the mixture of $LiPO_2F_2$ shows improvement in capacity retention and coulomb efficiency.

7.3.4 Flammability test of electrolyte

The flammability of electrolytes were evaluated by placing glass filters soaked with the electrolytes close to an open flame. A typical result of flammability test is shown in Fig. 7-10. It was confirmed that 0.5 M $LiPO_2F_2$+0.5 M $LiPF_6$/EC+TEP (2:8 v/v) did not ignite when in contact with flame, whereas the conventional electrolyte (1 M $LiPF_6$ / EC+DMC) burned violently. The phosphoric ester electrolyte containing $LiPO_2F_2$ in this study is expected to contribute greatly

toward improving the safety of next-generation batteries using lithium metal as the negative electrode.

7.4 Conclusions

$LiPO_2F_2$ was relatively easy to dissolve in triethyl phosphate up to about 2 M, but the conductivity was about 0.5 mS cm^{-2} at 1.0M, roughly 1/10 compared to the electrolyte using $LiPF_6$ at the same concentration. LC-MS analysis suggested that cluster ions formed by the coordination of Li^+ and $PO_2F_2^-$ generated by the solvation of TEP to the associated $LiPO_2F_2$, possibly responsible for the low ionic conductivity. Cyclic voltammetry of lithium deposition and dissolution in phosphoric ester electrolyte revealed that the coulomb efficiency in the TEP electrolyte with $LiPF_6$ or LiTFSI was very low and was greatly improved by using or mixing $LiPO_2F_2$ as the salt. According to SEM observations of the deposits' morphology at 100 mC cm^{-2}, the formation of fibrous deposits with a large aspect ratio of several tens to 100 nm in diameter and several μm to 10 μm in length were recognized in the case of LiTFSI or $LiPF_6$. In the case of $LiPO_2F_2$, dendrites appeared but fibrous deposits have not developed. In addition, the deposits seemed to have a rigid structure compared to LiTFSI or $LiPF_6$. One reason for the poor reversibility of lithium deposition and dissolution in the phosphoric ester electrolyte may be the fibrous morphology of Li emerging above a certain current density when LiTFSI or $LiPF_6$ is used as a salt. Significant improvements in charging and discharging characteristics were confirmed in coin cell tests by using the electrolytes based on $LiPO_2F_2$/TEP mixed with EC as film-forming agent and $LiPF_6$ to supplement the conductivity compared to $LiPF_6$/TEP. It was found that the presence of $LiPO_2F_2$ suppressed the degradation as seen when $LiPF_6$ is used alone as a salt. In the flammability test, the phosphoric ester electrolyte composition ($LiPO_2F_2$+$LiPF_6$/EC+TEP) found in this study exhibited excellent flame retardant properties. The knowledge obtained in this study on flame-retardant electrolytes using phosphoric ester could be very useful for battery systems aiming at the practical use of lithium metal negative electrodes.

References

[1] X. Fan, X. Ji, F. Han, J. Yue, J. Chen, L. Chen, T. Deng, J. Jiang and C.Wang, Fluorinated Solid Electrolyte Interphase Enables Highly Reversible Solid-State Li Metal Battery, Sci. Adv., 4, eaau9245 (2018).

[2] A. Varzi, R. Raccichini, S. Passerini and B. Scrosati, Challenges and Prospects of the Role of Solid Electrolytes in the Revitalization of Lithium Metal Batteries, J. Mater. Chem. A, 4, 17251−17259 (2016).

[3] H. Muramatsu, A. Hayashi, T. Ohtomo, S. Hama and M. Tatsumisago, Structural change of $Li_2S–P_2S_5$ sulfide solid electrolytes in the atmosphere, Solid State Ionics, 182, 116–119 (2011).

[4] J. Chen, A. Naveed, Y. Nuli, J. Yang, J. Wang, Designing an intrinsically safe organic electrolyte for rechargeable batteries, Energy Storage Materials, 31, 382–400 (2020).

[5] D. R. MacFarlane, N. Tachikawa, M. Forsyth, J. M. Pringle, P. C. Howlett, G. D. Elliott, J. H. Davis, M. Watanabe, P. Simon, C. A. Angell, Energy Applications of Ionic Liquids. Energy Environ. Sci., 7, 232−250 (2014).

[6] L. Jiang, C. Liang, H. Li, Q. Wang and J. Sun, Safer Triethyl-Phosphate-Based Electrolyte Enables Nonflammable and High-Temperature Endurance for a Lithium Ion Battery, ACS Appl. Energy Mater., 3, 1719−1729 (2020).

[7] P. Murmann, X. Mönnighoff, N. von Aspern, P. Janssen, N. Kalinovich, M. Shevchuk, O. Kazakova, G.-H. Röschenthaler, I. Cekic-Laskovic and M. Winter, J. Electrochem. Soc., 163, A751-A757 (2016).

[8] T. Shiga, C. Okuda, Y. Kato and H. Kondo, Highly Concentrated Electrolytes Containing a Phosphoric Acid Ester Amide with Self-Extinguishing Properties for Use in Lithium Batteries, J. Phys. Chem. C, 122, 9738−9745 (2018).

[9] X. L. Yao, S. Xie, C. H. Chen, Q. S. Wang, J. H. Sun, Y. L. Li and S. X. Lu, J. Power Sources, 144, 170–175 (2005).

[10] T. Dagger, C. Lurenbaum, F. M. Schappacher and M. Winter, J. Power Sources, 342, 266–272 (2017).

[11] S. R. Chen, J. M. Zheng, L. Yu, X. D. Ren, M. H. Engelhard, C. J. Niu, H. Lee, W. Xu, J. Xiao, J. Liu and J.-G. Zhang, High Efficiency Lithium Metal Batteries with Fire-Retardant Electrolytes. Joule, 2, 1548−1558 (2018).

[12] H. J. Yang, Q. Y. Li, C. Guo, A. Naveed, J. Yang, Y. Nuli, and J. L.Wang, Safer Lithium-Sulfur Battery Based on Nonflammable Electrolyte with Sulfur Composite Cathode. Chem. Commun., 54, 4132−4135 (2018).

[13] Y. Dong, N. Zhang, C. Li, Y. Zhang, M. Jia, Y. Wang, Y. Zhao, L. Jiao, F. Cheng and J. Xu, Fire-Retardant Phosphate-Based Electrolytes for High-Performance Lithium Metal Batteries, ACS Appl. Energy Mater., 2, 2708−2716 (2019).

[14] S. Matsuda and H. Asahina, Highly Efficient Oxygen Evolution Reaction in Rechargeable Lithium-Oxygen Batteries with Triethylphosphate-Based Electrolytes, J. Phys. Chem. C, 124, 25784−25789 (2020).

[15] J. H. Wang, Y. Yamada, K. Sodeyama, E. Watanabe, K. Takada, Y. Tateyama, A. Yamada, Fire-Extinguishing Organic Electrolytes for Safe Batteries. Nat. Energy, 3, 22−29 (2018).

[16] P. C. Shi, H. Zheng, X. Liang, Y. Sun, S. Cheng, C. H. Chen, H. F. Xiang, A Highly Concentrated Phosphate-Based Electrolyte for High-Safety Rechargeable Lithium Batteries. Chem. Commun., 54, 4453−4456 (2018).

[17] T. Nishida, Y. Fukunaka, T. Homma and T. Nohira, Galvanostatic Li Electrodeposition in LiTFSI-PC Electrolyte: Part I. Effects of Current Density in Initial Stage, J. Electrochem. Soc., 169, 100548 (2022).

[18] B. Yang, H. Zhang, L. Yu, W. Fan and D. Huang, Lithium difluorophosphate as an additive to improve the low temperature performance of $LiNi_{0.5}Co_{0.2}Mn_{0.3}O_2$/graphite cells, Electrochim. Acta, 221(10), 107-114 (2016).

[19] L. Ma, L. Ellis, S. L. Glazier, X. Ma, Q. Liu, J. Li and J. R. Dahn, $LiPO_2F_2$ as an Electrolyte Additive in $Li[Ni_{0.5}Mn_{0.3}Co_{0.2}]O_2$/Graphite Pouch Cells, J. Electrochem. Soc., 165, A891 (2018).

[20] A. C. Martinez, S. Rigaud, S. Grugeon, P. Tran-Van, M. Armand, D. Cailleu, S. Pilard and S. Laruelle, Chemical reactivity of lithium difluorophosphate as electrolyte additive in LiNi$_{0.6}$Co$_{0.2}$Mn$_{0.2}$O$_2$/graphite cells, Electrochim. Acta, 426(10), 140765 (2022).

[21] Q. Yang, N. Hu, Y. Dai and Y. Wu, Mechanisms of EC and PC solvated Li$^+$ in Li-ion battery electrolytes, Chemistry Bulletin, 77(8),795-803 (2014).
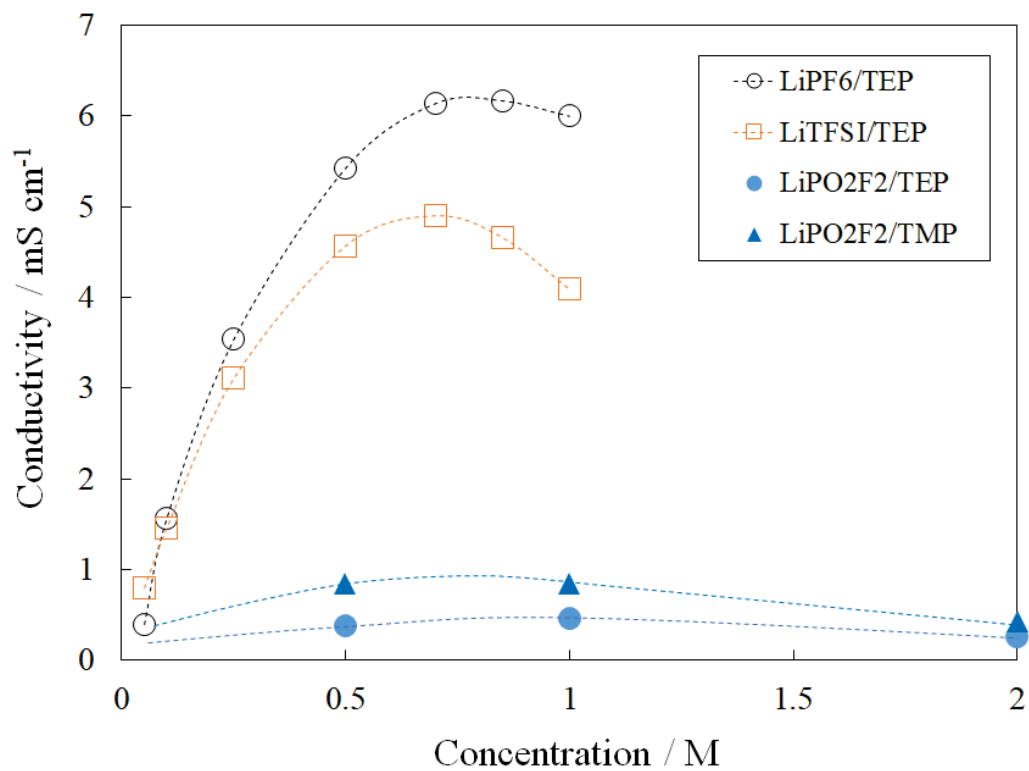
Figure 7-1. Concentration dependencies of conductivity for the solutions of LiPF$_6$, LiTFSI and LiPO$_2$F$_2$ in phosphoric ester (TEP or TMP) at 25 ℃.
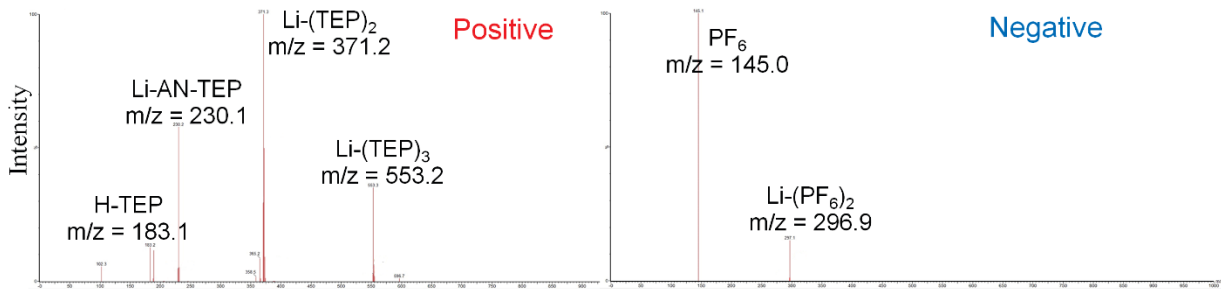
(a) 1M LiPF$_6$ in TEP

(b) 1M LiTFSI in TEP
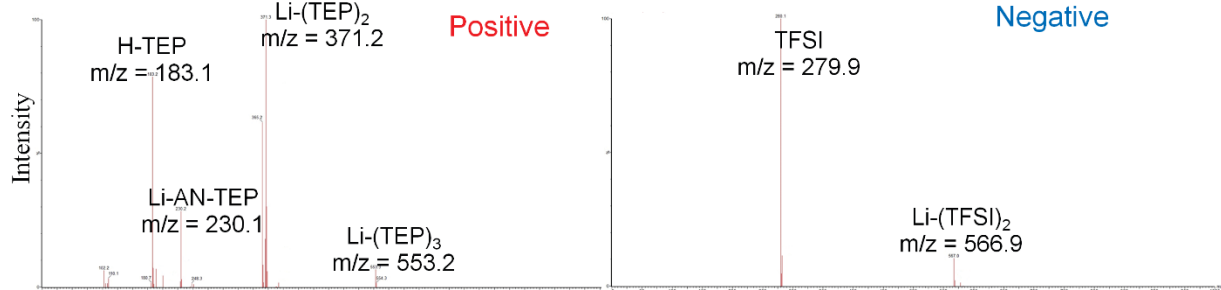
(c) 1M LiPO$_2$F$_2$ in TEP
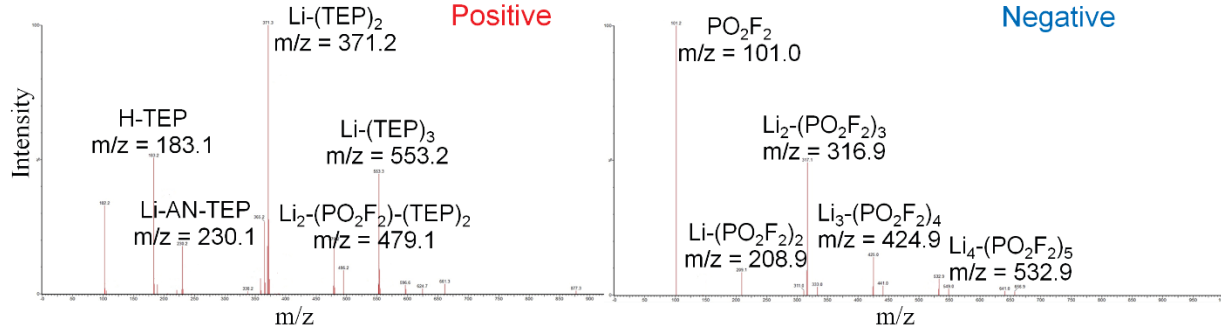
Figure 7-2. ESI-MS spectra of positive ion mode (left side) and negative ion mode (right side) for (a) 1 M LiPF$_6$/TEP, (b) 1 M LiTFSI/TEP and (c) 1 M LiPO$_2$F$_2$/TEP.
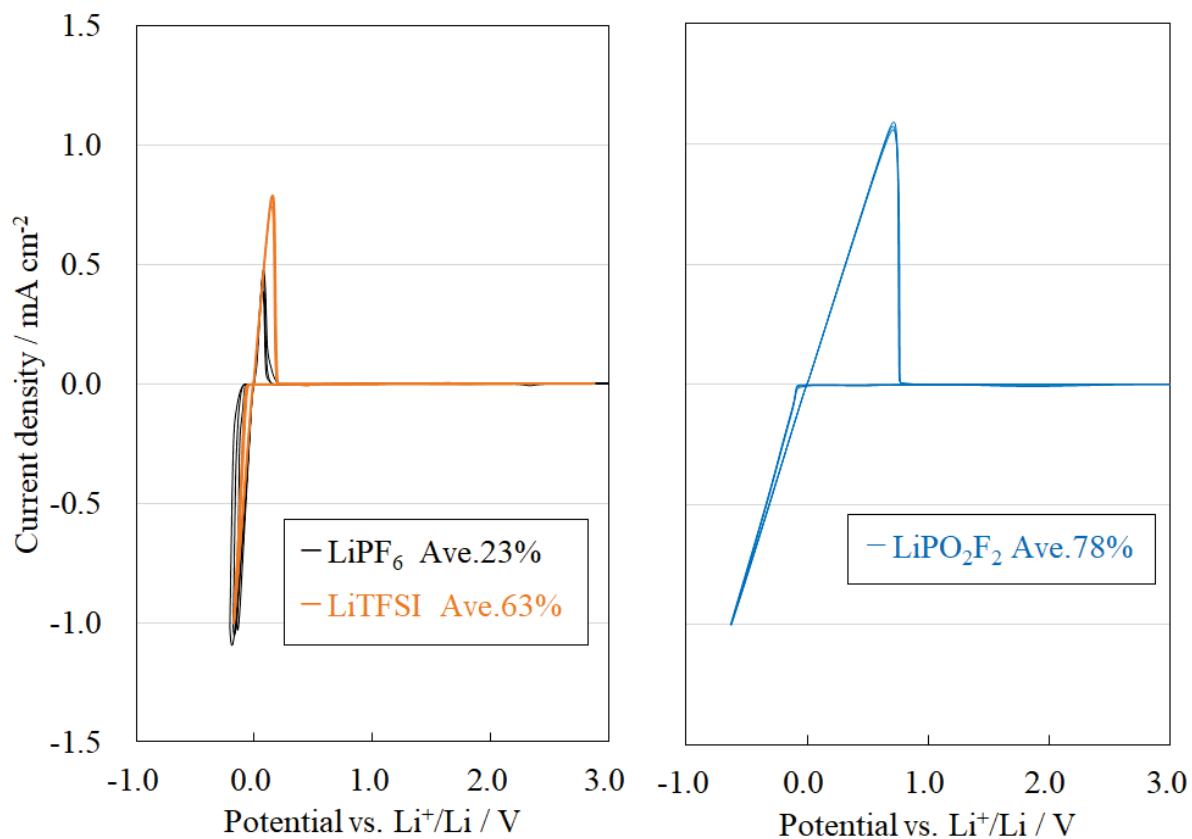
Figure 7-3. Cyclic voltammograms of Li electrodeposition in 1.0 M LiPF$_6$/TEP and 1.0 M LiTFSI/TEP (left side), and in 1.0 M LiPO$_2$F$_2$/TEP (right side).

(W.E.: 5 mm×5 mm×0.1 mm Ni sheet, C.E. and R.E.: Li foil. Scan rate: 1 mV s^{-1}.)
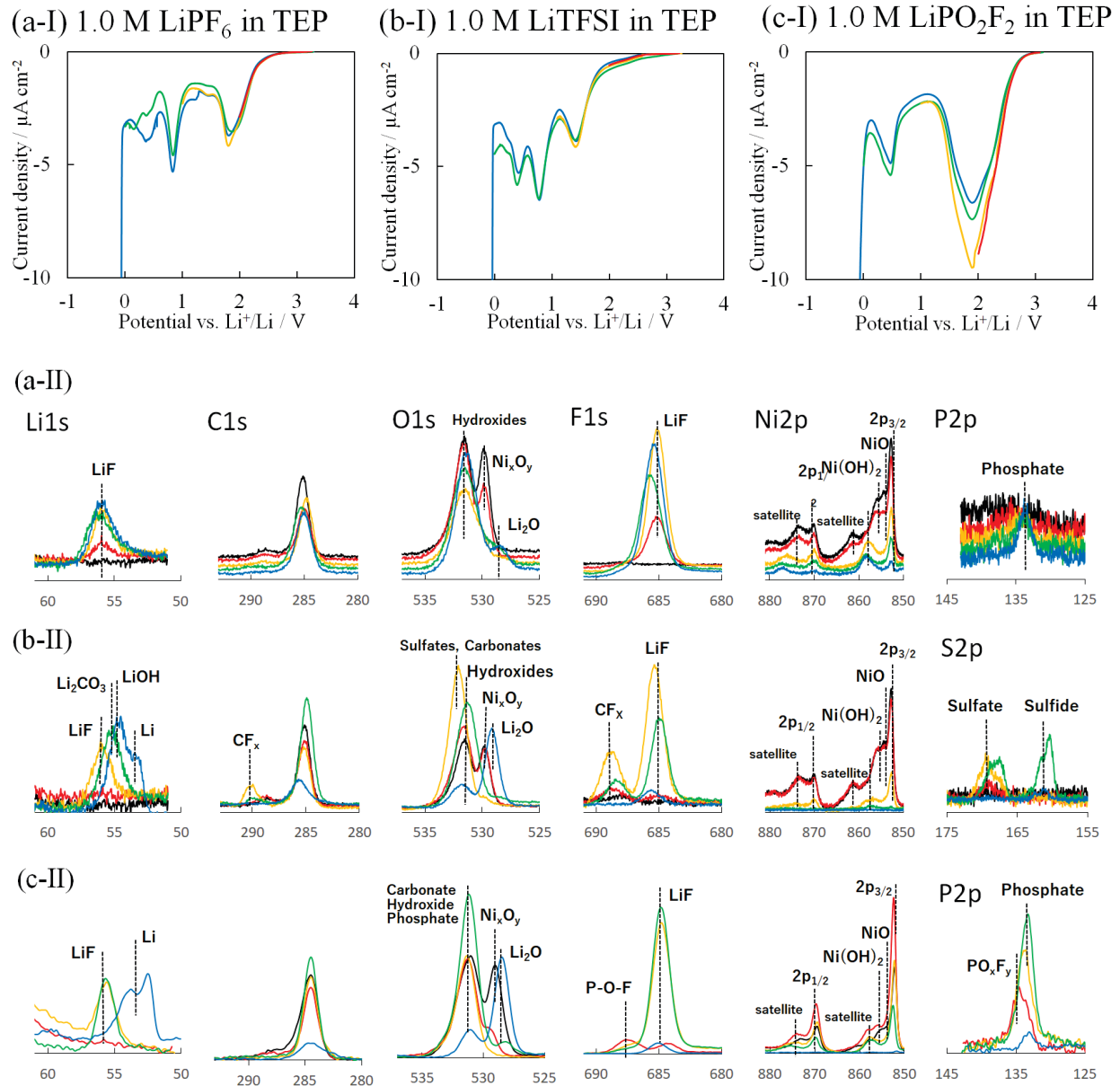
Figure 7-4. LSV curves when the potential is swept from OCV to 2, 1, 0 V and Li deposited potential in (a-I)1.0 M LiPF$_6$/TEP, (b-I)1.0 M LiTFSI/TEP and (c-I)1.0 M LiPO$_2$F$_2$/TEP. (W.E.: 5 mm×5 mm×0.1 mm Ni sheet, C.E. and R.E.: Li foil. Scan rate: 1 mV s^{-1}.). (a-II)～(c-II) Corresponding XPS spectra of the electrode surface after each LSV scan.
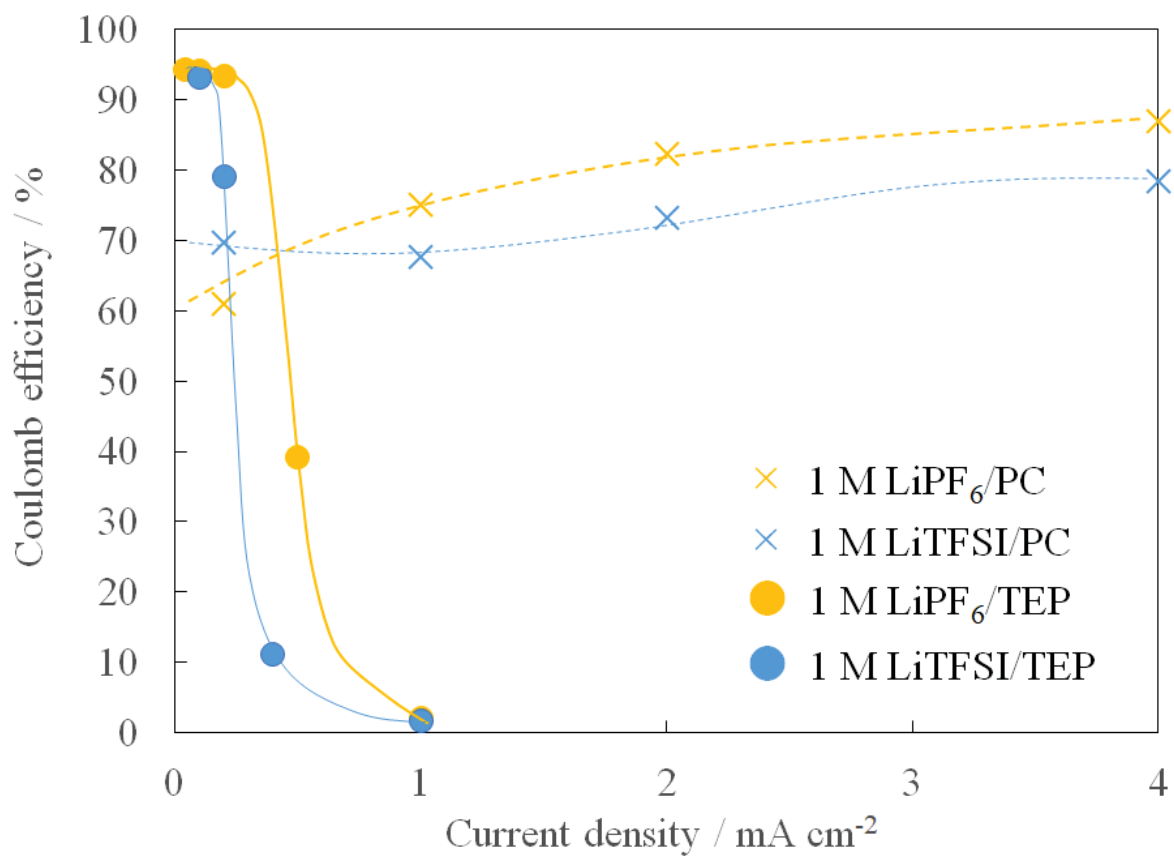
Figure 7-5. Coulomb efficiency of galvanostatic Li electrodeposition and dissolution at different current densities in TEP and PC electrolyte (Salt; LiPF$_6$ or LiTFSI, Salt concentration: 1 M, W.E.: L 10 mm × φ 0.5 mm Ni wire, C.E. and R.E.: Li foil).
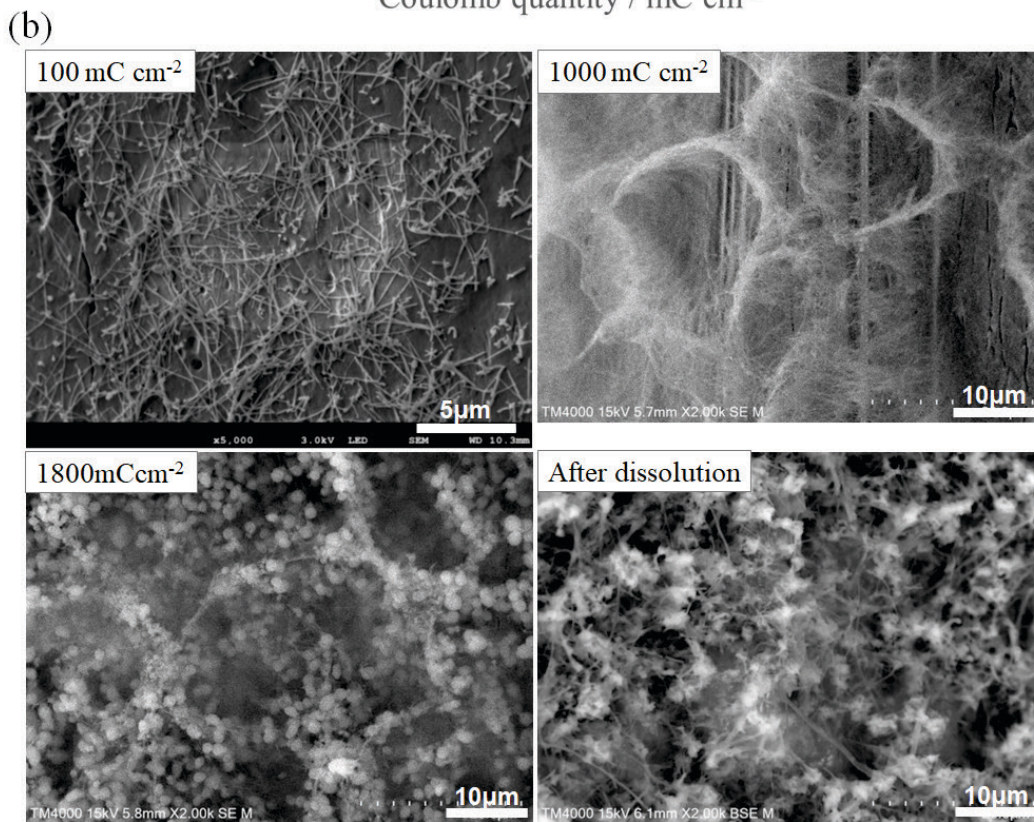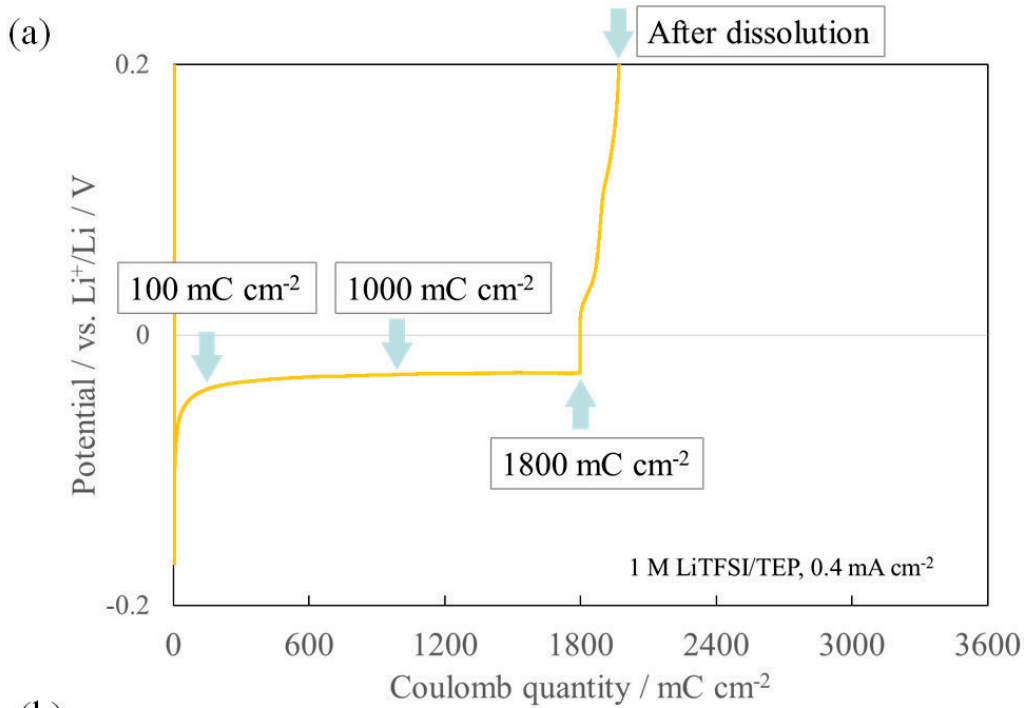
Figure 7-6. (a) Chronopotentiogram of galvanostatic Li electrodeposition and dissolution in 1M LiTFSI/TEP at 0.4 mA cm^{-2} (Coulomb quantity passed during deposition: 1800 mC cm^{-2}). (b) SEM images of electrodes at the coulomb quantity of 100, 1000, 1800 mC cm^{-2} and after dissolution.

(a) 1.0 M LiPF$_6$ in TEP

100 mC cm^{-2} 1000 mC cm^{-2} 1800 mC cm^{-2}

(b) 1.0 M LiPO$_2$F$_2$ in TEP
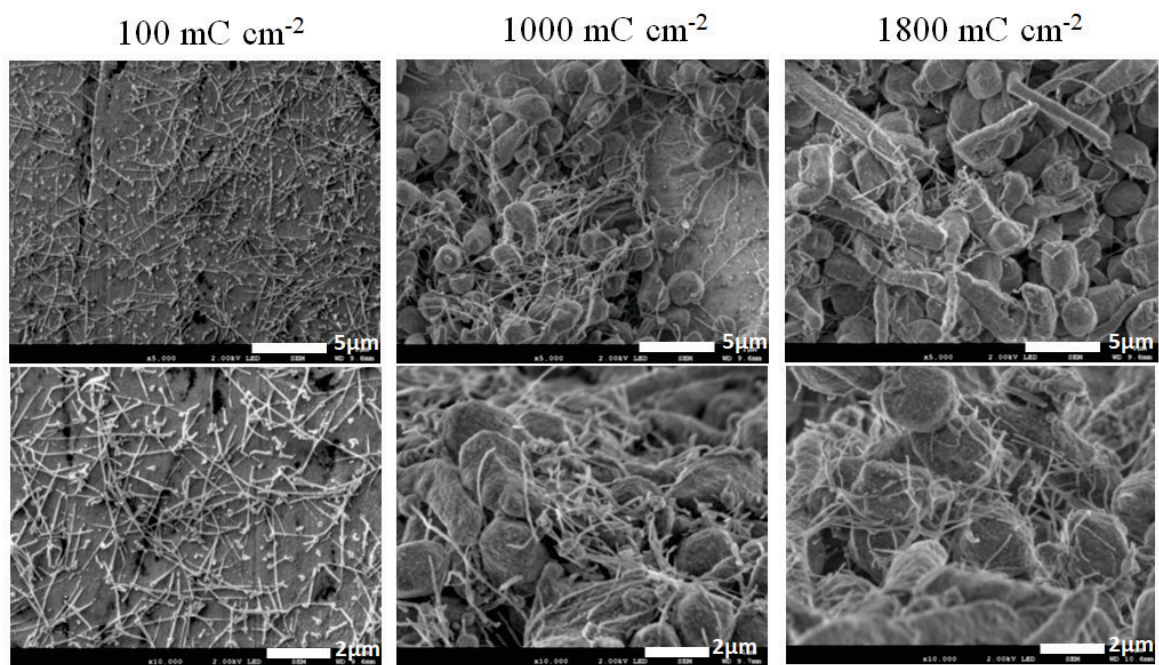
100 mC cm^{-2} 1000 mC cm^{-2} 1800 mC cm^{-2}
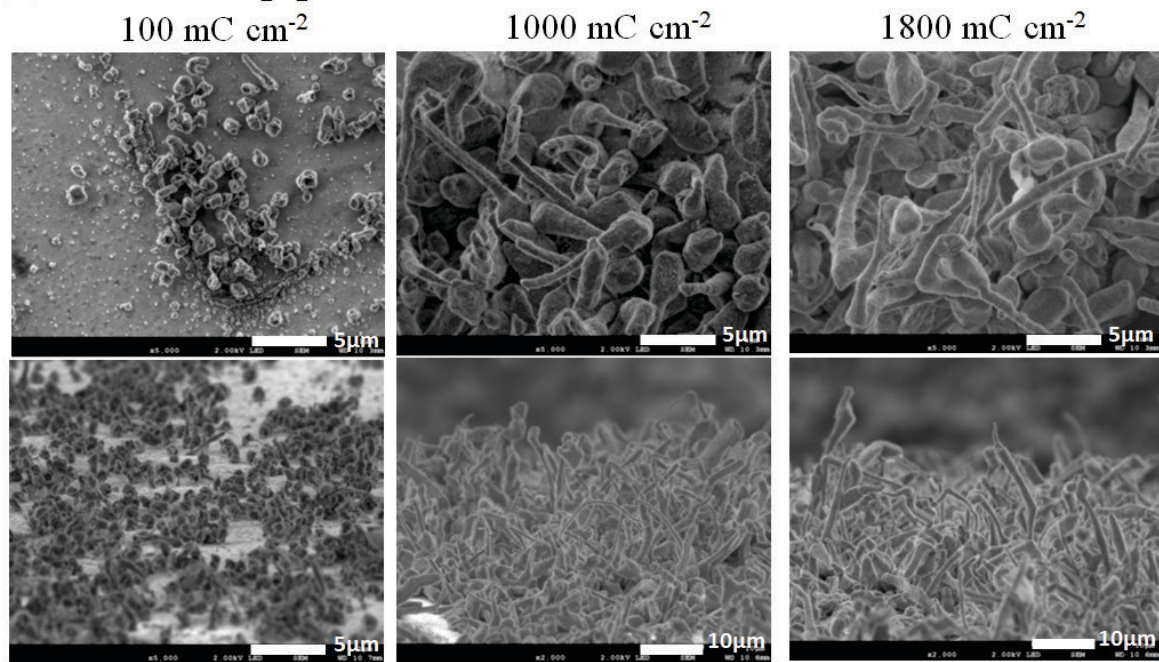
Figure 7-7. SEM images of galvanostatically electrodeposited Li in (a) 1 M LiPF$_6$/TEP and (b) 1 M LiPO$_2$F$_2$/TEP on Ni wire electrode at the coulomb quantity of 100, 1000, 1800 mC cm^{-2} (Current density: 0.4 mA cm^{-2}).
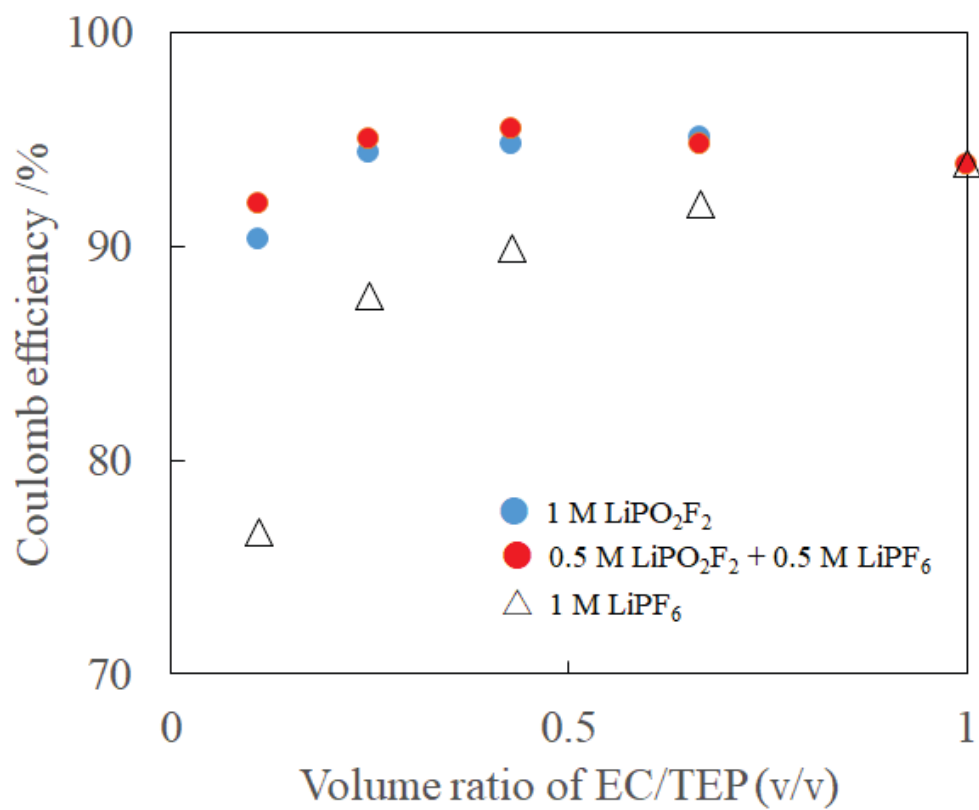
Figure 7-8. Effect of solvent ratio of EC/TEP on coulomb efficiency of Li electrodeposition and dissolution on Cu electrode.
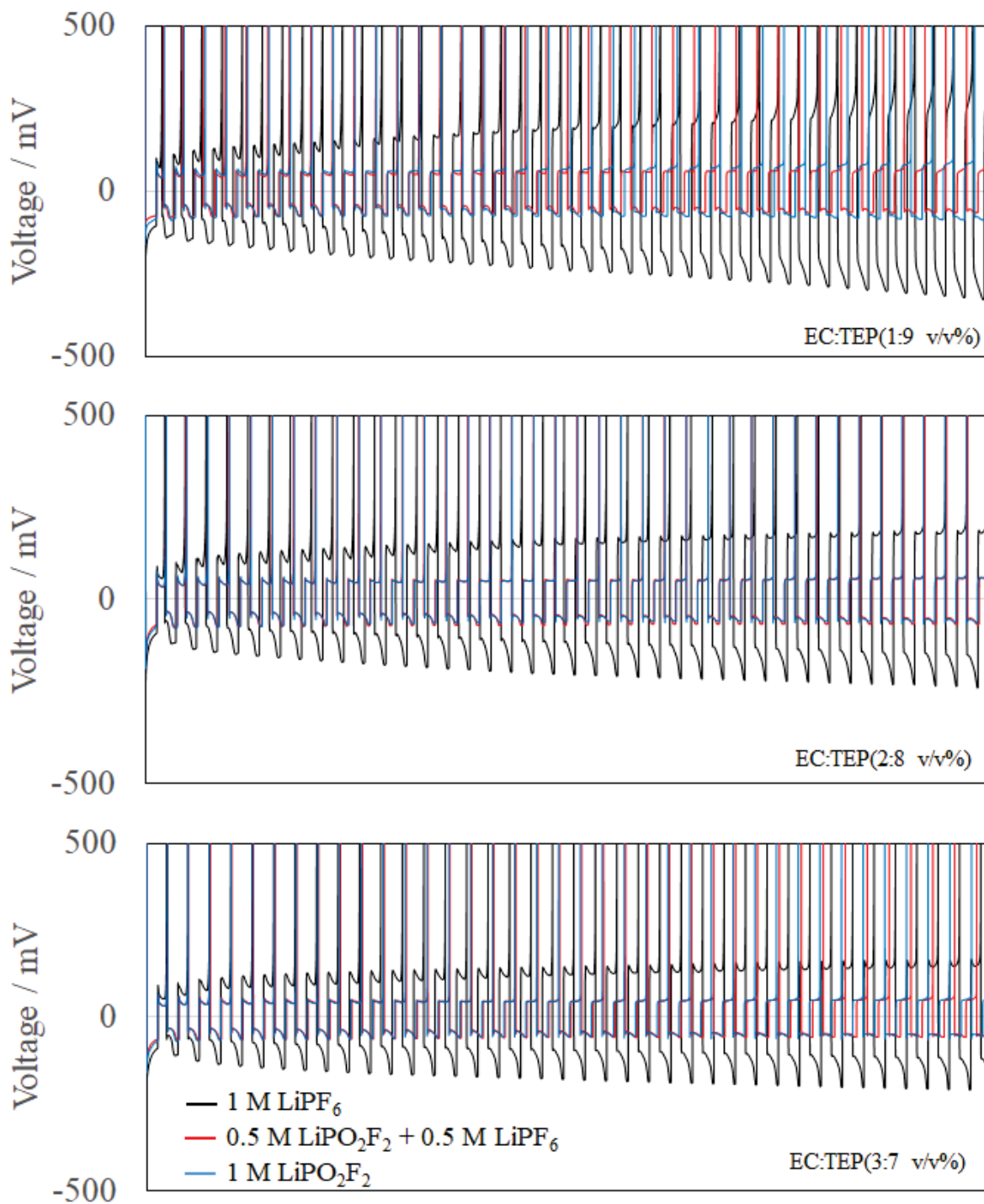
Figure 7-9. Charge-discharge characteristics of Cu | Li cells with EC+TEP (upper: 1:9 v/v%, middle: 2:8 v/v%, lower: 3:7 v/v%) based electrolyte solutions with $LiPF_6$, $LiPO_2F_2$ and $LiPO_2F_2+LiPF_6$ at 0.5 mA cm^{-2}. Li deposition capacity is 3600 mC cm^{-2} (1 mAh cm^{-2}) and discharge cutoff voltage is 1.0 V.
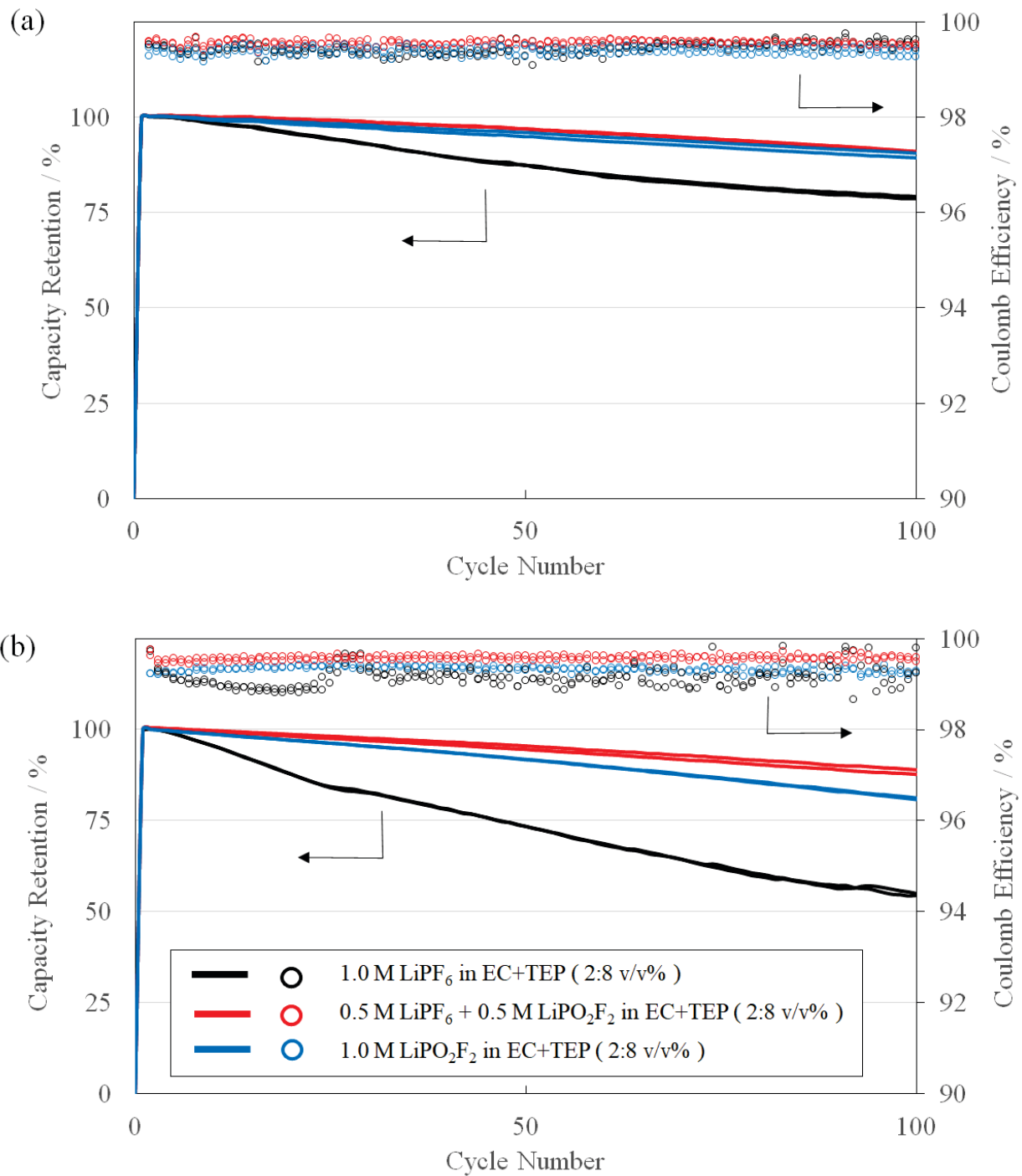
Figure 7-10. Cycling performance of Li｜NCM111 cells with three kinds of LiPF$_6$ or LiPO$_2$F$_2$ dissolved EC+TEP (2:8 v/v%) based electrolyte solutions. Capacity retention and coulomb efficiency at charging/discharging current density of (a) 0.5 mA cm^{-2} (0.33 C) and (b)1.5 mA cm^{-2} (1 C).
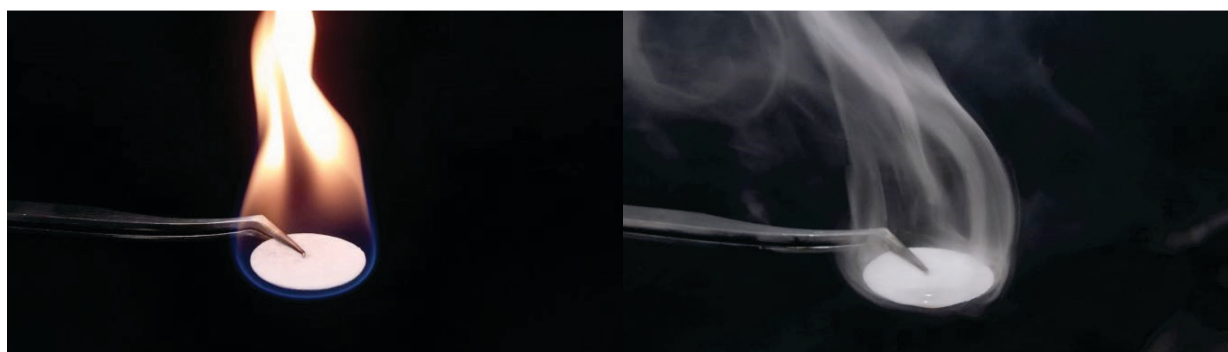
Figure 7-11. Photographs of flammability test for conventional organic electrolyte (left) and phosphoric ester electrolyte of this study (right).

Chapter 8

Improvement of Non-flammable Phosphoric Ester Electrolyte for Lithium Metal Batteries by Mixed Salts of $LiPF_6$, $LiPO_2F_2$ and $LiNO_3$

8.1 Introduction

From the viewpoint of energy density, lithium metal is the most attractive negative electrode material, but as is well known, it faces critical problems for practical use [1-3]. First of all, the deposition and dissolution potential of Li is the lowest and Li itself is very reactive, so it reacts immediately with substances in the electrolyte to form a surface film. In commercially available batteries, the decomposition of the electrolyte is self-terminating. However, degradation of the electrolyte will proceed if the decomposition reaction of the electrolyte is not suppressed by the SEI (solid electrolyte interface). Next, the Li deposition reaction is non-uniform, resulting in the dendrite formation and causing short circuits. Furthermore, the most serious problem is that an explosion or other catastrophic incident could occur in the event of a short circuit due to the extreme flammability of the conventional electrolyte. Therefore, it is essential to design lithium metal battery so that they do not burn even if a short circuit occurs.

The author has recently reported that the performance of lithium metal negative electrode can be improved by using electrolyte using $LiPF_6$ and $LiPO_2F_2$ as salt and triethyl phosphoric as the main solvent [4]. When $LiPF_6$ alone was used as an electrolyte, the decomposition behavior of phosphoric ester was confirmed. On the other hand, it was suggested that the mixed use of $LiPO_2F_2$ formed an effective SEI for improving Li precipitation and dissolution characteristics and suppressing solvent decomposition. Although the characteristics of coin cells using the same

electrolyte were greatly improved, they were by no means satisfactory from a practical standpoint and there was still room for improvement.

$LiNO_3$ is well known as an additive to suppress dendrites of lithium metal negative electrode, and there are many reports on the effect of its addition to electrolytes for Li-S batteries in particular [5-10]. Since the electrolyte does not require very high oxidation resistance in consideration of the working potential of the sulfur positive electrode, ether-based electrolytes have been used in many studies. However, the solubility of $LiNO_3$ in ether solvents such as dimethoxyethane (DME) and dioxolane (DOL) was around 5 wt%, which was not sufficient. In addition, the use of ether-based electrolyte is limited to positive electrode materials such as sulfur and $LiFePO_4$ [11] due to oxidation resistance limitations, and oxide-based positive electrode materials with their high operating voltage cannot be used. $LiNO_3$ has also been reported as an additive to carbonate ester electrolytes [12-13], but $LiNO_3$ has problems such as being even more difficult to dissolve in carbonate ester solvents than in ether solvents. Furthermore, to begin with, these electrolytes are highly flammable. It is extremely dangerous in the event of a short circuit.

It is known that $LiNO_3$ dissolves relatively well in phosphate ester solvents. Matsuda et al. reported that the oxygen evolution reaction ($Li_2O_2 \rightarrow O_2 + 2Li^+ + 2e^-$) during charging occurs efficiently in TEP electrolyte dissolving 1M or 3M $LiNO_3$ at the positive electrode of $Li-O_2$ batteries [14]. In this study, the author has tried to further improve the performance of nonflammable electrolyte by mixing $LiNO_3$ as an electrolyte in addition to $LiPF_6$ and $LiPO_2F_2$ used in the previous report, expecting a synergistic effect. Nonflammable electrolytes may be used not only as material for liquid batteries but also as aids for forming a smooth reaction interface in all-solid-state batteries. The applicability of the newly developed phosphoric ester-based electrolyte to lithium metal batteries with a ternary metal oxide positive electrode and the results of flammability tests will be presented.

8.2 Experimental

LiPF$_6$ and LiPO$_2$F$_2$ were obtained from Stellachemifa corp. as test samples. LiNO$_3$ was purchased from Ardrich reagent and dried at 150 °C for 24 h under nitrogen flow before use. Triethyl phosphate (TEP) was purchased from Tokyo Chemical Industry Co., Ltd. and battery-grade ethylene carbonate (EC), propylene carbonate (PC) and dimethylcarbonate (DMC) were purchased from Kishida Chemical. TEP was dehydrated by molecular sieves (ZMS LiX). EC, PC and DMC were used as received. Preparation of the electrolyte solutions and the measurement of their moisture content performed in the same manner as previously reported and the moisture value of each electrolyte was confirmed to be less than 30 ppm.

Coin cell (CR-2032) test was conducted in the same manner as previously reported. For the positive electrode, NCM electrode sheet (design capacity; 1.5 mAh cm^{-2}, manufactured by Piotrek Co., Ltd.) punched to φ11.30 mm (ca. 1 cm^2) was used. For the negative electrode, a lithium foil (0.2 mm thick, Honjo Metal Co., Ltd.) punched to φ11 mm in an argon glove box was used. Glass filter (Advantech Toyo, GC-50) with a thickness of 190 μm was punched to ø19 mm and used as separator. 100 μL of electrolyte was used for each coin cell. Charging/discharging cycle tests were performed using a BTS2004W (NAGANO Co., Ltd.) at the same current density and the terminal voltages were 4300 mV and 3000 mV, respectively.

The flammability test of the electrolyte was conducted at Kayaku Japan Co., Ltd. by a small gas flame ignition test to judge the classification of the electrolyte as a hazardous material. This method is used for confirmation tests of hazardous materials Class 2 (flammable solids) under the Japanese Fire Service Law and can be also applied to liquids to determine flammability. The electrolyte was weighed up to 10 mL in a sample cup, and a diffusion flame adjusted to a length of approximately 20 to 40 mm was used to ignite the electrolyte for 1 to 10 s. The flammability of the electrolyte was determined from the ignitability and the duration of combustion after the flame was released.

8.3　Results and Discussion

8.3.1　Conductivity of the electrolyte

Table 8-1 shows the electrical conductivity at 25 °C of electrolytes prepared by using LiPF$_6$, LiPO$_2$F$_2$ and LiNO$_3$ as salts and EC+TEP (2:8 v/v%) as a solvent so that the concentration of the salts is 1 M, either alone or mixed. For comparison, the result of a common electrolyte, 1M LiPF$_6$ in EC:DMC (1:1 v/v%), is also shown. Because LiPO$_2$F$_2$ and LiNO$_3$ have very low solubility in carbonate ester solvents, the conductivity results using EC:DMC as solvent are only available when the electrolyte is LiPF$_6$. Compared to 11.5 mS cm^{-1} for the conventional electrolyte using LiPF$_6$, the comparable 7.2 mS cm^{-1} for EC:TEP (2:8 v/v%) is rather lower, but still within the practical range. LiPF$_6$ provides the highest conductivity among the electrolytes using each of the salts alone. LiPO$_2$F$_2$ shows only very low conductivity because it is assumed to be dissolved in TEP by the formation of cluster ions, as previously reported. LiNO$_3$ lies between them. Although it is not desirable to use LiPO$_2$F$_2$ alone as an salt from the viewpoint of conductivity, it is found that the conductivity can be compensated to some extent by mixing with LiPF$_6$ or LiNO$_3$.

8.3.2　Cycle characteristics

Fig. 8-1 shows the cycling performance of Li | NCM111 cell at 0.5 mA cm^{-2} (0.33 C) up to 100 cycles. Comparisons were made between a conventional electrolyte, 1.0 M LiPF$_6$ in EC:DMC (1:1 v/v%), and EC:TEP (2:8 v/v%) with single or mixed salts of LiPF$_6$, LiPO$_2$F$_2$ and LiNO$_3$. The discharge capacities in the first cycle were 1.5 mA hcm^{-2} for both electrolytes, which is generally close to the designed capacity. The capacity retention indicates how much the discharged capacity has changed with respect to the first cycle.

The capacity retention of 1.0 M LiPF$_6$ in EC:DMC (1:1 v/v%) has decreased to 98% at 20 cycles and shows unstable behavior in the subsequent cycles. Coulomb efficiency remains at about 99% until 20 cycles, but then it declines sharply and fluctuates roughly below 99%. It is presumed that dendrites generate and micro-short is occurring. The capacity retention decreased with each

cycle from 92% at approximately 30 cycles to 77% by 100 cycles, showing significant degradation. As previously reported, 0.5 M LiPF$_6$ + 0.5 M LiPO$_2$F$_2$ has improved capacity retention from 77% to 91% at 100 cycles, and its coulomb efficiency has remained stable and high.

Then, 1.0 M LiNO$_3$ and 0.5 M LiPF$_6$ + 0.5 M LiNO$_3$, in which all or half of LiPF$_6$ is replaced by LiNO$_3$, also show significant improvements. The capacity retention at 100 cycles has improved to 98.0% and 96.7%, respectively. Coulomb efficiency of 1.0 M LiNO$_3$ remains slightly lower at 99.0%. 0.5 M LiPO$_2$F$_2$ + 0.5 M LiNO$_3$ and 1/3 M LiPF$_6$ + 1/3 M LiPO$_2$F$_2$ + 1/3 M LiNO$_3$ in combination with LiPO$_2$F$_2$ and LiNO$_3$ showed even better performance with very high capacity retention of 98.2% and 98.4% at 100 cycles, respectively. These Coulomb efficiencies have also remained well above 99.5%.

Fig. 8-2 shows the charging/discharging curves. The solid line represents the charging curve and the dashed line represents the discharging curve. (a) 1.0M LiPF$_6$ in EC:DMC (1:1 v/v%) has overlapping discharging curves and appears stable up to 10 cycles, but the capacity gradually decreases as the cycles proceed. (b) 1.0M LiPF$_6$ in EC:TEP (2:8 v/v%) shows potential oscillating behavior at the end of the initial charge curve and significant degradation in charge/discharge capacity thereafter. On the other hand, electrolytes in which a part of LiPF$_6$ was replaced with LiPO$_2$F$_2$ or LiNO$_3$ showed improvement in charging and discharging characteristics, as shown in (c)-(g), especially in (g) 1/3 M LiPF$_6$ + 1/3 M LiPO$_2$F$_2$ + 1/3 M LiNO$_3$ in EC:TEP (2:8 v/v%), where the charge-discharge curves almost overlap up to 50 cycles, indicating that the battery performance is very stable.

Fig. 8-3 shows the transition of capacity retention and coulomb efficiency for a cell with 1/3M LiPF$_6$ + 1/3 M LiPO$_2$F$_2$ + 1/3 M LiNO$_3$ in EC:TEP (2:8 v/v%) at 1 C rate for up to 500 cycles compared to conventional electrolyte. The cell performance with conventional electrolyte begins to decline rapidly after 200 cycles. Cells with 1/3 M LiPF$_6$ + 1/3 M LiPO$_2$F$_2$ + 1/3 M LiNO$_3$ show a capacity retention of about 85% at 500 cycles. Conventional electrolytes are unstable with hunting after 200 cycles, but 1/3 M LiPF$_6$ + 1/3 M LiPO$_2$F$_2$ + 1/3 M LiNO$_3$ is stable up to 500 cycles and maintains a coulomb efficiency over 99.5%.

8.3.3 Impedance measurement

For the Li | NCM111 cell after the charge-discharge cycle test in Fig. 8-1, resistance separation was performed by AC impedance measurement. Fig. 8-4 shows the equivalent circuit used in the impedance analysis. The equivalent circuit consists of a solution resistance (R_S), two parallel circuits of a resistance (R_{H1}, R_{H2}) and a Constant Phase Element (CPE_{H1}, CPE_{H2}) appearing in the high frequency, and one parallel circuit of a resistance (R_L) and a CPE_L appearing in the low frequency [15-16]. The Nyquist plot and fitting results (solid black line) for each cell are shown in Fig. 8-5. Table 8-2 summarizes R_S, R_{H1}, R_L and R_{Total} (sum of each resistance component) obtained from the impedance measurement.

For solution resistance (R_S), all electrolytes are inversely proportional to the conductivity results shown in Table 8-1, indicating a correlation between conductivity and Rs. The resistance (R_H) appearing in the high frequency band is higher for electrolytes dissolving only a single electrolyte salt, such as 1.0 M $LiPF_6$ in EC:TEP (2:8 v/v%) and 1.0 M $LiPO_2F_2$ in EC:TEP (2:8 v/v%). This resistance is reduced by mixing $LiPO_2F_2$ or $LiNO_3$ with $LiPF_6$. On the other hand, the resistance (R_L) appearing in the low-frequency band is larger than the solution resistance (R_S) and the resistance (R_H) appearing in the high-frequency band in conventional electrolytes and phosphate ester electrolytes with $LiPF_6$ or $LiPO_2F_2$ as the sole electrolyte, and it is dominant for the total value (R_{Total}). It can be seen that this R_L is also reduced by the mixed use of $LiPF_6$ and $LiPO_2F_2$ or $LiNO_3$ as well as R_H.

The resistance appearing in the high-frequency band is mainly attributed to the mass transport of Li^+ on the surface of the positive and negative electrodes, while the arc in the low-frequency band is attributed to the charge transfer resistance [17-20]. The Nyquist plot of the impedance measurement for a Li symmetric cell (Li | Li) [21] is shown in Fig. 8-6. The resistance appearing on the Li metal negative electrode in phosphate ester electrolyte with EC:TEP (2:8 v/v%) as solvent is $LiPO_2F_2 \approx$ 1/3 M $LiPF_6$ + 1/3 M $LiPO_2F_2$ + 1/3 M $LiNO_3$ < $LiNO_3$ <<< $LiPF_6$. The Li |

Li cell is expected to generate equal resistance at both electrodes. Approximately half of this resistance would contribute to the resistance of the NCM | Li cell. When $LiPF_6$ is used alone, it can be said that the influence of the Li negative electrode is significant. Since the resistance of the Li negative electrode is small when $LiPO_2F_2$ is used alone, the relatively high R_H and R_L in the case of $LiPO_2F_2$ alone in Table 8-2 are presumably due to the influence of the positive electrode side. When $LiNO_3$ is used alone, the resistance is kept low as can be seen in Table 8-2. However, Fig. 8-1(b) shows that the coulomb efficiency remained low when $LiNO_3$ was used alone, suggesting that a degradation factor may be involved that does not appear in the resistance. When $LiPF_6$ is used alone in the phosphate ester electrolyte, a smooth electrode reaction is expected to be inhibited, but this can be improved by mixing $LiPO_2F_2$ or $LiNO_3$.

8.3.4 Self-discharge characteristics

Fig. 8-7 shows a transient of the open circuit voltage of each battery after charge/discharge operation at 0.5 mA cm^{-2} in the voltage range of 3.0 V-4.3 V. $LiNO_3$ showed a linear decrease in voltage, dropping to 4.23 V after 24 h. On the other hand, self-discharge behavior from 4.3 V is suppressed for $LiPF_6$ and $LiPO_2F_2$. From the results of battery characteristics in 8.3.2 and 8.3.3, it is unlikely that the oxidation resistance of the electrolyte using $LiNO_3$ is lower than that of $LiPF_6$ and $LiPO_2F_2$. One possible factor is the difference in the characteristics of the passivation film formed on the aluminum current collector. It is well known that $LiPF_6$ forms fluorine-containing passivation film on the aluminum surface [22-23]. It is assumed that $LiPF_6$ and $LiPO_2F_2$ suppress oxidative corrosion of aluminum compared to $LiNO_3$ alone. While single use of $LiNO_3$ leads to corrosion of aluminum, mixed use with $LiPF_6$ or $LiPO_2F$ is expected to compensate for the oxidation resistance of aluminum.

8.3.5 *Flammability test*

A small gas flame ignition method is used for confirmation tests of hazardous materials Class 2 (flammable solids) under the Japanese Fire Service Law and can be also applied to liquids to determine flammability. As shown in Fig. 8-8, the test is conducted by weighing 10 mL of electrolyte into a sample cup and exposing a diffusion flame of ca. 20 to 40 mm in length to the electrolyte for 1 to 10 s to ignite it. Flammability is determined from the combustion behavior and combustion duration after the flame is released. Table 8-3 summarizes the test results of the conventional electrolyte and the developed electrolyte. The conventional electrolyte was determined to be "easily ignitable" because it easily ignited at a flame contact time of 1 s and continued to burn for more than 10 s after flame separation and the reproducibility for 3 times was obtained. On the other hand, 1/3 M $LiPF_6$ + 1/3 M $LiPO_2F_2$ + 1/3 M $LiNO_3$ in EC:TEP (2:8 v/v%) was determined to be "difficult to ignite" because no combustion was observed after 10 s of flame contact time and three repeatability. On the other hand, 1/3 M $LiPF_6$ + 1/3 M $LiPO_2F_2$ + 1/3 M $LiNO_3$ in EC:TEP (2:8 v/v%) was determined to be "difficult to ignite" because no combustion was observed after keeping flame contact for 10 s and reproducibility was obtained over 3 times.

8.4 Conclusions

The applicability of phosphoric ester electrolyte to lithium metal batteries combined with a 4.3 V class ternary metal oxide positive electrode was investigated. In the case of an electrolyte containing only $LiPF_6$ as a salt, such as 1.0 M $LiPF_6$ in EC:TEP (2:8 v/v%), the cycle characteristics show a decrease in capacity retention with cycles. Addition of $LiPO_2F_2$ and $LiNO_3$ dramatically improved the charge-discharge cycle performance and resistance characteristics. The impedance measurement results suggest that $LiPO_2F_2$ and $LiNO_3$ act on both the positive and negative electrode, forming an effective SEI for charge-discharge reactions and for inhibiting solvent degradation. On the other hand, when only $LiNO_3$ was used as a salt, although cycle characteristics were good, self-discharge behavior was observed to progress during storage after

charging to 4.3V. $LiPF_6$ and $LiPO_2F_2$ form a fluorine-containing passivation film on the aluminum current collector, whereas $LiNO_3$ alone is not expected to effectively inhibit oxidative corrosion of aluminum. 1/3 M $LiPF_6$ + 1/3 M $LiPO_2F_2$ + 1/3 M $LiNO_3$ in EC:TEP (2:8 v/v%), using a mixture of $LiPF_6$, $LiPO_2F_2$, and $LiNO_3$ as salts, showed approximately 85% capacity retention and 99.5% coulomb efficiency in cycle tests up to 500 cycles at 1 C. Results of an investigation of the flammability of electrolyte by small gas flame contact test. Conventional electrolyte was determined to be easily ignitable, while the newly developed phosphate ester electrolyte, a mixture of three kinds of salts, was determined to be difficult to ignite. More detailed investigation is necessary to understand the mechanism by which $LiPO_2F_2$ and $LiNO_3$ contribute to the improvement of battery characteristics. Based on that, further improvement can be expected by optimizing the composition of the electrolyte. The author will also investigate the compatibility of the electrolyte with other positive electrode materials to improve the safety and performance of lithium metal batteries.

References

[1] D. Lin, Y. Liu and Y. Cui, Reviving the lithium metal anode for high-energy batteries, Nature Nanotechnology, 12, 194-206 (2017).

[2] S. Li, M. Jiang, Y. Xie, H. Xu, J. Jia, and J. Li, Developing High-Performance Lithium Metal Anode in Liquid Electrolytes: Challenges and Progress, Adv. Mater., 30, 1706375 (2018).

[3] R. Xu, X.-B. Cheng, C. Yan, X.-Q. Zhang, Y. Xiao, C.-Z. Zhao, J.-Q. Huang and Q. Zhang, Artificial Interphases for Highly Stable Lithium Metal Anode, Matter, 1, 317–344 (2019).

[4] In preparation

[5] X. Liang, Z. Wen, Y. Liu, M. Wu, J. Jin, H. Zhang and X. Wu, Improved cycling performances of lithium sulfur batteries with $LiNO_3$-modified electrolyte, J. Power Sources, 196, 9839-9843 (2011).

[6] S. S. Zhang, Role of $LiNO_3$ in rechargeable lithium/sulfur battery, Electrochim. Acta, 70, 344-348 (2012).

[7] S. Xiong, K. Xie, Y. Diao, X. Hong, Properties of surface film on lithium anode with $LiNO_3$ as lithium salt in electrolyte solution for lithium sulfur batteries, Electrochim. Acta, 83, 78-86 (2012).

[8] W. Li, H. Yao, K. Yan, G. Zheng, Z. Liang, Y.M. Chiang and Y. Cui, The synergetic effect of lithium polysulfide and lithium nitrate to prevent lithium dendrite growth, Nat. Commun., 6, 7436 (2015).

[9] S. S. Zhang, A new finding on the role of $LiNO_3$ in lithium-sulfur battery, J. Power Sources, 322, 99-105 (2016).

[10] B. D. Adams, E. V. Carino, J. G. Connell, K. S. Han, R. Cao, J. Chen, J. Zheng, Q. Li, K.T. Mueller, W.A. Henderson and J.-G. Zhang, Long term stability of Li-S batteries using high concentration lithium nitrate electrolytes, Nano Energy, 40, 607-617 (2017).

[11] C. Zhang, Q. Lan, Y. Liu, J. Wu, H. Shao, H. Zhan and Y. Yang, Dual-layered artificial solid electrolyte interphase formed by controlled electrochemical reduction of LiTFSI/DME-LiNO$_3$ for dendrite-free lithium metal anode, Electrochim. Acta, 306. 407-419 (2019).

[12] J. Guo, Z. Wen, M. Wu, J. Jin, and Y. Liu, Vinylene carbonate-LiNO$_3$: a hybrid additive in carbonic ester electrolytes for SEI modification on Li metal anode, Electrochem. Commun., 51 59–63 (2015).

[13] L.-N. Wu, J. Peng, Y.-K. Sun, F.-M. Han, Y.-F. Wen, C.-G. Shi, J.-J. Fan, L. Huang, J.-T. Li and S.-G. Sun, High-Energy Density Li metal Dual-Ion Battery with a Lithium Nitrate-Modified Carbonate-Based Electrolyte, ACS Appl. Mater. Interfaces, 11, 18504−18510 (2019).

[14] S. Matsuda and H. Asahina, Highly Efficient Oxygen Evolution Reaction in Rechargeable Lithium-Oxygen Batteries with Triethylphosphate-Based Electrolytes, J. Phys. Chem. C, 124, 25784−25789 (2020).

[15] U. Westerhoff, K. Kurbach, F. Lienesch and M. Kurrat, Energy Technol., 4, 1620-1630 (2016).

[16] M. Gaberscek, J. Moskon, B. Erjavec, R. Dominko and J. Jamnik, Electrochem. Solid-State Lett., 11(10), A170-A174 (2008).

[17] W. Lee, S. Muhammad, T. Kim, H. Kim, E. Lee, M.Jeong, S. Son, J.-H. Ryou and W.-S. Yoon, Adv. Energy Mater, 8, 1701788 (2018).

[18] S.S. Zhang, K. Xu and T.R. Jow, Electrochim. Acta, 49(7), 1057-1061 (2004).

[19] Y. Xu, H. Wu, Y. He, Q.-S. Chen, J.-G. Zhang, W. Xu and C. Wang, Atomic to Nanoscale Origin of Vinylene Carbonate Enhanced Cycling Stability of Lithium Metal Anode Revealed by Cryo-Transmission Electron Microscopy, Nano Lett., 20, 418−425 (2020).

[20] W. Huang, D. T. Boyle, Y. Li, Y. Li, A. Pei, H. Chen and Y. Cui, Nanostructural and Electrochemical Evolution of the Solid-Electrolyte Interphase on CuO Nanowires Revealed by Cryogenic-Electron Microscopy and Impedance Spectroscopy. ACS Nano, 13, 737−744 (2019).

[21] T. Momma, T. Yokoshima, H. Nara, Y. Gima and T. Osaka, Electrochim. Acta, 131, 195-201 (2014).

[22] R. Marom, O. Haik, D. Aurbach and I. C. Halalay, Revisiting LiClO$_4$ as an Electrolyte for Rechargeable Lithium-Ion Batteries, J. Electrochem. Soc., 157(8), A972-A983 (2010).

[23] B. Markovsky, F. Amalraj, H. E. Gottlieb, Y. Gofer, S. K. Martha and D. Aurbach, On the Electrochemical Behavior of Aluminum Electrodes in Nonaqueous Electrolyte Solutions of Lithium Salts, J. Electrochem. Soc., 157(4), A423-A429 (2010).

Table 8-1. Ionic conductivities of conventional carbonate electrolyte solution and several kinds of EC+TEP (2:8 v/v%) based electrolyte solutions with single or mixed salts of $LiPF_6$, $LiPO_2F_2$ and $LiNO_3$.

Electrolyte	Conductivity / mS cm^{-1} (25°C)
1.0 M $LiPF_6$ in EC:DMC(1:1 v/v%) (Conventional)	11.48
1.0 M $LiPF_6$ in EC:TEP(2:8 v/v%)	7.22
1.0 M $LiPO_2F_2$ in EC:TEP(2:8 v/v%)	0.89
1.0 M $LiNO_3$ in EC:TEP(2:8 v/v%)	3.47
0.5 M $LiPF_6$ + 0.5 M $LiPO_2F_2$ in EC:TEP(2:8 v/v%)	4.50
0.5 M $LiPF_6$ + 0.5 M $LiNO_3$ in EC:TEP(2:8 v/v%)	5.39
0.5 M $LiPO_2F_2$ + 0.5 M $LiNO_3$ in EC:TEP(2:8 v/v%)	2.35
1/3 M $LiPF_6$ + 1/3 M $LiPO_2F_2$ + 1/3 M $LiNO_3$ in EC:TEP(2:8 v/v%)	4.17

Table 8-2. Fitting results of resistance in the equivalent circuit model for every electrolyte solution. R_H means sum of R_{H1} and R_{H2}, R_{total} means sum of R_s, R_H, R_L and R_{total}.

Electrolyte	Resistance / Ω			
	R_S	R_H	R_L	R_{Total}
1.0 M $LiPF_6$ in EC:DMC(1:1 v/v%) (Conventional)	2.7	22.5	149.0	174.1
1.0 M $LiPF_6$ in EC:TEP(2:8 v/v%)	3.8	53.6	394.0	451.4
1.0 M $LiPO_2F_2$ in EC:TEP(2:8 v/v%)	18.4	92.0	149.0	259.4
1.0 M $LiNO_3$ in EC:TEP(2:8 v/v%)	6.1	29.6	37.1	72.8
0.5 M $LiPF_6$ + 0.5 M $LiPO_2F_2$ in EC:TEP(2:8 v/v%)	4.9	28.6	53.8	87.3
0.5 M $LiPF_6$ + 0.5 M $LiNO_3$ in EC:TEP(2:8 v/v%)	5.0	23.7	43.2	71.8
0.5 M $LiPO_2F_2$ + 0.5 M $LiNO_3$ in EC:TEP(2:8 v/v%)	7.4	28.3	16.6	52.3
1/3 M $LiPF_6$ + 1/3 M $LiPO_2F_2$ + 1/ 3M $LiNO_3$ in EC:TEP(2:8 v/v%)	4.6	21.5	14.2	40.3

Table 8-3. Results of flammability test for the electrolytes by flame ignition test.

Exam Order	1 M LiPF$_6$ in EC:DMC(1:1 v/v%) (Conventional)		1/3 M LiPF$_6$ + 1/3 M LiPO$_2$F$_2$ + 1/3 M LiNO$_3$ in EC:TEP(2:8 v/v%)	
	T_{ig} / s	D_{com} / s	T_{ig} / s	D_{com} / s
1st	10	43	Noncombustion	-
2nd	3	77	Noncombustion	-
3rd	2	68	Noncombustion	-
4th	1	75	-	-
5th	1	74	-	-
6th	1	74	-	-

T_{ig}: Time required to ignite by flame contact up to 10 seconds.

D_{com}: Duration of combustion after ignition and keeping the flame away.
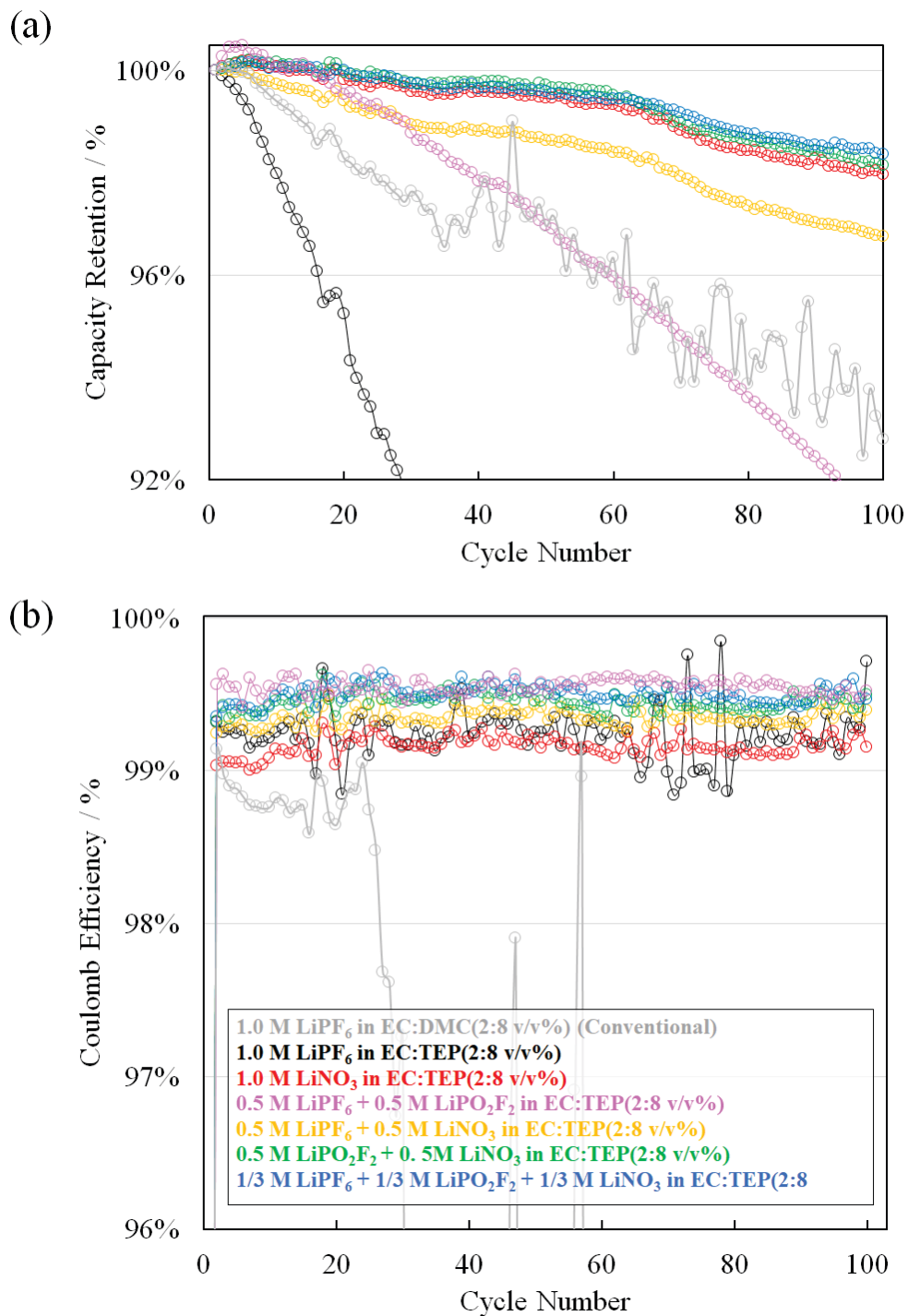
Figure 8-1. Cycling performance of NCM111 | Li cells with conventional carbonate electrolyte solution and several kinds of EC+TEP (2:8 v/v%) based electrolyte solutions containing single or mixed salts of $LiPF_6$, $LiPO_2F_2$ and $LiNO_3$ at current density of 0.5 mA cm^{-2} (0.33 C) and charge-discharge voltage range of 3.0 - 4.3V. (a) Capacity retention and (b) Coulomb efficiency.
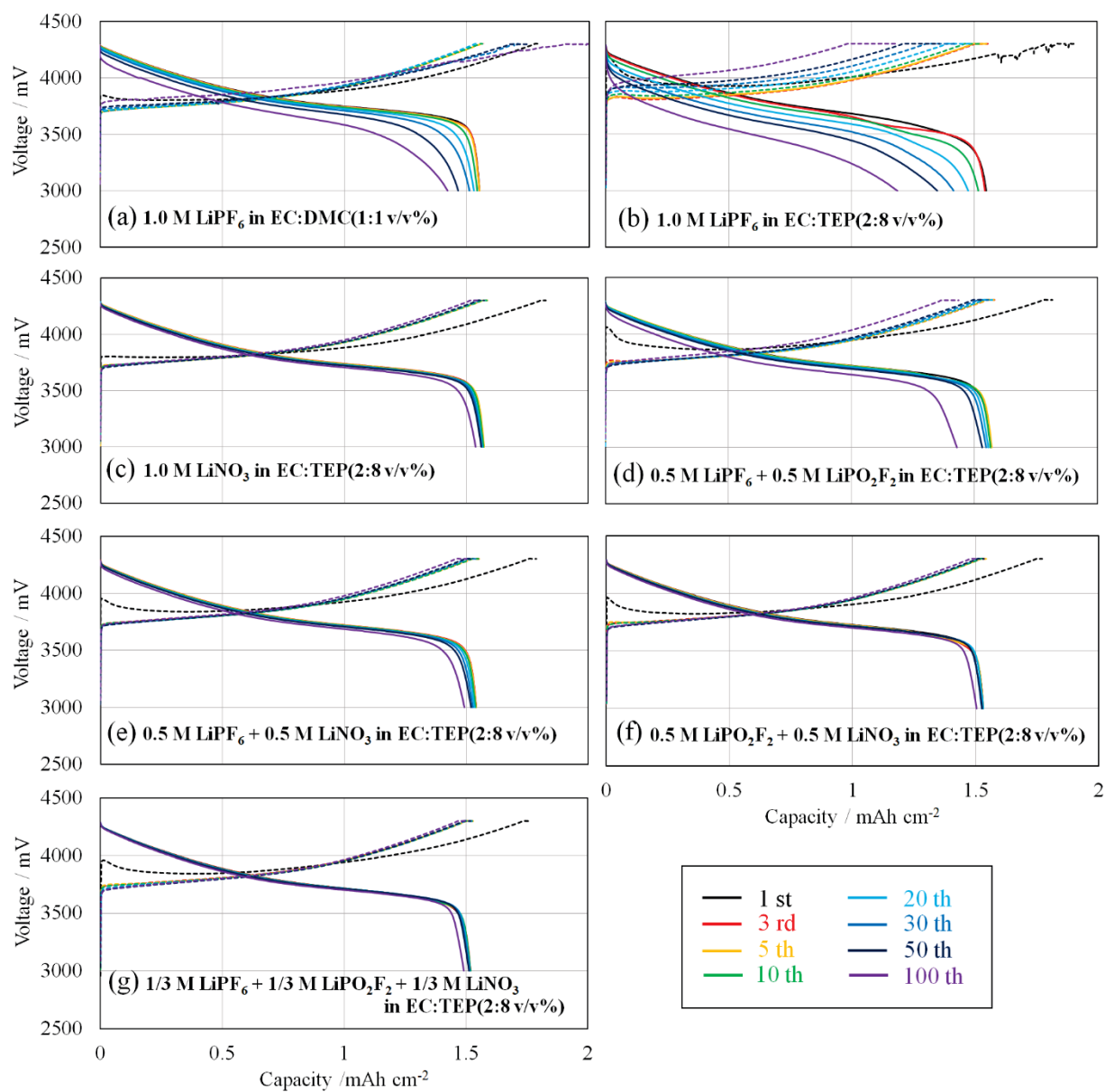
Figure 8-2. Charge and discharge curves of Li | NCM111 cells with conventional carbonate electrolyte solution and indicated several kinds of EC+TEP (2:8 v/v%) based electrolyte solutions with single or mixed salts of $LiPF_6$, $LiPO_2F_2$ and $LiNO_3$ at current density of 0.5 mA cm^{-2} (0.33C) and charge / discharge voltage range of 3.0 - 4.3V.
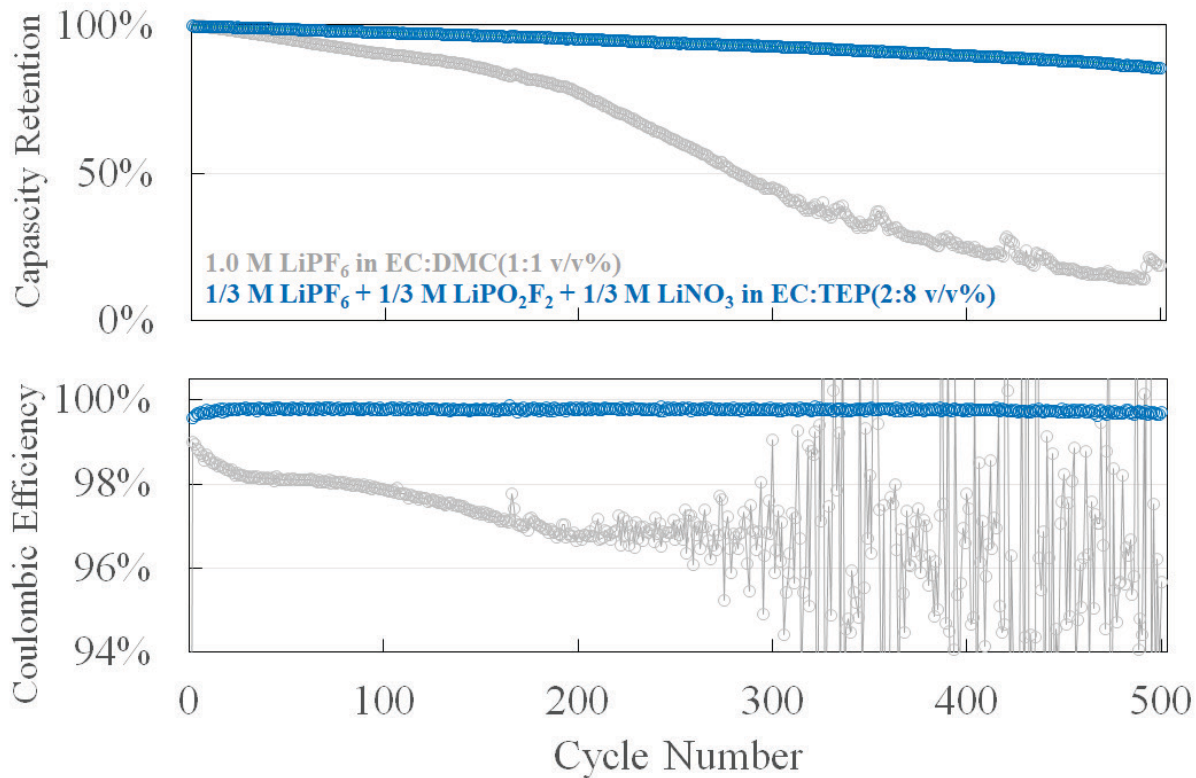
Figure 8-3. Cycling performance of Li | NCM111 cells with conventional carbonate electrolyte solution and 1/3 M LiPF$_6$ + 1/3 M LiPO$_2$F$_2$ + 1/3 M LiNO$_3$ in EC:TEP (2:8 v/v%) at current density of 1.5 mA cm^{-2} (1 C) up to 500 cycles.
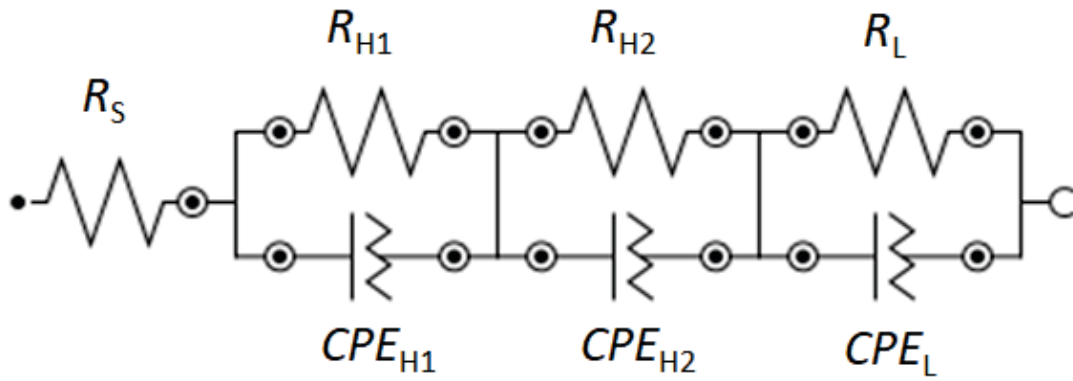
Figure 8-4. Equivalent circuit model for Li | NCM111 cells. R_s: Solution resistance, R_{H1}, R_{H2} and R_L: Polarization resistance, CPE_{H1}, CPE_{H2} and CPE_L: Constant phase element instead of capacitance component.
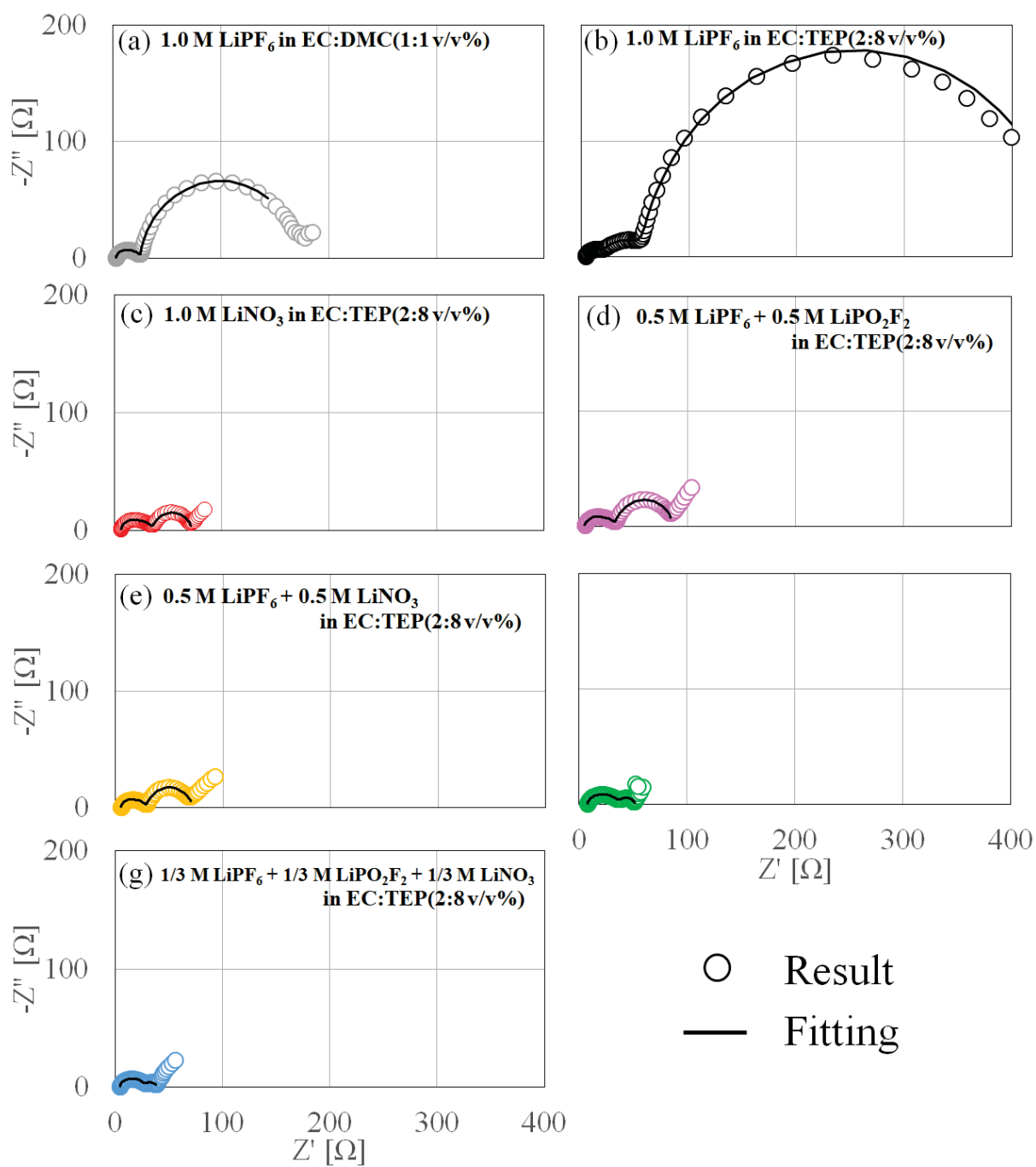
Figure 8-5. Nyquist plots and the fitting results for Li | NCM111 cells after 100 cycles.
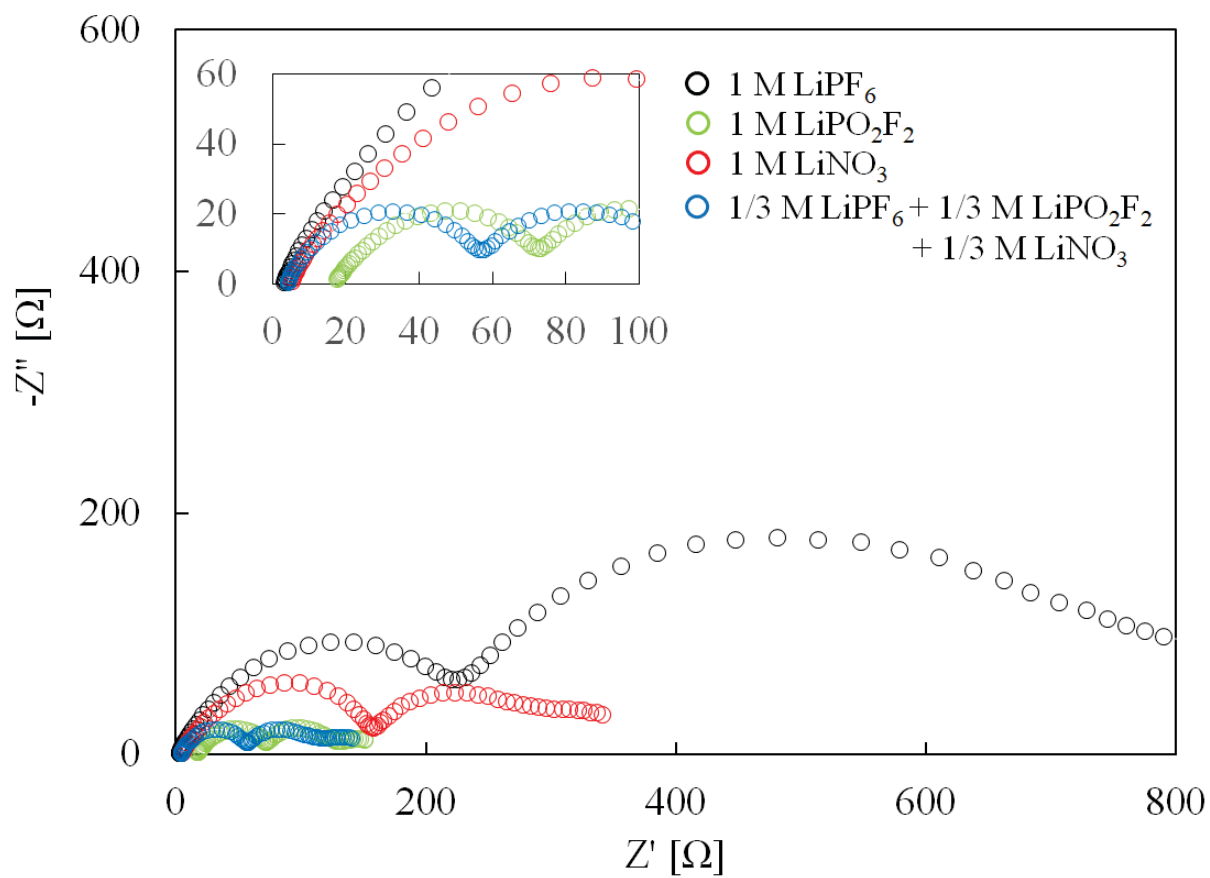
Figure 8-6. Nyquist plots for symmetry Li | Li cells after 100 cycles.
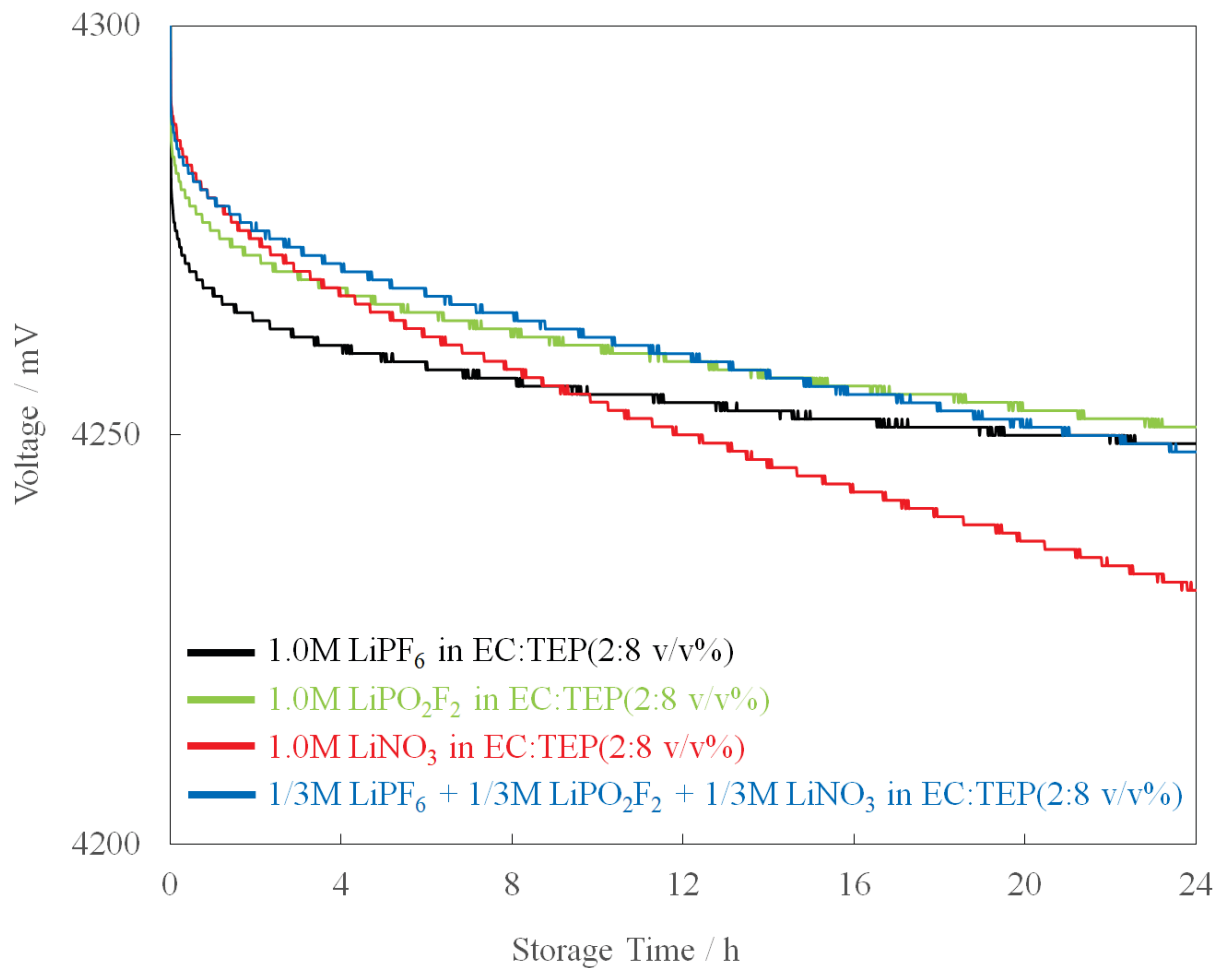
Figure 8-7. Comparison of the change in open circuit voltage between the electrolyte types after charging and storing at 25 °C for 24 h.
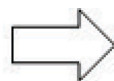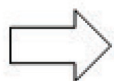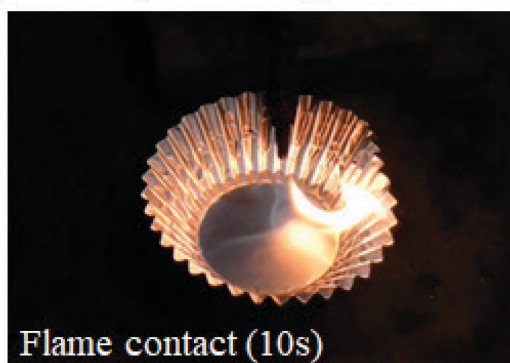
Figure 8-8. Appearance of flammability test conducted by flame contact method for (a)conventional electrolyte (1.0 M LiPF$_6$ in EC:DMC(1:1 v/v%)) and (b)newly developed electrolyte (1/3 M LiPF$_6$ + 1/3 M LiPO$_2$F$_2$ + 1/3 M LiNO$_3$ in EC:TEP(2:8 v/v%)).

Chapter 9

General Conclusions

In order to obtain knowledge on the coupling phenomena between morphological variations of electrodeposited Li and mass transfer of Li ion and to contribute to the development of safe and efficient lithium metal batteries, the author conducted galvanostatic and potentiostatic electrolysis in 1M LiTFSI/PC electrolyte and investigated the effects of current density and applied potential on the deposition behavior from the very initial stage of Li deposition to the development of dendrites. In addition, the author investigated the electrodeposition behavior in ionic liquids instead of 1 M LiTFSI/PC electrolyte and tried to develop a new nonflammable electrolyte using phosphoric ester toward safer lithium metal batteries. The results of this study can be summarized as follows.

In chapter 2, the effect of current density on the morphological variation during the initial stage (up to 100 mC cm^{-2}) of galvanostatic Li deposition on Ni wire was investigated at current densities ranging from 0.04 to 60 mA cm^{-2} in 1M LiTFSI/PC. The simultaneous growth of whisker-like and granular deposits was identified at lower current densities, while the development of uniform mesoscopic-sized Li rods was observed at higher current densities. A transition of morphological variations was observed at current densities around 4 mA cm^{-2}. The formation behavior of SEI, which occurs prior to the Li deposition reaction, also differed between higher and lower current densities. The event of sprouting, in which Li precipitates nucleated and grown underneath the SEI are extruded from the SEI into the organic electrolyte, was characterized as a change point that may have a significant influence on the subsequent growth mode. The diffusion coefficient of Li$^+$ in the SEI galvanostatically formed on Ni substrate was estimated to be in the order of 10^{-9} cm^2 s^{-1} by analyzing the behavior of potential change in the early stage of the electrolysis.

In chapter 3, Li electrodeposition in LiTFSI/PC electrolyte up to 2.22 mAh cm^{-2} was performed by changing the current density from 0.2 to 60 mA cm^{-2} under optical microscope observation. The evolution of morphological variation followed by the initial stage (less than 0.028 mAh cm^{-2} in Chapter 2) was carefully observed. At lower current densities, a non-uniform standalone or stochastic deposition containing filament-like deposition was observed. On the other hand, the morphological variation mode was shifted to macroscopically smooth curved surface enveloping the numerous tips of similar sized rod-like deposits at higher current density. Two-step linearity was obtained in the relationship between the time variations of apparent electrode diameter and the square root of the duration period. The movement of suspended particles was occasionally observed. It suggested the induction of natural convection in the organic electrolyte. The limiting current density accompanying Li electrodeposition along a vertical Ni cathode was calculated to be 44 mA cm^{-2}, which was well consistent with the LSV measurement.

In Chapter 4, the Li nucleation and growth behavior was investigated from SEM images during galvanostatic electrodeposition up to 10 mC cm^{-2} in 1M LiTFSI/PC varying current densities from 0.2 to 60 mA cm^{-2}. The number of deposits at 10 mC cm^{-2} increased from 2 to 4.5×10^{10} particles cm^{-2} with increasing current density, and the average particle size slightly decreased from about 19 nm to 15 nm. Analysis of the nearest neighbor distances of the deposits showed deviation from the Poisson distribution at high current densities, suggesting the influence of agglomeration between neighboring deposits. At higher current densities above 4 mA cm^{-2}, the number of nucleus obtained by analyzing the behavior of the potential change around the minima ranged from 1.2 to 4.5×10^{10} nuclei cm^{-2}. Their values were in relatively good agreement with the results of the SEM image analysis. It was found that conventional nucleation and growth theory can be applied to Li nucleation under certain conditions, although it is essentially different from metal electrodeposition in aqueous solution due to the presence of SEI.

In Chapter 5, Li deposition behavior was observed by optical microscopy in 1M LiTFSI/PC on Ni wire at constant potentials from 0 mV to -1000 mV up to 8000 mC cm^{-2}. Morphological variation was observed depending on the applied potential. Extremely localized deposition was

observed at applied potentials higher than -100 mV with a transition to uniform and smooth deposition at lower applied potentials. From the results of the double-pulse potential technique, nucleation behavior were assumed to be related to the morphological change. While similarities in deposition behavior were observed between the galvanostatic and potentiostatic conditions, a deviation in deposit morphology and I-V characteristics were observed when the applied potential was low. It was considered to originate from the fact that an overvoltage of -100 mV is required for Li nucleation and growth to occur on the Ni substrate in the presence of SEI. Analysis of the current transient at -400 mV showed that the diffusion coefficient of Li^+ in SEI was estimated to be 3.3×10^{-10} cm^2 s^{-1}, which is relatively close to the 4×10^{-10} cm^2 s^{-1} estimated from the potential variation during galvanostatic electrolysis.

In chapter 6, the electrodeposition process of Li metal in 1.0 M LiTFSI - ionic liquid (*N*-methoxymethyl-*N*-methylpyrrolidinium) bis (trifluoromethanesulfonyl) imide was observed in-situ by optical microscope. Morphological variations of electrodeposited Li dendrite and its growth rate were examined and the ionic mass transfer rate in the vicinity of the electrode surface was discussed. Once the dendrite starts to grow, its length is proportional to the square root of time. This indicates that the Li^+ mass transfer rate affects its growth. Dendrite growth process can be classified into two regions depending on its growth rate: the initiation period and the growing period with swinging behavior probably caused by residual stress.

In chapter 7, the Li deposition behavior in phosphoric ester electrolytes was investigated using $LiPO_2F_2$ as electrolyte compared to commonly used $LiPF_6$ or LiTFSI. $LiPO_2F_2$ was relatively easy to dissolve in triethyl phosphate up to about 2 M, but the electrical conductivity was about 0.5 mS cm^{-2} at 1 M. On the other hand, the use of $LiPO_2F_2$ electrolyte was confirmed to improve the reversibility of lithium deposition and dissolution. The appearance of fibrous morphology of electrodeposited Li in TEP electrolyte with LiTFSI or $LiPF_6$ above a certain current density was considered to be a factor in lowering the reversibility. Improved battery characteristics with an optimized TEP electrolyte using $LiPO_2F_2$ were confirmed.

In chapter 8, the applicability of phosphoric ester electrolyte to lithium metal batteries consisting of a lithium metal negative electrode and a 4.3 V class ternary oxide positive electrode was investigated. Improved performance of phosphate ester electrolyte was obtained by mixing $LiPO_2F_2$ or $LiNO_3$ with $LiPF_6$ as a salt. 1/3M $LiPF_6$ + 1/3M $LiPO_2F_2$ + 1/3M $LiNO_3$ in EC:TEP (2:8 v/v%) showed approximately 85% capacity retention and 99.5% coulomb efficiency in cycle tests up to 500 cycles at 1C. Progressive self-discharge behavior was observed when $LiNO_3$ was solely used as a salt, suggesting that the oxidative corrosion of aluminum was not effectively suppressed. As a result of flammability tests, the conventional electrolyte was determined to ignite easily, whereas the newly developed phosphoric ester electrolyte was determined to be difficult to ignite.

List of Publications

The main parts of this thesis are constructed from the following papers.

Chapter 2

T. Nishida, Y. Fukunaka, T. Homma and T. Nohira

"Galvanostatic Li Electrodeposition in LiTFSI-PC Electrolyte: Part I. Effects of Current Density in Initial Stage", Journal of The Electrochemical Society, 169 100548 (2022)

Chapter 3

T. Nishida, Y. Fukunaka, T. Homma and T. Nohira

"Galvanostatic Li Electrodeposition in LiTFSI-PC Electrolyte: Part II. Coupling Phenomena in Growth Process", Journal of The Electrochemical Society, 169 090529 (2022)

Chapter 4

T. Nishida, Y. Fukunaka, T. Homma and T. Nohira

"Galvanostatic Li Electrodeposition in LiTFSI-PC Electrolyte: Part III. Nucleation Behavior", in preparation.

Chapter 5

T. Nishida, Y. Fukunaka and T. Nohira

"Potentiostatic Li Electrodeposition in LiTFSI-PC Electrolyte", Journal of the American Chemical Society, submitted.

Chapter 6

T. Nishida, K. Nishikawa, M. Rosso and Y. Fukunaka

"Optical observation of Li dendrite growth in ionic liquid", Electrochimica Acta 100, 333–341 (2013)

Chapter 7

T. Nishida, Y. Fukunaka and T. Nohira

"Development of Non-flammable Electrolyte for Lithium Metal Batteries using Phosphoric Ester with $LiPO_2F_2$ Salt", in preparation.

Chapter 8

T. Nishida, Y. Fukunaka and T. Nohira

"Improvement of Non-flammable Phosphoric Ester Electrolyte for Lithium Metal Batteries by Mixed Salts of $LiPF_6$, $LiPO_2F_2$ and $LiNO_3$", in preparation.

Acknowledgements